

# Generically Orthogonal Event Decompositions and Measurement Combinations in Standard Model $VH$ ( $b\bar{b}$ ) Searches with the ATLAS Detector

A DISSERTATION PRESENTED  
BY  
STEPHEN K. CHAN  
TO  
THE DEPARTMENT OF PHYSICS

IN PARTIAL FULFILLMENT OF THE REQUIREMENTS  
FOR THE DEGREE OF  
DOCTOR OF PHILOSOPHY  
IN THE SUBJECT OF  
PHYSICS

HARVARD UNIVERSITY  
CAMBRIDGE, MASSACHUSETTS  
2018

<sup>18</sup> ©2017 – STEPHEN K. CHAN

<sup>19</sup> ALL RIGHTS RESERVED.

20                   **Generically Orthogonal Event Decompositions and**  
21                   **Measurement Combinations in Standard Model  $VH(b\bar{b})$**   
22                   **Searches with the ATLAS Detector**

23                   **ABSTRACT**

24         This thesis describes variations on the two lepton channel of the Run-2 search for the SM Higgs  
25         boson produced in association with a vector boson using different variable sets for multivariate anal-  
26         ysis (MVA) training. The three variable sets in question are the set of variables from the fiducial anal-  
27         ysis, a set based on the Lorentz Invariants (LI) concept, and a set based on a combination of masses  
28         and decay angles derived using the RestFrames (RF) package. Aside from the variable sets used for  
29         MVA training and discriminant distributions, the analysis is otherwise identical to the fiducial an-  
30         laysis. Both the LI and RF sets perform competitively on the basis of significances, with the RF set  
31         showing a  $\sim 3.5\%$  improvement in expected fits to Asimov and data, though neither set boosts ob-  
32         served significance. Both sets also reduce the observed error on  $\hat{\mu}$ , with the LI set reducing the error  
33         due to systematics by 7.5% and the RF set doing so by 16%.

34         The issue of combining multiple results from different channels and datasets is also examined  
35         through the combination of the fiducial Run 1 and Run 2 ATLAS  $VH(b\bar{b})$  results, which results in  
36         an observed signal strength of  $0.90^{+0.18}_{-0.18}(\text{stat.})^{+0.21}_{-0.19}(\text{syst.})$  and an observed (expected) significance  
37         of 3.6 (4.0) standard deviations, the first ever evidence of this process.

# Contents

38

39	o	INTRODUCTION	I
40	I	THE STANDARD MODEL HIGGS AND COLLIDER EVENT VARIABLES	4
41	1.1	The Standard Model Higgs Boson . . . . .	5
42	1.2	Higgs Boson Production and Decay at the Large Hadron Collider . . . . .	8
43	1.3	Collider Events and Event Level Variables . . . . .	II
44	1.4	Characterization with Event-Level Variables . . . . .	13
45	1.5	Lorentz Invariants . . . . .	16
46	1.6	RestFrames Variables . . . . .	18
47	1.7	Extensions to the $\ell$ and $\tau$ Lepton Channels . . . . .	20
48	2	THE LARGE HADRON COLLIDER AND THE ATLAS DETECTOR	24
49	2.1	The CERN Accelerator Complex . . . . .	25
50	2.2	The Large Hadron Collider . . . . .	25
51	2.3	ATLAS at a Glance . . . . .	31
52	2.4	The Inner Detector . . . . .	37
53	2.5	The ATLAS Calorimeters . . . . .	41
54	2.6	The Muon Spectrometer . . . . .	49
55	3	DATA AND SIMULATED SAMPLES	55
56	4	SIGNAL AND BACKGROUND MODELING	58
57	4.1	Event Generation In a Nutshell . . . . .	59
58	4.2	Description of Modeling Uncertainty Categories . . . . .	61
59	4.3	Process Specific Systematic Summaries . . . . .	72
60	5	OBJECT AND EVENT RECONSTRUCTION AND SELECTION	81
61	5.1	Triggers . . . . .	83
62	5.2	Electrons . . . . .	85
63	5.3	Muons . . . . .	87
64	5.4	Missing Transverse Energy . . . . .	89
65	5.5	Jets . . . . .	89
66	5.6	Flavor Tagging . . . . .	99
67	5.7	Miscellania and Systematics Summary . . . . .	109
68	5.8	Event Selection and Analysis Regions . . . . .	109

69	<b>6 MULTIVARIATE ANALYSIS CONFIGURATION</b>	112
70	6.1 Training Samples and Variable Selection . . . . .	113
71	6.2 MVA Training . . . . .	124
72	6.3 Statistics Only BDT Performance . . . . .	129
73	<b>7 STATISTICAL FIT MODEL AND VALIDATION</b>	135
74	7.1 The Fit Model . . . . .	136
75	7.2 Fit Inputs . . . . .	139
76	7.3 Systematic Uncertainties Review . . . . .	140
77	7.4 The VZ Validation Fit . . . . .	142
78	7.5 Nuisance Parameter Pulls . . . . .	146
79	7.6 Postfit Distributions . . . . .	154
80	7.7 VH Fit Model Validation . . . . .	161
81	<b>8 FIT RESULTS</b>	176
82	<b>9 MEASUREMENT COMBINATIONS</b>	182
83	9.1 Lepton Channel Combinations . . . . .	183
84	9.2 The Combined Fit Model . . . . .	187
85	9.3 Combined Fit Results . . . . .	202
86	<b>10 CLOSING THOUGHTS</b>	210
87	<b>APPENDIX A MICROMEGAS TRIGGER PROCESSOR SIMULATION</b>	213
88	A.1 Algorithm Overview . . . . .	214
89	A.2 Monte Carlo Samples . . . . .	219
90	A.3 Nominal Performance . . . . .	219
91	A.4 Fit Quantities . . . . .	220
92	A.5 Efficiencies . . . . .	226
93	A.6 Incoherent Background . . . . .	229
94	A.7 BCID . . . . .	234
95	A.8 Charge Threshold . . . . .	234
96	A.9 Misalignments and Corrections . . . . .	238
97	A.10 Individual Cases . . . . .	243
98	A.11 $ds \neq 0$ . . . . .	244
99	A.12 $dz \neq 0$ . . . . .	244
100	A.13 $dt \neq 0$ . . . . .	244
101	A.14 $\alpha \neq 0$ . . . . .	245
102	A.15 $\beta \neq 0$ . . . . .	245
103	A.16 $\gamma \neq 0$ . . . . .	245
104	A.17 Simulation Correction of the Algorithm Under Nominal Conditions . . . . .	248
105	A.18 Translation Misalignments Along the Horizontal Strip Direction ( $\Delta s$ ) . . . . .	251

106	A.19 Translation Misalignments Orthogonal to the Beamline and Horizontal Strip Direction ( $\Delta z$ ) . . . . .	253
108	A.20 Translation Misalignments Parallel to the Beamline ( $\Delta t$ ) . . . . .	255
109	A.21 Chamber Tilts Towards and Away from the IP ( $\gamma_s$ Rotation) . . . . .	256
110	A.22 Rotation Misalignments Around the Wedge Vertical Axis ( $\beta_z$ ) . . . . .	258
111	A.23 Rotation Misalignments Around the Axis Parallel to the Beamline ( $\alpha_t$ ) . . . . .	259
112	A.24 Conclusion . . . . .	261
113	<b>APPENDIX B TELESCOPING JETS</b>	263
114	B.1 Monte Carlo Simulation . . . . .	264
115	B.2 Jet Reconstruction and Calibration . . . . .	265
116	B.3 Event Reconstruction and Selection . . . . .	266
117	B.4 Validation of Jet Calibration . . . . .	269
118	B.5 Truth-Level Analysis . . . . .	272
119	B.6 Errors on Telescoping Significances . . . . .	275
120	B.7 Counting . . . . .	275
121	B.8 Multiple Event Interpretations . . . . .	276
122	B.9 $t(z) = z$ . . . . .	277
123	B.10 $t(z) = \rho_S(z) / \rho_B(z)$ . . . . .	278
124	B.11 Reconstructed-Level Analysis . . . . .	283
125	B.12 Conclusions and Prospects . . . . .	289
126	<b>APPENDIX C PROGRESS IN PARTICLE PHYSICS AND EXISTENTIAL THREATS TO THE AMERICAN WORLD ORDER</b>	290
128	<b>REFERENCES</b>	303



# Acknowledgments

<sup>131</sup> THIS THESIS WOULD NOT HAVE BEEN POSSIBLE without large amounts of espresso.

*Your life has a limit but knowledge has none...if you  
understand this and still strive for knowledge, you will  
be in danger for certain!*

Zhuangzi

# 0

132

133

## Introduction

134 SINCE THE DISCOVERY of a Standard Model (SM) like Higgs boson at the LHC in 2012[7][6], one  
135 of the main outstanding physics goals of the LHC has been to observe the primary SM Higgs decay  
136 mode,  $H \rightarrow b\bar{b}$ , with efforts primarily targeted at searching for Higgs bosons produced in associ-  
137 ation with a leptonically decaying vector ( $W$  or  $Z$ , denoted generically as  $V$ ) boson. This primary

138 Higgs decay mode also offers the best opportunity to observe direct Higgs coupling to quarks. As  
139 the integrated luminosity of data collected at the LHC increases,  $H \rightarrow b\bar{b}$  searches will increasingly  
140 become limited by the ability to constrain systematic uncertainties, with the latest result from AT-  
141 LAS at  $\sqrt{s} = 13$  TeV using  $36.1\text{ fb}^{-1}$  of  $pp$  collision data already approaching this regime, having a  
142  $VH(b\bar{b})$  signal strength of  $1.20^{+0.24}_{-0.23}(\text{stat.})^{+0.34}_{-0.28}(\text{syst.})$  at  $m_H = 125$  GeV [42].

143 While this effort will likely require a combination of several different methods at various differ-  
144 ent stages in the analysis chain, one possible avenue forward is to revise the multivariate analysis  
145 (MVA) discriminant input variables used, as various schemes offer the promise of reducing system-  
146 atic uncertainties through more efficient use of both actual and simulated collision data. This the-  
147 sis discusses two such alternate MVA schemes, the RestFrames (RF) and Lorentz Invariants (LI)  
148 variables, in the context of the 2-lepton channel of the Run 2 analysis in [42] and [65], henceforth  
149 referred to as the “fiducial analysis,” before a brief discussion of combinations across channels and  
150 datasets.

151 Electroweak symmetry breaking, Standard Model Higgs production and decay, and event level  
152 variables are treated in Chapter 1. The Large Hadron Collider and ATLAS detector are the subject  
153 of Chapter 2. Data and simulation samples used are described in Chapter 3. Signal and background  
154 modeling with accompanying systematics are defined in Chapter 4. Object and event reconstruction  
155 definitions and event selection requirements are outlined in Chapter 5. The multivariate analysis, in-  
156 cluding a description of the LI and RF variable sets and a summary of performance in the absence of  
157 systematic uncertainties, is described in Section 6. The statistical fit model and systematic uncertain-  
158 ties are described in Section 7, and the fit results may be found in Chapter 8. Combining channels

<sup>159</sup> and datasets at different  $\sqrt{s}$  values is discussed in the context of the Run 1 + Run 2 SM  $VH(b\bar{b})$

<sup>160</sup> combination in Chapter 9. Finally, conclusions and closing thoughts are presented in Chapter 10.

<sup>161</sup> Editorial notes:

<sup>162</sup> 1. pdf will be *probability* distribution function

<sup>163</sup> 2. PDF will be *parton* distribution function

<sup>164</sup> 3. Unless otherwise stated, ATLAS and LHC/CERN images are from public available material  
<sup>165</sup> from experiment webpages. Copyright terms may be found here [https://atlas.cern/  
<sup>166</sup> copyright](https://atlas.cern/copyright).

*The relationship between theorists and experimentalists  
is like that between a truffle farmer and his pig*

Howard Georgi

# 1

<sup>167</sup>

<sup>168</sup>

## The Standard Model Higgs and Collider

<sup>169</sup>

### Event Variables

<sup>170</sup> MUCH HAS BEEN SAID about the so-called Standard Model (SM) of particle physics, so only the

<sup>171</sup> bare essentials of electroweak symmetry breaking and Higgs production relevant to SM  $VH(b\bar{b})$  will

<sup>172</sup> be addressed here. This discussion follows [66] Chapter II in both content and notation. We then  
<sup>173</sup> move onto the treatment of kinematic variables in collider events, including the two novel schemes  
<sup>174</sup> considered in this thesis, the Lorentz Invariants (LI) and RestFrames (RF) concepts.

## <sup>175</sup> I.I THE STANDARD MODEL HIGGS BOSON

<sup>176</sup> The generic scalar Lagrangian potential (the kinetic term will be addressed later) for a scalar in the  
<sup>177</sup> SM is:

$$V(\Phi) = m^2 \Phi^\dagger \Phi + \lambda (\Phi^\dagger \Phi)^2 \quad (\text{I.1})$$

<sup>178</sup> where  $\Phi$  is a complex scalar doublet field under  $SU(2)$  from which the physical Higgs emerges after  
<sup>179</sup> symmetry breaking. Its four degrees of freedom are typically decomposed as follows:

$$\Phi = \frac{1}{\sqrt{2}} \begin{pmatrix} \sqrt{2}\phi^+ \\ \phi^0 + i\alpha^0 \end{pmatrix} \quad (\text{I.2})$$

<sup>180</sup>  $\phi^+$  is the complex charged component of the Higgs doublet, and  $\phi^0$  and  $\alpha^0$  are the CP-even and  
<sup>181</sup> CP-odd neutral components, respectively.

<sup>182</sup> If the sign of  $m^2 \Phi^\dagger \Phi$  is negative,  $\Phi$  acquires a *vacuum expectation value* or VEV:

$$\langle \Phi \rangle = \frac{1}{\sqrt{2}} \begin{pmatrix} 0 \\ \sqrt{\frac{2m^2}{\lambda}} \end{pmatrix} \quad (\text{I.3})$$

<sup>183</sup> with this value typically denoted  $v = \sqrt{2m^2/\lambda} = (\sqrt{2}G_F)^{-1/2} \approx 246 \text{ GeV}$  (with the coupling

<sup>184</sup> of the 4-Fermi effective theory of weak interactions measured through experiments involving muon  
<sup>185</sup> decay), and  $\phi^0$  is rewritten as  $\phi^0 = H + v$ .

<sup>186</sup> This non-zero VEV induces spontaneous symmetry breaking in the SM's gauge (local) symme-  
<sup>187</sup> try group of  $SU(3)_C \times SU(2)_L \times U(1)_Y$  since the VEV does not respect the  $SU(2)_L \times U(1)_Y$   
<sup>188</sup> symmetry of the Lagrangian (i.e.  $\langle \Phi \rangle$  is not invariant under a gauge transformation of this group).

<sup>189</sup> Three of the four generators of this subgroup are spontaneously broken, which implies the existence  
<sup>190</sup> of three massless Goldstone bosons, which are in turn “eaten” by linear combinations of the  $W^a$   
<sup>191</sup> (with coupling strength  $g$ ) and  $B$  (with coupling strength  $g'$ ) bosons to form the longitudinal polar-  
<sup>192</sup> izations of the familiar  $W^\pm$  and  $Z$  bosons, with the last generator giving rise to the usual, unbroken  
<sup>193</sup>  $U(1)_{EM}$  symmetry and its massless photon,  $A$ , as well as the scalar Higgs boson  $H$ . To see this, one  
<sup>194</sup> starts with the full Higgs SM Lagrangian (kinetic minus potential only)

$$\mathcal{L}_{Higgs} = (D_\mu \Phi)^\dagger (D_\mu \Phi) - V(\Phi), \quad D_\mu \Phi = (\partial_\mu + ig\sigma^a W_\mu^a + ig' Y B_\mu / 2) \Phi \quad (1.4)$$

<sup>195</sup> One simply plugs in the reparametrized  $\Phi$  with  $\phi^0 = H + v$ , collects the terms involving  $v$  together  
<sup>196</sup> with the appropriate  $W$  and  $B$  kinetic terms to extract:

$$M_W^2 = \frac{g^2 v^2}{4}, \quad M_Z^2 = \frac{(g'^2 + g^2) v^2}{4} \quad (1.5)$$

<sup>197</sup> This is left as an exercise for the reader; this exercise also makes manifest that the Higgs couples with  
<sup>198</sup> the  $W^\pm$  and  $Z$  with strength quadratic in the gauge boson masses. Since the Higgs field also respects

<sup>199</sup> the  $SU(3)_C$  color symmetry, the eight gluons are also left massless, and the  $H$  is left interacting with  
<sup>200</sup> photons and gluons primarily through heavy quark loops (i.e. no tree-level interactions).

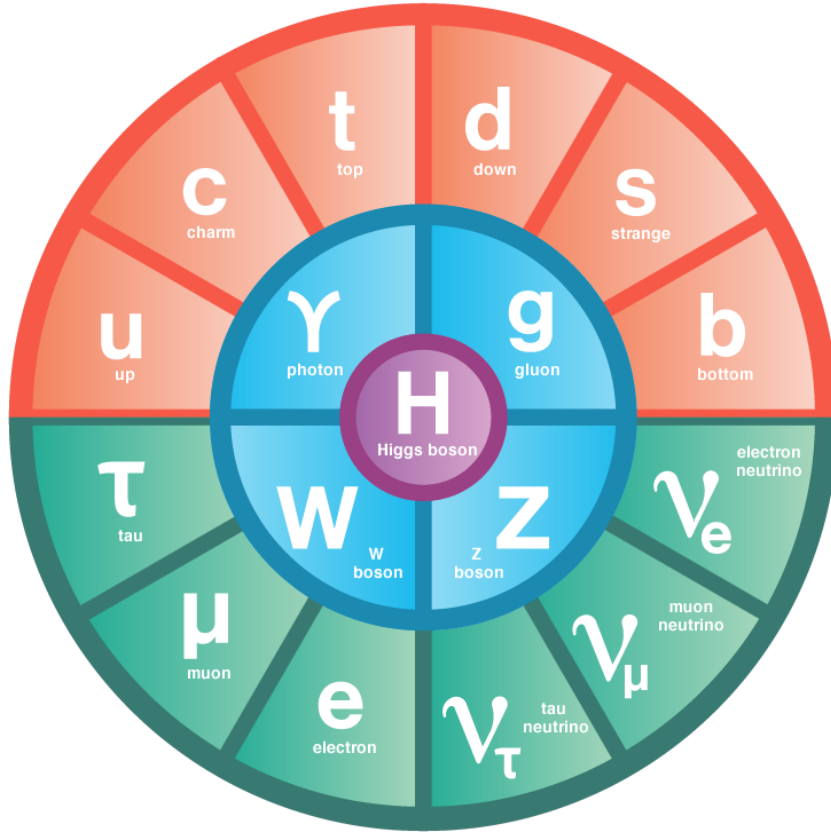


Figure 1.1: The fundamental particles of the Standard Model. IC: [75]

<sup>201</sup> The Higgs is often introduced to the public at large as the mechanism through which fundamen-  
<sup>202</sup> tal fermions (enumerated in Figure 1.1) acquire mass—this is through the Yukawa interactions of the  
<sup>203</sup> Higgs:

$$\mathcal{L}_{Yukawa} = -\hat{h}_{d_{ij}} \bar{q}_{L_i} \tilde{\Phi} d_{R_j} - \hat{h}_{u_{ij}} \bar{q}_{L_i} \tilde{\Phi} u_{R_j} - \hat{h}_{l_{ij}} \bar{l}_{L_i} \tilde{\Phi} e_{R_j} + h.c. \quad (1.6)$$

<sup>204</sup> where  $\tilde{\Phi} = i\sigma_2 \Phi^*$ ,  $q_L$  ( $l_L$ ) and  $u_R$ ,  $d_R$  ( $e_R$ ) are the quark (lepton) left-handed doublets and right

205 handed singlets of the weak  $SU(2)_L$  group, with each term parametrized by a  $3 \times 3$  matrix in family  
206 space (also known as the fermion generations). The neutrinos have been purposely omitted since  
207 the mechanism that generates their mass is as of yet unknown, though these Yukawa interactions  
208 could have a non-zero contribution to neutrino masses. Once the Higgs VEV value is known and  
209 the Yukawa interaction matrices  $\hat{b}_{f_i j}$  (with  $i, j \in \{1, 2, 3\}$ ) are diagonalized, the fermion masses  
210 can simply be written as  $m_{f_i} = b_{f_i} v / \sqrt{2}$ . The SM has no motivation for any of these mass values,  
211 instead leaving them as empirically determined free parameters.

212 Note that from  $\mathcal{L}_{Yukawa}$ , it is easy to see that the Higgs couplings with fermions scale linearly with  
213 fermion mass. Higgs self-couplings and beyond the standard model (BSM) Higgs scenarios are be-  
214 yond the scope of this thesis.

## 215 1.2 HIGGS BOSON PRODUCTION AND DECAY AT THE LARGE HADRON COLLIDER

216 The leading order Feynman diagrams for the four dominant modes of Higgs production at the LHC  
217 are shown in Figure 1.2, each described briefly in turn. The dominant process, accounting for some  
218 87% of Higgs production at the nominal LHC center of mass energy of 14 TeV, is gluon-gluon fu-  
219 sion (ggF), shown at top left in Figure 1.2. At high center of mass energies, most of a proton's mo-  
220 mentum is predominantly carried by gluons (as opposed to the constituent valence quarks associ-  
221 ated with the hadron's identity). This, along with the difficulties associated with high luminosity  
222 antiproton beam production, is why the LHC was designed as a proton-proton collider instead of  
223 a proton-antiproton collider (like the Tevatron or SppS). As mentioned above, the Higgs does not  
224 couple directly to gluons but must instead be produced through the fermion loop shown in the fig-

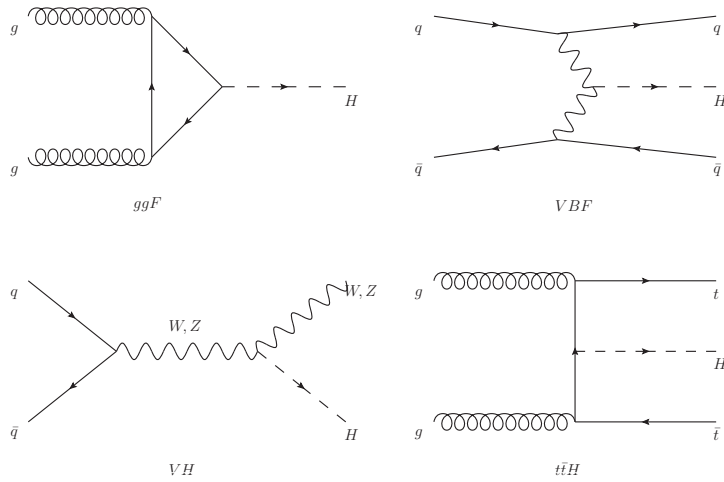


**Figure 1.2:** Dominant Higgs production modes.

ure. The heaviest fundamental fermion by far is the top quark, with  $m_t = 173$  GeV, so top loops dominate this process. While not particularly relevant for this thesis, about 14% of events in the lepton channel of the  $H \rightarrow b\bar{b}$  analysis are ggF initiated.

The next most prevalent process is vector boson fusion (VBF), where vector bosons ( $W$  or  $Z$ , denoted generically as  $V$ ) from quarks in the colliding protons “fuse” to form a Higgs. These quarks typically form jets in the forward region, which provide a unique signature for this process. This process is not relevant for this thesis.

The third leading process is “Higgsstrahlung” or Higgs production in association with a vector boson, often simply  $VH$  production. In this process, a quark-antiquark pair in the colliding protons forms an energetic vector boson, which then radiates a Higgs (this is similar to photon emission of accelerating electrons, called “Bremsstrahlung,” hence the name). Some fraction of the time (about 21% of the time for  $WH$  and 6.7% of the time for  $ZH$ ), the energetic  $V$  will decay leptonically (i.e.

237 into a decay involving an electron or a muon), which provides a unique and triggerable signature  
 238 for this process. Another 20% of the time for  $ZH$  production, the  $Z$  will decay to neutrinos, which  
 239 are not absorbed by detectors and show up as missing transverse energy ( $\vec{E}_T^{\text{miss}}$ ), another triggerable  
 240 signature. This ability to trigger on leptons and  $\vec{E}_T^{\text{miss}}$  and the requirement that this leptonic signa-  
 241 ture be consistent with a  $V$  allow one to significantly reduce the impact of multijet background (a  
 242 very common generic processes at the LHC) on analysis. Hence, this is the process of primary impor-  
 243 tance to this thesis.

244 The final important Higgs production process is  $t\bar{t}H$  production, the box diagram in the lower  
 245 right of Figure 1.2. Again, the top pair provides a useful signature for analysis. This, like VBF, is also  
 246 not considered in this thesis.

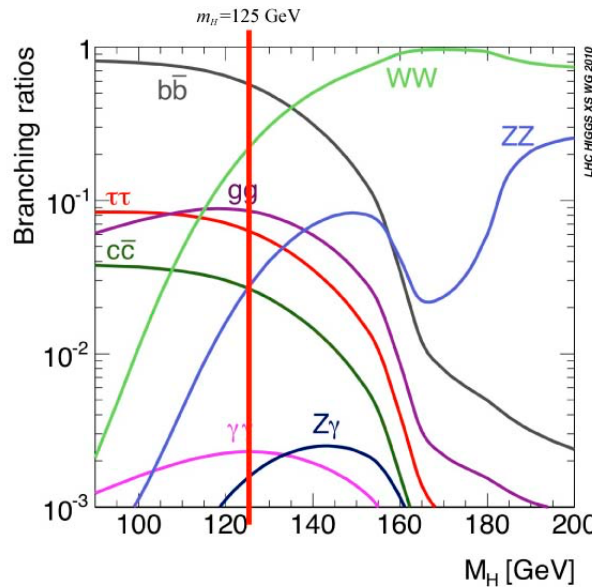


**Figure 1.3:** Higgs decay mode branching fractions as a function of its mass; a line has been drawn at the observed Higgs mass of 125 GeV.

Once the Higgs has been produced, it can decay in a number of ways, as shown in Figure 1.3. By far the most dominant decay mode of the Higgs is to  $b\bar{b}$  with a branching fraction of 58%. This  $b$ -quark pair then hadronizes into two  $b$ -jets (for a more thorough discussion of jets and  $b$ -jets in particular, see Section 5.5). However, many processes at the LHC create pairs of  $b$ -jets with invariant masses consistent with the Higgs and have much higher production rates ( $t\bar{t}$  production at the LHC is in the neighborhood of hundreds of pb, compared to Higgs cross sections of a few pb), so a clear process signature is necessary to study  $H \rightarrow b\bar{b}$  production at the LHC. This is why the bulk of search efforts have focused on  $VH$  production. A summary of Higgs production cross sections and simple extrapolations to raw numbers of Higgs bosons produced for  $VH$  for leptonically decaying  $V$  is shown in Table 1.1

$\sqrt{s}$ (TeV)	ZH	WH	ggF	total $\sigma$	$N_{V \rightarrow \ell^+ \nu} H$
7	$0.34^{+4\%}_{-4\%}$	$0.58^{+3\%}_{-3\%}$	$15.3^{+10\%}_{-10\%}$	17.5	$4.7 \text{ fb}^{-1} \rightarrow 589$
8	$0.42^{+5\%}_{-5\%}$	$0.70^{+3\%}_{-3\%}$	$19.5^{+10\%}_{-11\%}$	22.3	$20.3 \text{ fb}^{-1} \rightarrow 3100$
13	$0.88^{+5\%}_{-5\%}$	$1.37^{+2\%}_{-2\%}$	$44.1^{+11\%}_{-11\%}$	50.6	$36.1 \text{ fb}^{-1} \rightarrow 11100$
14	$0.99^{+5\%}_{-5\%}$	$1.51^{+2\%}_{-2\%}$	$49.7^{+11\%}_{-11\%}$	57.1	$1000 \text{ fb}^{-1} \rightarrow 343000$

**Table 1.1:** Cross sections (in pb) for processes important to the SM  $VH$  ( $b\bar{b}$ ) analysis and the total Higgs cross section as a function of center of mass energy. Also given are the total number of Higgs bosons produced for given luminosities through both  $WH$  and  $ZH$  processes. Uncertainties are theoretical.

### 1.3 COLLIDER EVENTS AND EVENT LEVEL VARIABLES

Collision data in experiments like ATLAS is structured using what is known as the *event data model*. In this model, one collision corresponds to one event. Since each bunch crossing contains more than one proton, there can be more than one collision per event and more than one hard scatter per col-

261 lision. For each collision, tracks in an experiment's inner detector are used to identify the most ener-  
 262 getic collision, which is taken to be the event. The raw data, the various tracks, energy deposits, and  
 263 hits in the detector, undergo reconstruction (described at length in Chapter 5) both through auto-  
 264 mated, experiment-wide, standardized production and through analysis-specific level selections, cor-  
 265 rections, and calibrations. The result of this considerable effort is a collection of labeled 4-vectors,  
 266 representing the final state objects. This is shown in Figure 1.4.

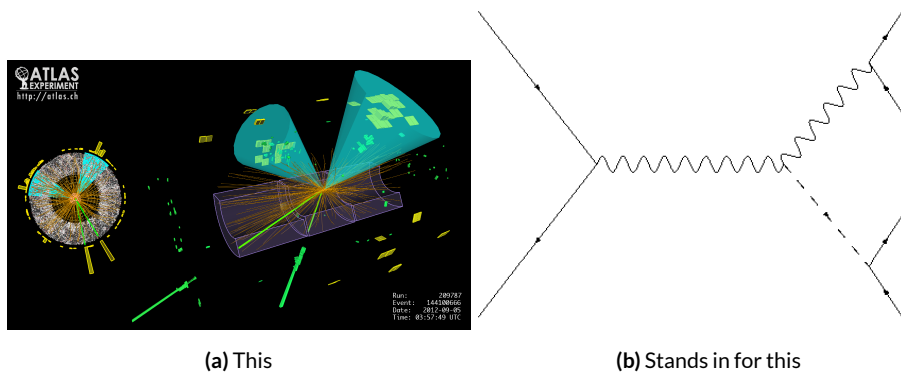


**Figure 1.4:** Reconstruction in a nutshell

267 In the process that is the focus of this thesis, every event ultimately is condensed into a lepton pair  
 268 (two electrons or two muons), two or three jets\*, all 4-vectors, and a  $\vec{E}_T^{\text{miss}}$  vector in the transverse  
 269 plane. Further selection then takes place to winnow down events into interesting regions of phase  
 270 space hopefully more rich in signal-like events. Once events are selected in a search like the one in  
 271 this thesis, one then analyzes the data to test its consistency with some background only hypothesis  
 272 to produce the usual statistical results. This can be done in various ways, with principal approaches

---

\*Sometimes more, though this is a small fraction of events, and the wisdom of this choice may be questioned

273 being: a simple counting experiment (often referred to as the “cut and count” approach), a func-  
274 tional fit for excesses over a falling background spectrum (the so-called “bump hunt” used in anal-  
275 yses like the  $H \rightarrow \gamma\gamma$  discovery channel), or the use of discriminant distributions as PDF’s in a  
276 likelihood fit (the approach of this analysis). These distributions can be simple counts (i.e. single bin  
277 distributions) in analysis regions, quantities of interest (the distribution of the invariant mass of the  
278 two  $b$ -jets in selected events with the greatest transverse momenta,  $m_{bb}$ , is used as a validation), or a  
279 multivariate analysis (MVA) discriminant.

#### 280 I.4 CHARACTERIZATION WITH EVENT-LEVEL VARIABLES

281 Traditionally, particle physicists have favored the approach of using distributions of physical vari-  
282 ables since it is easier to develop physical intuition for what these distributions should look like  
283 during validation, so it is no surprise that as many LHC analyses have transitioned to using MVA  
284 techniques that these variables form the basis of many very robust physics results. These variables  
285 do quite well summarize many of the main physics features of an event for the signal topology, cer-  
286 tainly much better than feeding all 18–22 4-vector components directly into a machine learning algo-  
287 rithm. In  $ZH \rightarrow \ell\ell b\bar{b}$  events, for example, one wishes to characterize the  $ZH$  system by using the  
288 lepton pair as a stand-in for the  $Z$  and the  $b$ -jet pair as a stand-in for the  $H$ , and composite variables  
289 like  $m_{bb}$  and  $m_{\ell\ell}$  can be used to check whether events are consistent with these objects. There are  
290 also variables like  $\vec{p}_T^V$  that characterize the momentum scale of the event, angles like  $\Delta R(b_1, b_2)$  and  
291  $\Delta\phi(V, H)$  that can be further used to characterize the overall “shape” of these events, and variables  
292 like  $\vec{E}_T^{\text{miss}}$  that can discriminate against backgrounds like  $t\bar{t}$  that do not have a closed topology.

293 Nevertheless, the intuition based approach, with incremental addition of variables as they prove  
294 useful in the lifetime of an analysis's iterations, does beg the question of whether there is a more sys-  
295 tematic way to treat this information. There are clearly patterns to which variables are useful: these  
296 correspond to important information about the hypothesized physics objects and their relation-  
297 ships, and there have been many attempts to systematize the way these variables are found. Such  
298 systematic, top-down approaches often promise to increase performance in two ways. The first is by  
299 having higher descriptive power, often through some sophisticated treatment of the missing trans-  
300 verse energy in an event,  $\vec{E}_T^{\text{miss}}$ .  $\vec{E}_T^{\text{miss}}$  is just a single quantity, and if there is just one invisible object  
301 in a desired event topology, using  $\vec{E}_T^{\text{miss}}$  on its own often provides sufficient sensitivity. In more com-  
302 plicated topologies with multiple invisible particles in the final state, for example in many supersym-  
303 metry searches, a more careful treatment of the missing energy is often necessary.

304 The second means of improvement is through using a more orthogonal basis of description,  
305 which allows one to more efficiently use data and simulation samples. A more orthogonal basis im-  
306 plies that variables contain less overlapping information with each other and so allow for a more  
307 efficient exploration of parameter space. This means one can gain higher sensitivity from equivalent  
308 datasets using a more orthogonal basis. To see why this might be the case, take an MVA discrimi-  
309 nant for  $ZH \rightarrow \ell\ell b\bar{b}$  formed using only the classic variables  $\Delta R(b_1, b_2)$  and  $p_T^V$ . In the  $ZH \rightarrow$   
310  $\ell\ell b\bar{b}$  topology, the transverse mass of the  $Z$  and  $H$  (and hence the lepton pair and jet pair) are equiv-  
311 alent. This means that at higher  $p_T^V$  the  $p_T$  of  $b$ -jets will also be higher, which in turn implies that  
312 they will have a smaller angle of separation and hence a smaller  $\Delta R(b_1, b_2)$ . This correlation is not  
313 unity—each variable still does have information the other does not—but is still very high. Hence,

314 when training an MVA, which in principle knows nothing about these variables other than some  
315 set limits, an undue number of training events will be wasted converging upon relations that could  
316 be known *a priori*, and while this might be easy to hard code in for a two variable toy example, the  
317 dimensionality of any real discriminant makes this prohibitive. An MVA that uses data (both ac-  
318 tual and simulated) more efficiently will also tend to be have lower variance, offering a potential av-  
319 enue for reduction in the error on quantities of interest due to systematic uncertainties. Details of  
320 how this plays out in a likelihood fit will be deferred to the discussion of the fit model used in the  
321  $VH(b\bar{b})$  search in Chapter 7.

322 Many of these novel schemes are designed to explicitly address the first issue of invisibles in the  
323 final state in channels where it is of paramount importance while having the second issue as some-  
324 thing of a fringe benefit. However, as the amount of data taken at the LHC grows, analyses will in-  
325 creasingly become systematics limited, so an exploration to the veracity of the second claim has great  
326 potential for the high luminosity era of the LHC. The  $ZH \rightarrow \ell\ell b\bar{b}$  process offers a great setting for  
327 investigating this issue on its own since its closed topology largely mitigates any improvement from  
328 more sophisticated treatments of  $\vec{E}_T^{\text{miss}}$ . We introduce two of these more top-down approaches to  
329 event-level variables below: the “Lorentz Invariant” (LI) [53] and “RestFrames inspired” (RF) [56]  
330 variable schemes. A broad overview of the concepts behind these schemes will be given here, with a  
331 more in-depth discussion of their implementation deferred until Chapter 6.

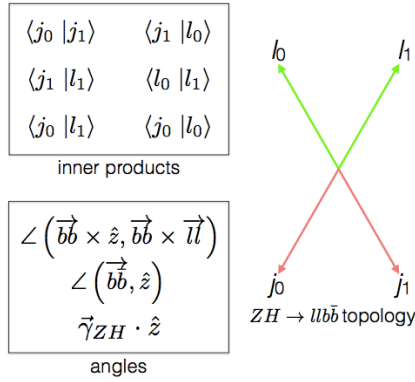


**Figure 1.5:** Summary of LI variables in the  $ZH \rightarrow \ell\ell b\bar{b}$  topology.

332    **I.5 LORENTZ INVARIANTS**

333    The LI variables, first put forth by S. Hagebeck and others [53], are based upon the concept that  
 334    once the 4-vectors of an event are determined, all of the information in an event are encoded into  
 335    their inner products (Lorentz invariant quantities, hence the name) and the angles between them.  
 336    This makes for 16 quantities in all: the ten inner products of the 4-vectors, the three Euler angles,  
 337    and the three parameters specifying the boost of the  $ZH$  system. The masses of the four final state  
 338    objects are not considered very useful and so can be removed to leave six meaningful inner products  
 339    (the  ${}_4C_2$  combinations<sup>†</sup> between distinct final state 4-vectors). Since these inner products can have  
 340    an ill-defined physical interpretation and in order to help MVA training, each inner product is scaled

---

<sup>†</sup> ${}_nC_r = \frac{n!}{r!(n-r)!}$ , read “ $n$  choose  $r$ ” and known as the binomial coefficient, is the number of unique possible ways to choose combinations of  $r$  objects from a total set of  $n$  without regard to ordering within combinations.

<sup>341</sup> by:

$$x \rightarrow \frac{x}{x + c} \quad (1.7)$$

<sup>342</sup> where  $c$  is the mean of the distribution in the signal MC distribution. These inner products are de-  
<sup>343</sup> noted  $x_i y_j$ , where  $x$  and  $y$  are either  $j$  (for jet) or  $l$  (for lepton) and the indices are either  $o$  ( $i$ ) for  
<sup>344</sup> the leading (subleading) object by  $p_T$  in the event.

<sup>345</sup> The number of useful angles can be reduced by recognizing some symmetries inherent in the fi-  
<sup>346</sup> nal state. The symmetry around the beam axis eliminates one angle. Furthermore, the boost of the  
<sup>347</sup>  $VH$  system is primarily in the beam direction ( $z$ ) direction, marginalizing the utility of the trans-  
<sup>348</sup> verse boost angles. This leaves the boost in the  $z$  direction, denoted `gamma_ZHz`, and two angles  
<sup>349</sup> chosen to be the angle between the  $b\bar{b}$  system and the beam (`angle_bb_z`) and the angle between  
<sup>350</sup>  $(\vec{b}_1 + \vec{b}_2) \times \hat{z}$  and  $(\vec{b}_1 + \vec{b}_2) \times (\vec{l}_1 + \vec{l}_2)$  (`angle_bbz_bbll`).

<sup>351</sup> These variables do contain a lot of information similar to the usual set: there are mass equivalents  
<sup>352</sup> ( $j_0 \leftrightarrow m_{bb}$ , and  $l_0 \leftrightarrow m_{\ell\ell}$ ) and angles. Instead of individual final state object scales, there  
<sup>353</sup> are the four jet/lepton inner products, though this correspondence (and indeed any physical inter-  
<sup>354</sup> pretation) is far from clear. An important advantage of the LI variable set is that all of the variables  
<sup>355</sup> are in it are orthogonal in the signal case by construction. A drawback of this framework in a com-  
<sup>356</sup> pletely closed final state is that there is no way to treat  $E_T^{miss}$  in a Lorentz invariant way.

<sup>357</sup> There is also no prescription for any additional jets in the event beyond the two  $b$ -tagged jets.  
<sup>358</sup> They are simply ignored in these variable calculations since the fiducial analysis requirement of ex-

<sup>359</sup> actly two  $b$ -tagged jets eliminates any combinatoric ambiguity, and additional, untagged jets are as-  
<sup>360</sup> sumed (not entirely rigorously) to be unrelated to the signal-like hard scatter.

## <sup>361</sup> 1.6 RESTFRAMES VARIABLES

<sup>362</sup> The RestFrames variables [56], calculated using the software package of the same name, is based  
<sup>363</sup> upon the idea that the most natural frame in which to analyze objects of the signal decay tree is in  
<sup>364</sup> their individual production (rest) frames. The signal decay tree for  $ZH \rightarrow \ell\ell b\bar{b}$  is show in Figure  
 1.6. Generally, one does not typically have enough information to determine exactly each of the in-

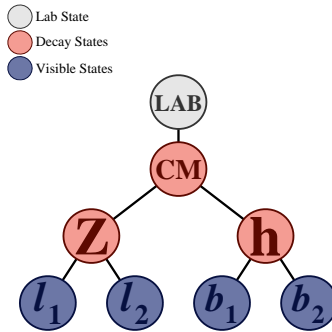


**Figure 1.6:** The  $ZH \rightarrow \ell\ell b\bar{b}$  decay tree.

<sup>365</sup>

<sup>366</sup> termediate rest frames or the boosts between the frames, but in a completely closed final state like  
<sup>367</sup>  $ZH \rightarrow \ell\ell b\bar{b}$ , this can be done in the usual way by adding the 4-vectors of the final state objects and  
<sup>368</sup> solving the usual equations from special relativity (RestFrames does this automatically for each  
<sup>369</sup> event).

<sup>370</sup> Each frame has associated with it the boost from its immediate parent and a mass scale; that mass  
<sup>371</sup> (in this case the correspondence between RF mass variables and standard mass variables is exact) and  
<sup>372</sup> the angles between the Euclidean three vector associated with boost and the axis of the decay prod-

373   ucts provide useful variables. In general, the polar angle (typically given as a cosine) is considered  
 374   more useful than the azimuthal angle (typically just a  $\Delta\phi$ ), though this is dependent on the candi-  
 375   date decay tree. The  $Z$  frame, for example, has  $M_Z$ , which is just the usual  $m_{\ell\ell}$ ,  $\cos Z$ , the cosine of  
 376   the polar angle between the lepton momentum axis in their production frame and the boost from  
 377   the  $ZH$  center of mass (CM) frame, and the angle  $d\phi_{hCMZ}$ .

378   In addition to the masses and angles attached to individual object rest frames, energy scales associ-  
 379   ated with the CM frame can be used to contextualize other event level quantities. In particular, one  
 380   can use the mass of the CM frame as a natural scale to evaluate the momentum of the CM frame,  
 381   and the  $p_T$  of the CM frame as a natural scale for the event's  $E_T^{miss}$ , yielding the variables:

$$R_{p_T} = \frac{p_{T,CM}}{p_{T,CM} + M_{CM}}, \quad R_{p_z} = \frac{p_{z,CM}}{p_{z,CM} + M_{CM}}, \quad R_{met} = \frac{E_T^{miss}}{E_T^{miss} + p_{T,CM}} \quad (1.8)$$

382   denoted  $R_{pT}$ ,  $R_{pZ}$ , and  $R_{met}$ . These can be thought of as behaving like significance based variables  
 383   in particle physics, like METHT or impact parameter significances, or event level defined versions  
 384   of the scalings applied to the LI inner products. These are used instead of the final state object scales  
 385   and standard  $E_T^{miss}$  of the standard variable set.

386   Unlike the LI variables, the physical interpretation of RF variables is very clear. Everything has  
 387   physical units, and these are variables one might have introduced in the usual process of develop-  
 388   ing an MVA with the traditional mindset. The solution to the issue of additional jets in an event is  
 389   not immediately clear. In order to keep the two non-standard MVA's on as equal footing as possi-  
 390   ble, the approach of simply ignoring additional jets is taken in this thesis. Nevertheless, it would be

391 easy enough to redefine the  $H$  intermediate frame to have, for example, the two  $b$ -tagged jets and the  
 392 highest  $p_T$  untagged jet for any subset of events. This flexibility is not a feature of the Lorentz Invari-  
 393 ants framework. Of course, `RestFrames` cannot tell you what approach to take, but it is capable of  
 394 handling more flexible topologies once optimization studies have been completed.

### 395 1.7 EXTENSIONS TO THE 1 AND 0 LEPTON CHANNELS

396 Both the LI and RF variable concepts are readily extendable to the 1-lepton channel. In this topol-  
 397 ogy, one of the leptons in the  $ZH \rightarrow \ell\ell b\bar{b}$  diagram is replaced by a neutrino, the lone invisible  
 398 particle in this final state. We can assume that the neutrino has zero mass and transverse momentum  
 399 equal to the  $\vec{E}_T^{\text{miss}}$  in the event, leaving one undetermined degree of freedom, the longitudinal mo-  
 400 mentum of the neutrino,  $p_z^\nu$ .

401 The LI concept was in fact initially formulated to improve sensitivity in the 1-lepton channel,  
 402 with the same orthogonality of variables described in the 2-lepton case being the main draw. The LI  
 403 approach to estimating the neutrino longitudinal momentum is outlined in [53], which we repro-  
 404 duce here. We first guess the neutrino energy in its rest frame and then boost to the lab frame:

$$\langle E_\nu \rangle = \frac{1}{4} m_{WH} \implies \langle p_z^\nu \rangle = \beta \gamma \langle E_\nu \rangle = \frac{p_z^{WH}}{m_{WH}} \langle E_\nu \rangle = \frac{1}{4} p_z^{WH} \quad (1.9)$$

405 Finally, assuming energy and momentum in aggregate are equally shared among final state con-  
 406 stituents, we arrive at

$$\langle p_z^\nu \rangle = \frac{1}{4} \times \frac{4}{3} (p_z^l + p_z^{j0} + p_z^{j1}) \quad (1.10)$$

407 The RF approach for the 1-lepton case amounts to replacing the  $Z \rightarrow \ell\ell$  in 1.6 with  $W \rightarrow \ell\nu$ .  
408 As alluded to in the 2-lepton discussion, when there is missing information in the final state from  
409 invisible particles and/or combinatoric ambiguities, recursive jigsaw reconstruction (RJR) offers a  
410 standard toolkit for deriving estimated boosts between rest frames by analytically minimizing on  
411 unknown quantities. While in more exotic final states with multiple invisible particles and combi-  
412 natoric ambiguities the choice of jigsaw rule can be subjective, the case of  $W$  is well-studied and out-  
413 lined in detail in Section V.A. of [56]. It reproduces the usual transverse mass of the  $W$  in place of  
414 MZ in the 2-lepton case. Not surprisingly, the underlying calculation is also much the same as the LI  
415 case (where rest frames and boost were explicitly invoked); again, information is the same, only its  
416 decomposition is different.

417 The 0-lepton channel would appear to present some difficulty as two neutrinos in the final state  
418 introduce extra degrees of freedom, but both concepts may be extended by treating the invisibly de-  
419 caying  $Z$  as a single invisible particle and requiring the  $Z$  to be on-shell. Both of these requirements  
420 may be folded into the 1-lepton framework to produce similar sets of variables.

421 While the precise variables that would be included in 0- and 1-lepton LI and RF MVA discrimi-  
422 nants is beyond the scope of this thesis, looking at Table 9.1, we can see the dimensionality and in-  
423 puts of the discriminants of the fiducial analysis. The correspondence for LI/RF variables and stan-  
424 dard variables extends nicely to the other lepton channels. The reduction in multiplicity of variables  
425 owing the lower number of degrees of freedom provided by treating the  $Z$  as a single invisible par-  
426 ticle in the 0-lepton channel would likely not be an issue, as one would just be able to use a greater  
427 fraction of available variables in the MVA discriminant.

Variable	Name	0-lepton	1-lepton	2-lepton
$\vec{p}_T^V$	pTV		✓	✓
$\vec{E}_{\text{T}}^{\text{miss}}$	MET	✓	✓	✓
$\vec{p}_T^{\text{jet}1}$	pTB1	✓	✓	✓
$\vec{p}_T^{\text{jet}2}$	pTB2	✓	✓	✓
$\text{MV}_{2\text{C10}}(\text{jet}_1)^*$	$\text{MV}_{2\text{C10B1}}$	✓	✓	✓
$\text{MV}_{2\text{C10}}(\text{jet}_2)^*$	$\text{MV}_{2\text{C10B2}}$	✓	✓	✓
$m_{jj}$	mBB	✓	✓	✓
$\Delta R(\text{jet}_1, \text{jet}_2)$	dRBB	✓	✓	✓
$ \Delta\eta(\text{jet}_1, \text{jet}_2) $	dEtaBB	✓		
$\Delta\phi(V, H)$	dPhiVBB	✓	✓	✓
$\Delta\eta(V, H)$	dEtaVBB			✓
$M_{\text{eff}}(M_{\text{eff}3})$	HT	✓		
$\min(\Delta\phi(\ell, \text{jet}))$	dPhiLBmin		✓	
$m_{\text{T}}^W$	mTW		✓	
$m_{ll}$	mLL			✓
$\Delta Y(W, H)$	dYWH		✓	
$m_{\text{top}}$	mTop		✓	
Only in 3 Jet Events				
$\vec{p}_T^{jet3}$	pTJ3	✓	✓	✓
$\text{MV}_{2\text{C10}}(\text{jet}_3)^*$	$\text{MV}_{2\text{C10B3}}$	✓	✓	✓
$m_{jjj}$	mBBJ	✓	✓	✓

**Table 1.2:** Variables used to train the multivariate discriminant. Starred variables ( $b$ -tag scores) are not included in current versions of the standard discriminants, but have traditionally been included and most likely will be reintroduced as soon as their accompanying systematics are available.

<sup>428</sup>     *Maybe do the o-lep calculation and o/1-lep RF cartoons*

*Noli turbare circulos meos*

Archimedes

# 2

<sup>429</sup>

## <sup>430</sup> The Large Hadron Collider and the ATLAS

### Detector

<sup>431</sup>

<sup>432</sup> THE CERN ACCELERATOR COMPLEX AND ITS EXPERIMENTS stand as a testament to human in-  
<sup>433</sup> genuity and its commitment to the pursuit of fundamental knowledge. In this chapter, we give a

<sup>434</sup> cursory overview of the CERN accelerator complex, including the Large Hadron Collider (LHC),  
<sup>435</sup> before moving on to a more detailed review of the ATLAS detector.

<sup>436</sup> **2.1 THE CERN ACCELERATOR COMPLEX**

<sup>437</sup> The journey of protons from hydrogen canister to high energy collisions through the CERN ac-  
<sup>438</sup> celerator complex, illustrated in Figure 2.1, is also one through the history of CERN’s accelerator  
<sup>439</sup> program. After being ionized in an electric field, protons are first accelerated in a linear accelera-  
<sup>440</sup> tor, LINAC 2<sup>\*</sup>, to a kinetic energy of 50 MeV. From there, they are fed into the Proton Synchotron  
<sup>441</sup> Booster<sup>†</sup>, which further accelerates them to 1.4 GeV and, as its name implies, feeds them to the 628  
<sup>442</sup> m Proton Synchotron (PS, 1959[8]) and up to 25 GeV. The penultimate stage is the 7 km Super  
<sup>443</sup> Proton Synchotron (SPS, 1976; responsible for the discovery of the  $W$  and  $Z$  bosons and the 1983  
<sup>444</sup> Nobel Prize [10]), which accelerates the protons to a kinetic energy of 450 GeV. Finally, these 450  
<sup>445</sup> GeV protons are injected into the LHC[50], a proton-proton collider housed in the 27 km circumfer-  
<sup>446</sup> ence tunnel that housed the Large Electron Positron Collider (LEP) before its operations ceased in  
<sup>447</sup> 2000.

<sup>448</sup> **2.2 THE LARGE HADRON COLLIDER**

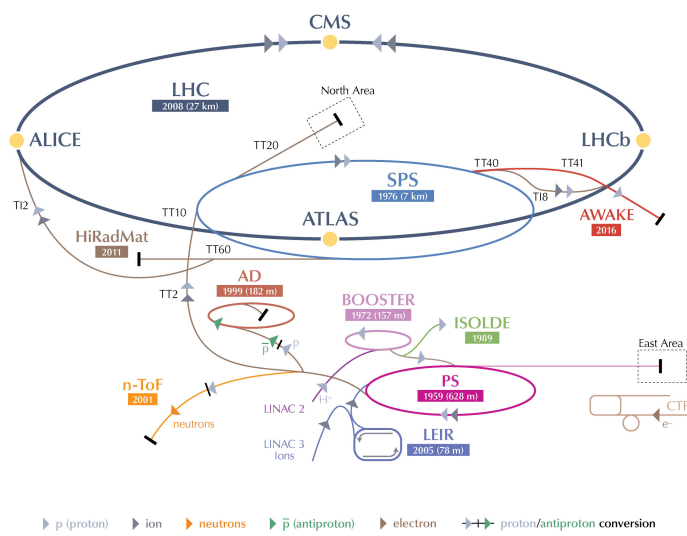
<sup>449</sup> The LHC was designed to function primarily as a proton-proton collider with a center of mass en-  
<sup>450</sup> ergy  $\sqrt{s} = 14$  TeV and an instantaneous luminosity of  $1 \times 10^{34} \text{ cm}^{-2} \cdot \text{s}^{-1}$ , though it is also capable

---

<sup>\*</sup>1978’s LINAC 2 is the successor to 1959’s LINAC 1; it will be replaced in 2020 by LINAC 4; LINAC 3 is responsible for ion production.

<sup>†</sup>Protons can be directly from a LINAC into the PS, but the higher injection energy allows for approximately 100 times more protons to be used at once[9], 1972.

## CERN's Accelerator Complex



LHC Large Hadron Collider   SPS Super Proton Synchrotron   PS Proton Synchrotron

AD Antiproton Decelerator   CTF3 Clic Test Facility   AWAKE Advanced WAKEfield Experiment   ISOLDE Isotope Separator OnLine Device  
LEIR Low Energy Ion Ring   LINAC LINear ACcelerator   n-ToF Neutrons Time Of Flight   HiRadMat High-Radiation Materials

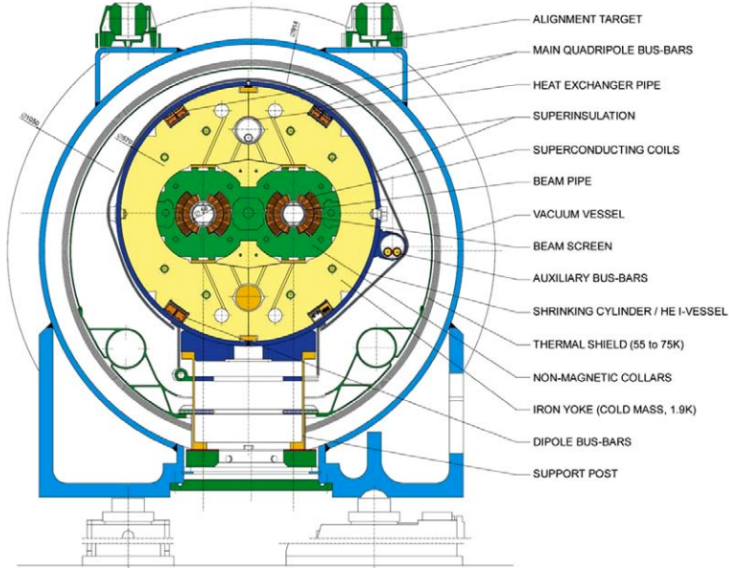
©CERN 2013

Figure 2.1: The CERN Accelerator Complex [64]

<sup>451</sup> of producing heavy ion (Pb-Pb) collisions, which it does for approximately one month in a typical  
<sup>452</sup> year of physics collisions. Owing to an accident at the beginning of the LHC's initial run, the acceler-  
<sup>453</sup> ator has operated at center of mass energies of 7, 8, and now 13 TeV.

<sup>454</sup> One of the major cost-saving features of the he LHC is that, unlike the defunct Superconducting  
<sup>455</sup> Supercollider (SSC), its construction did not call for a purpose built tunnel, with the LHC instead  
<sup>456</sup> being housed in the old LEP tunnel. LEP, however, like the Tevatron, was a particle-antiparticle  
<sup>457</sup> collider, which meant that both beams could circulate within the same beam pipe, so the LEP tun-  
<sup>458</sup> nel was never built to house two separate storage rings and magnet systems (as the SSC would have  
<sup>459</sup> had). To accomplish the technically challenging task of housing two storage rings and sets of mag-  
<sup>460</sup> nets in one system, the LHC magnets feature a "twin bore" design. The magnets themselves make  
<sup>461</sup> use of superconducting NbTi cables and are cooled using superfluid helium to a temperature of 2  
<sup>462</sup> K, which allows for operational field strengths in excess of 8 T. A stable design is achieved by having  
<sup>463</sup> the magnets share a common cold mass (a 27.5 ton iron yoke for each dipole kept at 1.9 K in which  
<sup>464</sup> the magnets and beam pipes are embedded) and cryostat and by arranging the superconductor wind-  
<sup>465</sup> ings so that the magnetic fluxes of the two systems rotate in opposite directions. This results in an  
<sup>466</sup> extremely complicated magnetic structure. The design layout of an LHC dipole magnet is shown  
<sup>467</sup> in Figure 2.2. These dipole magnets are responsible for bending the LHC's proton beams, and their  
<sup>468</sup> strength is the principal limiting factor in the center of mass energy achievable at a circular collider.

<sup>469</sup> The ideal version of a proton beam in the LHC consists of infinitely small bunches of protons  
<sup>470</sup> of equal momentum equally spaced in the LHC ring (itself not a perfect circle). In reality, the pro-  
<sup>471</sup> tons in the beam deviate from each of these assumptions, with dispersion in both physical space

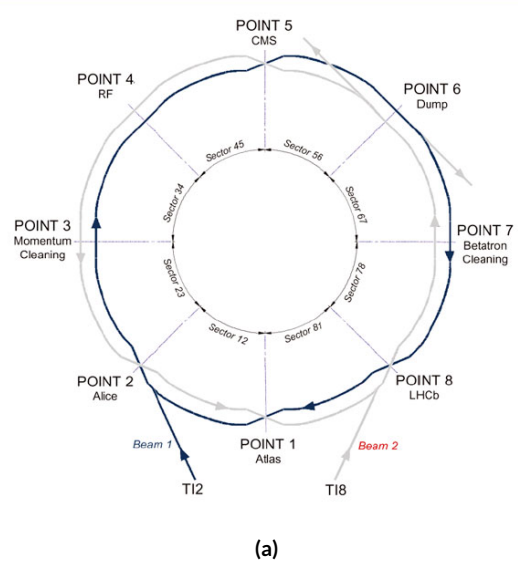


**Figure 2.2:** Schematic drawing of an LHC dipole magnet and cryogenics system.

and momentum space. In general, charged particles in an accelerator ring will demonstrate pseudo-harmonic “betatron” oscillations about the ideal orbit, the amplitude of which gives a characteristic of the beam’s size. In order to get high energy protons to actually collide, different magnets are used to focus the beam and help nudge deviating particles back into more ideal behavior. There are quadrupole magnet assemblies in the short straight sections to accomplish this, as well as quadrupole, octupole, and sextupole magnets interspersed throughout the length of the LHC ring for beam stabilization and other higher order corrections. The interior of the LHC beam pipe operates at a nominal pressure of  $\sim 10^{-7}$  Pa, famously more rarefied than outer space.

The LHC ring itself is between 45 m and 170 m below ground and has a 1.4% incline towards Lac Léman with eight arcs and eight straight sections. In the middle of each of the eight straight sections,

482 there are potential interaction points (each colloquially referred to by its number as “Point  $N$ ”),  
483 with each point housing either accelerator infrastructure or an experiment. A schematic of the con-  
484 tents of each component, as well as a more detailed view of the infrastructure in the LHC ring, can  
485 be found in Figure 2.4.



(a)

Figure 2.3: Schematic and detailed views of the LHC ring. IC: [35], [73]

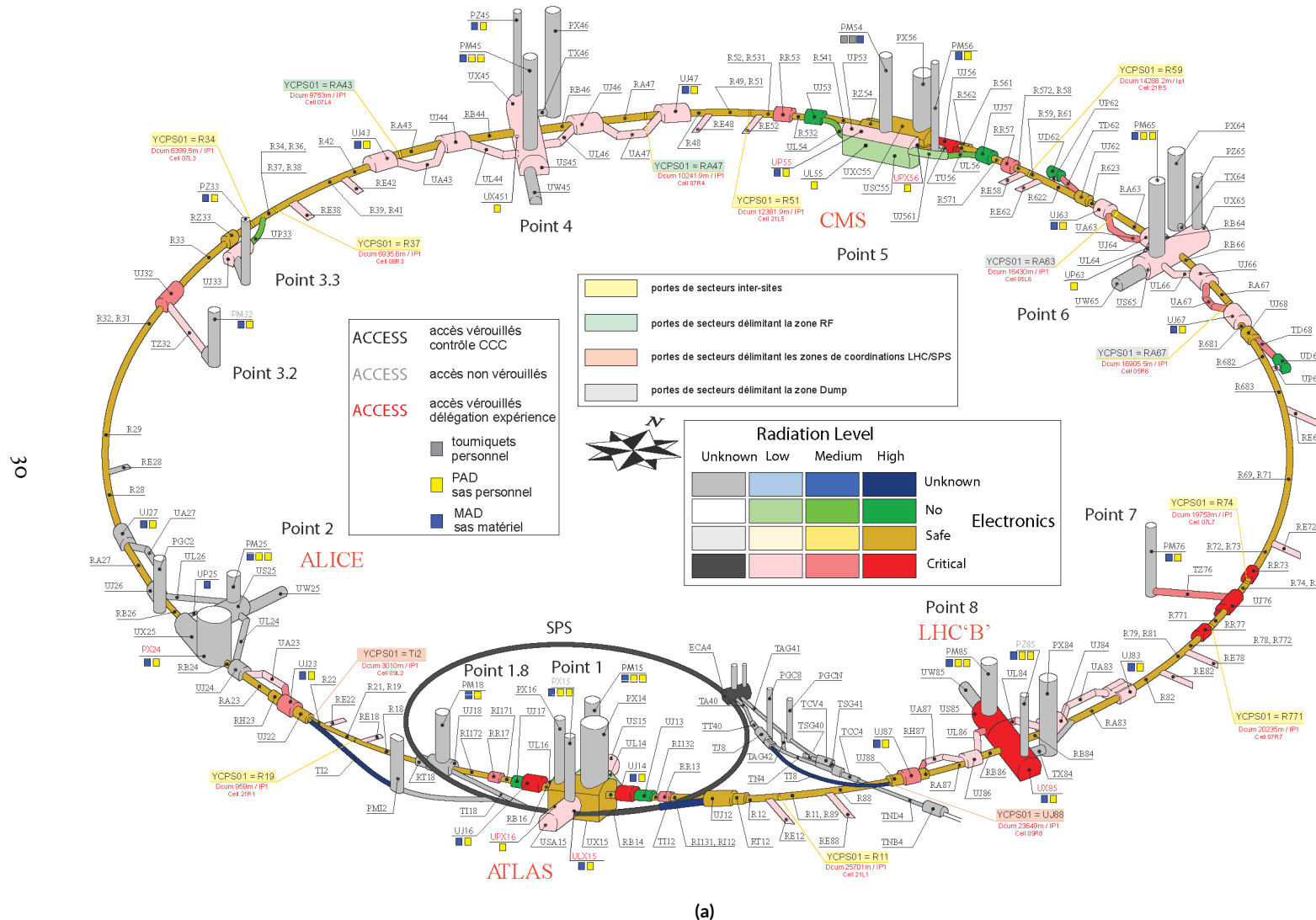


Figure 2.4: Schematic and detailed views of the LHC ring. IC:[35],[73]

486 Points 1, 2, 5, and 8 house the LHC’s experiments, ATLAS (*A Toroidal LHC ApparatuS*, one  
487 of the two general purpose detectors, discussed in detail below), ALICE (A Large Ion Collider Ex-  
488 periment, a dedicated heavy ion experiment), CMS (Compact Muon Solenoid, the other general  
489 purpose detector), and LHCb (LHC beauty, a *B* physics experiment), respectively. Point 3 houses a  
490 series of collimators that scatter and absorb particles in the beam with a large momentum deviation  
491 (which will have different orbital radii) from other particles in the beam (“momentum cleaning”),  
492 while Point 7 has a similar setup to remove particles with large betatron amplitudes (“betatron clean-  
493 ing”). Both of these dedicated cleaning assemblies are in addition to the magnetic focusing assem-  
494 blies discussed above and address the same issues. Point 4 contains the LHC’s RF (radio frequency;  
495 400 MHz) acceleration system, responsible for taking protons from their injection energy of 450  
496 GeV to their collision energy of 3.5, 4, 6.5, or 7 TeV. Point 6 is where the energetic ionizing radiation  
497 of circulating beams can be safely taken out of the collider into a block of absorbing material, either  
498 at the end of a data-taking run or in the event of an emergency (in the event of irregular behavior,  
499 it is essential to do this as quickly as possible to minimize damage to the accelerator and to experi-  
500 ments); this is known as a “beam dump.”

501 2.3 ATLAS AT A GLANCE

502 2.3.1 COORDINATES AND DISTANCES IN THE ATLAS DETECTOR

503 *A Toroidal LHC ApparatuS* is one of the two (the other being CMS) general purpose, high lumi-  
504 nosity detectors at the LHC, located at Interaction Point 1, as described above. With a length of 44

505 m and a height of 25 m, it is the detector with largest physical dimensions at the LHC.<sup>‡</sup>. While pri-  
 506 marily a high luminosity proton-proton collision detector, ATLAS does collect heavy ion collision  
 507 data, typically for one month during a year of typical operation.

508 The ATLAS coordinate system is shown in Figure 2.5. It is a right-handed coordinate system cen-  
 509 tered at the nominal collision point, with the  $x$  axis pointing towards the center of the LHC ring,  
 510 the  $z$  axis pointing up, and the  $y$  axis completing the right-handed coordinate system.

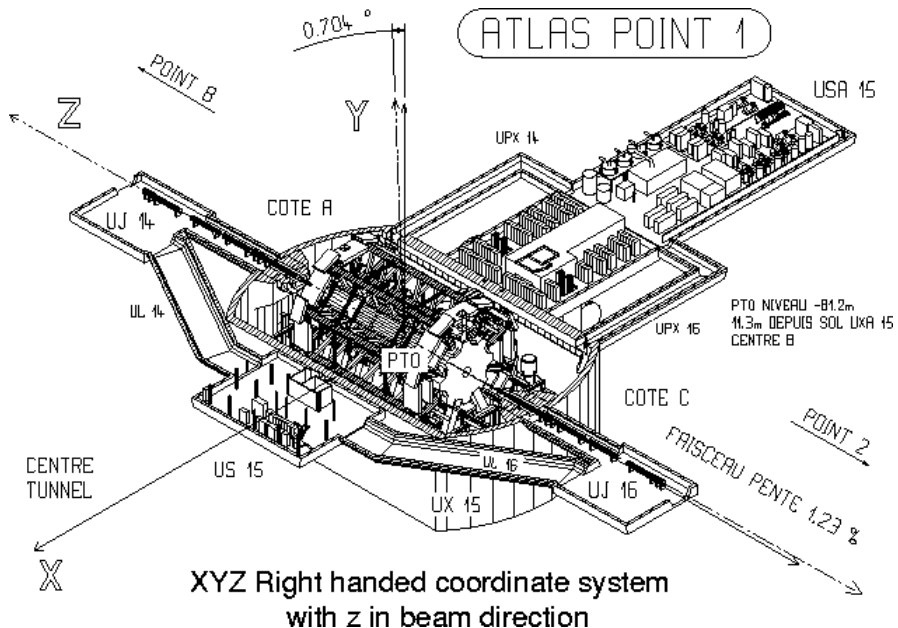


Figure 2.5: The ATLAS coordinate system. "A" side is the airport, and "C" side is "Charlie's," a pub in Saint-Genis, France.

511 While the Cartesian coordinates are useful for specifying the locations of things like detector com-  
 512 ponents and activated calorimeter cells, cylindrical polar coordinates with the same origin,  $z$  axis, and  
 513 handedness are often more suitable, with a point in 3-space expressed as  $(r, \phi, \eta)$ .  $r$  is the perpen-

---

<sup>‡</sup>This is the only reason CMS can call itself “compact.”

514 dicular distance from the beam axis. This differs from the usual spherical  $\rho$ , the distance of a point  
 515 from the origin, because the ATLAS detector is cylindrical<sup>§</sup>, and so detector components are more  
 516 easily located using  $r$  instead of  $\rho$ . In some contexts, the latter is used, though this is (or should be)  
 517 made clear.  $\phi$  is the usual (right-handed) azimuthal angle around the beam axis, with  $o$  at the  $+x$   
 518 axis.

519 In a lepton collider where total momentum is conserved, a useful coordinate is the relativistic  
 520 rapidity of a particle:

$$y = \frac{1}{2} \ln \left[ \frac{E + p_z}{E - p_z} \right] \quad (2.1)$$

521 with  $E$  and  $p_z$  as the energy and longitudinal momentum of the particle, respectively. The rapidity  
 522 is the relativistic analog of a rotation angle; boosts can be added in a manner similar to rotations<sup>¶</sup>,  
 523 and differences in rapidity are invariant under boosts. In a hadronic collider, where the participants  
 524 in the hard scatter are partons inside of the proton of unknown momentum fraction, longitudinal  
 525 momentum is not conserved. Nevertheless, since the incident momentum is entirely longitudinal,  
 526 momentum is still conserved in the transverse plane, so quantities like transverse momentum  $\vec{p}_T$   
 527 or energy ( $E_T$ )<sup>||</sup> are often very useful in analysis. However, in the massless limit<sup>\*\*</sup>, we can take  $E =$

---

<sup>§</sup>“toroidal;” the hole is the beam pipe

<sup>¶</sup>Generally, one need only insert the appropriate factor of  $i$ , the square root of  $-1$ ; this introduces differences in sign and changes all of the trigonometric functions associated with rotations into hyperbolic trigonometric functions.

<sup>||</sup>Energy is not a vector quantity, but one can take the scalar or vectorial sum of vectors formed from energy deposits with their location as the direction and energy value as magnitude. In practice, primitives are almost always assumed to be massless, so transverse energy and momentum may loosely be thought of as equivalent, with  $E_T = |\vec{p}_T| = p_T$

<sup>\*\*</sup>not a terrible one for most particles depositing energy in the calorimeter; pions have masses of  $\sim 130$  MeV, and typical energies of calorimeter objects are  $\sim 10^3$  GeV, making for a boost of roughly 100.

528  $\sqrt{p_T^2 + p_z^2}$ . Hence, with  $\theta$  taken as the zenith angle and  $o$  corresponding to the  $+z$  direction, for a  
 529 massless particle,  $p_z = E \cos \theta$ . Using the usual half angle formula  $\cos \theta = (1 - \tan^2 \theta) / (1 + \tan^2 \theta)$

530

$$\gamma = \frac{1}{2} \ln \left[ \frac{1 + \cos \theta}{1 - \cos \theta} \right] = \frac{1}{2} \ln \left[ \frac{(1 + \tan^2(\theta/2)) + (1 - \tan^2(\theta/2))}{(1 + \tan^2(\theta/2)) - (1 - \tan^2(\theta/2))} \right] = -\ln \left( \tan \frac{\theta}{2} \right) \quad (2.2)$$

531 This last expression, denoted  $\eta$ , is known as the pseudorapidity and is used instead of the polar  
 532 angle as a coordinate in hadron colliders. Moreover, pion production (the most common hadronic  
 533 process) is constant as a function of  $\eta$  in  $p\bar{p}$  collisions.

$$\eta = -\ln \left( \tan \frac{\theta}{2} \right) \quad (2.3)$$

534 Lower values of  $|\eta|$  ( $\lesssim 1.3$ ) correspond to more central areas of the detector known as the “barrel,”  
 535 with the typical layout here being concentric, cylindrical layers. Larger values of  $|\eta|$  (to  $\sim 2.5$  for  
 536 some systems and up to as much as  $\sim 4.5 - 5$  for others) are known as the “end caps,” where ma-  
 537 terial is typically arranged as disks of equal radius centered on the beam pipe stacked to ever greater  
 538 values of  $|z|$ . This terminology will be useful when discussing the various subsystems of the ATLAS  
 539 detector. Since decay products from a collision propagate radially (in the calorimeter portions of  
 540 the detector with no magnetic field), the radial coordinate is not so important for composite physics  
 541 objects like electrons or jets, which are typically expressed as momentum 4-vectors. Hence,  $\eta$  and  $\phi$   
 542 are often the only useful spatial coordinates. Distances between objects are often expressed not as a

543 difference in solid angle, but as a distance,  $\Delta R$ , in the  $\eta - \phi$  plane, where

$$\Delta R_{12} = (\eta_1 - \eta_2)^2 + (\phi_1 - \phi_2)^2 \quad (2.4)$$

544 Two important concepts when discussing particles traveling through matter (e.g. particle detec-

545 tors) are radiation lengths and (nuclear) interaction lengths, which characterize typical lengths for

546 the energy loss of energetic particles traveling through materials. In general, the energy loss is mod-

547 eled as an exponential

$$E = E_0 e^{-l/L} \quad (2.5)$$

548 where  $E_0$  is the initial energy, and  $L$  is a characteristic length. These lengths depend both on the in-

549 cident particle and the material through which they pass. In the case of uniform, composite mate-

550 rials, the length may be found by calculating the reciprocal of the sum of mass fraction weighted

551 reciprocal characteristic lengths of the components. This formula works quite well for modeling the

552 very regular behavior of electromagnetic showers (energetic photons convert into electron/positron

553 pairs, which emit photons...). In this case,  $L$  is denoted  $X_0$ ; this is the radiation length. Hadronic

554 showers are far more complicated, with shower multiplicity and makeup being much more vari-

555 able<sup>††</sup>. Nevertheless, a characteristic length can be tabulated for a standard particle type, typically

556 pions, and is called the nuclear interaction length.

---

<sup>††</sup>Different initial hadrons will shower very differently, and hadronic showers will have phenomena like neutral pions converting to photons (which then shower electromagnetically), making them much trickier to deal with.

557 2.3.2 GENERAL LAYOUT OF ATLAS

558 The ATLAS detector and its main components are shown in Figure 2.6. ATLAS is designed as a  
559 largely hermetic detector, offering full coverage in  $\phi$  and coverage in  $|\eta|$  up to 4.7. The multiple sub-  
560 systems allow for good characterization of the decay products from collisions in the LHC. The in-  
561 nermost system is the inner detector (ID); composed primarily of silicon pixels and strips immersed  
562 in a magnetic field, it is designed to reconstruct the curved trajectories of charged particles produced  
563 in collisions while taking up as little material as possible.

564 Surrounding the ID is the liquid argon based electromagnetic calorimeter (ECAL), which is de-  
565 signed to capture all of the energy of the electromagnetic showers produced by electrons and pho-  
566 tons coming from particle collisions. The ECAL is in turn encapsulated by a scintillating tile and  
567 liquid argon based hadronic calorimeter (HCAL) that captures any remaining energy from the jets  
568 produced by hadronizing quarks and gluons.

569 The outermost layer of ATLAS is the muon spectrometer (MS), which has its own magnetic field  
570 produced by toroidal magnets. Muons are highly penetrating particles that escape the calorimeters  
571 with most of their initial momentum, so the MS and its magnets are designed to curve these charged  
572 particles and measure their trajectories to measure their outgoing momenta. Each of these detector  
573 systems has several principal subsystems and performance characteristics, which will be described in  
574 turn below.

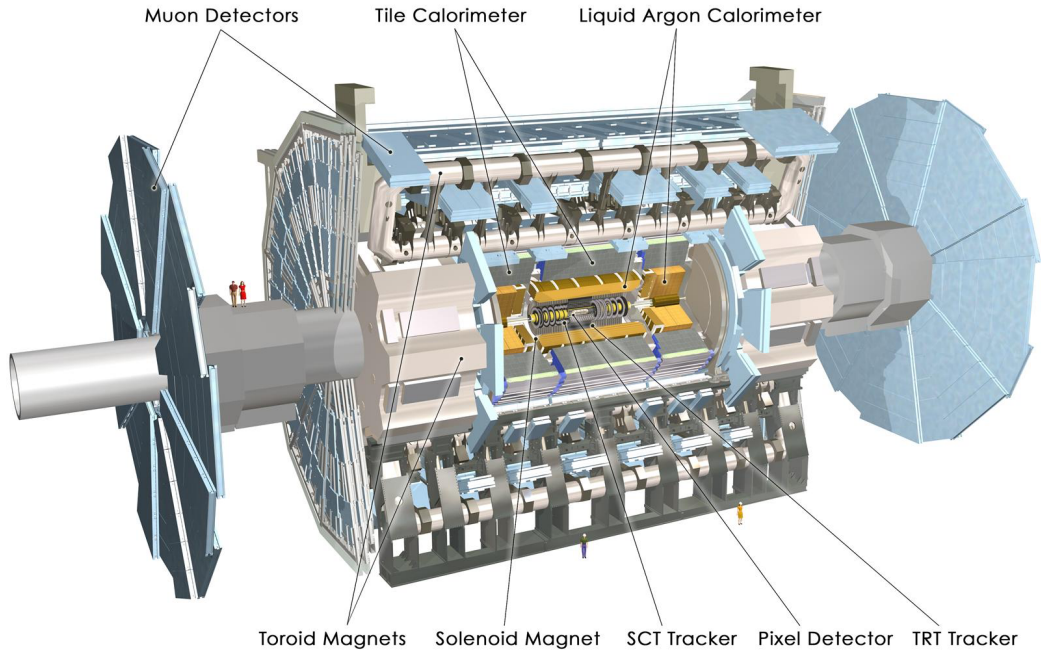


**Figure 2.6:** The ATLAS detector with principal subsystems shown.

575    **2.4 THE INNER DETECTOR**

576    ATLAS's inner detector (ID) is surrounded by a 2 T superconducting solenoid that is cryogenically  
 577    cooled to a temperature of 4.5 K. The ID uses two silicon detector subsystems (the Pixel and Semi-  
 578    Conductor (strip) Tracker (SCT)) to track the curved trajectories of charged particles emanating  
 579    from particle collisions and a Transition Radiation Tracker (TRT) composed of gas straw detectors  
 580    with filaments for  $e/\pi$  discrimination, as shown in Figure 2.7. The ID offers full coverage in  $\phi$  and  
 581    extends to an  $|\eta|$  of 2.5.

582       Since the components of the ID do not provide an energy measurement, it is desirable for a track-  
 583       ing system to have as small a material budget as possible so that more accurate energy measurements

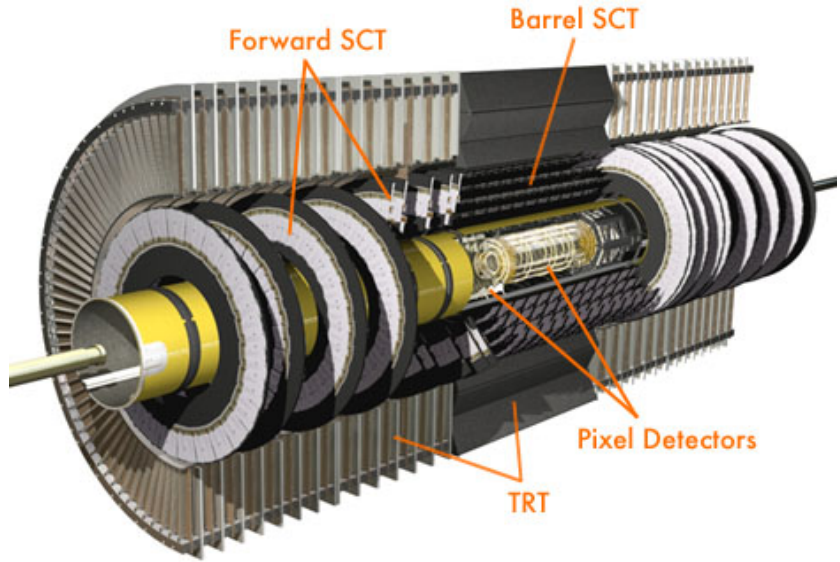


**Figure 2.7:** The ATLAS inner detector. IC: [44]

584 may be done in the calorimeters. Generally, there are two radiation lengths in the inner detector (the  
 585 precise figure varies with  $\eta$ ); the full material budget, with the layout of the individual layers in each  
 586 subsystem, can be seen in Figure 2.8.

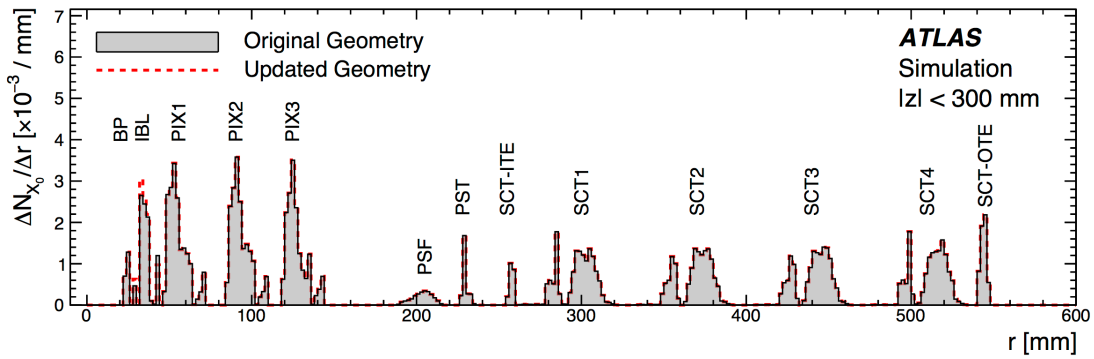


**Figure 2.8:** The ID material budget. IC: [43]

587    2.4.I    THE PIXEL DETECTOR

588    The innermost part of ATLAS is the Pixel Detector, which, as the name suggests, is comprised of  
589    four layers of silicon pixels in the barrel at 32, 51, 89, and 123 mm from the beam pipe, and three lay-  
590    ers in the end caps at 495, 580, and 650 mm from the beam pipe, with over 80 million channels total.

591    The innermost layer of pixels, the insertable *B* layer (IBL) was installed during the 2013–14 LHC  
592    shutdown. The pixels are cooled to a temperature of  $\sim -5^\circ\text{C}$ , with  $N_2$  gas and operate at 150–600  
593    V. The pixels themselves come in two sizes  $50 \times 400(600) \times 250 \mu\text{m}$ , with the larger pixels in the  
594    outer layers. They provide nominal resolution of  $10(115) \mu\text{m}$  resolution in  $r - \phi(z)$  direction.

595    In order to improve total coverage in the detector and prevent any gaps, pixels are not installed  
596    flush with each other. Pixels in the barrel are tilted at about  $20^\circ$ , with an overlap in  $r - \phi$ , as shown  
597    in Figure 2.9. The disks of the ID end caps are rotated with respect to each other by  $3.75^\circ$ .

598    2.4.2    THE SILICON MICROSTRIP DETECTOR (SCT)

599    The layout of the SCT is similar to that of the Pixel detector, except that, for cost considerations, the  
600    SCT uses silicon strips. These strips are also cooled to  $\sim -5^\circ\text{C}$  with  $N_2$  gas and operate from 150–  
601    350 V. Strip dimensions are  $80 \times 6000 \times 285 \mu\text{m}$ , and provide nominal  $17(580) \mu\text{m}$  resolution in  
602     $r - \phi(z)$ . Barrel strips feature an  $11^\circ$  tilt and come in four layers at 299, 371, 443, and 514 mm. There  
603    are nine end cap disks on each side at  $z$  values varying from 934–2720 mm.

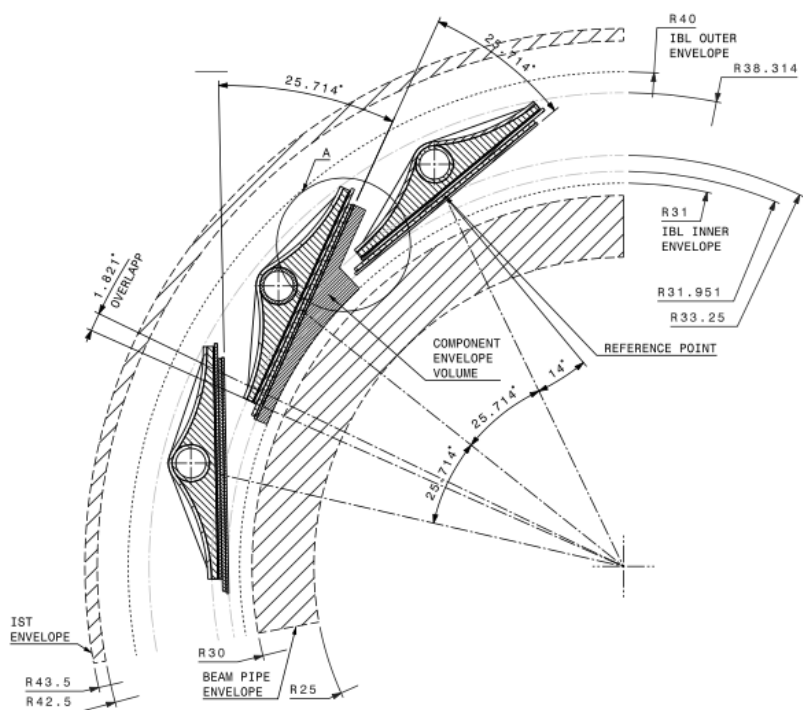


Figure 2.9: Arrangement of pixels in the barrel. IC: [34]

604 2.4.3 TRANSITION RADIATION TRACKER (TRT)

605 The final and outermost subsystem in the ID is the Transition Radiation Tracker (TRT). It provides  
606 coverage for  $|\eta|$  up to 2.0 and is composed of straw detectors with a 4 mm diameter that run the  
607 length of the detector module. The straws provide  $130 \mu\text{m}$  resolution, are filled with a Xe-CO<sub>2</sub>-O<sub>2</sub>  
608 (70-27-3) gas combination, and operate at  $-1500$  V. The filaments and foil lining inside the straws  
609 induce X-ray emission in electrons and pions passing through the TRT as they move from a dielec-  
610 tric to a gas; this “transition radiation” is the source of the TRT’s name. Since the energy deposited  
611 due to transition radiation is proportional to the relativistic boost  $\gamma$ , for constant momentum, this  
612 is inversely proportional to mass. Thus, electrons will have  $\sim 130/0.5 = 260\times$  more transition  
613 radiation than pions, in principle enabling excellent electron/pion discrimination. The TRT will be  
614 replaced by silicon strips in the Phase II upgrade.

615 2.5 THE ATLAS CALORIMETERS

616 ATLAS has four main calorimeter systems: the liquid argon based Electromagnetic Calorimeter  
617 (ECAL), the Hadronic End Cap (HEC), the Forward Calorimeters (FCAL), and the scintillating  
618 tile based hadronic Tile Calorimeter in the barrel. Their layout and material budget in interaction  
619 lengths can be seen in Figure 2.11.

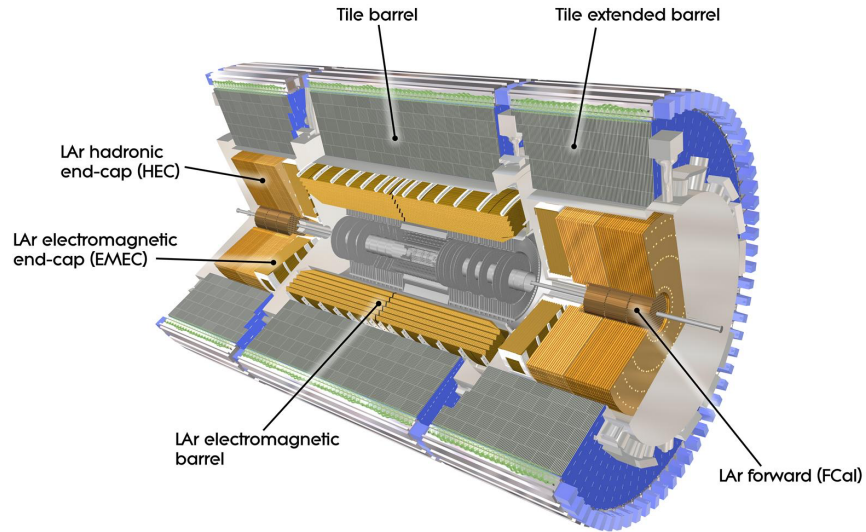


Figure 2.10: The ATLAS calorimeters.

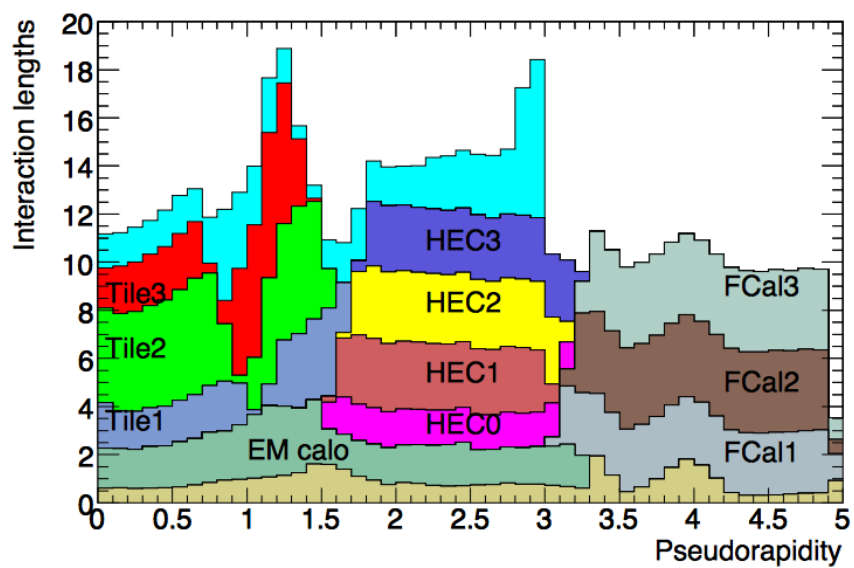


Figure 2.11: Material depth of the ATLAS calorimeters. IC: [44]

620 2.5.1 CALORIMETER RESOLUTION

621 Before diving into the specifics of each of the ATLAS calorimeters, we review some aspects of calorime-  
622 ter energy resolution performance. A calorimeter’s relative energy resolution (a ratio) can be broken  
623 up into three orthogonal components, as shown in Equation 2.6.

$$\frac{\sigma_E}{E} = \frac{S}{\sqrt{E}} \oplus \frac{N}{E} \oplus C \quad (2.6)$$

624  $S$  is the photoelectron statistics or stochastic term and represents the coefficient to the usual count-  
625 ing term (assuming Gaussian statistics);  $N$  is a noise term, which is constant per channel (and hence  
626 comes in as  $1/E$  in the relative energy resolution); and  $C$  is a constant “calibration” term, which re-  
627 flects how well one intrinsically understands a detector (i.e. mismodelling introduces an irreducible  
628 component to the energy resolution). If any detector were perfectly modeled/understood, it’s  $C$   
629 term would be zero.  $N \sim 0.1 - 0.5$  GeV for a typical calorimeter regardless of type, so  $S$  and  $C$   
630 are typically quoted.

631 A typical stochastic term scales as  $S \sim \text{few\%} \sqrt{d_{\text{active}} [\text{mm}] / f_{\text{samp}}}$ , where  $f_{\text{samp}}$  is the sampling  
632 fraction or the ratio of a calorimeter by mass is composed of an active material (i.e. one that regis-  
633 ters energy deposits). The tile calorimeter, for example, has a sampling fraction of about 1/36. There  
634 are several reasons that this fraction is so low. First, many active volumes have insufficient stopping  
635 power; one wants to capture as much energy as possible from electromagnetic and hadronic showers  
636 inside the calorimeter, and this simply is not possible for most active media (one notable exception

637 to this is the CMS crystal-based calorimeter; ATLAS is a more conservative design), so well-behaved  
638 absorbers like lead or iron are necessary to ensure all the energy is contained within a calorimeter.  
639 Another factor is cost; things like liquid argon are expensive. Finally, most active media are unsuit-  
640 able for structural support, so sturdy absorbing materials help relieve engineering constraints.

641 **2.5.2 THE ELECTROMAGNETIC CALORIMETER (ECAL)**

642 The ECAL has liquid argon (LAr) as an active material and lead as an absorber. The ECAL barrel  
643 extends to  $|\eta|$  of 1.475, with three layers at 1150, 1250, and 2050 mm, and its end cap, comprised of  
644 two wheels, covers  $1.375 < |\eta| < 2.5$ , (3.2) for the inner (outer) wheel, with 3 (2) layers out to  
645 3100 mm. There is a 1.1 (0.5) cm thick layer of LAr pre-sampler up to  $|\eta|$  of 1.8 in the barrel (end cap)  
646 of the ECAL, which is designed to aid in correcting for electron and photon energy loss in the ID.

647 The LAr and lead absorber are arranged in alternating, beveled, sawtooth layers in what is known  
648 as an “accordion” geometry, shown in Figure 2.12, which shows the layout of a barrel module in the  
649 ECAL. The absorber thickness is 1.53 (1.13) mm for  $|\eta|$  less (more) than 0.8 to ensure a constant sam-  
650 pling fraction. This arrangement helps provide greater coverage in  $\phi$ .

651 The ECAL overall typically covers 2–4 interaction lengths or about 20–40 radiation lengths. Its  
652 performance corresponds to resolution coefficients  $S = 0.1 \text{ GeV}^{-1/2}$  and  $C = 0.002$  with a 450  
653 ns drift time. In order to optimize the material budget and overall detector construction, the ECAL  
654 barrel infrastructure is integrated with that of the ID’s solenoid. The granularity of the ECAL barrel  
655 middle layer,  $\Delta\eta \times \Delta\phi$  cells of size  $0.025 \times 0.025$ , are used to define the granularity of calorimeter  
656 cluster reconstruction in ATLAS.

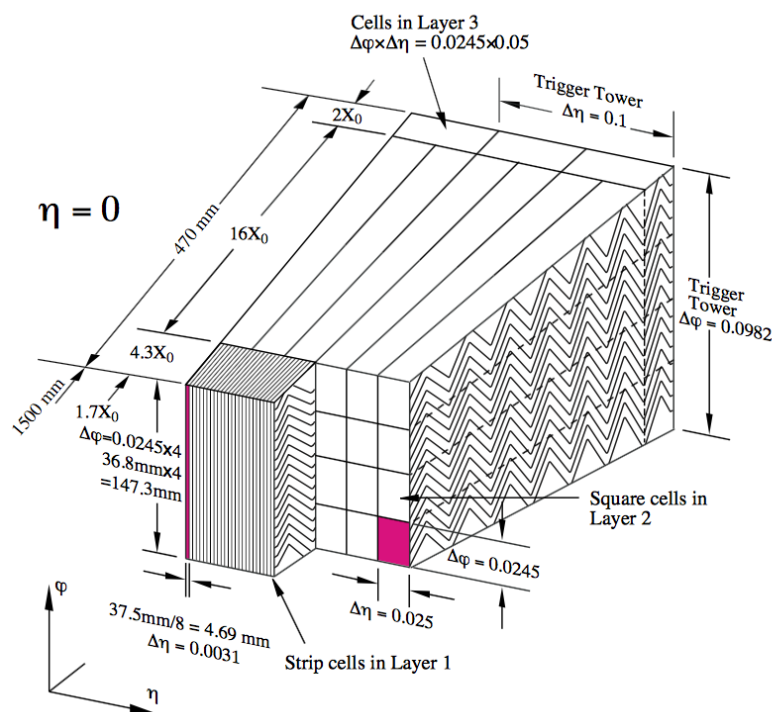


**Figure 2.12:** The accordion geometry of the LAr electromagnetic calorimeters is prominently shown in this illustration of an ECAL barrel module. IC: [44]

<sup>657</sup> 2.5.3 HADRONIC END CAPS (HEC)

<sup>658</sup> The HEC covers an  $|\eta|$  range of 1.5 to 3.2. Like the ECAL end caps, the HEC consists of two identi-  
<sup>659</sup> cal wheels out to a distance from the beam axis of 2030 mm; its layout is shown in Figure 2.13. The  
<sup>660</sup> HEC also has LAr as the active material, but instead has flat copper plates as absorbers for sampling  
<sup>661</sup> fraction of 4.4% and 2.2% in the first and second wheels, respectively. Its granularity in  $\eta - \phi$  is  
<sup>662</sup>  $0.1 \times 0.1$  for  $|\eta|$  up to 2.5 and  $0.2 \times 0.2$  in the more forward regions.

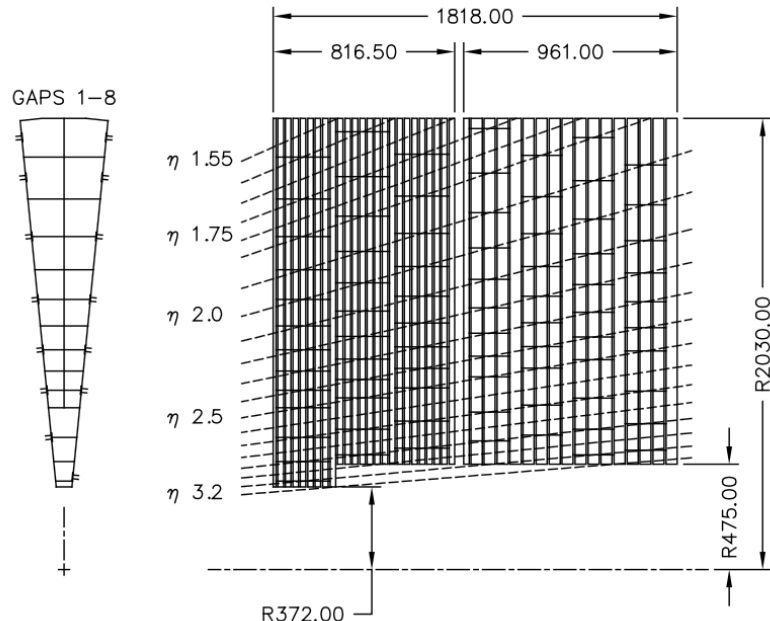


Figure 2.13: The layout of the HEC in  $r - \phi$  and  $r - z$ ; dimensions are in millimeters. IC: [44]

663    2.5.4    THE FORWARD CALORIMETER (FCAL)

664    The FCAL covers an  $|\eta|$  range from 3.1 to 4.9, again using LAr as the active material in gaps between  
665    rods and tubes in a copper-tungsten matrix, as shown in Figure 2.14. These system has characteris-  
666    tic performance corresponding to stochastic term of  $S \approx 1 \text{ GeV}^{-1/2}$ . There are three modules in  
667    the FCAL: one electromagnetic and two hadronic, with the latter two featuring a higher tungsten  
668    content for a larger absorption length.

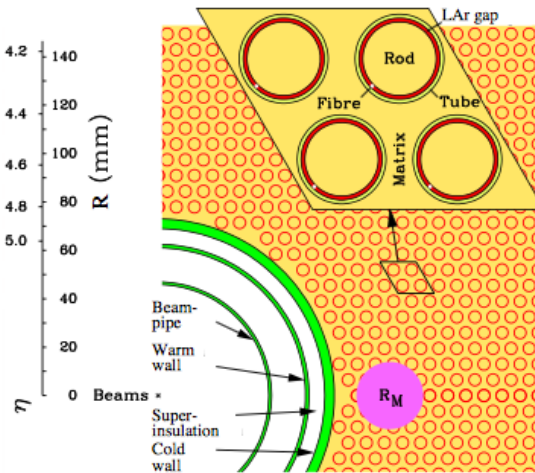


Figure 2.14: The material layout for a typical section of the FCAL in the transverse plane. IC: [44]

669    2.5.5    THE HADRONIC TILE CALORIMETER

670    The tile calorimeter, covering an  $|\eta|$  of up to 1.7 is made up of 64 modules in the barrel (each cover-  
671    ing  $\Delta\phi$  of  $360/64 = 5.625^\circ$ ), each with a layout as in Figure 2.15. It is designed to be self-supporting  
672    for structural reasons, and so is the only calorimeter without LAr as a an active medium, with a stag-  
673    gered matrix of active scintillating polystyrene and supporting steel. It operates at 1800 V with a 400

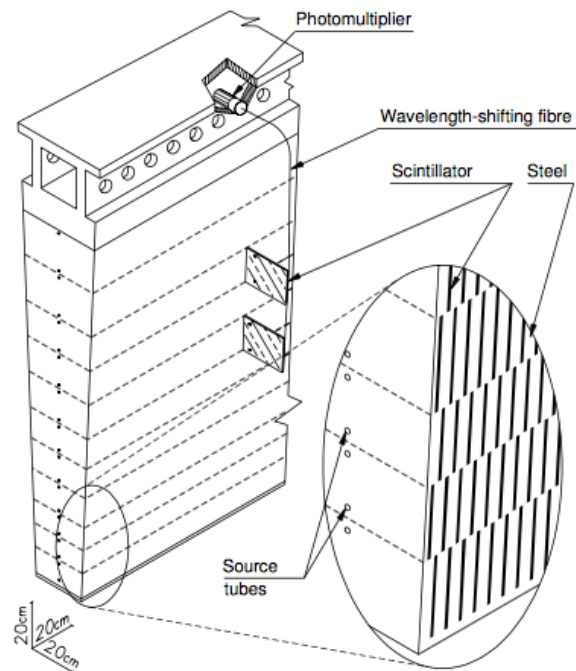


Figure 2.15: The material layout for a typical section of the hadronic tile calorimeter. IC: [44]

674 ns dead time and has a thickness corresponding to 10–20 interaction lengths (2.28–4.25 m). Its cells  
675 have a  $\Delta\eta \times \Delta\phi$  granularity of  $0.1 \times 0.1$  in the first two layers and  $0.2 \times 0.1$  in the last layer. Its  
676 performance corresponds to  $S = 0.5 \text{ GeV}^{-1/2}$  and  $C = 0.05$  (0.03 after calibration).

## 677 2.6 THE MUON SPECTROMETER

678 Since the energy of muons is not captured within the calorimeters, the stations of the ATLAS MS  
679 surround the entire detector and provide tracks of outgoing muons that can be matched to tracks in  
680 the ID. The ATLAS toroids, which provide field strengths of up to 2.5 (3.5) T in the barrel (end cap)  
681 with typical strengths of 0.5–1.0 T, bend the muons, which allows for a muon momentum measure-  
682 ment since the muon mass is known. The relative momentum resolution of a tracker (assuming, as  
683 in ATLAS, that bending primarily happens in the  $\phi$  direction) may be expressed as

$$\frac{\sigma_{p_T}}{p_T} = c_0 \oplus c_1 \cdot p_T \quad (2.7)$$

684 The  $c_0$  term represents a degradation in resolution due to multiple scattering, and is typically 0.5–  
685 2% [78]. The  $c_1$  term describes the phenomenon of, holding magnetic field constant, higher momen-  
686 tum muons curving less. This term has typical values of  $10^{-3} - 10^{-4} \text{ GeV}^{-1}$ . At very high  $p_T$  val-  
687 ues, this is of particular concern since a very small curvature can result in charge misidentification.

688 A cross-sectional view (in  $r-z$ ) of the muon spectrometer with station names, detector types, and  
689 layouts is shown in Figure 2.16. There are three layers of muon detectors in both the barrel (at 5 000,  
690 7 500, and 10 000 mm) and end cap (at 7 000 (11 000), 13 500, and 21 000 mm), with the innermost

<sup>691</sup> end cap layer split in two due to the end cap toroid. This corresponds to an  $|\eta|$  range up to 2.4 for both precision and trigger coverage, and up to 2.7 for precision detection only.<sup>††</sup>

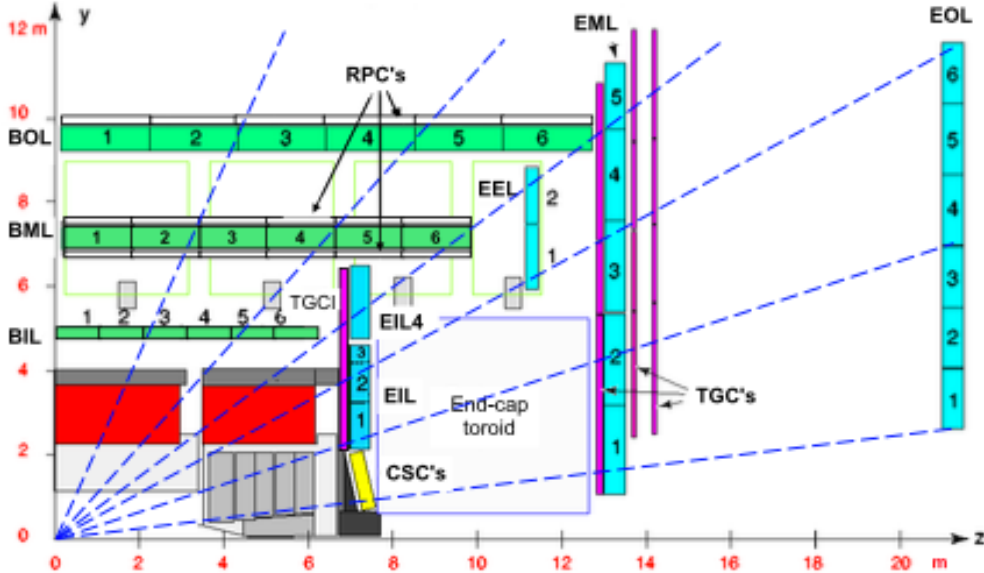


**Figure 2.16:** The ATLAS muon spectrometer. Naming of the MDT stations obeys the following convention [BE] (barrel or end cap) [IEMO] (inner, inner extended (end cap only), middle, or outer layer) [1-6] (increasing in  $z$  ( $r$ ) for the barrel (end cap)), so EI1 is the station in the inner most end cap layer closest to the beam pipe. IC: [44]

<sup>692</sup>

<sup>693</sup> The MS can reconstruct muons with transverse momenta from 5 GeV up to 3 TeV (with 10% res-

<sup>694</sup> olution at 1 TeV (3% at 100 GeV)). Detectors in the MS fall into two broad headings, precision detec-

<sup>695</sup> tors and trigger detectors, both described below. Nominal performance of the current detector types

<sup>696</sup> in the MS is summarized in Figure 2.17, a table taken from [44]. It should be noted that  $|\eta|$  ranges

<sup>697</sup> quoted below, where applicable, do not include the range 0-0.1, where this a gap in the MS to allow

<sup>698</sup> for cabling and other services to the ATLAS detector; for a discussion of compensatory measures in

---

<sup>††</sup>This will change with the New Small Wheel Phase I Upgrade. cf. Appendix A

<sup>699</sup> muon reconstruction, see Chapter 5.

Type	Function	Chamber resolution (RMS) in			Measurements/track		Number of	
		$z/R$	$\phi$	time	barrel	end-cap	chambers	channels
MDT	tracking	35 $\mu\text{m}$ ( $z$ )	—	—	20	20	1088 (1150)	339k (354k)
CSC	tracking	40 $\mu\text{m}$ ( $R$ )	5 mm	7 ns	—	4	32	30.7k
RPC	trigger	10 mm ( $z$ )	10 mm	1.5 ns	6	—	544 (606)	359k (373k)
TGC	trigger	2–6 mm ( $R$ )	3–7 mm	4 ns	—	9	3588	318k

Figure 2.17: ATLAS MS detector performance. IC: [44]

### <sup>700</sup> 2.6.1 PRECISION DETECTORS

<sup>701</sup> The ATLAS MS has two types of precision detectors: Monitored Drift Tubes (MDT's) and Cathode Strip Chambers (CSC's). An MDT is a tube with a 3 cm diameter with length depending on  
<sup>702</sup> the station in which the tube is located. The tube is filled with an Ar/CO<sub>2</sub> gas mixture and has a  
<sup>703</sup> tungsten-rhenium wire at its center that is kept at 3 000 V when operational. The MDT's provide 35  
<sup>704</sup>  $\mu\text{m}$  resolution (per chamber) in their cross-sectional dimension (there is no sensitivity along the axis  
<sup>705</sup> of the wire). Resolution of this magnitude requires very precise knowledge of the location of the  
<sup>706</sup> wires within the MDT's; this is generally true for detectors in the MS (trigger as well as precision);  
<sup>707</sup> to this end, stations of the MS are aligned using an optical laser system. For a detailed description  
<sup>708</sup> of how misalignment can affect performance, see Appendix A for a detailed discussion of misalign-  
<sup>709</sup> ment's simulated effects on the performance of the proposed Micromegas trigger processor in the  
<sup>710</sup> New Small Wheel (NSW) of the Phase I upgrade. Their 700 ns dead time, however, precludes their  
<sup>711</sup> use as trigger detectors and also in the region of the small wheel (innermost endcap) closest to the  
<sup>712</sup> beam pipe ( $|\eta|$  from 2.0 to 2.7), where rates are highest.

714 In this region, the precision detectors are the CSC's, which have a much lower dead time of  $\sim 40$   
715 ns. These are multiwire proportional chambers with cathode planes that have orthogonal sets of  
716 strips, allowing for a measurement in both principal directions. CSC detector sizes also vary by sta-  
717 tion, coming in both small and large chambers. The CSC strip pitch is 5.31 (5.56) mm for the large  
718 (small) chambers, with position determined from the induced charge distribution in the strips. This  
719 corresponds to a nominal resolution of 60 (5 000)  $\mu\text{m}$  per plane in the bending (non-bending) direc-  
720 tion. These are slated to be replaced by Micromegas detectors in the NSW.

721 **2.6.2 TRIGGER DETECTORS**

722 Trigger detectors have a fundamentally different role than the precision detectors, instead needing to  
723 deliver “good enough” approximate values of muon track positions and  $p_T$  values. The MS has two  
724 types of trigger detectors: Resistive Plate Chambers (RPC’s) in the barrel and Thin Gap Chambers  
725 (TGC’s) in the end caps. They collectively cover an  $|\eta|$  range to 2.4, and their arrangement is shown  
726 in Figure 2.18.

727 The RPC’s are parallel plate detectors with a dead time of 5 ns and a thickness of 2 mm, kept at  
728 a potential of 9 800 V; they are deployed in three layers. RPC’s, too, feature strips with orthogonal  
729 arrangements on the top and bottom planes, with a strip pitch of 23–35 mm.

730 The TGC’s are multiwire proportional chambers with a dead time of 25 ns. Also, featuring or-  
731 thogonal strips, the TGC’s also provide a  $\phi$  measurement to compensate for the lack of MDT sensi-  
732 tivity in this direction. There are four layers of TGC’s in the end cap. TGC’s will be supplanted by  
733 sTGC’s (small thin gap chambers) in the NSW.

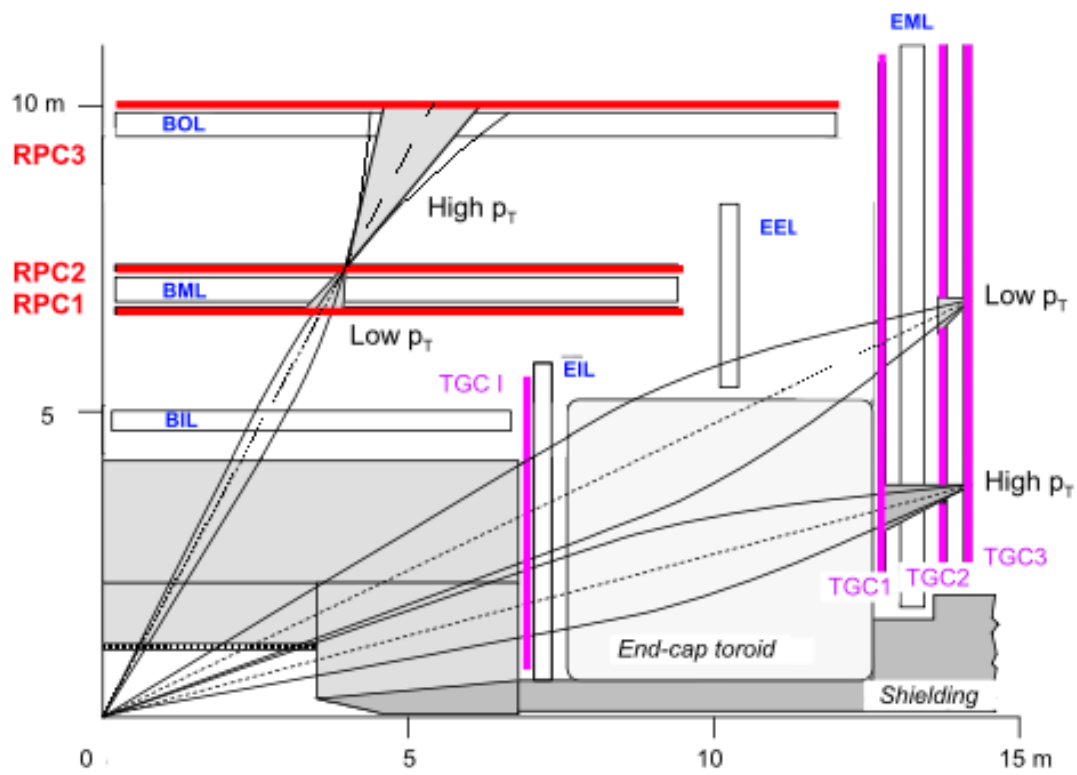


Figure 2.18: ATLAS MS trigger detector arrangement. IC: [44]

<sup>734</sup> For more details on how detector level trigger objects work in the ATLAS MS, see Appendix A  
<sup>735</sup> for details on the Micromegas trigger processor algorithm.

*What do you read, my lord?*

*Words, words, words.*

Hamlet, 2:2

# 3

736

737

## Data and Simulated Samples

738 THE DATA AND Monte Carlo simulation (MC) samples used in this thesis are the same as in the fidu-  
739 cial analysis. The data corresponds to  $36.1 \text{ fb}^{-1}$  of  $pp$  collision data collected in 2015+16 at the AT-  
740 LAS detector at  $\sqrt{s} = 13 \text{ TeV}$ . Details of the Run 1 analysis referenced in Chapter 9, may be found  
741 in [20]. Only events recorded with all systems in ATLAS in good working order and passing certain

742 quality requirements, according to a Good Run List (GRL), are analyzed.

743 Details about MC samples may be found in [67], and signal and background modeling are dis-  
744 cussed in the next. The  $ZH \rightarrow \ell\ell b\bar{b}$  process is considered for both multivariate analysis (MVA)  
745 optimization and the final statistical analysis, while  $WH \rightarrow \ell\nu b\bar{b}$  and  $ZH \rightarrow \nu\nu b\bar{b}$  production  
746 are included in the final statistical analysis only. Signal MC samples were generated separately for  $qq$   
747 and  $gg$  initiated  $VH$  processes.  $qqVH$  samples were generated with Powheg MiNLO + Pythia8  
748 [68, 72] with the AZNLO [19] tune set and NNPDF3.0 PDF [28], with alternate samples gener-  
749 ated using MadGraph5\_AMC@NLO [23] for the hard scatter generation and Pythia8 for the  
750 hardronization, parton shower (PS), underlying event (UE), and multiple parton interactions (MPI).  
751 Nominal  $ggZH$  samples were generated using Powheg for the matrix element (ME) and Pythia8  
752 for the parton shower (PS), underlying event (UE), and multiple parton interactions (MPI), again  
753 applying the AZNLO tune and NNPDF3.0 PDF set. [60]

754 The background processes considered in these studies are  $Z+jets$ ,  $t\bar{t}$ , and diboson production for  
755 both MVA optimization and the final statistical analysis with single top production and  $W+jets$   
756 only considered in the final statistical analysis.  $V+jets$  samples are generated using Sherpa 2.2.1 [40]  
757 for both the ME and PS. These samples are generated in different groups, according to the identity  
758 of the  $V$ , the max ( $H_T, p_T^V$ ) of events, with further subdivisions according to the flavor of the two  
759 leading jets in an event,  $b$ ,  $c$ , or  $l$ , for a total of six categories.  $t\bar{t}$  samples are generated using Powheg  
760 with the NNPDF3.0 PDF set interfaced with Pythia8 using the NNPDF2.3 PDF's and the Al4  
761 tune [46]. Single top samples use Powheg with the CT10 PDF's interfaced with Pythia6 using  
762 the CTEQ6L1 PDF's [21, 57]. Diboson samples are generated with Sherpa 2.2.1 interfaced with the

<sup>763</sup> NNPDF<sub>3.0</sub> NNLO PDF set normalized to NLO cross sections [33].

*There are certain calculations one simply doesn't do in  
public.*

Alan Blaer

# 4

764

765

## Signal and Background Modeling

766 THIS CHAPTER summarizes the modeling of the dominant signal and background processes in  
767 this analysis, including corrections and systematic uncertainties (systematic uncertainty, also called  
768 nuisance parameter (NP), titles are set in **this** font) related to each process. Further details on the  
769 specifics of these topics, including in-depth studies for the derivation and definitions of some of the

770 quantities cited, may be found in [67]. We start with a general discussion of modeling and associated  
771 major categories of uncertainties before addressing each of the physics processes.

#### 772 4.1 EVENT GENERATION IN A NUTSHELL

773 Before diving into the specifics of modeling and systematic uncertainties associated with each ma-  
774 jor set of physics processes considered in this analysis, we review at a schematic level\* the problem  
775 of simulation event generation. Once a physics processes of interest has been determined, how one  
776 simulates an ensemble of particle collisions to model the process in question. This is illustrated in  
777 Figure 4.1. Note that the scope of this problem does not include how these generated collision prod-  
778 ucts propagate through one's detector. This problem is left for Chapter 5.

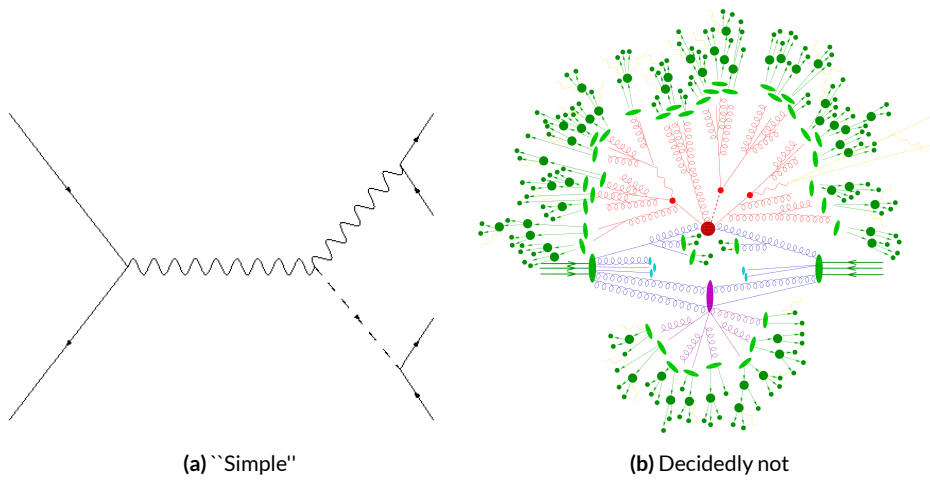


Figure 4.1: The problem here is how to get from (a) to (b).

779 The primary source of complication in event generation comes from dealing with hadronic ob-

---

\*i.e. this will not be a technically rigorous discussion. For a more thorough treatment, the reader is di-  
rected to the usual references.

jects both in the initial state (the lefthand side of Figure 4.1 (a); the LHC is a hadron collider) and the final state (this analysis searches for Higgs decays to  $b$ -jets, the lower righthand side of Figure 4.1).  
Common to all hadronic objects, by definition, are the many considerations that go into calculations in quantum chromodynamics (QCD). In calculating the hard scatter process itself, one must make a variety of choices, such as the parton distribution function (PDF) set to use and to what order in perturbation theory to do the calculation (common choices are leading order (LO), (next to) next to leading order ((N)NLO), and (next to) next to leading log (NNLL)) [71]. Similar considerations often need to be made for the electroweak parts of an event. These considerations and others in event generation (broadly called event generator “tuning”) will be discussed in more detail below.

The initial state includes not only the hard scatter partons that generate the physics process of interest, but also the rest of the partons in the colliding protons, known as the underlying event (UE). Moreover, the hard scatter partons may not be the only interacting partons in an event, further complicating matters; this phenomenon is known as multiple parton interactions (MPI). Specific to the final state are the kinematic distributions of the final state objects—what their energies and angular distributions will be—in addition to the overall cross section of the process that is measurable by the detector (acceptance effects). Furthermore, one has to model hadronization, the process by which any free (colored) partons in an event transform into colorless hadrons.

Typically, it takes several steps and tools to accomplish this. The hard scatter itself is often modelled with a dedicated event generator like PowHEG [68] or MADGRAPH [23], with events generated then interfaced with a tool like PYTHIA [72] for the PS, UE, and MPI, though there are exceptions (SHERPA [51], for example, can do both the hard scatter and hadronization/ for some pro-

801 cesses).

802 4.2 DESCRIPTION OF MODELING UNCERTAINTY CATEGORIES

803 Each of the steps in event generation described above has associated uncertainties. Some uncertain-  
804 ties are inherent in the calculations themselves. The choice of which order in perturbation theory  
805 to do a calculation, for example, comes with it an implicitly defined level of precision<sup>†</sup>. Extrapolat-  
806 ing from one energy/momentum scale to another also introduces uncertainty. Furthermore, there  
807 is no *a priori* correct choice to make at each step in event generation, so each choice (the choice of  
808 generator, PDF set, parton shower calculator, all of their configurable parameters, etc.) implies an  
809 additional layer of uncertainty.

810 In order to quantify these choices, each source of systematic uncertainty is treated separately and  
811 given a unique name. To make this more concrete, take the specific example of the uncertainty asso-  
812 ciated with the  $H \rightarrow b\bar{b}$  branching ratio of 58%, called ATLAS\_BR\_bb, which encapsulates a num-  
813 ber of effects (higher order terms, the mass of the  $b$  quark, and choice of  $\alpha_S$ ). The quoted (in prin-  
814 ciple asymmetric) uncertainty on the Higgs BR is not itself a direct input into the analysis model.  
815 Instead, the effect of varying the branching ratio up and down by one standard deviation is propa-  
816 gated to simulated collision events and recorded (i.e. the analysis is run with the Higgs branching  
817 ratio at  $\pm 1\sigma$ , and the results are recorded alongside the nominal result). The nominal and “up” and  
818 “down” variations are then typically taken to define a normally distributed, freely floating param-

---

<sup>†</sup>though this is less well-defined in QCD calculations than for electroweak calculations since they don’t converge

819 eter in the statistical fit model. Since these parameters associated with systematic uncertainties are  
820 not typically considered interesting quantities, they are often referred to as “nuisance parameters”  
821 (NP’s). The terms “systematic,” “systematic uncertainty,” and “nuisance parameter” are often used  
822 interchangeably.

823 The specifics of exactly how the effects of variations are saved and propagated to the full fit model  
824 are deferred to Chapter 7. The discussion here is confined to how systematic uncertainties for signal  
825 and background modeling and their accompanying variations are defined. Modeling systematics are  
826 derived separately for each physics process (simulation sample). Sometimes, all of the variation for  
827 a given process is encapsulated in a single systematic, but oftentimes the variations from multiple  
828 considerations are distinct enough to be treated separately. Furthermore, each of these separate sys-  
829 tematics for a given sample/process may be treated in a number of ways (e.g. 0-lepton events may  
830 be treated differently from 2-lepton events). An additional subtlety is that a continuous parameter  
831 like a branching ratio lends itself quite naturally to defining Gaussian  $\pm 1\sigma$  variations, while for dis-  
832 crete variations, like choice of PDF set for parton showers, how to proceed is less obvious. This is  
833 addressed on a case-by-case basis, as described below.

834 Before enumerating each of the principal physics processes and their systematics, we begin by  
835 describing considerations and choices that must be addressed for every physics process in order to  
836 make the discussion of individual samples and systematics both clearer and less repetitive.

837    4.2.1 PHYSICS CONSIDERATIONS

838    In general, evaluating the uncertainties arising from the many choices in event generation entails  
839    producing alternate samples of events, which practically means tuning parameters in the various soft-  
840    ware packages and/or using alternate packages/libraries to make new samples. Once these samples  
841    have been created, they are compared at truth-level (particle level) using a package called Rivet [30]  
842    instead of using the full ATLAS detector reconstruction for computational considerations. Given  
843    the nature of the problem and the tools, there are generally three main categories of physics issues,  
844    each described below.

845    UNDERLYING EVENT AND PARTON SHOWER

846    The modeling of the underlying event (UE) and parton shower (PS) are usually handled by the same  
847    package and so are usually treated together. The typical nominal choice in the fiducial analysis is  
848    PYTHIA8. One approach to modeling these uncertainties is simply to see what happens when a  
849    different model is used and then compare this alternate set of events to the nominal set, taking the  
850    difference as the (implicitly one standard deviation) scale of variation. Another approach is to vary  
851    some parameter within a given model, for example, using different tunes in the A14 set for PYTHIA8  
852    with their accompanying variations, to characterize the scale of variation.

853    A natural question is how to treat these two approaches on the same footing. When examining  
854    a set of potential variations related to the same process or effect, oftentimes the largest single varia-  
855    tion in a set is picked as defining the scale for the systematic uncertainty. Another approach is to use

856 the average over a set of variations.<sup>‡</sup> The ATLAS\_UEPS\_VH\_hbb systematic, for example, uses the  
857 Pythia8 + A14 tunes approach to determine the scale of UE variation and compares Pythia8 with  
858 Herwig7 to characterize the PS variation. Each of the A14 tunes comes with an up and down varia-  
859 tion, and the difference between each of these variations and a nominal setup may be expressed as a  
860 ratio,  $R$ , of total events.

861 As is often done when a physical argument can be made for combining related, but ultimately  
862 orthogonal categories/measurements/uncertainties/systematics, the combined UE+PS systematic is  
863 taken to be the sum in quadrature of these two effects:

$$\sum_{tunes} \max_{tune} (|R_{up} - R_{down}|) \oplus \sigma_{PS} \quad (4.1)$$

864 QCD SCALE

865 The term “QCD scale” in the context of modeling uncertainties refers to the choice of renormal-  
866 ization ( $\mu_R$ ) and factorization ( $\mu_F$ ) scales used in QCD calculations. These are typically treated to-  
867 gether. Usually, some multiplicative scale factor,  $f$ , is chosen, and each scale is varied in concert with  
868 the other scale by 1,  $f$ , and  $1/f$  (nine total combinations), sometimes with a cap on how large the  
869 combined variation can be (so ignoring the  $(f, f)$  and  $(1/f, 1/f)$  cases). Just as in the UE+PS, the  
870 largest variation is usually taken as the systematic uncertainty.

871 Another important choice in the context of renormalization, to deal with infinities inherent in

---

<sup>‡</sup>Generally, the maximum is used if it is much larger than other variations, and the average is used if scales are comparable. In general, the historical preference is to be conservative.

872 quantum field theory calculations with loops, is the choice of regularization (to keep track of the  
873 infinities) and subtraction schemes (to eliminate them). A common combination is dimensional reg-  
874 ularization (deforming the four dimensional integral to  $4 - \varepsilon$  dimensions and then taking  $\varepsilon \rightarrow 0$ )  
875 with  $\overline{\text{MS}}$  (“MS-bar” (MS for “minimal subtraction”) subtracts off only the infinities plus some com-  
876 mon factors that always appear in dimensional regularization). For more details, see, for example,  
877 [71]. While each scheme is internally consistent, each can yield different answers at a given order of  
878 calculation (and different subtraction schemes may be used for calculations at different orders).

879 **PARTON DISTRIBUTION FUNCTIONS AND  $\alpha_s$**

880 Finally, separate uncertainties are often made for the choice of parton distribution function (PDF)  
881 set and associated choice of strong coupling for  $\text{QCD}(\alpha_s)$ . Much as in the previous two cases, one  
882 can vary the parameter  $\alpha_s$  and study what samples of simulation events made using different PDF  
883 sets relative some nominal setup look like. Similarly, one can take the maximum, average, or sum in  
884 quadrature of different variations to characterize a systematic uncertainty.

885 **4.2.2 MODELING SYSTEMATIC TYPES**

886 With the concept of what type of effect is taken as a single systematic uncertainty and how its varia-  
887 tions are generally evaluated, it is now time to turn to the issue of what exactly is being varied.

888 ACCEPTANCE/NORMALIZATION

889 The most basic type of modeling uncertainty is a normalization uncertainty, often called an accep-  
890 tance uncertainty. This simply denotes the uncertainty on the number of predicted events for a  
891 given process in a given region of phase space (usually delineated by the number of leptons in the  
892 final state and sometimes also by the number of and jets the  $p_T^V$ <sup>§</sup> of an event) and is usually expressed  
893 as a percent.

894 As an example, the uncertainty on the theoretical prediction of the  $H \rightarrow b\bar{b}$  branching ratio,  
895 denoted ATLAS\_BR\_bb (it is an ATLAS-wide systematic), is expressed as a normalization system-  
896 atic with a value of 1.7%, affecting all  $VH$  processes. Now imagine we have an event in a  $VH$  sample  
897 with weight 1.0. The nominal histograms for this region gets filled with this event's relevant informa-  
898 tion with weight 1.0, while the ATLAS\_BR\_bb\_\_1up (\_\_1do) histograms get filled with weight 1.017  
899 (0.983).

900 SHAPE SYSTEMATICS

901 In addition to normalization systematics expressed as single numbers attached to different processes  
902 in different regions, there are also the so-called “shape systematics” and “shape corrections,” heuristi-  
903 cally differences in distributions that exist in distributions even after correcting for normalizations,  
904 which gives distributions a different “shape” even if their integrals are the same (c.f. Figure 4.3).

---

§This is the transverse mass of the lepton pair for 2-lepton events, the vectorial sum of the single lepton  
and  $\vec{E}_T^{\text{miss}}$  for 1-lepton events, and the  $\vec{E}_T^{\text{miss}}$  for 0-lepton events.

905 These have the schematic form

$$w_{event} = A_{region} \times f_{region}(event) \quad (4.2)$$

906 where  $w_{event}$  is the simulated event's weight,  $A_{region}$  is the overall normalization (in principle includ-  
907 ing any systematics), and  $f_{region}(event)$  is some function of event-level variables, usually a single vari-  
908 able, like  $p_T^V$  or  $m_{bb}$ . The purpose of these systematics is to take into account (in the case of a system-  
909 atic) or correct (in the case of a correction applied to the event weight) the non-trivial dependence  
910 of a normalization on one of these quantities. Some of these are taken from histograms while others  
911 are parametric functions (in this analysis, usually linear ones).

912 An example of the former case is the quantity  $\delta_{EW}$ , the difference between the nominal  $qqVH$   
913 cross section and the differential cross section as a function of  $p_T^V$  at next to leading order (NLO). As  
a correction, this term is simply used as a correction factor  $k_{EW}^{NLO} = (1 + \delta_{EW})$ .

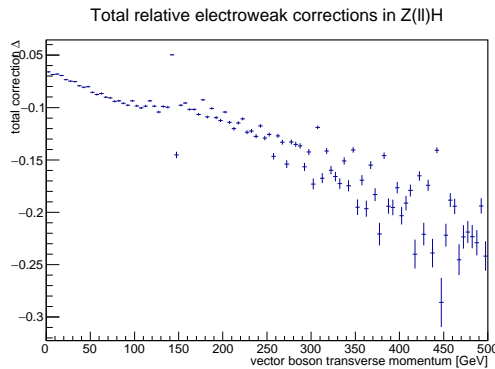


Figure 4.2: The  $\delta_{EW}$  correction term for 2-lepton  $qqZH$ .

914

915 An example of the latter case is the systematic associated with the  $m_{bb}$  dependence of the the

916     $t\bar{t}$  normalization for 2 jet,  $p_T^V \in [75, 150]$  GeV, 2 lepton events. In this case, a variety of effects are  
 917    studied (ME, PS, UE), as shown in Figure 4.3. The top half of the plot is the  $m_{bb}$  plot for this re-  
 918    gion, with the black bars representing the nominal spectrum and spectra generated with different  
 919    ME, PS, and UE choices. The ratio plot in the bottom half of the figure shows the scale of varia-  
 920    tion normalized to bin content. From this ratio plot, it is clear that the choice of ME (pink points)  
 921    was seen to have the largest effect on normalization. The linear fit in the plot reasonably envelopes  
 922    this maximum variation was done, and so is taken as the systematic variation. Hence, in this case,  
 923     $f_{region}(event)$  is a linear function of  $m_{bb}$ , with positive (negative) slope for the up (down) variation.

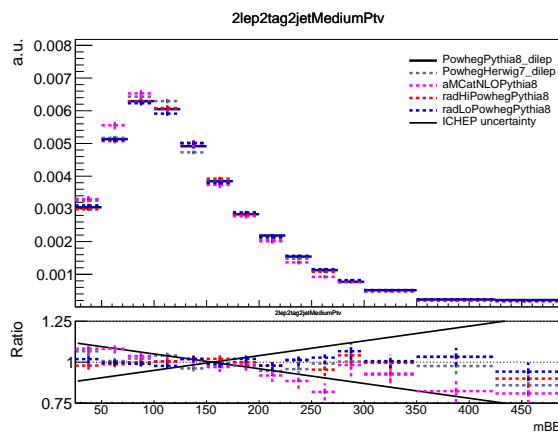


Figure 4.3: The derivation of the 2-lepton  $t\bar{t} m_{bb}$  shape systematic.

#### 924 DIVIDING MODELING UNCERTAINTIES: ACCEPTANCE RATIOS

925    In addition to uncertainties on absolute normalizations (both inclusive and region specific), mod-  
 926    eling uncertainties are sometimes introduced for the ratio of normalizations between different re-  
 927    gions. While these can be simple ratios, evaluating a systematic's effect between regions means eval-

928 uating nominal and alternate choices between regions, so the so-called “double ratio” is often taken  
 929 as the scale of variation (plus one). The ATLAS\_UEPS\_VH\_hbb systematic mentioned above, for ex-  
 930 ample, has associated with it, ATLAS\_UEPS\_VH\_hbb\_32JR. This systematic is evaluated by dividing  
 931 the 3 jet to 2 jet ratio in the nominal setup by the same ratio in an alternate setup. These ratios gener-  
 932 ically look like:

$$\frac{\text{Acceptance}[\text{Category}_A(\text{nominalMC})]}{\text{Acceptance}[\text{Category}_B(\text{nominalMC})]} \Big/ \frac{\text{Acceptance}[\text{Category}_A(\text{alternativeMC})]}{\text{Acceptance}[\text{Category}_B(\text{alternativeMC})]} \quad (4.3)$$

933 Double ratio systematics are often included in addition to single systematics when a single system-  
 934 atic could potentially overestimate the total variation due to a single effect. In the above example,  
 935 the choice of UE+PS in signal events may cause different overall variation in 2 jet events as compared  
 936 to events with 3 or more jets due to QCD considerations. However, extrapolating between jet mul-  
 937 tiplicities can be a non-trivial exercise entirely regardless of the choice of generator for UE+PS (cf.  
 938 the discussion of the Stewart-Tackman approach 4.2.2 below), so to include this variation in a single  
 939 systematic would lead to overly conservative systematic uncertainties. Hence, using previous knowl-  
 940 edge of this separate variation between jet multiplicity regions, one can define a double ratio system-  
 941 atic for a more accurate fit model.

942 The three main categories are ratios between different flavor regions, ratios between different lep-  
 943 ton channels<sup>¶</sup>, and ratios between regions with different numbers of jets,  $n_{jet}$ . The first category is  
 944 only relevant for  $V+jets$  systematics and will be treated in that process’s dedicated section below. As

---

<sup>¶</sup>e.g.  $Z+$ heavy flavor jets (at least one  $b$ -jet in the event; often denoted “hf” normalizations in 0- and 2-lepton events

945 this thesis is primarily concerned with the 2-lepton channel, the second category will not be treated  
 946 in detail, though the treatment is much the same as other ratio systematics.<sup>||</sup> In order to discuss the  
 947  $n_{jet}$  ratios in systematics (e.g. the ratios in the double ratio example), we must first describe how ex-  
 948 clusive  $n_{jet}$  cross section calculations are done.

949 **THEORETICAL ASIDE: STEWART-TACKMANN** A way to calculate uncertainties on processes in re-  
 950 gions with different numbers of jets was developed by Stewart and Tackmann and is implicitly used  
 951 for most  $n_{jet}$  ratio systematics [74]. The problem is how to calculate the cross section and associated  
 952 uncertainty for a process with exclusively  $N$  jets in the final state. Generically:

$$\sigma_{\geq N} = \sigma_N + \sigma_{\geq N+1} \quad (4.4)$$

953 The physical interpretation of one parton to one jet is an idealized case. In order to demarcate  
 954 between jets, one has some quantity that is used as a cutoff in an integral that defines the border be-  
 955 tween jet regions.

$$\sigma_{\geq N} = \int_0^{p_{cut}} \frac{d\sigma_N}{dp} + \int_{p_{cut}} \frac{d\sigma_{\geq N+1}}{dp} \quad (4.5)$$

956 Since these cutoffs (not necessarily constant, etc.) can make calculations more complicated, inclu-  
 957 sive cross sections tend to be easier to calculate. Hence, it is usually much easier to evaluate the two  
 958 inclusive cross sections and find the uncertainties on these by varying  $\alpha_S$  in the usual way (cf. Sec-

---

||Such ratios allow for information in one channel to help constrain other channels, particularly for hard to model processes like  $Z+hf$ . This helps to reduce final overall uncertainties in combined fits. For a discussion of the interplay of nuisance parameters in combined fits, cf. Chapter 9.

<sup>959</sup> tion 4.2.1). One then assumes the inclusive uncertainties are uncorrelated, for a covariance matrix for  
<sup>960</sup>  $\{\sigma_{\geq N}, \sigma_N, \sigma_{\geq N+1}\}$  of (with  $\Delta_x^2$  as the variance associated with  $x$ ):

$$\Sigma = \begin{pmatrix} \Delta_{\geq N}^2 & \Delta_{\geq N}^2 & 0 \\ \Delta_{\geq N}^2 & \Delta_{\geq N}^2 + \Delta_{\geq N+1}^2 & -\Delta_{\geq N+1}^2 \\ 0 & -\Delta_{\geq N+1}^2 & \Delta_{\geq N+1}^2 \end{pmatrix} \quad (4.6)$$

<sup>961</sup> These calculations contain Sudakov double logs of  $\ln^2(p/Q)$ , where  $Q$  corresponds to the scale  
<sup>962</sup> of the hard scatter process ( $m_H$ ), and  $p_{cut}$  is usually something like a  $p_T$  cutoff. When integrating  
<sup>963</sup> over all of the phase space, these terms can come to dominate calculations when  $p \gg Q$ . The  $N+1$   
<sup>964</sup> term in the covariance matrix is an uncertainty associated with the cutoff, but the Sudakov double  
<sup>965</sup> logs will dominate any higher order terms. Stewart and Tackmann give the following reasoning:

<sup>966</sup> “In the limit  $\alpha_S^2 \approx 1$ , the fixed-order perturbative expansion breaks down and the logarithmic  
<sup>967</sup> terms must be resummed to all orders in  $\alpha_S$  to obtain a meaningful result. For typical experimental  
<sup>968</sup> values of  $p_{cut}$  fixed-order perturbation theory can still be considered, but the logarithms cause large  
<sup>969</sup> corrections at each order and dominate the series. This means varying the scale in  $\alpha_S$  in Eq. (9) di-  
<sup>970</sup> rectly tracks the size of the large logarithms and therefore allows one to get some estimate of the size  
<sup>971</sup> of missing higher-order terms caused by  $p_{cut}$ , that correspond to  $\Delta_{cut}$ . Therefore, we can approxi-  
<sup>972</sup> mate  $\Delta_{cut} = \Delta_{\geq 1}$ , where  $\Delta_{\geq 1}$  is obtained from the scale variation for  $\sigma_{\geq 1}$ .”

<sup>973</sup> The above considerations are important for this analysis since phase space is separated into 2 and  
<sup>974</sup>  $\geq 3$  jet regions, and the uncertainties for these regions are anti-correlated.

975    4.3    PROCESS SPECIFIC SYSTEMATIC SUMMARIES

976    Brief descriptions of modeling systematics, including recapitulations of nominal sample generation,  
977    are given in the following sections. The general approach here is to copy the relevant summary tables  
978    and describe any major deviations from the general procedures described in the previous section.  
979    The dominant backgrounds for the 2-lepton channel are  $Z+hf$  and  $t\bar{t}$ , accounting for well over 90%  
980    of all background events. Diboson samples are the next-leading background and are an important  
981    validation sample; others are included for completeness. A summary of all the modeling systematics  
in this analysis are given in Table 4.1.

Process	Systematics
Signal	$H \rightarrow bb$ decay, QCD scale, PDF+ $\alpha_S$ scale, UE+PS (acc, $p_T^V$ , $m_{bb}$ , 3/2 jet ratio)
$Z+jets$	Acc, flavor composition, $p_T^V+m_{bb}$ shape
$t\bar{t}$	Acc, $p_T^V+m_{bb}$ shape
Diboson	Overall acc, UE+PS (acc, $p_T^V$ , $m_{bb}$ , 3/2 jet ratio), QCD scale (acc (2, 3 jet, jet veto), $p_T^V$ , $m_{bb}$ )
Single top	Acc, $p_T^V+m_{bb}$ shape

Table 4.1: Summary of modeling systematic uncertainties, with background samples listed in order of importance.

982

983    4.3.1    SIGNAL PROCESSES

984    Nominal signal  $qqVH$  samples are generated using PowHeg with the MiNLO (multiscale improved  
985    NLO) [62] procedure applied interfaced with PYTHIA8 using the AZNLO tune [19] and NNPDF3.0  
986    PDF set [28]. For the 2-lepton case, gluon fusion initiated Higgs production is also considered (ac-  
987    counting for  $\sim 14\%$  of the total cross section in this channel), with samples generated with PowHeg interfaced

988 with PYTHIA8 using the AZNLO tune. The NNPDF2.3 set [27] is used for both the ME and UE+PS.

989 Alternate samples  $qqVH$  samples are generated using MADGRAPH5\_aMC@NLO [22] for the

990 ME and PYTHIA8 for the UE+PS, hadronization and MPI. The NNPDF2.3\_5f FFN PDF sets and

991 the Al4 tune [13]; the latter has variations included. PowHEG+MINLO+HERWIG7 were samples

992 were also used for systematics.

993 The signal systematics categories are  $H \rightarrow bb$  decay cross section, QCD scale, PDF+ $\alpha_s$  scale, and

994 UE+PS. Additionally, there is the NLOEWK correction described above. The correction scale factor

995 is derived using the HAWK MC software. To encapsulate NNLOEW effects the maximum of 1%,

996 the square of the correction factor, and the photon induced cross section is used as a systematic.

997 Table 4.2, reproduced from [67], summarizes the signal cross section systematics, which are ap-

998 plied uniformly across the analysis channels (as applicable).

Sys Name	source	Norm. effect	applied to
ATLAS_BR_bb	$H \rightarrow bb$ dec. unc, (HO effects, $m_b$ , $\alpha_s$ )	1.7%	all $VH$ processes
ATLAS_QCDscale_VH	QCD scale uncertainty	0.7%	$qq \rightarrow VH$ processes
ATLAS_QCDscale_ggZH	QCD scale uncertainty	27%	$gg \rightarrow ZH$
ATLAS_pdf_Higgs_VH	PDF+ $\alpha_s$ uncertainty	1.9% 1.6%	$qq \rightarrow WH$ $qq \rightarrow ZH$
ATLAS_pdf_Higgs_ggZH	PDF+ $\alpha_s$ uncertainty	5.0%	$gg \rightarrow ZH$

Table 4.2: Summary of all systematic uncertainties on the  $VH$  cross section including their value, source and the corresponding nuisance parameter name.

999 The remaining signal systematics are analysis channel specific and are summarized in Table 4.3.

1000 The methodologies match those described in Section 4.2. The UE+PS systematics were derived us-

1001 ing the alternate samples mentioned above; QCD scale uncertainties were derived by varying scales

1002 by 1/3 and 3; and PDF uncertainties were derived by comparing the nominal set with the PDF4LHC15\_30

1003 PDF set [29].

NP name	oL: $ZH \rightarrow \nu\nu b\bar{b}$		iL: $WH \rightarrow \ell\nu b\bar{b}$		zL: $ZH \rightarrow \ell\ell b\bar{b}$	
	2j	3j	2j	3j	2j	$\geq 3j$
ATLAS_UEPS_VH_hbb	10.0%	10.0%	12.1%	12.1%	13.9%	13.9%
ATLAS_UEPS_VH_hbb_32JR	–	13.0%	–	12.9%	–	13.4%
ATLAS_UEPS_VH_hbb_VPT	shape only				shape+norm	
ATLAS_UEPS_VH_hbb_MBB	shape only					
QCDscale_VH_ANA_hbb_J2	6.9%	–	8.8%	–	3.3%	–
QCDscale_VH_ANA_hbb_J3	-7%	+5%	-8.6%	+6.8%	-3.2%	+3.9%
QCDscale_VH_ANA_hbb_JVeto	–	-2.5%	–	3.8%	–	–
QCDscale_VH_ANA_hbb_VPT	shape only				shape+norm	
QCDscale_VH_ANA_hbb_MBB	shape only					
pdf_HIGGS_VH_ANA_hbb	1.1%	1.1%	1.3%	1.3%	0.5%	0.5%
pdf_VH_ANA_hbb_VPT	shape only				shape+norm	
pdf_VH_ANA_hbb_MBB	shape only					

**Table 4.3:** Summary of all systematic uncertainties on the  $VH$  acceptance and shapes originating from altering the PDF and  $\alpha_S$  uncertainties, including their corresponding nuisance parameter name.

### 1004 4.3.2 $V + \text{jets}$

1005 Nominal  $V + \text{jets}$  samples are generated using SHERPA 2.2.1@NLO\*\* [52] for both the ME and PS,  
1006 interfaced with the NNPDF’s and using a five quark flavor scheme, and alternative samples are de-  
1007 rived using MADGRAPH5 interfaced with PYTHIA8. In order to increase statistics in important re-  
1008 gions of phase space, these samples were separated into kinematic slices based on  $p_T^V$  and into bins of  
1009 jet flavor. The kinematic slices were in the quantity  $\max(H_T, P_T^V)$  and had the intervals [0–70, 70–  
1010 140, 140–280, 280–500, 500–1000,  $> 1000]$  GeV. The jet flavor slices were made using flavor vetoes  
1011 and filters:

- 1012 • BFilter: at least 1 b-hadron with  $|\eta| < 4, p_T > 0$  GeV

---

\*\*SHERPA 2.1 is used for some variations not available in SHERPA 2.2.1.

- 1013     • CFilterBVeto: at least 1 c-hadron with  $|\eta| < 3, p_T > 4$  GeV; veto events which pass the  
1014       BFilter

- 1015     • CVetoBVeto: veto events which pass the BFilter and/or the CFilterBVeto

1016       These in turn are related to the main flavor regions used in the analysis, based on the flavor of  
1017       the two leading jets in an event (based on  $p_T$ ). These five flavors (with up, down, and strange collec-  
1018       tively known as “light”) yield six different flavor combinations:  $bb, bc, bl$  (these first three collectively  
1019       known as “heavy flavor” or  $V+hf$ ),  $cc, cl, ll$  (or just “light” or  $l$ ). Ratio systematics are often made  
1020       with respect to the acceptance in the  $bb$  region.

1021        $V+jet$  systematics are derived in several steps. The first is to use double ratios of acceptances be-  
1022       tween analysis regions and nominal versus alternative MC’s (so  $(\text{Region}_1\text{-nominal}/\text{Region}_2\text{-nominal})/(\text{Region}_1\text{-}$   
1023       alternate}/\text{Region}\_2\text{-alternate})). The main region comparisons are 2 jet versus 3 jet (3+ jet for 2-lepton)  
1024       and then 0-lepton versus 2-lepton (1-lepton) for  $Z+hf$  ( $W+hf^{\dagger\dagger}$ ). The final uncertainty contains the  
1025       sum in quadrature of four effects:

- 1026       1. Variation of 0.5 and 2 of QCD scales in the SHERPA sample  
1027       2. Sum in quadrature of half the variation from different resummation and CKKW merging  
1028       scales <sup>††</sup>  
1029       3. Maximal variation between nominal setup and SHERPA 2.2.1 with the MMHT2014nnlo68cl  
1030       and CT14nnlo PDF sets  
1031       4. Difference between the SHERPA and MADGRAPH<sub>5</sub> sets

---

<sup>††</sup>The  $W+hf$  CR versus the SR is also considered for  $W+hf$

<sup>‡‡</sup>cf. [59], Section 2 for a summary of the CKKW method for different parton multiplicities used in  
SHERPA

<sup>1032</sup> Summaries of the  $Z$ +jets uncertainties are provided here; the reader is referred to [67] for the  
<sup>1033</sup>  $W$ +jets systematics, as these events are virtually non-existent in the 2-lepton case with which this  
<sup>1034</sup> thesis is almost exclusively concerned. In Table 4.4, from [67] are the normalization systematics.

Process	Name	prior in region					
		$\geq 1$ jet	$\geq 2$ L: low Vpt	$\geq 2$ L: high Vpt	$\geq 0$ L	$\geq 2$ L: low Vpt	$\geq 2$ L high Vpt
$Z+1$	SysZclNorm	18%					
$Z+cl$	SysZlNorm	23%					
$Z+hf$	norm_Zbb	Floating Normalization					
$Z+hf$	SysZbbNorm_L2_J3	-	-	-	30%	30%	-
$Z+hf$	SysZbbNorm_J3	-	-	-	-	-	17%
$Z+hf$	SysZbbNorm_0L	-	-	7%	-	-	7%
$Z+hf$	SysZbbPTV	effect on each region obtained from shape rw					

**Table 4.4:** Effect of modelling systematics on  $Z$ +jets normalization in the 2lepton regions. For systematic uncertainties implemented with a prior the effect of  $1-\sigma$  variation is reported. The uncertainties labelled as  $Zbb$  act on the entire  $Z+hf$  background.

<sup>1035</sup> The flavor composition ratio systematics are in Table 4.5, also from [67].

<sup>1036</sup> Finally, the  $p_T^V$  and  $m_{bb}$  shape systematics are derived using control regions in data. The func-  
<sup>1037</sup> tional form for the  $p_T^V$  systematic is  $\pm 0.2 \log 10(p_T^V/50\text{GeV})$ , and that of the  $m_{bb}$  systematic is  $\pm 0.0005 \times$   
<sup>1038</sup>  $(m_{jj} - 100\text{ GeV})$ .

### <sup>1039</sup> 4.3.3 TOP-PAIR PRODUCTION

<sup>1040</sup> Nominal  $t\bar{t}$  samples are produced with POWHEG at NLO for the ME calculation using the NNPDF3.0  
<sup>1041</sup> PDF set interfaced with PYTHIA8.210 using the A14 tune and the NNPDF2.3 PDF set at LO. The

---

These use the same selections as the signal regions except for  $b$ -tags (0, 1, and 2 tags are studied), with the added requirement in 2tag regions that  $m_{bb}$  not be in the range of 110–140GeV.

Category	Nuisance Parameter Name	Prior	Applied to
$Z+bc/Z+bb$	SysZbcZbbRatio	40%	$Z+bc$ events (0-Lepton)
		40%	$Z+bc$ events (2-Lepton 2jet)
		30%	$Z+bc$ events (2-Lepton $\geq 3$ jet)
$Z+bl/Z+bb$	SysZblZbbRatio	25%	$Z+bl$ events (0-Lepton)
		28%	$Z+bl$ events (2-Lepton 2jet)
		20%	$Z+bl$ events (2-Lepton $\geq 3$ jet)
$Z+cc/Z+bb$	SysZccZbbRatio	15%	$Z+cc$ events (0-Lepton)
		16%	$Z+cc$ events (2-Lepton 2jet)
		13%	$Z+cc$ events (2-Lepton $\geq 3$ jet)

**Table 4.5:** The priors on the relative acceptance variations for  $Z+hf$ . The first column details the flavor components across which the acceptance variation is being considered, the second column lists the names of the corresponding nuisance parameter in the Profile Likelihood Fit, the third contains the value of the prior and the fourth column the processes and categories to which this nuisance parameter is applied.

parameters `hdamp` (nominal value  $1.5m_{top}$ , a resummation damping factor for ME/PS matching that can heuristically thought of as tuning high  $p_T$  radiation) in PowHEG and `pThard` (nominal value 0) and `pTdef` (nominal value 2) in Pythia (both control merging with PowHEG) are varied to evaluate certain systematics. Alternative  $t\bar{t}$  samples use PowHEG+Herwig7, MadGraph5\_aMC@NLO+Pythia8.2, and the nominal setup with varied tunes and parameter values. Uncertainties are taken to cover the largest difference between the nominal and any of these alternate configurations. The overall  $t\bar{t}$  normalization is a floating normalization, and further systematics attached to the ratio of acceptances between regions (3-to-2 jet, SR-to-WhfCR, and 1-to-0 lepton) are defined using double ratios; these are summarized in Tables 4.6 and 4.7, taken from [67]. Shape systematics for  $\hat{p}_T^V$  and  $m_{bb}$  are linear and taken to cover the largest difference reasonably well, as described above in 4.2.2. These are summarized in Table 4.8, again taken from [67].

The use of a top  $e - \mu$  control region helps constrain this.

	o-lepton		r-lepton			
Systematic	2j	3j	WCR 2j	SR 2j	WCR 3j	SR 3j
norm_ttbar	floating normalization					
SysttbarNorm_L0	8%	8%	-	-	-	-
SysttbarNorm_J2	9%	-	9%	9%	-	-
SysttbarNorm_DWhfCR_L1	-	-	25%	-	25%	-

**Table 4.6:** Effect of modelling systematics on  $t\bar{t}$  normalization in the 0 and 1-lepton analysis region.

	2jet		$\geq 3$ jets	
	low Vpt [SR/CR]	high Vpt [SR/CR]	low Vpt [SR/CR]	high Vpt [SR/CR]
norm_ttbar_J2_L2	floating normalization		-	
norm_ttbar_J3_L2	-		floating normalization	
SysTTbarPTV_L2_L2	effect on each region obtained from shape rw			

**Table 4.7:** Effect of modelling systematics on  $t\bar{t}$  normalization in the 2lepton regions. The SysTTbarPTV\_L2\_L2 systematic is implemented as a shape systematic over the full  $VpT > 75$  GeV range, and as a result has different acceptance effects in the low and high  $VpT$  regions.

Analysis region	Uncertainty	Value	Source	Nuisance Parameter
o,r lepton	$p_T^V$ shape	shape	fit through largest deviation (aMC@NLO+PYTHIA8)	TTbarPTV
2 lepton	$p_T^V$ shape	norm + shape	fit through largest deviation (aMC@NLO+PYTHIA8)	TTbarPTV_L2
o,r lepton	$m_{b\bar{b}}$ shape	shape only	fit through largest deviation (aMC@NLO+PYTHIA8)	TTbarMBB
2 lepton	$m_{b\bar{b}}$ shape	shape only	fit through largest deviation (aMC@NLO+PYTHIA8)	TTbarMBB_L2

**Table 4.8:** Summary of all shape uncertainties for the  $t\bar{t}$  process with short descriptions and the name of the corresponding nuisance parameters.

#### 1053 4.3.4 DIBOSON PRODUCTION

1054 Three diboson production processes (collectively denoted  $VV$ ) are important for these analyses:  $ZZ$ ,  
 1055  $WZ$ , and  $WW$ . Nominal samples are created using SHERPA 2.2.1 using the NNPDF3.0 PDF set. Al-

1056 alternative samples use PowHEG+PYTHIA8 and PowHEG+HERWIG++. The methodology here is  
 1057 similar to that of the  $t\bar{t}$  systematics, with both overall acceptance and lepton channel specific uncer-  
 1058 tainties, with the exception that UE+PS and QCD scale are treated separately (PDF+ $\alpha_S$  was found  
 1059 to be negligible).  $p_T^V$  shape systematics are described using linear fits, while  $m_{bb}$  shape systematics  
 1060 are described using hyperbolic tangents (third degree polynomials) in the 2 jet (3 jet) regions. Once  
 1061 again, summary tables from [67] are reproduced here.

Sys Name	source	Norm. effect	applied to
SysWWNorm	overall cross section uncertainty	25%	WW in all regions
SysWZNorm	overall cross section uncertainty	26%	WZ in all regions
SysZZNorm	overall cross section uncertainty	20%	ZZ in all regions

**Table 4.9:** Summary of all systematic uncertainties on the diboson cross section including their value, source and the corresponding nuisance parameter name.

NP name	oL: $ZZ \rightarrow \nu\bar{\nu}bb$		1L: $WZ \rightarrow \ell\nu bb$		2L: $ZZ \rightarrow \ell^+\ell^- bb$	
	2j	3j	2j	3j	2j	$\geq 3j$
SysVZ_UEPS_Acc	5.6%	5.6%	3.9%	3.9%	5.8%	5.8%
SysVZ_UEPS_32JR	-	7.3%	-	10.8%	-	3.1%
SysVZ_UEPS_VPT	shape+norm		shape only		shape+norm	
SysVZ_UEPS_MBB				shape only		
SysVZ_QCDscale_J2	10.3%	-	12.7%	-	11.9%	-
SysVZ_QCDscale_J3	-15.2%	+17.4%	-17.7%	+21.2%	-16.4%	+10.1%
SysVZ_QCDscale_JVeto	-	+18.2%	-	+19.0%	-	-
SysVZ_QCDscale_VPT	shape+norm		shape only		shape+norm	
SysVZ_QCDscale_MBB				shape only		

**Table 4.10:** Summary of the systematic uncertainties on the VH acceptance in each analysis region and on the  $p_T^V$  and  $m_{bb}$  shapes originating from altering the QCD scale, including their nuisance parameter name.

1062 4.3.5 SINGLE TOP PRODUCTION

1063 Single top sample are generated separately for the different production channels ( $s$ ,  $t$ , and  $Wt$ ) using  
1064 Powheg with the CT10 NLO PDF's interfaced with Pythia6 using the PERUGIA2012 PS tune  
1065 and the corresponding CTEQ6L LO PDF's and PHOTOS (TAUOLA) for QED final state ( $\tau$ ) de-  
1066 cays.

Production	Uncertainty	Value	Source	Nuisance Parameter
$s$ -channel	overall normalization	4.6%	sum in quadrature of $\mu_R$ , $\mu_F$ , $\alpha_S$ and PDF uncertainties	<code>stopNorm</code>
$t$ -channel	overall normalization	4.4%	sum in quadrature of $\mu_R$ , $\mu_F$ , $\alpha_S$ and PDF uncertainties	<code>stopNorm</code>
$t$ -channel	2 jet region acceptance	17%	sum in quadrature of deviations in alternative generators	<code>stopAcc</code> correlated with 2 jet and 3 jet case
$t$ -channel	3 jet region acceptance	20%	sum in quadrature of deviations in alternative generators	<code>stopAcc</code> correlated with overall and 3 jet case
$Wt$ channel	overall normalization	6.2%	sum in quadrature of $\mu_R$ , $\mu_F$ , $\alpha_S$ and PDF uncertainties	<code>stopWtNorm</code> correlated with 2 jet and 3 jet case
$Wt$ channel	2 jet region normalization	35%	sum in quadrature of deviations in alternative generators	<code>stopWtAcc</code> correlated with overall and 3 jet case
$Wt$ channel	3 jet region normalization	41%	sum in quadrature of deviations in alternative generators	<code>stopWtAcc</code> correlated with overall and 2 jet case
$t$ -channel	$p_T^V$ shape	shape	fit through largest deviation (Powheg+Herwig++) $\pm 0.001 \times p_T^V \mp 0.17 + 1$	<code>StopPTV</code>
$t$ -channel	$m_{b\bar{b}}$ shape	shape	fit through largest deviation (Powheg+Pythia6  radHi-radLo ) $\pm 0.0008 \times m_{b\bar{b}} \mp 0.12 + 1$	<code>StopMBB</code>
$Wt$ channel	$p_T^V$ shape	shape	fit through largest deviation (Powheg+Pythia6 with diagram subtraction) $\pm 0.003 \times p_T^V \mp 0.69 + 1$	<code>StopWtPTV</code>
$Wt$ channel	$m_{b\bar{b}}$ shape	shape	fit through largest deviation (Powheg+Pythia6 with diagram subtraction) $\pm 0.0036 \times m_{b\bar{b}} \mp 0.52 + 1$ ( $m_{b\bar{b}} < 275$ GeV) $\mp 0.47 + 1$ ( $m_{b\bar{b}} \geq 275$ GeV)	<code>StopWtMBB</code>

**Table 4.11:** Summary of all uncertainties for the single top process with short descriptions and the name of the corresponding nuisance parameters, updated for the winter baseline analysis.

*“...what would you do first?”*

*The Master said, “It would have to be rectifying names.”*

Confucius, *The Analects*

# 5

1067

1068

## Object and Event Reconstruction and

1069

## Selection

1070 IN BREAKING WITH THE STANDARD CONVENTION both object definitions and their associated

1071 experimental systematic uncertainties will be defined in this chapter: the hope is that the proximity

1072 of these descriptions will allow them to elucidate each other. Summary tables are almost exclusively  
1073 taken from [31] or [65]. This analysis, like most analyses in ATLAS, use central object definitions  
1074 from collaboration combined performance (CP) groups<sup>\*</sup> using standard analysis tools and recom-  
1075 mendations from these groups for the various objects and their accompanying systematic uncertain-  
1076 ties.

1077 Before proceeding to the objects used in this analysis, we begin with a few remarks on uncertain-  
1078 ties associated with object reconstruction. Event-level variables and selections are discussed more in  
1079 depth in Chapters 1 and 6. As described in Section 4.2, systematics quantify the uncertainty asso-  
1080 ciated with certain effects, and are generally treated in an analysis by saving histograms of discrimi-  
1081 nating distributions corresponding to the nominal analysis except with the systematic in question  
1082 varied by plus and minus one standard deviation each (one histogram each). While for modeling  
1083 systematics this only corresponds to different event weights, for experimental systematics like those  
1084 described in this chapter (with the exception of flavor tagging and certain trigger systematics), this is  
1085 done by varying the parameter in question and re-running reconstruction with the systematic varied  
1086 before recomputing all event level quantities and then saving discriminant values in their appropri-  
1087 ate distributions. This is, in general, a much more computationally intensive process in the analysis,  
1088 which is why an entire software framework, the `CxAODFramework`, was created for this analysis (see  
1089 Section 3 of [31] for more details).

---

\*Teams of physicists within ATLAS dedicated to studying different aspects of reconstruction general to very many analyses. An example is the ATLAS Muon CP group, whose duties include providing definitions for how muons are reconstructed in ATLAS, different quality requirements and thresholds, and muon related systematic uncertainties, as well as software packages to make these definitions and guidelines easier to implement.

<sup>1090</sup> 5.1 TRIGGERS

<sup>1091</sup> Tables of the triggers used with the 2015 and 2016 datasets are given in Tables 5.1 and 5.2.

0 lep	1 lep	2 lep
HLT_xe70	HLT_xe70 HLT_e24_lhmedium_L1EM20VH OR HLT_e60_lhmedium OR HLT_e120_lhloose	HLT_mu20_iloose_L1MU15 OR HLT_mu40 HLT_e24_lhmedium_L1EM20VH OR HLT_e60_lhmedium OR HLT_e120_lhloose

**Table 5.1:** Summary table of triggers used in 2015 Data.

period	0 lep	1 lep	2 lep
A	HLT_xe90_mht_L1XE50	HLT_xe90_mht_L1XE50 HLT_e26_lhtight_nod0_ivarloose OR HLT_e60_lhmedium_nod0 OR HLT_e60_medium OR HLT_e140_lhloose_nod0	HLT_mu24_ilosse(data) HLT_mu24_ilosse_L1MU15(MC) OR HLT_mu40 HLT_e26_lhtight_nod0_ivarloose OR HLT_e60_lhmedium_nod0 OR HLT_e60_medium OR HLT_e140_lhloose_nod0
B-D <sub>3</sub>	HLT_xe90_mht_L1XE50	HLT_xe90_mht_L1XE50 HLT_e26_lhtight_nod0_ivarloose OR HLT_e60_lhmedium_nod0 OR HLT_e60_medium OR HLT_e140_lhloose_nod0	HLT_mu24_ivarmedium OR HLT_mu50 HLT_e26_lhtight_nod0_ivarloose OR HLT_e60_lhmedium_nod0 OR HLT_e60_medium OR HLT_e140_lhloose_nod0
D <sub>4</sub> -E <sub>3</sub>	HLT_xe110_mht_L1XE50	HLT_xe110_mht_L1XE50 HLT_e26_lhtight_nod0_ivarloose OR HLT_e60_lhmedium_nod0 OR HLT_e60_medium OR HLT_e140_lhloose_nod0	HLT_mu24_ivarmedium OR HLT_mu50 HLT_e26_lhtight_nod0_ivarloose OR HLT_e60_lhmedium_nod0 OR HLT_e60_medium OR HLT_e140_lhloose_nod0
$\geq F_1$	HLT_xe110_mht_L1XE50	HLT_xe110_mht_L1XE50 HLT_e26_lhtight_nod0_ivarloose OR HLT_e60_lhmedium_nod0 OR HLT_e60_medium OR HLT_e140_lhloose_nod0	HLT_mu26_ivarmedium OR HLT_mu50 HLT_e26_lhtight_nod0_ivarloose OR HLT_e60_lhmedium_nod0 OR HLT_e60_medium OR HLT_e140_lhloose_nod0

**Table 5.2:** Summary table of triggers used in 2016 Data.

1092     The 0-lepton channel uses a  $\vec{E}_T^{\text{miss}}$  trigger, while the 2-lepton channel uses single lepton triggers,  
 1093    with the 1-lepton analysis using both. Since the 0- and 1-lepton channels are largely beyond the scope  
 1094    of this thesis, the discussion here will be limited to the single lepton triggers; the interested reader is  
 1095    directed towards [31] and its cited sources for an in-depth discussion of the use of the  $\vec{E}_T^{\text{miss}}$  trigger.

1096    The efficiency of triggers is in general different on simulated datasets than in actual data collected  
 1097    in ATLAS, so a scale factor to correct for this difference in efficiency must be applied to simulation  
 1098    events. This scale factor is given by the muon CP group for muons for both the 1- and 2-lepton cases  
 1099    and from the electron CP group for the 1-lepton case. For the two electron case, this was calculated  
 1100    by the analysis team as (details in [31]):

$$\frac{1 - (1 - \epsilon_{\text{MC}}^{e1} \times \text{SF}^{e1}) \times (1 - \epsilon_{\text{MC}}^{e2} \times \text{SF}^{e2})}{1 - (1 - \epsilon_{\text{MC}}^{e1}) \times (1 - \epsilon_{\text{MC}}^{e2})} \quad (5.1)$$

1101    There are also systematic uncertainties associated with these trigger efficiencies. The single elec-  
 1102    tron trigger efficiency systematic uncertainty is encapsulated in a single systematic, `EL_EFF_Trigger_-`  
 1103    `Total_1NPCOR_PLUS_UNCOR`, while the single muon trigger efficiency has two components, one  
 1104    each for the sample statistics, `MUON_EFF_TrigStatUncertainty`, and systematic uncertainties  
 1105    `MUON_EFF_TrigSystUncertainty` associated with that efficiency's measurement.

1106    While the momentum associated with the lowest un-prescaled single lepton triggers changes de-  
 1107    pending on data-taking conditions (the numbers associated with the triggers in the tables can be  
 1108    thought of as nominal  $p_T$  values for trigger level objects), the lowest typical value is  $\sim 25$  GeV. In  
 1109    order to maintain this triggering capability on low  $p_T$  muons in the higher luminosity environment

1110 of the Run 3 LHC and beyond, trigger-capable detectors will be installed in upgraded New Small  
1111 Wheels (NSW) of the ATLAS muon detector during the Phase I upgrade. Detailed studies in sim-  
1112 ulation of the trigger algorithm performance under nominal and misaligned conditions for the Mi-  
1113 cromegas detectors to be installed in the NSW may be found in Appendix A.

1114 **5.2 ELECTRONS**

1115 Electrons in ATLAS are reconstructed using a combination of the ATLAS electromagnetic calorime-  
1116 ter (ECAL) and inner detector (ID). Reconstruction begins by searching for so-called “seed clusters”  
1117 in the ECAL. The ECAL is divided into a  $200 \times 256$  tower grid in the  $\eta - \phi$  plane, with each tower  
1118 having a size of  $0.025$  square in  $\eta$  and  $\phi$ , corresponding to the granularity of the ECAL in its middle  
1119 layer, with all energy in a tower summed longitudinally. A “sliding window” of  $3 \times 5$  cells in the  
1120  $\eta - \phi$  plane is then used to identify EM clusters associated with electrons based on criteria detailed  
1121 in [49]. This comparatively simple algorithm (in contrast to jet reconstruction detailed below) is  
1122 effective since electromagnetic showers have a well defined behavior and shape.

1123 Once seed clusters have been formed, they are associated with tracks in the inner detector. Com-  
1124 bined cluster-tracks pairs form electron candidates. In order for a electron candidate to be consid-  
1125 ered a suitable electron for analysis, it must pass certain quality requirements, based on a cut on the  
1126 value of a likelihood-based (LH) discriminant (cf. [14] for details). This discriminant is given by:

$$d_{\mathcal{L}} = \frac{\mathcal{L}_S}{\mathcal{L}_S + \mathcal{L}_B}, \quad \mathcal{L}_S(\vec{x}) = \prod_{i=1}^n P_{s,i}(x_i) \quad (5.2)$$

1127 where the  $s$  and  $S$  ( $b$  and  $B$ ) subscripts refer to distributions in fiducial signal (background) distri-  
 1128 butions in bins of  $|\eta|$  and  $E_T$ . The  $P(x_i)$  are probability distributions functions (pdf)'s for input  
 1129 variables. Several sets of input variables exist for increasingly stringent quality requirements on elec-  
 1130 trons; this analysis uses Loose LH electrons as the base for electron selection, with the input vari-  
 1131 ables relating to leakage into the hadronic calorimeter (HCAL), shower and energy deposits in each  
 1132 of the ECAL layers, track quality requirements, TRT hits, and track-cluster matching. This analysis  
 1133 adds a LooseTrackOnly isolation requirement (the  $p_T$  sum of tracks within a certain  $\eta - \phi$  distance  
 1134 of the candidate track must be below a certain value), impact parameter significance cuts, and an ex-  
 1135 plicit B-layer hit requirement. The  $ZH$ -signal electrons must further pass a  $27\text{ GeV}$   $p_T$  cut ( $1.05 \times$   
 1136  $p_T^{\text{trigger}}$ ). These requirements are summarized in Table 5.3.

Electron Selection	$p_T$	$\eta$	ID	$d_0^{\text{sig}}$	$ \Delta z_0^{BL} \sin \theta $	Isolation
$VH - \text{loose}$	$>7\text{ GeV}$	$ \eta  < 2.47$	LH Loose + B-layer cut	$< 5$	$< 0.5\text{ mm}$	LooseTrackOnly
$ZH - \text{signal}$	$>27\text{ GeV}$	$ \eta  < 2.47$	LH Loose + B-layer cut	$< 5$	$< 0.5\text{ mm}$	LooseTrackOnly
$WH - \text{signal}$	$>27\text{ GeV}$	$ \eta  < 2.47$	LH Tight	$< 5$	$< 0.5\text{ mm}$	FixedCutHighPtCaloOnly

Table 5.3: Electron selection requirements.

### 1137 5.2.1 ELECTRON SYSTEMATICS

1138 The electron CP group has tabulated standard systematic uncertainties to be associated with the use  
 1139 of reconstructed electrons in ATLAS analyses in two main categories. The first category is related  
 1140 to efficiency corrections and is broken into three components: identification (`EL_EFF_ID_Total-`  
 1141 `CorrUncertainty`), reconstruction (`EL_EFF_Reco_TotalCorrUncertainty`), and isolation  
 1142 (`EL_EFF_Iso_TotalCorrUncertainty`). The second category deals with electron energy scale

1143 (roughly, the uncertainty in taking the energy deposits in an EM cluster and turning them into an  
1144 electron energy) and energy resolution (the width associated with this). This is in practice a very  
1145 complicated procedure, with over 60 systematics associated, but this analysis is not at all sensitive  
1146 to these effects and so a simplified model of two systematics, EG\_RESOLUTION\_ALL and EG\_SCALE-  
1147 \_ALL, is used.

1148 5.3 MUONS

1149 This analysis uses the standard CP muon collection in an event, though these muons in ATLAS are  
1150 constructed in a variety of ways; for full details see [25] and [17]. Most muons are constructed using  
1151 tracks in the chambers of the muon spectrometer (MS), with a variety of algorithms available. MS  
1152 tracks are sufficient to reconstruct a muon (a fit on these tracks can be used to point back to an in-  
1153 teraction point for vertex matching, for example) and, in the  $|\eta| \in (2.5, 2.7)$  interval where there  
1154 is no tracking, these standalone (SA) muons are the default. The most common and robust form  
1155 of muon reconstruction combines tracks in the MS with tracks in the ID (more precisely, a global  
1156 refit with hits from both subsystems is typically done) to form combined (CB) muons. CB and SA  
1157 muons automatically pass the loose reconstruction requirements for the Loose muons used in this  
1158 analysis. Additionally, since there is a gap in the  $|\eta| < 0.1$  range in the MS to make room for cabling  
1159 and other detector services, there are two further muon types used in this range: the segment tagged  
1160 (ST) muons that match ID tracks to segments in the MDT or CSC chambers and the calorimeter  
1161 tagged (CT) muons that match ID tracks to calorimeter clusters consistent with minimum ionizing  
1162 particles (which muons in ATLAS generally are).

1163      Further quality requirements are imposed on Loose muons for the different muon categories  
 1164      used in this analysis. Isolation requirements similar to the electrons in corresponding categories are  
 1165      imposed, and impact parameter requirements are also imposed. The  $ZH$  signal muons also have a  
 1166       $p_T$  cut at 27 GeV and a requirement that the muon fall within the  $|\eta|$  range of the ID.

Muon Selection	$p_T$	$\eta$	ID	$d_0^{\text{sig}}$	$ \Delta z_0^{\text{BL}} \sin \theta $	Isolation
$VH - \text{loose}$	$> 7 \text{ GeV}$	$ \eta  < 2.7$	Loose quality	$< 3$	$< 0.5 \text{ mm}$	LooseTrackOnly
$ZH - \text{signal}$	$> 27 \text{ GeV}$	$ \eta  < 2.5$	Loose quality	$< 3$	$< 0.5 \text{ mm}$	LooseTrackOnly
$WH - \text{signal}$	$> 25 \text{ GeV}$	$ \eta  < 2.5$	Medium quality	$< 3$	$< 0.5 \text{ mm}$	FixedCutHighPtTrackOnly

**Table 5.4:** Muon selection requirements.

### 1167 5.3.1 MUON SYSTEMATICS

1168      Similar to the treatment of systematic uncertainties associated with the electrons, muons have CP de-  
 1169      fined systematics. The muon momentum scale and resolution systematics are divided into three cat-  
 1170      egories associated one for uncertainties related to ID tracks (`MUONS_ID`), one for MS tracks (`MUONS-`  
 1171      `_MS`), one for the overall scale (`MUONS_SCALE`), and two for charge dependent momentum scales  
 1172      (`MUON_SAGITTA_RHO` and `MUON_SAGITTA_RESBIAS`). The remaining systematics have a STAT and  
 1173      SYS component corresponding to the sample statistics and systematic uncertainties for their individ-  
 1174      ual components. Efficiency scale factors use different standard candles in different  $p_T$  ranges ( $J/\psi$ 's  
 1175      ( $Z$ 's) below (above) 15 GeV), and so these systematics are broken up into two categories (`MUON_EFF-`  
 1176      `_STAT` and `MUON_EFF_SYS`; `MUON_EFF_STAT_LOWPT` and `MUON_EFF_SYS_LOWPT`). There are also  
 1177      isolation systematics (`MUON_ISO_STAT`, `MUON_ISO_SYS`) and track to vertex association systematics  
 1178      (`MUON_TTVA_STAT`, `MUON_TTVA_SYS`).

1179 5.4 MISSING TRANSVERSE ENERGY

1180 High precision performance of  $\vec{E}_T^{\text{miss}}$  is not so crucial to the 2-lepton analysis (though it is very im-  
1181 portant to the other channels), so the interested reader is referred to [26].  $\vec{E}_T^{\text{miss}}$  in ATLAS is the neg-  
1182 ative vectoral sum of physics objects (in this analysis just jets and leptons, though in principle also  
1183 including  $\tau$ 's and  $\gamma$ 's) and a so-called track based soft term (TST). The TST is comprised of valid  
1184 ID tracks not associated with any physics objects in an event. These tracks must be associated to an  
1185 event's primary vertex, have a  $p_T > 0.4$  GeV, and pass other quality requirements.

1186 The  $\vec{E}_T^{\text{miss}}$  systematic uncertainties relevant to this analysis are related to track based energy scale  
1187 and resolutions in both the soft term and in the jets and are: MET\_SoftTrk\_ResoPara, MET\_Soft-  
1188 Trk\_ResoPerp, MET\_SoftTrk\_ScaleDown, MET\_SoftTrk\_ScaleUp, MET\_JetTrk\_Scale-  
1189 Down , and MET\_JetTrk\_ScaleUp.

1190 5.5 JETS

1191 Unlike leptons, all analyses considered in this thesis are sensitive to factors regarding jet reconstruc-  
1192 tion and associated systematic uncertainties. A general discussion of jets precedes jet reconstruction  
1193 in ATLAS and associated systematics relevant to this thesis.

1194 5.5.1 JET ALGORITHMS

1195 The hadronic nature of jets makes jet reconstruction a lot more complicated than electron or photon  
1196 reconstruction, where a regular shower shape and track matching (or lack thereof in the case of the

1197 chargeless photon) provide a fairly straightforward and robust approach. The interested reader is  
1198 referred to [70] for an excellent survey, from which this discussion is greatly abbreviated.

1199 Looking at an event like the one in Figure 5.1, unambiguous individual jets are particularly easy to  
1200 identify, more or less popping out of the  $\eta - \phi$  plane plot, but this is not always the case.

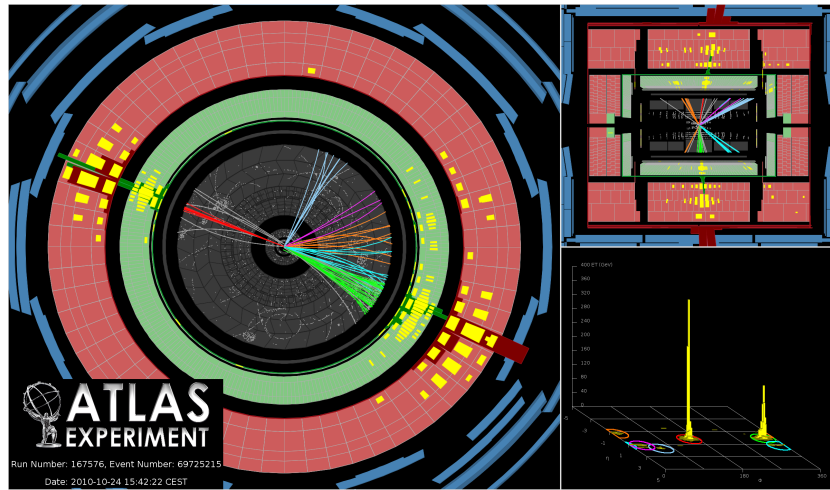


**Figure 5.1:** A clean ATLAS dijet event.

1201 Two general methods of turning particles/calorimeter towers into jets exist: cone-based and se-  
1202 quential recombination. The general theme of the former is to find a hard (energetic) particle and  
1203 draw a circle around it in the  $\eta - \phi$  plane in an intelligent manner, while the theme of the latter  
1204 is to find some metric of distance between particles and then to cluster pairs based on this distance  
1205 into jets in an intelligent way. Cone-based algorithms are simple (and therefore generally quite fast)  
1206 but generally lack some properties of the sequentially recombined jets (though there are notable ex-  
1207 ceptions like SISCone). Cone algorithm reconstructed jets are important for trigger level objects in  
1208 ATLAS, though since no jet triggers are used in this analysis, they will not be discussed any further

1209 here.

1210 The general drawback of cone-based algorithms is that they are not infrared and collinear (IRC)  
 1211 safe. That is, neither the emission of a soft (IR) quark or gluon during hadronization nor the collinear  
 1212 splitting of hard particles during hadronization should not change the final jet collection in an event.  
 1213 These are fairly common edge cases and can lead to certain pathologies in QCD calculations. In-  
 1214frared and collinear safety are diagrammed schematically in Figures 5.2 (a) and (b), taken from [70].

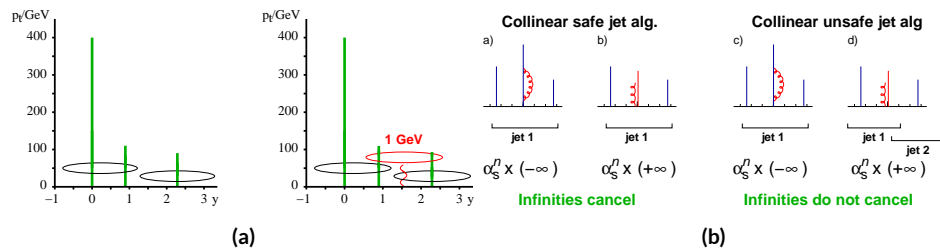


Figure 5.2: Infrared (a) and collinear (b) safety.

1215 Sequential recombination algorithms are generally safe from these effects, as these edge cases are  
 1216 very “close” to each other by construction. A sequential recombination algorithm proceeds as fol-  
 1217 lows

- 1218 1. Evaluate the set of distances  $d_{ij}$  (for pairs of objects) and  $d_{iB}$  (the “beam distance” for each  
 1219 individual object)

$$d_{ij} = \min \left( p_{Ti}^{2p}, p_{Tj}^{2p} \right) \frac{\Delta R_{ij}^2}{R^2}, \quad d_{iB} = p_{Ti}^{2p} \quad (5.3)$$

- 1220 2. Find the minimum distance  
 1221 3. If the minimum distance is:

- 1222 • A  $d_{ij}$ : cluster these objects together, and go to step 1  
 1223 • A  $d_{iB}$ : call the  $i^{\text{th}}$  object a jet, remove it from the set of objects to be clustered, and go to  
 1224 step 1

1225        4. Repeat until all objects are clustered into jets

1226        The choices one must make in sequential recombination are the size parameter  $R$ , akin to a cone  
1227        radius in cone-based algorithms, and the momentum power  $p$ . Common choices and their trade-offs  
1228        are:

- 1229        • +1: the  $k_t$  algorithm; favors the softer particles in an event, so the cluster sequence gives a his-  
1230        tory of hadronization, but jet shapes are irregular (i.e. not circular in the  $\eta - \phi$  plane)
- 1231        • 0: the Cambridge-Aachen algorithm: a pure distance metric; less substructure but jets tend to  
1232        be more circular
- 1233        • -1: the anti- $k_t$  algorithm: clustering begins with hardest particles in an event; regular, localized  
1234        jet shapes, but virtually no substructure in clustering history

1235        Jet reconstruction using all three algorithms on the same event, as well as SISCone, are shown in

1236        Figure 5.3.

1237        All three algorithms have uses for different applications in ATLAS, with anti- $k_t R = 0.4$  jets  
1238        being the default jet collection.<sup>†</sup> These are the jets used in this analysis.

1239        If the choice of jet algorithm seems a little arbitrary, it is. There is no one-size-fits-all jet collection  
1240        perfect for every application, and analyzers have to make these choices for themselves. One interest-  
1241        ing choice is the jet size parameter,  $R$ . A large  $R$  jet will contain more of the radiation coming from a  
1242        final state object, but its large size makes it susceptible to contamination from the underlying event  
1243        and pileup (as well as other analysis objects if  $R$  is sufficiently large or objects sufficiently boosted),  
1244        with small  $R$  jets having the opposite features.  $R = 0.4$  is a fairly middle-of-the-road choice. A natu-  
1245        ral question to ask is whether there needs to be just one jet collection in an analysis. Might there not

---

<sup>†</sup>The other collections find their primary uses in jet substructure techniques. For an example, cf. the discussion of jet trimming in Appendix B.

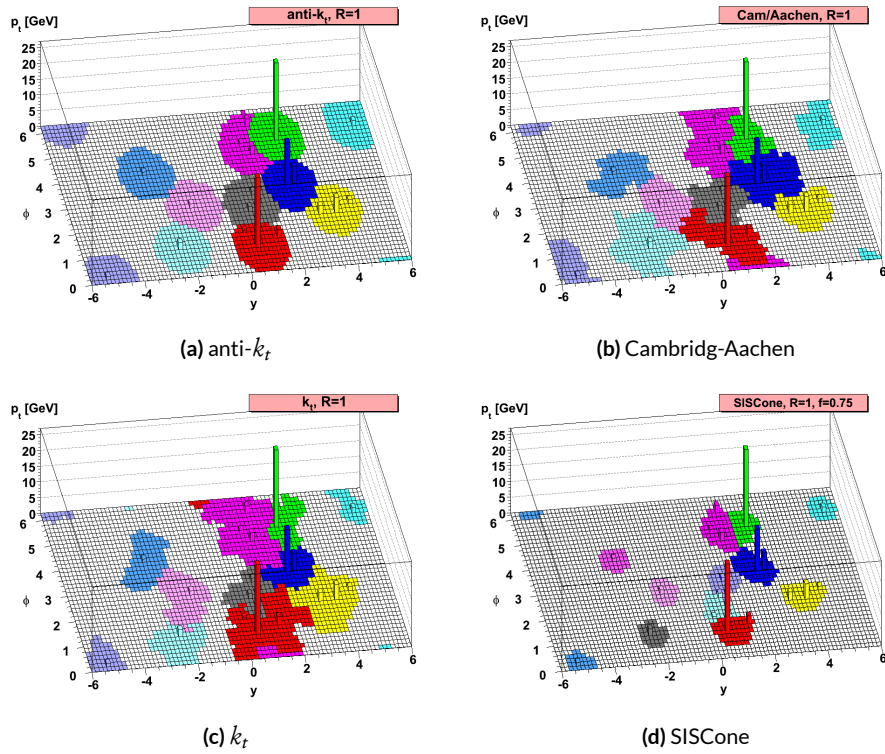


**Figure 5.3:** Different jet algorithms used on the same event. IC:[70]

<sub>1246</sub> be more information to be gained from looking at more jet sizes or clusterings? Preliminary studies  
<sub>1247</sub> point to this answer being yes and are addressed in Appendix B.

<sub>1248</sub> 5.5.2 STANDARD ATLAS HBB JETS

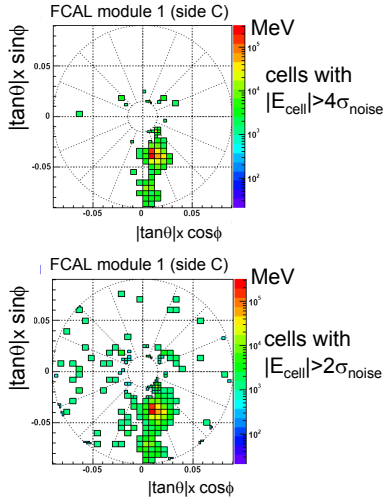
<sub>1249</sub> There are a few considerations that arise with jets in physical detectors. The first is what type of ob-  
<sub>1250</sub> ject to use as the stand in for “particles” since ATLAS measures energy deposits, not pions. The ap-  
<sub>1251</sub> proach ATLAS has settled upon are calorimeter topological clusters (or CaloTopoClusters for short)  
<sub>1252</sub> [58]. Unlike the sliding window algorithm used for electron clusters, CaloTopoClusters use a noise  
<sub>1253</sub> significance based approach in the “4-2-0” algorithm. Each cell in the electromagnetic and hadronic  
<sub>1254</sub> calorimeters (ECAL and HCAL, respectively) has associated with it a characteristic noise level ( $N$  in  
<sub>1255</sub> Equation 2.6), with this noise level in each channel, it is possible to construct a “significance” for the  
<sub>1256</sub> registered energy deposit in a given channel for a given event by dividing the measured value by its  
<sub>1257</sub> characteristic noise. Groups of cells having a significance of 4 are taken as the centers of clusters in  
<sub>1258</sub> the  $\eta - \phi$  plane. The second layer in a cluster includes all neighboring cells to the central layer with  
<sub>1259</sub> significance of at least 2, and the final layer includes all the nearest neighbors to the second layer.  
<sub>1260</sub> This is described in Figure 5.4 from [61].

<sub>1261</sub> Once CaloTopoClusters have been formed and clustered into jets, they are calibrated using the  
<sub>1262</sub> electromagnetic (EM) scale (the scale for clusters coming form EM showers). Further details may be  
<sub>1263</sub> found in [16].

<sub>1264</sub> Jets in this analysis fall into two categories, “signal” and “forward” jets, and are required to pass  
<sub>1265</sub> certain quality requirements, described in Table 5.5. All jets must pass a series of jet cleaning require-

## Local Hadronic Calibration: Clusters

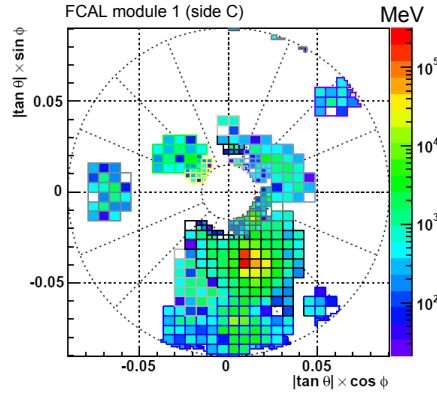
Sven Menke



□ Topological clustering

❖ 4,2,0 clusters in FCal

➢ jets with  $p_T > 50 \text{ GeV}$



3rd Hadronic Calibration Workshop, Milan, Italy, 26-27 April, 2007

M. Lefebvre, P. Loch

33

**Figure 5.4:** A description of the 4-2-0 clustering algorithm.

1266 ments using calorimeter level variables to eliminate jets coming from problematic calorimeter cells  
 1267 and certain backgrounds. Some signal jet candidates also make use of a Jet Vertex Tagger (JVT) that  
 1268 uses primary vertex and jet and track  $p_T$  information to decide whether certain soft jets are likely to  
 1269 have come from the the primary (hard scatter) vertex in an event or are to be considered pileup. Fur-  
 1270 ther details on JVT may be found in [24]. Jets are further corrected using standard CP tools and a  
 1271 dedicated PtReco correction, all outlined in Section 7.3 of [31].

1272 Overlap removal in this analysis is done according to the following precedence, taken from [31]  
 1273 with further steps only taken into account if an object survives previous steps:

- 1274 • tau-electron: If  $\Delta R(\tau, e) < 0.2$ , the  $\tau$  lepton is removed.
- 1275 • tau-muon: If  $\Delta R(\tau, \mu) < 0.2$ , the  $\tau$  lepton is removed, with the exception that if the  $\tau$  lepton

Jet Category	Selection Requirements
Forward Jets	jet cleaning $p_T > 30 \text{ GeV}$ $2.5 \leq  \eta  < 4.5$
Signal Jets	$p_T > 20 \text{ GeV}$ and $ \eta  < 2.5$ jet cleaning $\text{JVT} \geq 0.59$ if ( $p_T < 60 \text{ GeV}$ and $ \eta  < 2.4$ )

**Table 5.5:** `AntiKt4EMTopoJets` selection requirements. The jet cleaning is applied via the `JetCleaningTool`, that removes events in regions corresponding to hot calorimeter cells.

1276 has  $p_T > 50 \text{ GeV}$  and the muon is not a combined muon, then the  $\tau$  lepton is not removed.

1277 • electron-muon: If a combined muon shares an ID track with an electron, the electron is re-  
1278 moved.

1279 If a calo-tagged muon shares an ID track with an electron, the muon is removed.

1280 • electron-jet: If  $\Delta R(\text{jet}, e) < 0.2$  the jet is removed.

1281 For any surviving jets, if  $\Delta R(\text{jet}, e) < \min(0.4, 0.04 + 10 \text{ GeV}/p_T^e)$ , the electron is removed.

1282 • muon-jet If  $\Delta R(\text{jet}, \mu) < 0.2$  or the muon ID track is ghost associated to the jet, then the jet is  
1283 removed if the jet has less than three associated tracks with  $p_T > 500 \text{ MeV}$  (`NumTrkPt500PVjet < 3`)

1284 or both of the following conditions are met: the  $p_T$  ratio of the muon and jet is larger than 0.5 ( $p_T^\mu/p_T^{\text{jet}} >$   
1285 0.5) and the ratio of the muon  $p_T$  to the sum of  $p_T$  of tracks with  $p_T > 500 \text{ MeV}$  associated to the  
1286 jet is larger than 0.7 ( $p_T^{\text{muon}}/\text{SumPtTrkPt500PVjet} > 0.7$ ).

1287 For any surviving jets, if  $\Delta R(\text{jet}, \mu) < \min(0.4, 0.04 + 10 \text{ GeV}/p_T^\mu)$ , the muon is removed.

1288 • tau-jet: If  $\Delta R(\tau, \text{jet}) < 0.2$ , the jet is removed.

1289 • electron-fat jet: If  $\Delta R(e, \text{fat jet}) < 1.2$ , the fat jet is removed.

1290 Jets are corrected using a muon-in-jet correction and then a kinematic fitter (Appendix D of [65])  
1291 for the 2-lepton case (PtReco correction for the 0- and 1- lepton case). The muon-in-jet correction  
1292 is designed for  $b$ -jets. Since the decay of a  $b$ -quark to a  $c$ -quark and finally to a light quark (these are  
1293 the multiple vertices for which JetFitter in Section 5.6.1 searches) involves two weak decays, there are  
1294 two  $W$ -bosons involved in the decay. Some of these will decay semileptonically, and, while electron  
1295 and  $\tau$  energy will be captured by the calorimeters, semileptonic  $\mu$ 's will only be registered in the MS,  
1296 which occurs in some 44% of all decays from a theoretical standpoint, which amounts to about 12%  
1297 in practice (due to track isolation requirements for the leptons). This value is about 1–2% for elec-  
1298 trons, which deposit their energy in the calorimeter and so require no correction; any jet with a valid  
1299 lepton associated to it is deemed semileptonic (all others are called hadronic). Any jet with muons  
1300 associated with it has the closest muon's 4-vector (in the  $\eta - \phi$  plane) added to it.

1301 The PtReco correction is a scale factor on the muon-in-jet corrected jet's 4-vector based on the  
1302 jet's  $p_T$  and whether the jet is hadronic or semileptonic. This correction factor is based on particle  
1303 level studies done on a TruthWZ sample. As the 0- and 1-lepton cases are not the focus of this thesis,  
1304 the interested reader is directed to Section 7.3 of [31].

1305 The kinematic fitter used in 2-lepton events with two or three jets takes as its input 12 fit parame-  
1306 ters,

- 1307 • energies of 2 electron or  $p_T$  of 2 muons
- 1308 • energies of 2  $b$ -jets
- 1309 •  $\eta, \phi$  of 2 leptons and 2 jets
- 1310 •  $p_X$  and  $p_Y$  of  $\ell\ell b\bar{b}$  system.

1311 •  $m_{\ell\ell}$

1312 and 3 constraints for the variation of these parameters,

1313 • parameters : Gaussian (b-jet energy : Transfer Functions (TF); these are denoted  $L$ , with an  
1314  $L_{truth}$  as a prior) (the  $\phi$  parameters)

1315 •  $p_x$  and  $p_y$  of  $\ell\ell b\bar{b}$  system : zero with a width of 9 GeV obtained from  $ZH$  signal MC.

1316 •  $m_{ll}$  : Breit-Wigner (BW) distribution of  $Z$  boson (final term, leptons denoted  $\Omega$ )

1317 which leads to test statistic from the usual likelihood formalism to be minimized in each event:

$$\begin{aligned} -2 \ln \mathcal{L} = & \sum_{i=j} \left( \frac{(\phi_i^n - \phi_i^0)^2}{\sigma_\phi^2} \right) + \left( \frac{(\Omega_l^n - \Omega_l^0)^2}{\sigma_\Omega^2} \right) - 2 \ln(L^j) - 2 \ln(L_{truth}^j) \\ & + \sum_{i=x,y} \frac{(\sum p_i^n - \sum P_i)^2}{\sigma_{\sum p_i}^2} + 2 \ln((m_{\ell\ell} - M_X^2)^2 + M_X^2 \Gamma^2) \end{aligned} \quad (5.4)$$

### 1318 5.5.3 JET SYSTEMATICS

1319 As with the electron systematics, jet energy scale (JES) and resolution (JER) are the two principal

1320 considerations for systematic uncertainties, with even more standard. JER, as with the electron en-

1321 ergy resolution, is a single systematic uncertainty, `JET_JER_SINGLE_NP`. There is also a single JVT

1322 efficiency `JET_JvtEfficiency` systematic uncertainty. There are 88 nominal JES systematics, and

1323 this analysis is sufficiently sensitive to these variations that a single systematic is grossly insufficient.

1324 Nevertheless, some simplification is possible, with the 75 of these nuisance parameters (mostly statis-

1325 tical uncertainties related to the  $Z$ +jet and  $\gamma$ +jet calibrations) being reduced to 8, and several explic-

1326 itly named nuisance parameter. These remaining named NP's are: 3 NP's related to the  $\eta$  intercali-

1327 bration used to extrapolate standard calibrations to other jet  $\eta$  regions, 4 NP's related to the flavor

1328 composition of principle background samples ( $W/Z$ +jets, top, and diboson), 4 pileup systematics, a  
1329 single NP for the  $b$ -jet energy scale, a high  $p_T$  jet energy scale systematic, and one for jets that punch  
1330 through the HCAL to leave energy deposits in the MS. These are listed explicitly in Table 5.7.

## 1331 5.6 FLAVOR TAGGING

1332 Given that the final state in this analysis involves pairs of jets originating from  $b$ -quarks, deploying  
1333 effective flavor tagging algorithms is imperative. While flavor tagging in general can be used to isolate  
1334 any flavor ( $b$ ,  $c$ , or light ( $u$ ,  $d$ ,  $s$ , or gluon-initiated jets)), this analysis exclusively looks for  $b$ -jets, so  
1335 this discussion will focus on  $b$ 's. At truth-level in simulation, this is fairly straightforward: one need  
1336 only look at the particles contained within a jet and seeing if any include a  $b$ -quark (sometimes a  $B$   
1337 hadron) in the decay chain.

### 1338 5.6.1 DIRECT TAGGING

1339 One of the most distinctive features of  $b$ -jets is the presence of secondary vertices, as illustrated in Fig-  
1340 ure 5.5. While most partons created in particle collisions will hadronize promptly,  $b$ -quarks will first  
1341 hadronize into  $B$ -hadrons, which have lifetimes of about a picosecond. This small but finite lifetime  
1342 means that these particles will travel about half a millimeter or so before decaying into a jet in much  
1343 the usual way, and the tracks from this decay will point back to this displaced, secondary vertex.

1344 There are various secondary vertex algorithms used as inputs to the nominal  $b$ -tagging algorithm  
1345 [15], with three main types of algorithms used as inputs

- 1346 i. Track impact parameter based algorithms: L2PD (signed transverse only; more pileup ro-

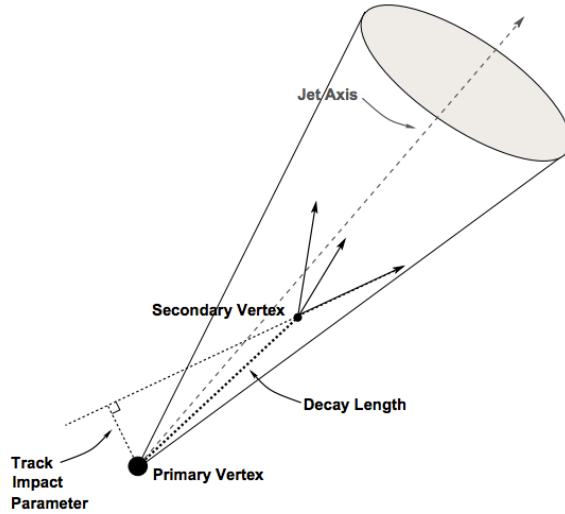


**Figure 5.5:** An illustration of a secondary vertex in a  $b$ -jet. Image credit: [54]

<sub>1347</sub> bust), I<sub>3</sub>PD (signed transverse and longitudinal)

- <sub>1348</sub> 2. Inclusive secondary vertex reconstruction: SV1 (start with two track vertex pairs and con-
- <sub>1349</sub> struct a secondary vertex)
- <sub>1350</sub> 3. Multiple vertex reconstruction (decay chain): JetFitter ( $PV \rightarrow b \rightarrow c$  decay chain using Kalman
- <sub>1351</sub> filter)

<sub>1352</sub> All of these are combined into a boosted decision tree (BDT) and trained on five million  $t\bar{t}$  events  
<sub>1353</sub> with an 90%/10% light/ $c$  jet background to form the MV<sub>2c10</sub> algorithm, with 10 referring to the per-  
<sub>1354</sub> centage of charm events in the training background. The 10% charm ratio was found to be a good  
<sub>1355</sub> balance between increased charm rejection capability (as opposed to MV<sub>2c00</sub>, which has no charm  
<sub>1356</sub> in the background training samples) and loss in light jet rejection (compared to MV<sub>2c20</sub>, which has  
<sub>1357</sub> 20% charm events in background training samples).

1358 ANALYSIS SPECIFIC CONCERNS AND SYSTEMATIC UNCERTAINTIES In addition to specifying  
 1359 the tagging algorithm, the working point efficiency must be specified. As with selection algorithms  
 1360 in general, there is a trade off between efficiency/recall (identifying all the  $b$ -jets, minimizing type  
 1361 II error) and purity/precision (making sure all jets positively identified are in fact  $b$ -jets, minimiz-  
 1362 ing type I error). Nominal efficiency working points have been calibrated by the flavor tagging CP  
 1363 group and are outlined in Table 5.6.

name	MV2c10 weight cut	$b$ -tagging efficiency [%]	$c$ RR	light RR
FixedCutBEff_60	0.9349	60.03	34.54	1538.78
FixedCutBEff_70	0.8244	69.97	12.17	381.32
FixedCutBEff_77	0.6459	76.97	6.21	134.34
FixedCutBEff_85	0.1758	84.95	3.10	33.53

**Table 5.6:**  $b$ -tagging working points available for MV2c10 for AntiKt4EMTopoJets. RR is the rejection rate (the inverse of efficiency).

1364 These values are aggregate figures, as both the jet's  $p_T$  and  $\eta$  are inputs to the MV2c10 discrim-  
 1365 inant. The working point chosen for this analysis is the 70% FixedCutBEff\_70 working point,  
 1366 with "fixed cut" referring to the fact that this particular usage of the MV2c10 BDT value is a simple  
 1367 cut value.

1368 Just as with the trigger and lepton identification efficiencies, flavor tagging efficiencies differ from  
 1369 their nominal values somewhat depending on what simulation or data sample is being used. To  
 1370 account for this difference, just as in the other cases, scale factors are applied to simulation event  
 1371 weights. It is through these event weights, as with the modeling systematics, that the flavor tagging  
 1372 systematic uncertainties are applied. Given that there are 24 input variables to MV2c10 and that fla-  
 1373 vor tagging is in general a very difficult problem, it is not surprising that, as with the JES, there are

1374 very many systematic uncertainties associated with flavor tagging. However, as with JES, the CP  
1375 group has compacted the full systematic set into a reduced set of 13 systematic uncertainties: 3 each  
1376 associated with  $c$  and light jets, 5 for  $b$ -jets (with the naming convention `FT_EFF_Eigen_(B|C|Light)N`),  
1377 one for the extrapolation of scale factors to different jet  $p_T$  regimes (`FT_EFF_Eigen_extrapolation`),  
1378 and one for the charm to bottom extrapolation (`FT_EFF_Eigen_extrapolation_from_charm`)  
1379 [80]. This schematic is a middle-of-the-road “Medium” set of systematics.

### 1380 5.6.2 TRUTH TAGGING

1381 Since imposing a 2  $b$ -tag requirement overwhelmingly rejects events dominated by  $c$ - and light jets,  
1382 statistics in such MC samples are very low. In order to circumvent this problem and restore full MC  
1383 statistics, the tag rate function, or “truth-tagging” procedure (in contrast to the standard or “direct  
1384 tagging” procedure) is applied, in which all events are kept but given a weight that preserves the over-  
1385 all shape and normalization of underlying distributions. Intuitively, this is done by giving events with  
1386 real  $b$ -jets in MC a much higher weight than events having only  $c$ - or light jets. Truth-tagging is ap-  
1387 plied to all samples when conducting MVA training in order to maximize statistics and reduce the  
1388 risk of overtraining. Truth-tagging is also used for data-MC comparison plots in 2-tag regions and  
1389 for  $V + cc$ ,  $V + c\ell$ ,  $V + \ell$ , and  $WW$  samples used in the final likelihood fit. A detailed description of  
1390 the truth-tagging process is provided below.

1391 Each jet in a given event has associated with it a  $b$ -tagging efficiency, denoted  $\varepsilon$ , that is a function  
1392 of its  $p_T$ ,  $\eta$ , and real flavor ( $b$ ,  $c$ , or light) from truth-level information in MC. Intuitively, this effi-  
1393 ciency can be thought of as the likelihood that a given jet will be  $b$ -tagged. Hence,  $b$ -jets have a much

1394 higher  $b$ -tagging efficiency than  $c$ -jets, which in turn have a higher  $b$ -tagging efficiency than light jets.

1395 We define a truth-tag weight for a given combination of tagged and untagged jets as the product of

1396 the efficiencies of the tagged jets times the product of the complement of the efficiencies of the un-

1397 tagged jets. For example, for an event with three jets, labeled 1, 2, and 3, if jets 1 and 2 are tagged, and

1398 jet 3 is untagged, the truth-tag weight associated with this combination is

$$\varepsilon_1 \varepsilon_2 (1 - \varepsilon_3) \quad (5.5)$$

1399 In order to obtain a truth-tag weight for an event, one takes the sum of the weights for each pos-

1400 sible tag combination. The current analysis requires that all events have exactly two  $b$ -tagged jets, so

1401 the truth-tag weight is the sum of all the weights of all possible pairs of tagged jets (events with fewer

1402 than two jets are discarded). Going back to the three jet example, one has the possible combinations:

1403 jets 1+2 as tagged and jet 3 as untagged; jets 1+3 as tagged and jet 2 as untagged; and finally jets 2+3 as

1404 tagged and jet 1 as untagged, which yields a total event weight of

$$w_{tot} = \varepsilon_1 \varepsilon_2 (1 - \varepsilon_3) + \varepsilon_1 \varepsilon_3 (1 - \varepsilon_2) + \varepsilon_2 \varepsilon_3 (1 - \varepsilon_1) \quad (5.6)$$

1405 For some applications (e.g. in order to use variables like pTB<sub>1</sub>, the  $p_T$  of the harder  $b$ -tagged jet in

1406 an event, in MVA training), it is necessary to choose a combination of jets in an event as “tagged.”

1407 This combination is chosen randomly, with the probability for a given combination to be chosen

1408 being proportional to its truth-tag weight. In the three jet example, the probability of tagging jets

1409 I+2 is:

$$\frac{\varepsilon_1 \varepsilon_2 (1 - \varepsilon_3)}{w_{tot}} = \frac{\varepsilon_1 \varepsilon_2 (1 - \varepsilon_3)}{\varepsilon_1 \varepsilon_2 (1 - \varepsilon_3) + \varepsilon_1 \varepsilon_3 (1 - \varepsilon_2) + \varepsilon_2 \varepsilon_3 (1 - \varepsilon_1)} \quad (5.7)$$

1410 Though not used in the current analysis, functionality exists for generic truth-tagging require-  
1411 ments (i.e. an arbitrary number of tags on an arbitrary number of jets) through the logical combina-  
1412 toric extension and for so-called “pseudo-continuous tagging,” where a  $b$ -tag score is generated for  
1413 each jet in a given event. Since a random combination of jets is set by hand to pass the  $b$ -tagging cuts  
1414 regardless of its  $b$ -tag score, a new score must be generated if this information is to be used in further  
1415 analysis. Under current settings, jets that are tagged are assigned a random  $b$ -tag score that is sampled  
1416 from the MV2c10 cumulative distribution above the 70% efficiency working point cut. All other  
1417 jets in the event are assigned a random  $b$ -tag score below the 70% working point cut. Since these dis-  
1418 tributions are discrete, the scores are not truly continuous (cf. example distributions in Figure 5.6),  
hence the “pseudo-continuous” nomenclature.

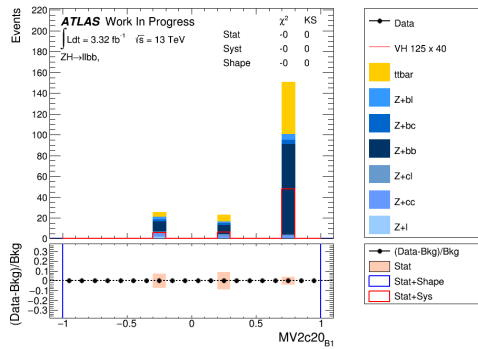


Figure 5.6: An example of a pseudo-continuous  $b$ -tagging distribution

1419

1420 A number of closure tests were performed on both the nominal and several systematics cases. In  
1421 the plots that follow, truth (solid) and direct (dashed) tagging distributions for  $m_{bb}$  and  $\Delta R(b_1, b_2)$

1422 in different  $p_T^V$  regimes for 2 lepton, 2 jet events. Agreement between the truth and direct tagging  
 1423 cases is generally very good, an example of which can be seen in Figure 5.7 for a signal  $\text{qqZIIH125}$   
 1424 sample, and the overall benefit of truth-tagging can be somewhat dramatically seen in the corre-  
 1425 sponding plots  $Z + \ell$  samples in Figure 5.8. At high  $p_T^V$  ( $p_T^V > 200$  GeV), however, in events with two  
 1426 real  $b$ -jets, there is a much greater likelihood that the  $b$ -jets will merge into a single jet, which render  
 1427 the naïve assumption that jets remain discrete invalid. While this does not appear to be a problem in  
 1428 most samples (cf.  $t\bar{t}$  in Figure 5.9), there is a mismodelling effect at low  $m_{bb}$  and low  $\Delta R(b_1, b_2)$  at  
 1429  $p_T^V > 200$  GeV for  $W/Z + bb$  samples where truth-tagging overestimates the number of events in  
 this merged regime, as can be seen in Figure 5.10

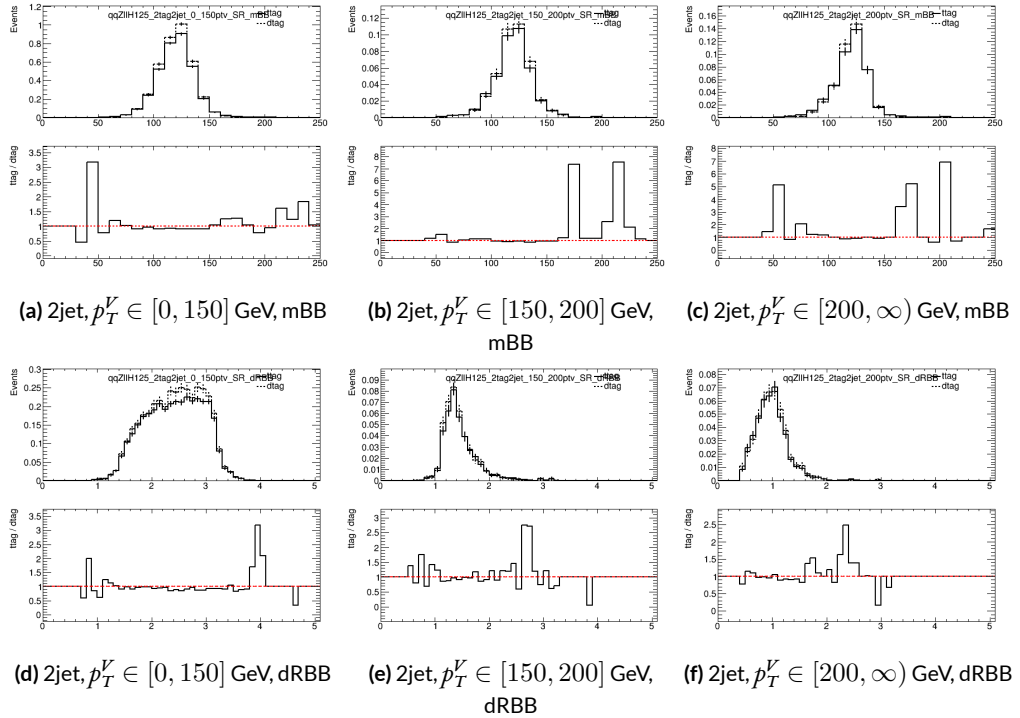
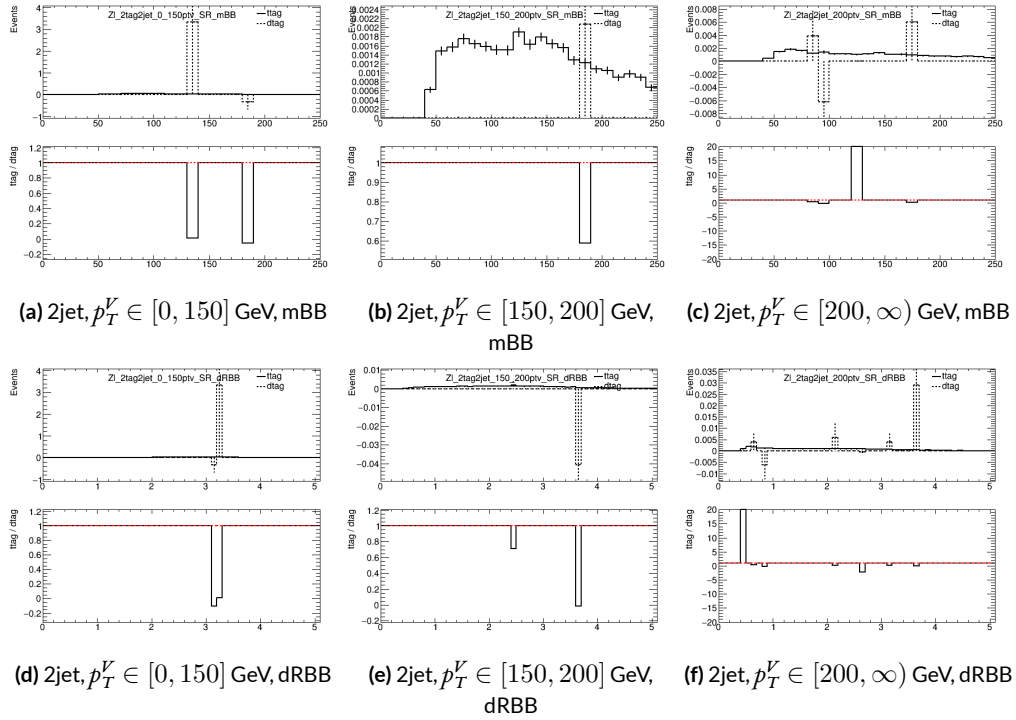
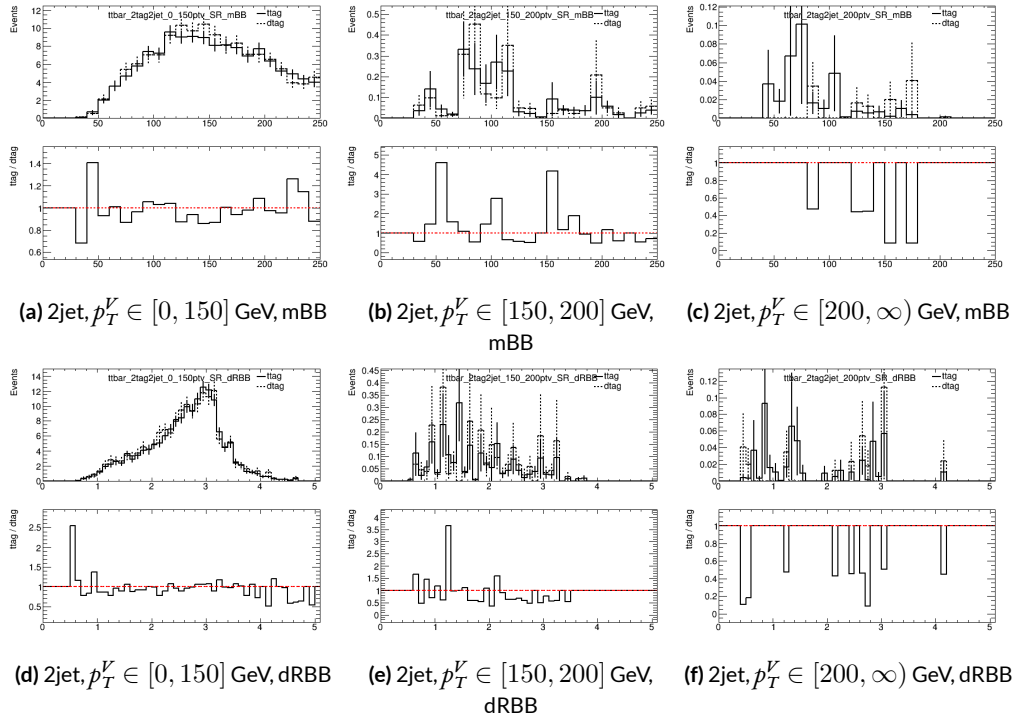


Figure 5.7: Truth-tagging closure tests for 2 lepton, 2 jet  $\text{qqZIIH125}$  samples in three different  $p_T^V$  regions.

1430



**Figure 5.8:** Truth-tagging closure tests for 2 lepton, 2 jet  $Z + \ell$  samples in three different  $p_T^V$  regions.



**Figure 5.9:** Truth-tagging closure tests for 2 lepton, 2 jet  $t\bar{t}$  samples in three different  $p_T^V$  regions.

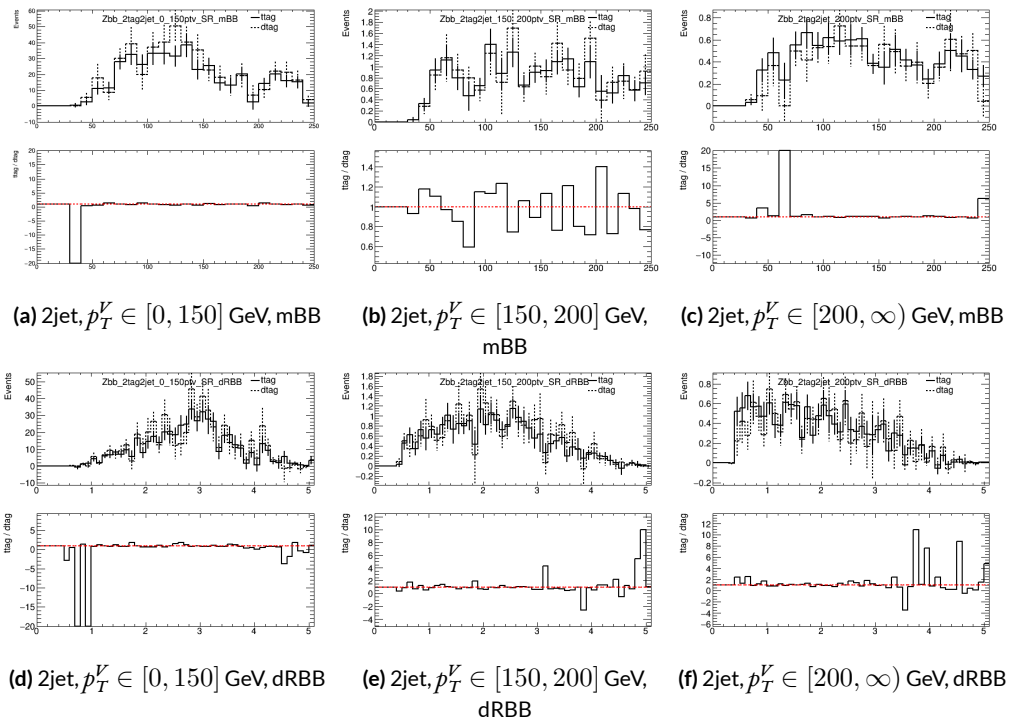


**Figure 5.10:** Truth-tagging closure tests for 2 lepton, 2 jet  $Z + bb$  samples in three different  $p_T^V$  regions.

1431 5.7 MISCELLANIA AND SYSTEMATICS SUMMARY

1432 A summary of all experimental systematics, taken from [65], may be found below. In addition to the  
1433 systematics discussed above, there are also two further systematics, on the total integrated luminosity  
1434 and on the event reweighting factor used to account for pileup, both included in Table 5.7.

1435 5.8 EVENT SELECTION AND ANALYSIS REGIONS

1436 With object and event reconstruction described, it is now time to address which events are actually  
1437 selected for use in analysis. This analysis focuses specifically on the 2-lepton channel of the fiducial  
1438 analysis, with the event selection and analysis region definitions being identical. Common to all  
1439 lepton channels in the fiducial analysis is the set of requirements on the jets in a given event. There  
1440 must be at least two central jets and exactly two signal jets that have been “*b*-tagged” according to the  
1441 MV2c10 algorithm [15], with at least one of these *b*-jets having  $p_T > 45$  GeV. For MVA training and  
1442 certain background samples, a process known as “truth-tagging” is applied instead of the standard  
1443 *b*-tagging to boost sample statistics and stabilize training/fits (cf. [65] Section 4.2 for details). After  
1444 event selection, the *muon-in-jet* and *PtReco* corrections, described in [31] 6.3.3-4, are applied to the  
1445 *b*-jets.

1446 In addition to the common selections, there are 2-lepton specific selections. All events are re-  
1447 quired to pass an un-prescaled single lepton trigger, a full list of which may be found in Tables 5 and  
1448 6 of [31] with the requirement that one of the two selected leptons in the event must have fired the  
1449 trigger. There must be 2 VH-loose leptons, and at least one of these must be a ZH-signal lepton (cf.

Systematic uncertainty	Short description	Reference
Luminosity	uncertainty on total integrated luminosity	Section 11.1 in Ref. [31]
Pileup Reweighting	uncertainty on pileup reweighting	Section 11.1 in Ref. [31]
	Electrons	
EL_EFF_Trigger_Total_1NPCOR_PLUS_UNCOR	trigger efficiency uncertainty	Section 11.2.2. in Ref. [31]
EL_EFF_Reco_Total_1NPCOR_PLUS_UNCOR	reconstruction efficiency uncertainty	Section 11.3.1. in Ref. [31]
EL_EFF_ID_Total_1NPCOR_PLUS_UNCOR	ID efficiency uncertainty	Section 11.3.1. in Ref. [31]
EL_EFF_Iso_Total_1NPCOR_PLUS_UNCOR	isolation efficiency uncertainty	Section 11.3.1. in Ref. [31]
EG_SCALE_ALL	energy scale uncertainty	Section 11.3.2. in Ref. [31]
EG_RESOLUTION_ALL	energy resolution uncertainty	Section 11.3.2. in Ref. [31]
	Muons	
MUON_EFF_TrigStatUncertainty	trigger efficiency uncertainty	Section 11.2.2. in Ref. [31]
MUON_EFF_TrigSystUncertainty	reconstruction and ID efficiency uncertainty for muons with $p_T > 15$ GeV	Section 11.4.1. in Ref. [31]
MUON_EFF_STAT	reconstruction and ID efficiency uncertainty for muons with $p_T < 15$ GeV	Section 11.4.1. in Ref. [31]
MUON_EFF_SYS	isolation efficiency uncertainty	Section 11.4.1. in [31]
MUON_EFF_STAT_LOWPT	track-to-vertex association efficiency uncertainty	Section 11.4.1. in Ref. [31]
MUON_EFF_SYST_LOWPT	momentum resolution uncertainty from inner detector	Section 11.4.2. in Ref. [31]
MUON_ISO_STAT	momentum resolution uncertainty from muon system	Section 11.4.2. in Ref. [31]
MUON_ISO_SYS	momentum scale uncertainty	Section 11.4.2. in Ref. [31]
MUON_TTVA_STAT	charge dependent momentum scale uncertainty	Section 11.4.2 in Ref. [31]
MUON_TTVA_SYS		
MUON_ID		
MUON_MS		
MUON_SCALE		
MUON_SAGITTA_RHO		
MUON_SAGITTA_RESBIAS		
	Jets	
JET_21NP_JET_EffectiveNP_1	energy scale uncertainty from the in situ analyses splits into 8 components	Section 11.5.1. in Ref. [31]
JET_21NP_JET_EffectiveNP_2	energy scale uncertainty from the in situ analyses splits into 8 components	Section 11.5.1. in Ref. [31]
JET_21NP_JET_EffectiveNP_3	energy scale uncertainty from the in situ analyses splits into 8 components	Section 11.5.1. in Ref. [31]
JET_21NP_JET_EffectiveNP_4	energy scale uncertainty from the in situ analyses splits into 8 components	Section 11.5.1. in Ref. [31]
JET_21NP_JET_EffectiveNP_5	energy scale uncertainty from the in situ analyses splits into 8 components	Section 11.5.1. in Ref. [31]
JET_21NP_JET_EffectiveNP_6	energy scale uncertainty from the in situ analyses splits into 8 components	Section 11.5.1. in Ref. [31]
JET_21NP_JET_EffectiveNP_7	energy scale uncertainty from the in situ analyses splits into 8 components	Section 11.5.1. in Ref. [31]
JET_21NP_JET_EffectiveNP_8restTerm	energy scale uncertainty from the in situ analyses splits into 8 components	Section 11.5.1. in Ref. [31]
JET_21NP_JET_EtaIntercalibration_Modeling	energy scale uncertainty on eta-intercalibration (modeling)	Section 11.5.1. in Ref. [31]
JET_21NP_JET_EtaIntercalibration_TotalStat	energy scale uncertainty on eta-intercalibrations (statistics/method)	Section 11.5.1. in Ref. [31]
JET_21NP_JET_EtaIntercalibration_NonClosure	energy scale uncertainty on eta-intercalibrations (non-closure)	Section 11.5.1. in Ref. [31]
JET_21NP_JET_Pileup_OffsetMu	energy scale uncertainty on pile-up (mu dependent)	Section 11.5.1. in Ref. [31]
JET_21NP_JET_Pileup_OffsetNPV	energy scale uncertainty on pile-up (NPV dependent)	Section 11.5.1. in Ref. [31]
JET_21NP_JET_Pileup_PtTerm	energy scale uncertainty on pile-up (pt term)	Section 11.5.1. in Ref. [31]
JET_21NP_JET_Pileup_RhoTopology	energy scale uncertainty on pile-up (density $\rho$ )	Section 11.5.1. in Ref. [31]
JET_21NP_JET_Flavor_Composition_Zjets	energy scale uncertainty on $Z+jets$ sample's flavour composition	Section 11.5.1. in Ref. [31]
JET_21NP_JET_Flavor_Composition_Wjets	energy scale uncertainty on $W+jets$ sample's flavour composition	Section 11.5.1. in Ref. [31]
JET_21NP_JET_Flavor_Composition_top	energy scale uncertainty on top sample's flavour composition	Section 11.5.1. in Ref. [31]
JET_21NP_JET_Flavor_Composition	energy scale uncertainty on $VV$ and $VH$ sample's flavour composition	Section 11.5.1. in Ref. [31]
JET_21NP_JET_Flavor_Response	energy scale uncertainty on samples' flavour response	Section 11.5.1. in Ref. [31]
JET_21NP_JET_BJES_Response	energy scale uncertainty on b-jets	Section 11.5.1. in Ref. [31]
JET_21NP_JET_PunchThrough_MC15	energy scale uncertainty for punch-through jets	Section 11.5.1. in Ref. [31]
JET_21NP_JET_SingleParticle_HighPt	energy scale uncertainty from the behaviour of high- $p_T$ jets	Section 11.5.1. in Ref. [31]
JET_JER_SINGLE_NP	energy resolution uncertainty	Section 11.5.1. in Ref. [31]
JET_JvtEfficiency	JVT efficiency uncertainty	Section 11.5.1 in Ref. [31]
FT_EFF_Eigen_B	$b$ -tagging efficiency uncertainties ("BTAG_MEDIUM"): 3 components for $b$ jets, 3 for $c$ jets and 5 for light jets	Section 11.7. in Ref. [31]
FT_EFF_Eigen_C		
FT_EFF_Eigen_L		
FT_EFF_Eigen_extrapolation	$b$ -tagging efficiency uncertainty on the extrapolation to high- $p_T$ jets	Section 11.7. in Ref. [31]
FT_EFF_Eigen_extrapolation_from_charm	$b$ -tagging efficiency uncertainty on tau jets	Section 11.7. in Ref. [31]
	MET	
METTrigStat	trigger efficiency uncertainty	Section 11.2.1. in Ref. [31]
METTrigTop/Z	track-based soft term related longitudinal resolution uncertainty	Section 11.6. in Ref. [31]
MET_SoftTrk_ResoPara	track-based soft term related transverse resolution uncertainty	Section 11.6. in Ref. [31]
MET_SoftTrk_ResoPerp	track-based soft term related longitudinal scale uncertainty	Section 11.6. in Ref. [31]
MET_SoftTrk_Scale	track MET scale uncertainty due to tracks in jets	Section 11.6. in Ref. [31]

**Table 5.7:** Summary of the experimental systematic uncertainties considered. Details on the individual systematic uncertainties can be found in the given Sections of Ref. [31].

<sup>1450</sup> Tables 5.3 and 5.4 for definitions). This lepton pair must have an invariant mass between 81 and 101  
<sup>1451</sup> GeV. In addition to the jet corrections described above, a kinematic fitter is applied to the leptons  
<sup>1452</sup> and two leading corrected jets in an event with three or fewer jets<sup>‡</sup> to take advantage of the fact that  
<sup>1453</sup> the 2-lepton final state is closed (cf. [20]); these objects are only used for MVA training/fit inputs.

<sup>1454</sup> In order to increase analysis sensitivity, the analysis is split into orthogonal regions based on the  
<sup>1455</sup> number of jets and the transverse momentum of the  $Z$  candidate (the vectoral sum of the lepton  
<sup>1456</sup> pair; this  $p_T$  is denoted  $p_T^V$ ): 2 and  $\geq 3$  jets;  $p_T^V$  in  $[75, 150), [150, \infty)$  GeV. In addition to the signal  
<sup>1457</sup> regions where the leptons are required to be the same flavor ( $e$  or  $\mu$ ), there are top  $e - \mu$  control  
<sup>1458</sup> regions used to constrain the top backgrounds.

<sup>1459</sup> All of these requirements are summarized in 5.8.

Category	Requirement
Trigger	un-prescaled, single lepton
Jets	$\geq 2$ central jets; 2 $b$ -tagged signal jets, harder jet with $p_T > 45$ GeV
Leptons	2 VH-loose leptons ( $\geq 1$ ZH-signal lepton); same (opp) flavor for SR (CR) $m_{\ell\ell} \in (81, 101)$ GeV
$p_T^V$ regions (GeV)	$[75, 150), [150, \infty)$

**Table 5.8:** Event selection requirements

<sup>1460</sup> It should be noted that the use of  $\geq 3$  jet events is a 2-lepton specific selection. These regions are  
<sup>1461</sup> exclusive 3 jet regions in the 0- and 1-lepton channels, but the fiducial 2-lepton analysis was found to  
<sup>1462</sup> see a  $\sim 4\%$  gain in sensitivity in studies by including  $\geq 4$  jet events [65].

---

<sup>‡</sup>The gain from using the kinematic fitter is found to be smeared out in events with higher jet multiplicities.

猛き者も遂には滅びぬ、

偏に風の前の塵に同じ。

Heike monogatari

# 6

1463

1464

## Multivariate Analysis Configuration

1465 IN ORDER TO fully leverage the descriptive power of the 13 TeV dataset, this analysis makes use of a

1466 multivariate (MVA) discriminant. Where traditionally event counts or single discriminating vari-

1467 ables per region of phase space have been fed to fits, MVA discriminants seek to integrate additional

1468 information not captured in the conventional phase space cuts plus dijet invariant mass distribu-

1469 tions. Formulating the MVA discriminant is an exercise in supervised learning to construct a binary  
1470 classifier, where one uses labeled “signal” and “background” MC events to optimize the parameters  
1471 of a statistical model—in this case a boosted decision tree (BDT) with some set of physically moti-  
1472 vated variables (or “factors”). The interested reader is directed to the standard references on machine  
1473 learning for further details. Sample and variable selection, including variables derived using the the  
1474 RestFrames and Lorentz Invariants concepts introduced in Sections 1.5–1.7, are discussed in Section  
1475 6.1; MVA training is treated in Section 6.2; and the data statistics only (no systematics) performance  
1476 of the three MVA discriminants is explored in Section 6.3.

## 1477 6.1 TRAINING SAMPLES AND VARIABLE SELECTION

1478 A subset of samples described in Chapter 3 is used for multivariate analysis training, with  $qqZH \rightarrow$   
1479  $\ell\ell b\bar{b}$  and  $ggZH \rightarrow \ell\ell b\bar{b}$  used as signal samples and  $Z+jets$ ,  $t\bar{t}$ , and  $VV$  used as background samples.  
1480 Truth-tagging (Section 5.6.2) is used on all samples in MVA training to improve training statistics  
1481 and stability. All figures quoted in this section scale distributions to a luminosity of  $36.1 \text{ fb}^{-1}$ .

### 1482 6.1.1 STANDARD VARIABLES

1483 The standard set of variables taken as a baseline is the same as used in the fiducial analysis. The vari-  
1484 ables fall into several main categories: energy/momenta scales of composite objects ( $m_{bb}$ ,  $m_{bbj}$ ,  
1485  $p_T^V$ ,  $m_{\ell\ell}$ ), angles ( $\Delta R(b_1, b_2)$ ,  $\Delta\phi(V, H)$ ,  $\Delta\eta(V, H)$ ), transverse momenta of the jets in the event  
1486 ( $p_T^{b_1}$ ,  $p_T^{b_2}$ ,  $p_T^{j_3}$ ), and  $E_T^{miss}$ . Input distributions for these variables in all the 2 ( $\geq 3$  jet) analysis signal  
1487 regions may be found in Figure 6.1 (6.2). The “kf” at the end of variable names denotes that these

are derived using 4-vectors that are the result of the kinematic fitter. The distributions in the figure

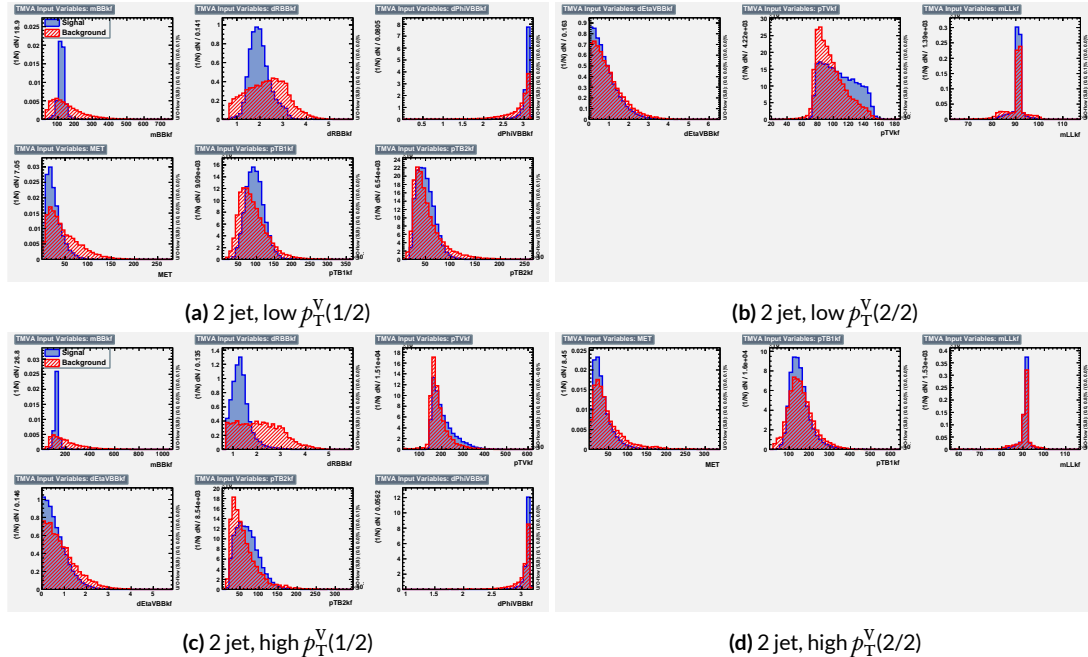


**Figure 6.1:** Input variables in 2 jet signal regions for the standard variable set. Signal distributions are in red, and background distributions are in blue.

1488

1489 are used as inputs for one of the two k-folded final discriminants, and the order of the distributions  
 1490 is the hyperparameter optimized order for feeding into the BDT; what precisely this means will be  
 1491 discussed in following sections. While variables in the analysis regions are generally similar, there are  
 1492 some notable exceptions.  $p_T^V$  and the correlated  $\Delta R(b_1, b_2)$  have different shapes, by construction  
 1493 for the former and by correlation for the latter, at low and high  $p_T^V$ . \* The  $\geq 3$  jet regions also have  
 1494 variables that are not applicable to the 2 jet regions; the inclusion of  $m_{BBJ}$  (the invariant mass of the  
 1495 two  $b$ -jets and leading untagged jet) in particular is of note and suggests a potential avenue forward

\*Recall that higher  $p_T^V$  means, in a balanced final state like  $ZH \rightarrow \ell\ell b\bar{b}$ , the  $b$ -jet pair will have higher  $p_T$  and hence be more collimated (lower  $\Delta R(b_1, b_2)$ ); this is not necessarily the case for background events, as the distributions show.

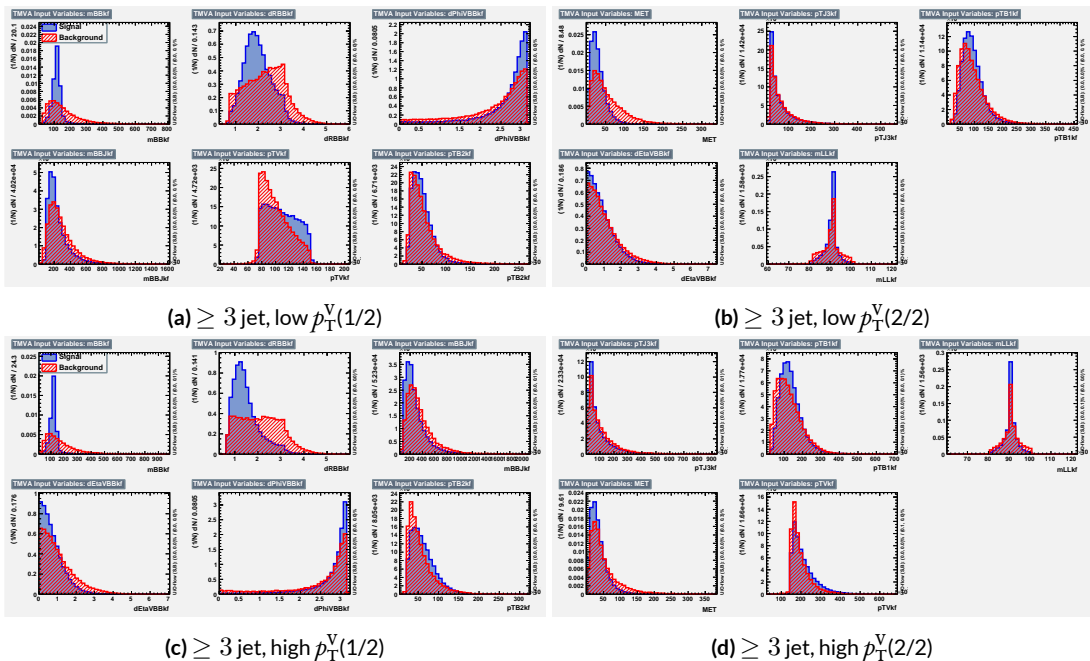


**Figure 6.2:** Input variables in  $\geq 3$  jet signal regions for the standard variable set. Signal distributions are in red, and background distributions are in blue.

1496 for refinements of the non-standard variables.

1497 Looking at the correlation matrices for the standard variables in Figure 6.3, it is easy to see that

there are large number of non-trivial correlations

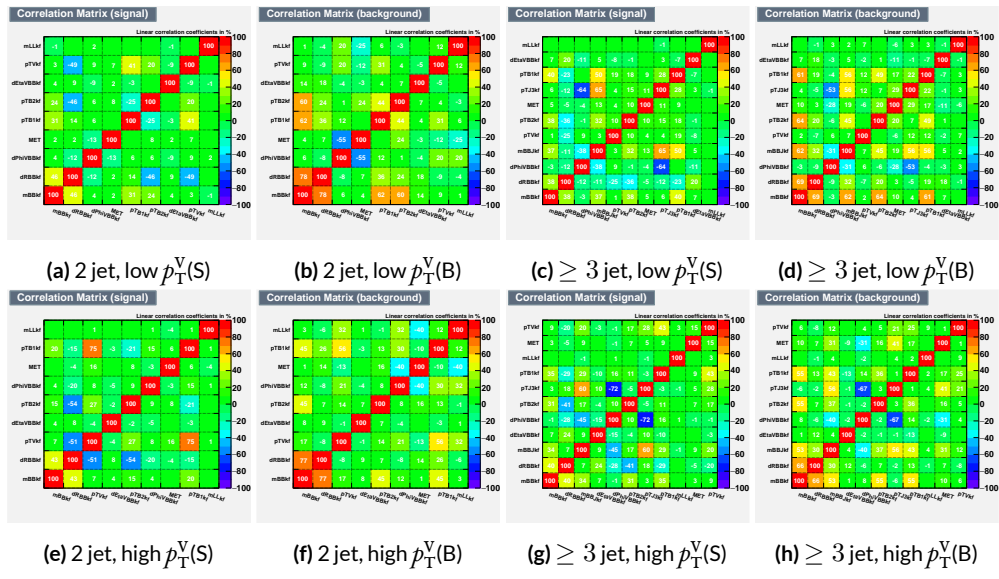


Figure 6.3: Signal and background variable correlations for the standard variable set.

1498

1499    6.1.2    LORENTZ INVARIANTS

1500    In choosing the set of variables used for a set of Lorentz Invariants based discriminants, we decided  
 1501    to use S. Hagebeck's set from [53] and related studies. Distributions of these variables in the same  
 arrangement as with the standard variables may be seen in Figures 6.4 and 6.5. One thing to note

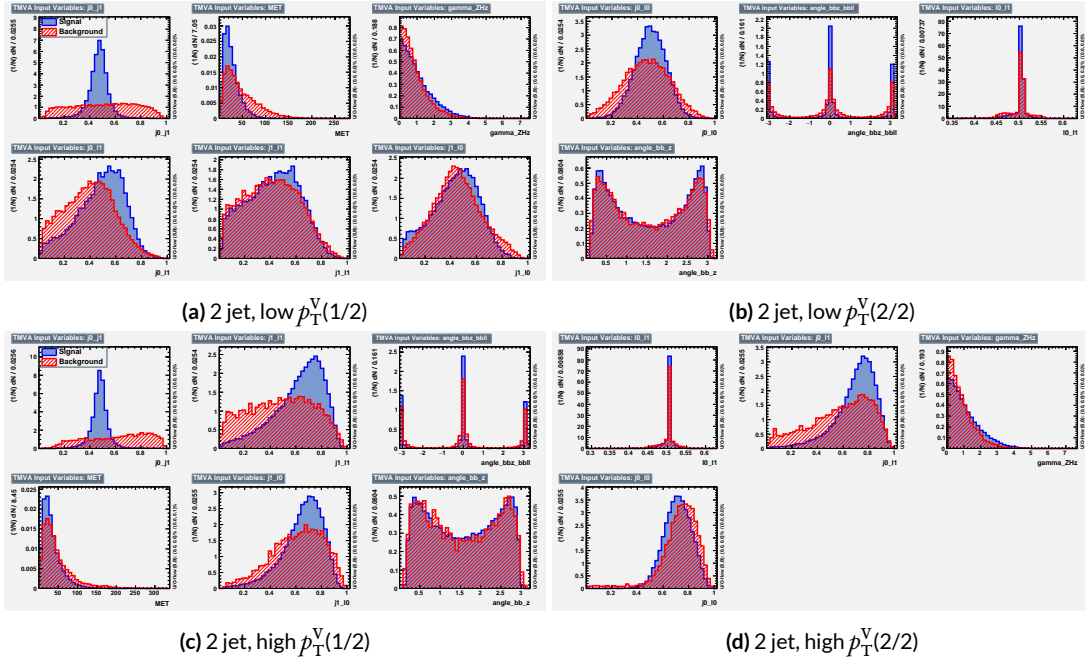
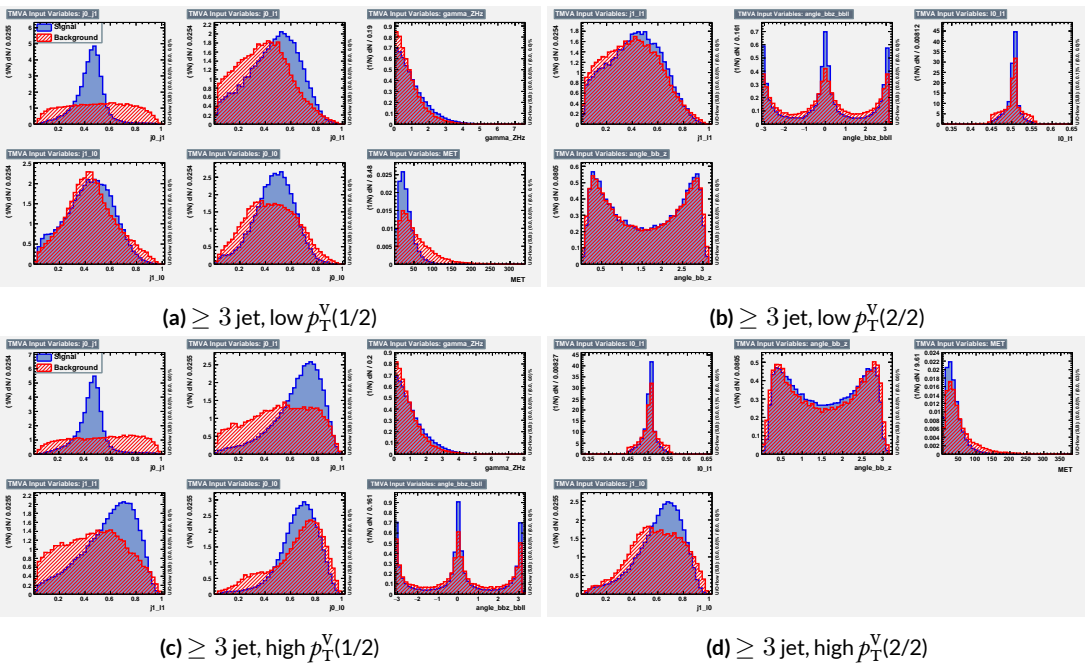


Figure 6.4: Input variables in 2 jet signal regions for the LI variable set. Signal distributions are in red, and background distributions are in blue.

1502

1503    about the variable set chosen here is that  $\vec{E}_T^{\text{miss}}$  has been added to the standard LI set. Since the LI  
 1504    construction assumes that this quantity is zero, there is no obvious way to include it. Nevertheless,  
 1505    as the correlation matrices for the LI variables show in Figure 6.6, there is actually very little correla-  
 1506    tion between  $\vec{E}_T^{\text{miss}}$  and the other variables (with this being slightly less the case for the background  
 1507    correlations, as to be expected since  $t\bar{t}$ , a principal background, is  $\vec{E}_T^{\text{miss}}$ -rich). Hence, if including



**Figure 6.5:** Input variables in  $\geq 3$  jet signal regions for the LI variable set. Signal distributions are in red, and background distributions are in blue.

<sup>1508</sup>  $\vec{E}_T^{\text{miss}}$  violates the spirit somewhat of the LI variables, it does not break terribly much with the aim of

having a more orthogonal set.

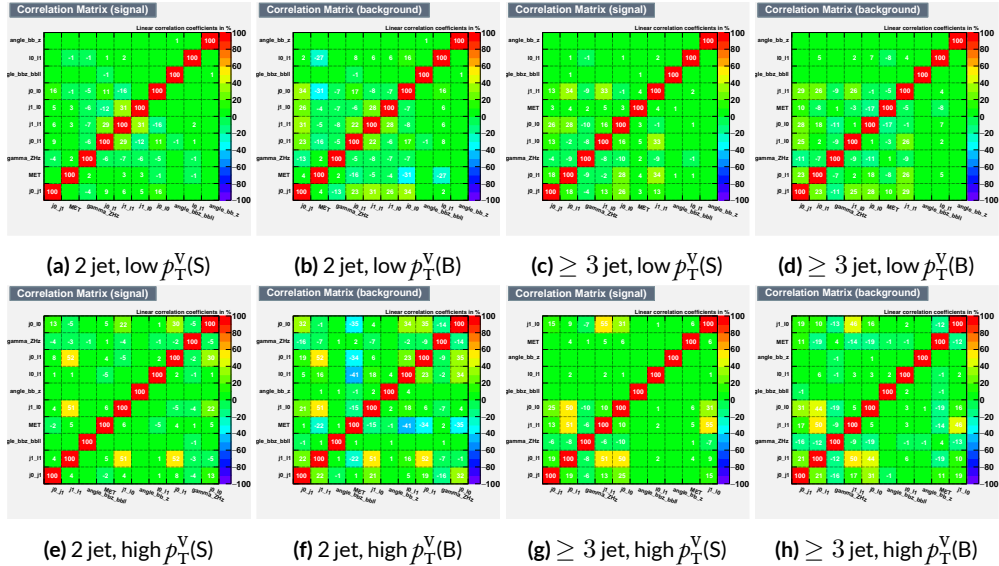


**Figure 6.6:** Signal and background variable correlations for the LI variable set.

1510 6.1.3 RESTFRAMES VARIABLES

1511 There is no precedent for using the RestFrames variables in the  $ZH \rightarrow \ell\ell b\bar{b}$  analysis, so a subset  
1512 of possible RF variables had to be selected as the basis of a discriminant. The masses and cosines of  
1513 boost angles from parent frames for the CM,  $Z$ , and  $H$  frames gives six variables, and it was decided  
1514 that it would be good to match the LI in terms of variable number and treatment (i.e. no special  
1515 treatment of the third jet), which leaves four more variables. In addition to the cosines, there are  
1516 also the  $\Delta\phi$  angles. Furthermore, there are the event-by-event scaled momentum ratios, both lon-  
1517 gitudinal and transverse. There is also both a  $\Delta\phi$  and an CM-scaled ratio for the  $\vec{E}_T^{\text{miss}}$ . All of these  
1518 variables were included in a ranking using slightly different training settings as the main hyperpa-  
1519 rameter optimization variable ranking described below. The goal of this study was not to develop a  
1520 discriminant, as the number of variables is too high, but rather to see which ones are generally use-  
1521 ful. Table 6.1 shows the results of this study. Percent gains (losses) at each step by adding the variable  
1522 with biggest gain (smallest loss) are shown in green (red). The final row shows an aggregate rank-  
1523 ing, calculated simply by adding up a variables ranks in all bins and ordering the variables smallest  
1524 to greatest. This simple aggregation does not take into account which regions are potentially more  
1525 sensitive and so where taken simply to give an idea of how variables generally performed. With this  
1526 in mind, the RF variables were chosen to be the masses  $M_{CM}$ ,  $M_H$ , and  $M_Z$ , the angles  $\cos CM$ ,  $\cosh$ ,  
1527  $\cos Z$ ,  $\cos \phi CMH$ , and the ratios  $R_{pt}$ ,  $R_{pz}$ , and  $R_{met}$ . Their distributions may be seen in Figures 6.7  
1528 and 6.8.

1529 Correlations for the chosen RF variables are shown in Figure 6.9. These correlations are much

Region	Variable Chain
2jet pTVbin1	Rpt (65.8%), Rpz (29.0%), cosZ (11.4%), MZ (-1.75%), dphiCMH (7.26%), cosCM (3.95%), cosH (0.142%), MCM (2.18%), dphiCMZ (-2.3%), dphiCMMet (-0.236%), dphiLABCM (0.404%), Rmet (-4.04%)
3jet pTVbin1	Rpt (50.8%), Rpz (15.6%), MZ (14.8%), cosZ (3.08%), MCM (3.79%), dphiCMH (3.24%), cosH (0.755%), dphiCMMet (1.04%), Rmet (-1.03%), cosCM (5.31%), dphiCMZ (-1.27%), dphiLABCM (-2.88%), pTJ3 (-1.27%)
2jet pTVbin2	Rpt (52.0%), Rpz (13.8%), cosZ (16.9%), cosH (6.49%), MCM (1.71%), cosCM (6.21%), Rmet (4.25%), dphiCMMet (-1.53%), dphiLABCM (-0.757%), dphiCMH (0.213%), MZ (-0.788%), dphiCMZ (-2.39%)
3jet pTVbin2	Rpt (31.5%), Rpz (21.6%), cosH (8.97%), cosZ (1.42%), cosCM (11.3%), dphiCMZ (-2.84%), MCM (8.17%), dphiCMH (-0.841%), dphiLABCM (-0.00318%), dphiCMMet (-2.6%), pTJ3 (-3.21%), MZ (-1.8%), Rmet (-6.29%)
Aggregate	Rpt (o,o,o,o), Rpz (i,i,i,i), cosZ (2,3,2,3), cosH (6,6,3,2), MCM (7,4,4,6), MZ (3,2,10,11), dphiCMH (4,5,9,7), cosCM (5,9,5,4), dphiCMMet (9,7,7,9), dphiCMZ (8,10,11,5), Rmet (11,8,6,12), dphiLABCM (10,11,8,8)

**Table 6.1:** Full RF variable ranking study summary. Green (red) percentages represent gains (losses) in a validation significance at each step.

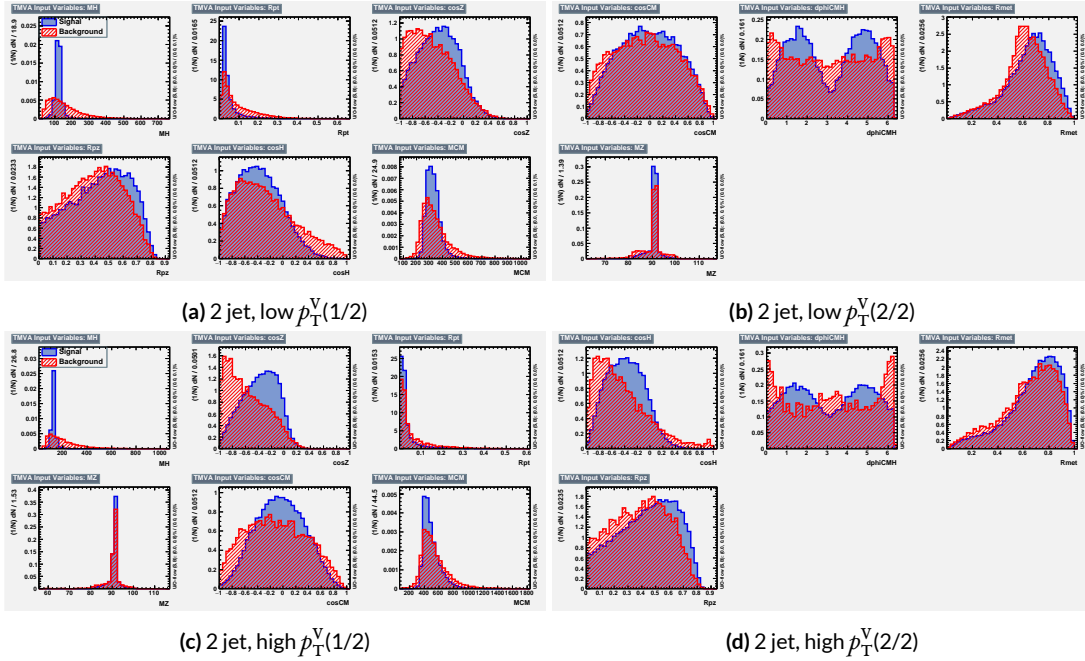


**Figure 6.7:** Input variables in 2 jet signal regions for the RF variable set. Signal distributions are in red, and background distributions are in blue.

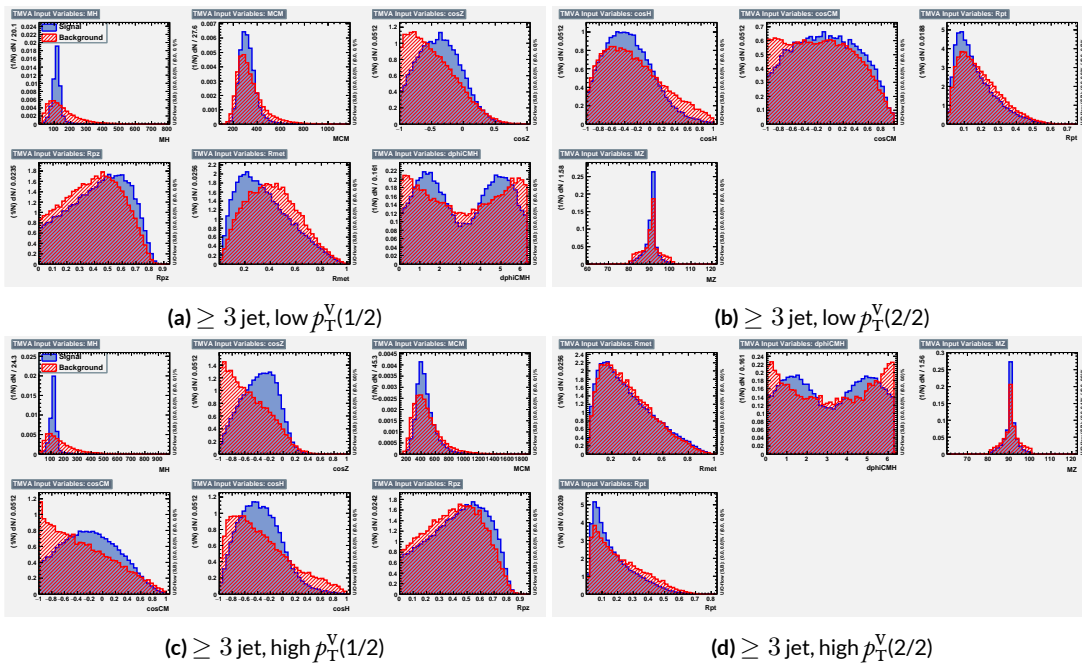


**Figure 6.8:** Input variables in  $\geq 3$  jet signal regions for the RF variable set. Signal distributions are in red, and background distributions are in blue.

1530 lower than for the standard case but still slightly higher than for the LI case. Notably, many strong  
 1531 correlations that exist for signal events do not exist in background events and vice versa, so what is  
 1532 lost in orthogonality may very well be recuperated in greater separation<sup>†</sup>. Given the generally better  
 1533 performance of the RF sets, as we shall see in following sections and chapters, this slight tradeoff is  
 1534 likely an aesthetic one, with the main benefits of a more orthogonal basis likely realized at this level  
 1535 of correlation.

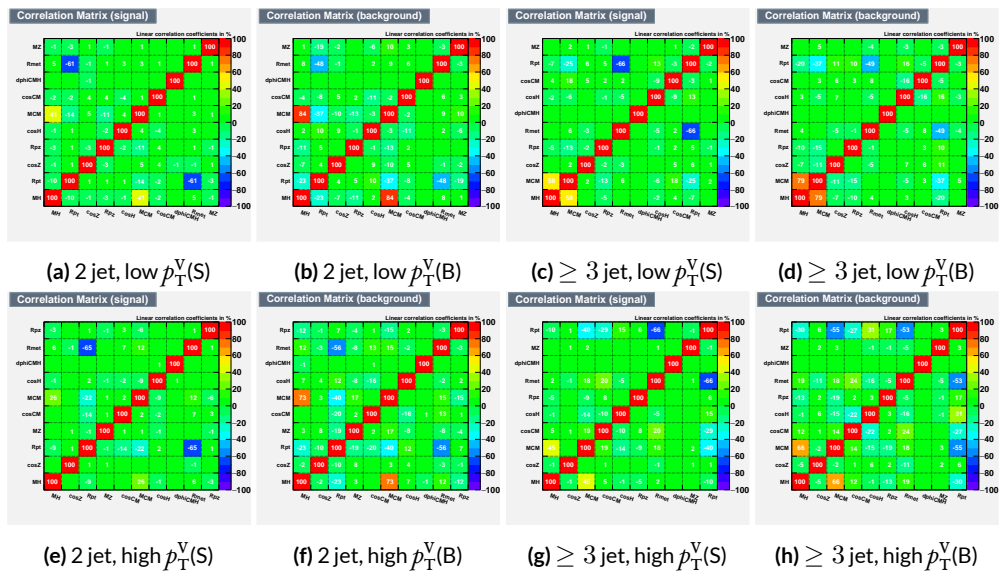


Figure 6.9: Signal and background variable correlations for the RF variable set.

1536 A summary of the variables used in the three cases is given in 6.2.

---

<sup>†</sup>It is very hard to say for certain whether this is the case for MVA discriminants, and such dedicated studies might make worthwhile future studies.

Variable Set	Variables
Standard	mBB, mLL, (mBBJ), pTV, pTB1, pTB2, (pTJ3), dRBB, dPhiVBB, dEtaVBB, MET 9(11) vars
Lorentz Invariants	j0_j1, j0_l1, l0_l1, j1_l1, j0_l0, j1_l0, gamma_ZHz, angle_bbz_bbll angle_bb_z, MET 10 vars
RestFrames	MH, MCM, MZ, cosH, cosCM, cosZ, Rpz, Rpt, dphiCMH, Rmet 10 vars

**Table 6.2:** Variables used in MVA training. Variables in parentheses are only used in the  $\geq 3$  jet regions.

## 1537 6.2 MVA TRAINING

1538 With variables chosen, the MVA discriminants must be trained and optimized. MVA training and  
 1539 hyperparameter optimization (in this case, just the order in which variables are fed into the MVA) is  
 1540 conducted using the “holdout” method. In this scheme, events are divided into three equal portions  
 1541 (in this case using `EventNumber%3`), with the first third (the “training” set) being used for the initial  
 1542 training, the second third (the “validation” set) being used for hyperparameter optimization, and  
 1543 the final third (the “testing” set) used to evaluate the performance of the final discriminants in each  
 1544 analysis region.

1545 The MVA discriminant used is a boosted decision tree (BDT). Training is done in TMVA using  
 1546 the training settings of the fiducial analysis [65]<sup>‡</sup>. For the purposes of hyperparameterization and  
 1547 testing, transformation D with  $z_s = z_b = 10$  is applied to the BDT distributions, and the cumula-  
 1548 tive sum of the significance  $S/\sqrt{S + B}$  in each bin is calculated for each pair of distributions.

1549 Transformation D is a histogram transformation, developed during the Run 1 SM  $VH(b\bar{b})$  search,

---

<sup>‡</sup>Namely, !H:!V:BoostType=AdaBoost:AdaBoostBeta=0.15:SeparationType=GiniIndex:-PruneMethod=NoPruning:NTrees=200:MaxDepth=4:nCuts=100:nEventsMin=5%

1550 designed to reduce the number of bins in final BDT distributions and thereby mitigate the effect of  
 1551 statistical fluctuations in data while also maintaining sensitivity. Such an arbitrary transformation  
 1552 may be expressed as:

$$Z(I[k, l]) = Z(z_s, n_s(I[k, l]), N_s, z_b, n_b(I[k, l]), N_b) \quad (6.1)$$

1553 where

- 1554 •  $I[k, l]$  is an interval of the histograms, containing the bins between bin  $k$  and bin  $l$ ;
- 1555 •  $N_s$  is the total number of signal events in the histogram;
- 1556 •  $N_b$  is the total number of background events in the histogram;
- 1557 •  $n_s(I[k, l])$  is the total number of signal events in the interval  $I[k, l]$ ;
- 1558 •  $n_b(I[k, l])$  is the total number of background events in the interval  $I[k, l]$ ;
- 1559 •  $z_s$  and  $z_b$  are parameters used to tune the algorithm.

1560 Transformation D uses:

$$Z = z_s \frac{n_s}{N_s} + z_b \frac{n_b}{N_b} \quad (6.2)$$

1561 Rebinning occurs as follow:

- 1562 1. Begin with the highest valued bin in the original pair of distributions. Call this the “last” bin  
1563 and use it as  $l$ , and have  $k$  be this bin as well.
- 1564 2. Calculate  $Z(I[k, l])$
- 1565 3. If  $Z \leq 1$ , set  $k \rightarrow k - 1$  and return to step 2. If not, rebin bins  $k-l$  into a single bin and name  
1566  $k - 1$  the new “last” bin  $l$ .
- 1567 4. Continue until all bins have been iterated through; if  $Z \leq 1$  for any remaining  $n$  of the  
1568 lowest-valued bins (as is often the case), simply rebin these as a single bin.

1569 Variable ranking is done iteratively (greedily) in each analysis region. In each set, the validation  
 1570 significance of a BDT using an initial subset of variables is calculated ( $dRBB$  and  $mBB$  for the stan-  
 1571 dard set;  $j0\_j1$  for the LI set; and  $MH$  for the RF set). Each of the remaining unranked variables  
 1572 are then added separately, one at a time, to the BDT. The variable yielding the highest validation  
 1573 significance is then added to the set list of ranked variables and removed from the list of unranked  
 1574 variables. This process is repeated until no variables remain. These rankings are shown in Figures  
 1575 **6.10–6.12.** Rankings tend to be fairly stable.

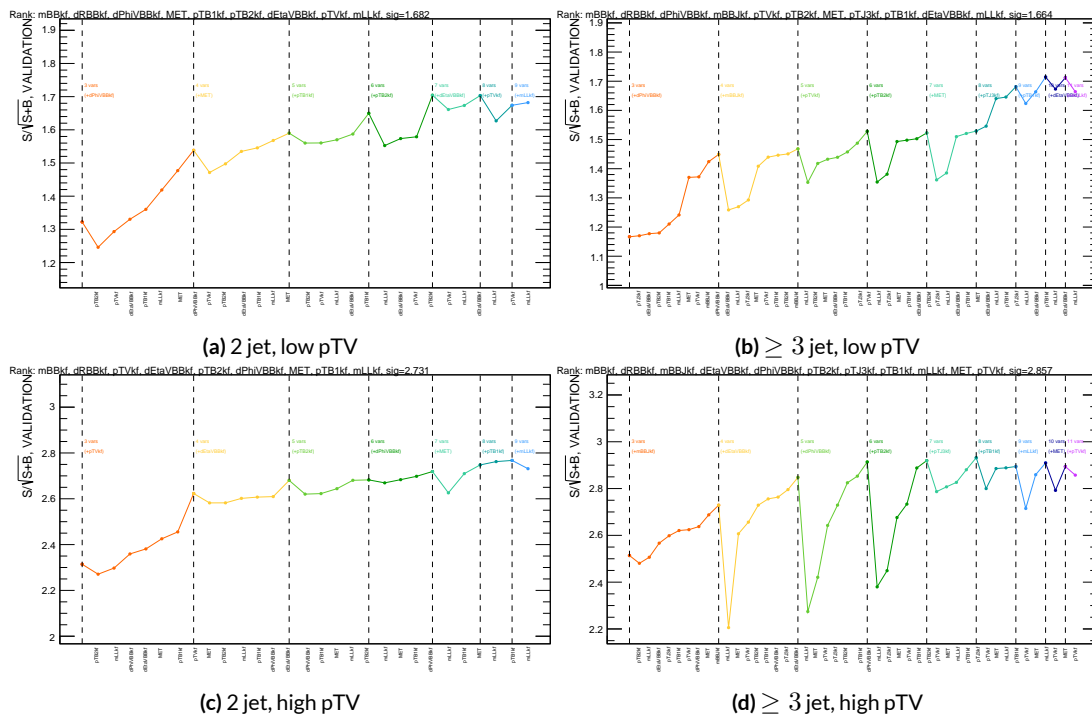


**Figure 6.10:** Rankings for the standard variable set.

1566 Once variables have been ranked, the BDT may be used both to evaluate performance in a simpli-  
 1567 fied analysis scenario in the absence of systematic uncertainties (described below in Section 6.3) and

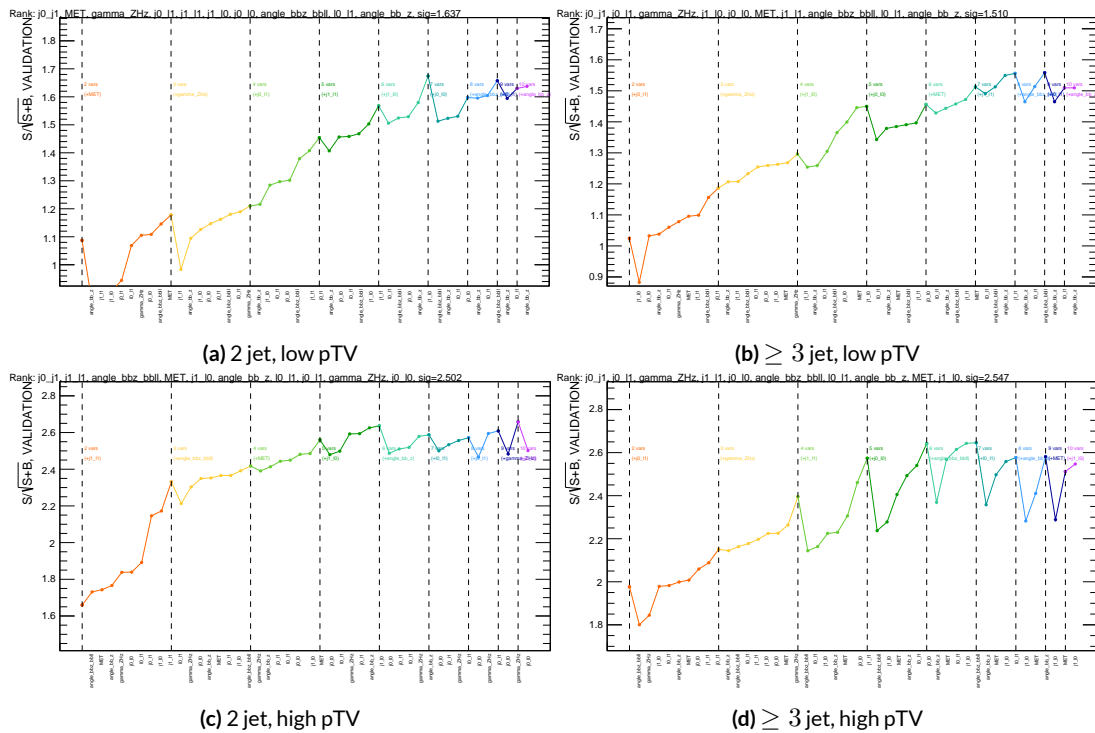
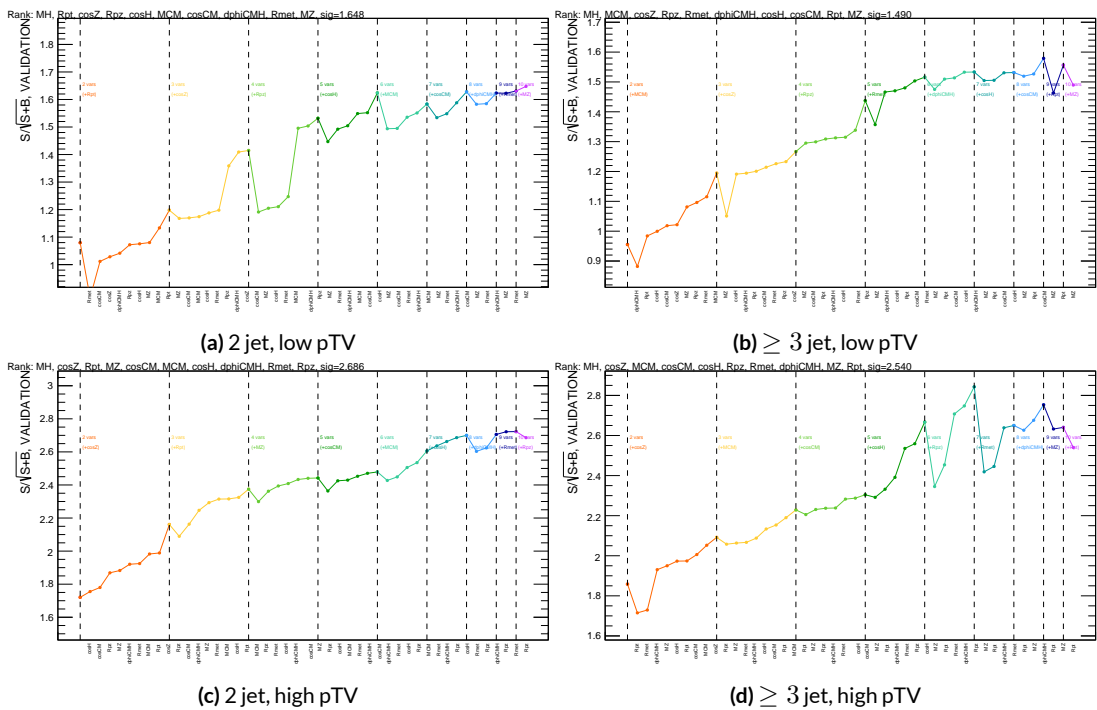


Figure 6.11: Rankings for the L1 variable set.



**Figure 6.12:** Rankings for the RF variable set.

1578 to create xml files for the production of fit inputs for an analysis including systematics. Following  
1579 the approach taken in the fiducial analysis, BDT discriminants using two “k-folds” are produced to  
1580 prevent overtraining, since the samples used for training are the same as those used to produce in-  
1581 puts for the full profile likelihood fit. In this scheme, a BDT trained on events with an even (odd)  
1582 `EventNumber` are used to evaluate events with an odd (even) `EventNumber`.

### 1583 6.3 STATISTICS ONLY BDT PERFORMANCE

1584 As described above, cumulative significances can be extracted from pairs of signal and background  
1585 BDT output distributions in a given region. In order to evaluate performance of variable sets in the  
1586 absence of systematic uncertainties, such pairs can be constructed by evaluating BDT score on the  
1587 testing set of events using the optimal variable rankings in each region. We show two versions of  
1588 each testing distribution for each variable set in each signal region in Figures 6.13–6.15. The training  
1589 distribution is always shown as points. The plots with block histograms with numbers of bins that  
1590 match (do not match) the training distribution do not (do) have transformation D applied. Trans-  
1591 formation D histograms are included to show the distributions actually used for significance evalu-  
1592 ation, while the untransformed histograms are included to illustrate that the level of overtraining is  
1593 not too terrible<sup>§</sup>. For better comparison of the distributions, all histograms have been scaled to have  
1594 the same normalization.

1595 As can be seen in the summary of cumulative significances for each of these analysis regions and  
1596 variable sets in Figure 6.16, the performance of each of the variable sets is quite similar. The standard

---

<sup>§</sup>The raw distributions include a K-S test statistic for signal (background) distributions.

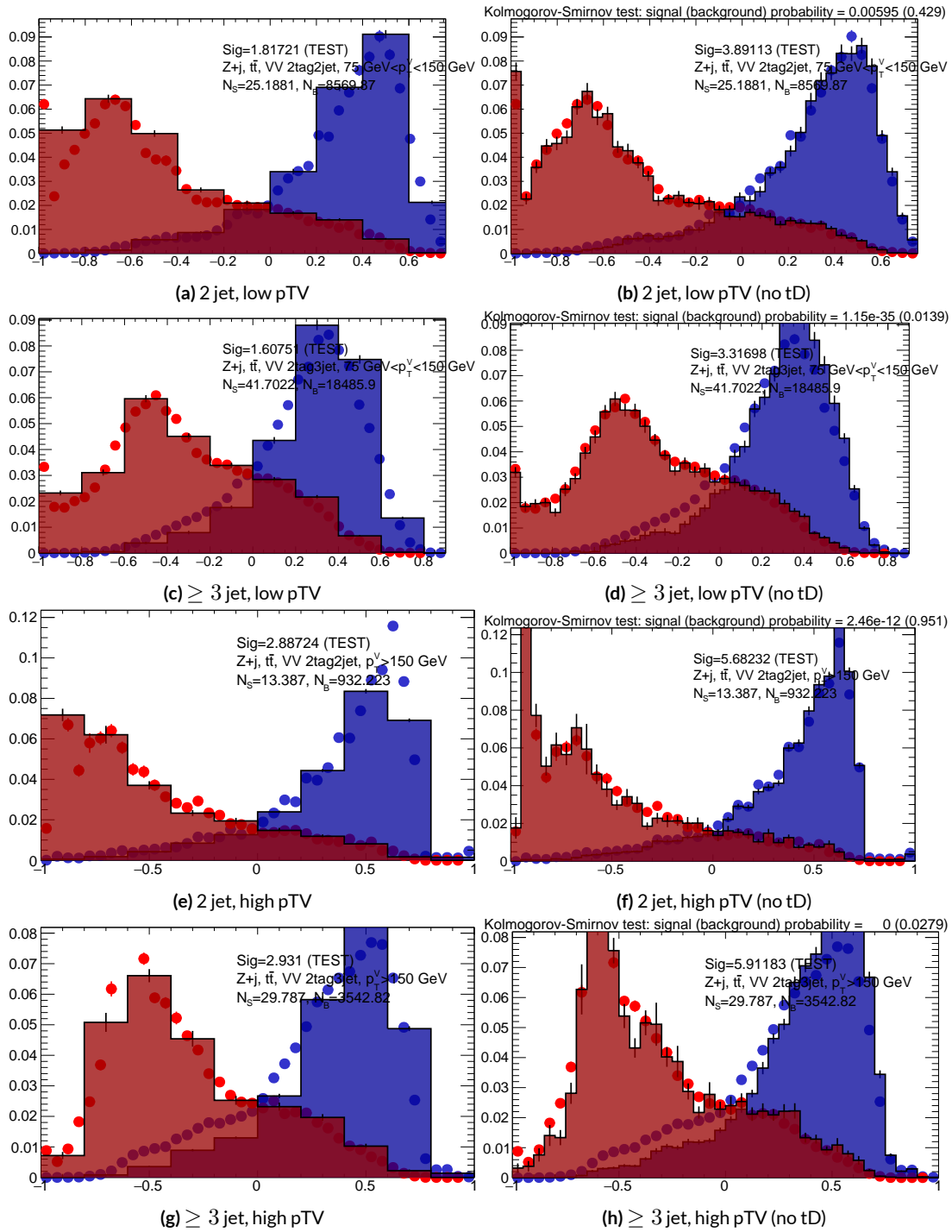


**Figure 6.13:** Training (points) and testing (block histogram) MVA distributions used for stat only testing for the standard variable set.

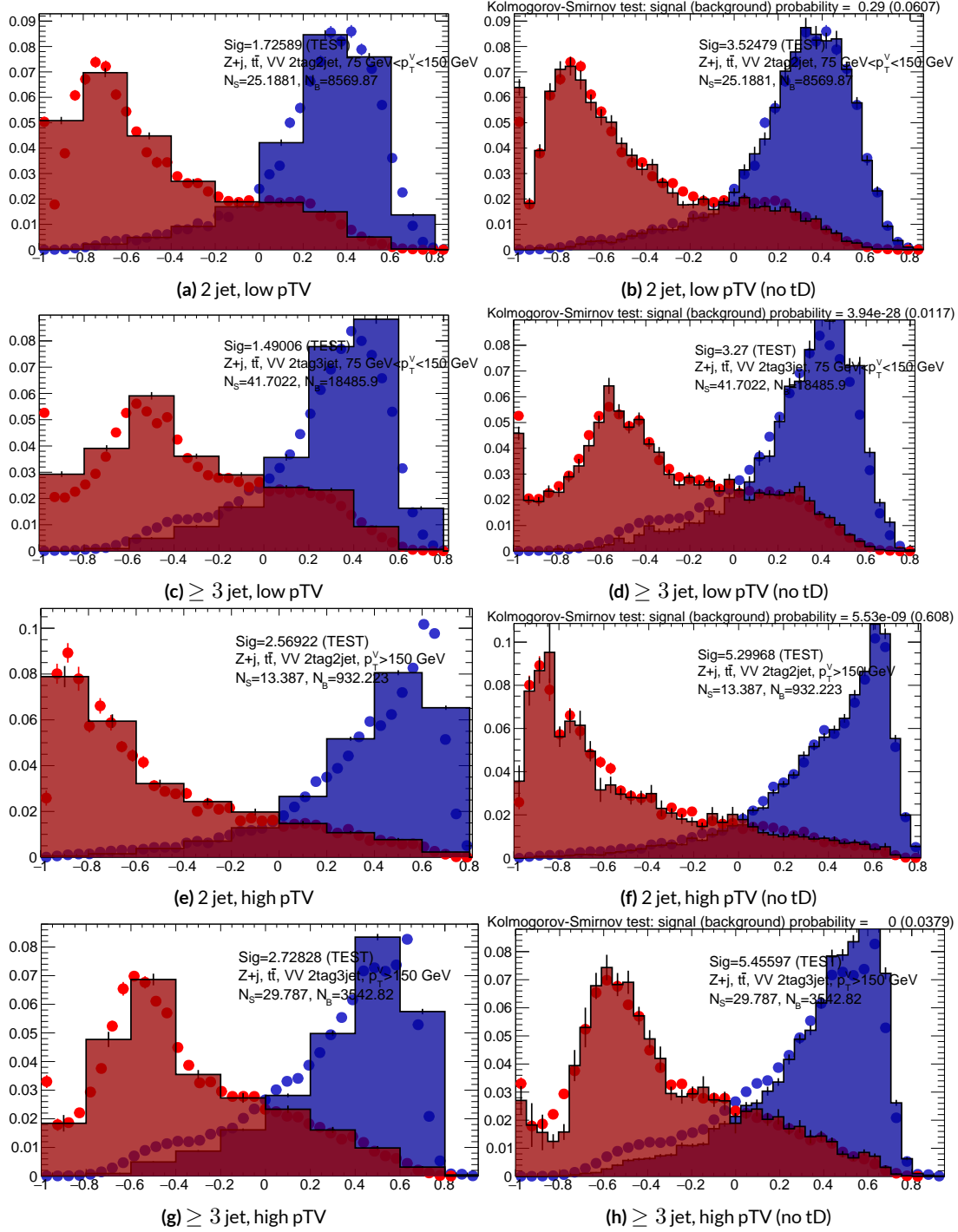


**Figure 6.14:** Training (points) and testing (block histogram) MVA distributions used for stat only testing for the LI variable set.

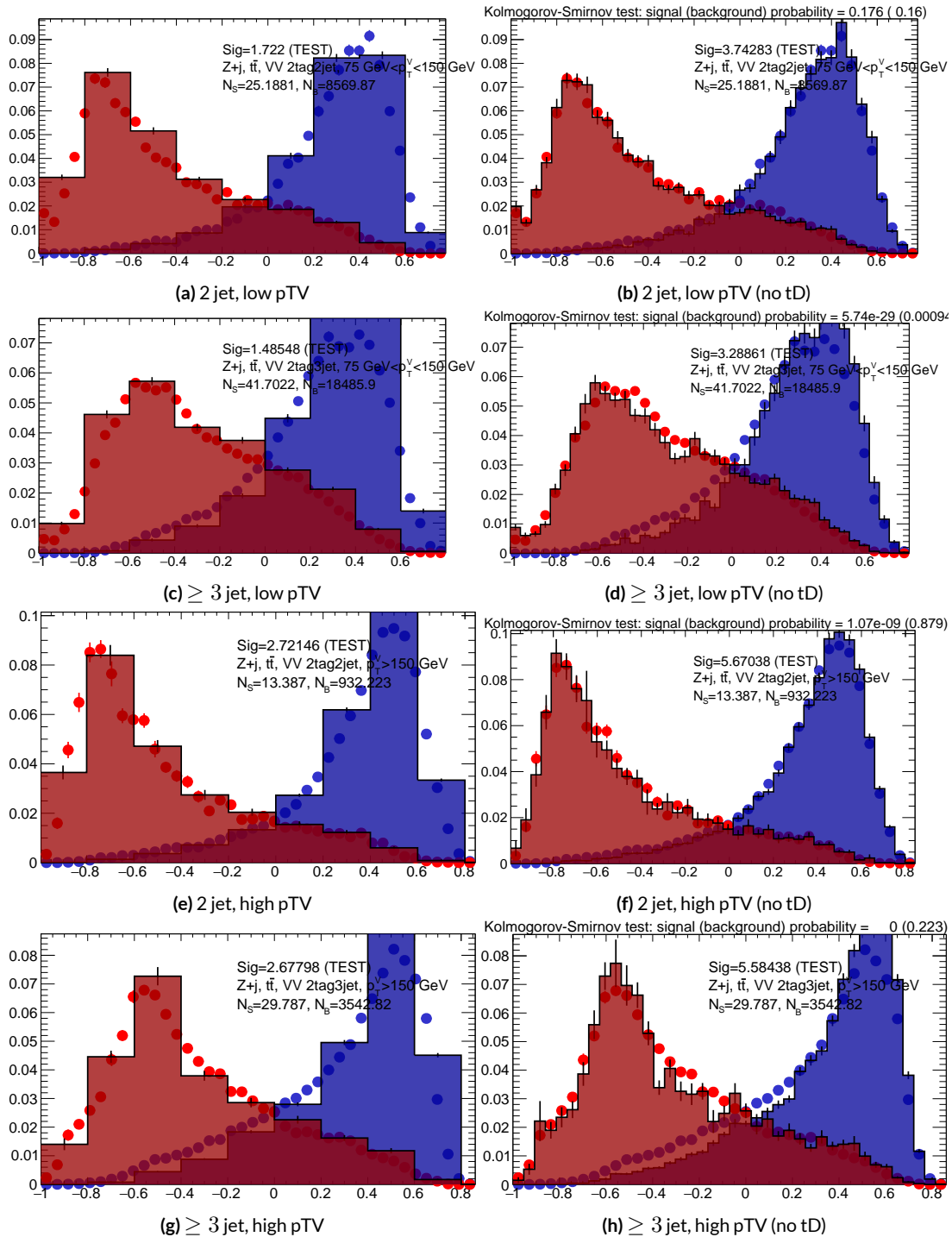


**Figure 6.15:** Training (points) and testing (block histogram) MVA distributions used for stat only testing for the RF variable set.

1597 set performs best, with the LI (RF) set having a cumulative significance that is 7.9% (6.9%) lower.  
 1598 This suggests that the LI and RF variables, in the  $ZH \rightarrow \ell\ell b\bar{b}$  closed final state, have no more in-  
 1599 trinsic descriptive power than the standard set. That these figures are all relatively high ( $\sim 4.5$ ) is  
 1600 due largely to the absence of systematics and possibly in part due to the fact that many of the most  
 1601 significant bins occur at high values of the BDT output, which, as can be seen in any of the testing  
 distributions, contain a small fraction of background events. An interesting feature to note in Fig-

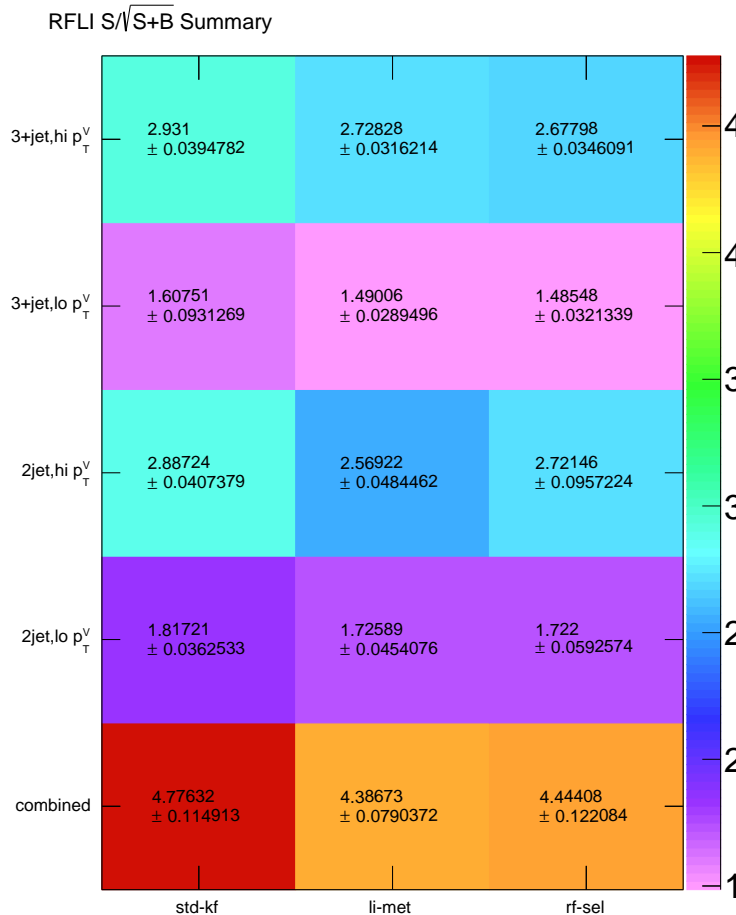


Figure 6.16: Results of testing significances sorted by analysis region and variable set.

1602

1603 ure 6.16 is that while the standard set does perform better in all regions, the gap is larger in the  $\geq 3$   
1604 jet regions, suggesting that further optimization in the  $\geq 3$  jet case could be useful. Moreover, as  
1605 discussed at the end of Chapter 5, the choice of  $\geq 3$  jet and not exclusive 3 jet regions is a 2-lepton  
1606 specific choice and may not be justified for the non-standard variable sets.

*Multivac picked you as most representative this year.*

*Not the smartest, or the strongest, or the luckiest, but*

*just the most representative. Now we don't question*

*Multivac, do we?*

Isaac Asimov, "Franchise"

1607

# 7

1608

## Statistical Fit Model and Validation

1609 THE ULTIMATE GOAL of an analysis like the search for SM  $VH(b\bar{b})$  decay is to say with as much  
1610 justified precision as possible with the ATLAS collision data whether or not the SM-like Higgs ob-  
1611 served in other decay modes also decays to  $b$ -quarks and, if so, whether this rate is consistent with  
1612 the SM prediction. In the limit of perfect modeling of both background processes and detector/reconstruction,

<sub>1613</sub> the only free parameter is this production rate, referred to typically as a “signal strength,” denoted  $\mu$ ,  
<sub>1614</sub> with  $\mu = 1$  corresponding to the SM prediction and  $\mu = 0$  corresponding to the SM with no  
<sub>1615</sub> Higgs.

<sub>1616</sub> To get a better sense of what this might look like, take a look at the example discriminant distri-  
<sub>1617</sub> bution in Figure 7.1. The black points are data (with statistical error bars), and the colored block  
<sub>1618</sub> histograms have size corresponding to the number of predicted events for each process in each bin of  
<sub>1619</sub> the final BDT. In the limit of perfect understanding, a fit would correspond to a constant scale fac-  
<sub>1620</sub> tor on the red, signal histogram, where one would choose a best fit  $\mu$  value, denoted  $\hat{\mu}$ , that would  
<sub>1621</sub> minimize the sum in quadrature of differences between the number of observed data events and  
<sub>1622</sub>  $\mu s_i + b_i$ , where  $s_i$  and  $b_i$  are the predicted number of signal and background events in each bin.

<sub>1623</sub> The only source of uncertainty would be due to data statistics, so for an infinitely large dataset with  
<sub>1624</sub> perfect understanding,  $\mu$  could be fitted to arbitrary precision. This, of course, is not the case since  
<sub>1625</sub> there is a finite amount of data and very many sources of systematic uncertainty, discussed in pre-  
<sub>1626</sub> vious chapters. This chapter will first describe how systematic uncertainties are integrated into the  
<sub>1627</sub> statistical fit of this analysis before describing two sets of cross checks on both a validation  $VZ$  fit and  
<sub>1628</sub> on the fit for the  $VH$  fit of interest.

## <sub>1629</sub> 7.1 THE FIT MODEL

<sub>1630</sub> In order to derive the strength of the signal process  $ZH \rightarrow \ell\ell b\bar{b}$  and other quantities of interest  
<sub>1631</sub> while taking into account systematic uncertainties or nuisance parameters (NP’s, collectively de-  
<sub>1632</sub> noted  $\theta$ ), a binned likelihood function is constructed as the product over bins of Poisson distribu-

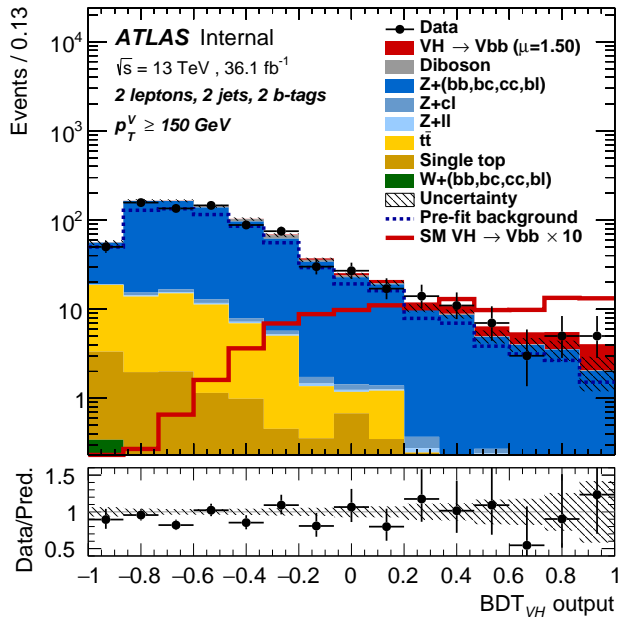


**Figure 7.1:** An example postfit distribution. The reason this looks different from postfit distributions later in this chapter is that this is a log plot.

1633 tions:

$$\mathcal{L}(\mu, \theta) = \text{Pois}(n | \mu S + B) \left[ \prod_{i \in \text{bins}} \frac{\mu s_i + b_i}{\mu S + B} \right] \prod_{j \in \text{NP's}} \mathcal{N}_{\theta_j}(\theta_j, \sigma_j^2 | 0, 1) \quad (7.1)$$

1634 where  $n$  is the total number of events observed,  $s_i$  and  $b_i$  are the number of expected signal and back-

1635 ground events in each bin, and  $S$  and  $B$  are the total expected signal and background events. The

1636 signal and background expectations generally are functions of the NP's  $\theta$ . NP's related to the nor-

1637 malization of signal and background processes fall into two categories. The first set is left to float

1638 freely like  $\mu$  while the second set are parametrized as log-normally distributed to prevent negative

1639 predicted values. All other NP's are parametrized with Gaussian priors. This results in a “penalty”

1640 on the NLL discussed below of  $(\hat{\alpha} - \mu_\alpha)^2 / \sigma_\alpha^2$ , for NP  $\alpha$ , normally parametrized with mean  $\mu_\alpha$

1641 (corresponding to the nominal prediction) and variance  $\sigma_\alpha^2$  (derived as discussed in Chapters 4 and

1642 5) for an MLE of  $\hat{\alpha}$ .

1643 One can maximize<sup>\*</sup> the likelihood in Equation 7.1 for a fixed value of  $\mu$  to derive estimators for  
1644 the NP's  $\theta$ ; values of  $\theta$  so derived are denoted  $\hat{\theta}_\mu$  to emphasize that these are likelihood maximizing  
1645 for a given  $\mu$ . The profile likelihood technique finds the likelihood function's maximum by compar-  
1646 ing the values of the likelihood over all possible values of  $\mu$  using these "profiles" and picking the  
1647 one with the greatest  $\mathcal{L}(\mu, \hat{\theta}_\mu)$  value; these values of  $\mu$  and  $\theta$  are denoted  $\hat{\mu}$  and  $\hat{\theta}$ . The profile like-  
1648 lihood can further be used to construct a test statistic<sup>†</sup>

$$q_\mu = -2 \left( \log \mathcal{L}(\mu, \hat{\theta}_\mu) - \log \mathcal{L}(\hat{\mu}, \hat{\theta}) \right) \quad (7.2)$$

1649 This statistic can be used to derive the usual significance ( $p$  value), by setting  $\mu = 0$  to find the com-  
1650 patability with the background-only hypothesis [45]. If there is insufficient evidence for the signal  
1651 hypothesis, the  $CL_s$  method can be used to set limits [18].

1652 In order to both validate the fit model and study the behavior of fits independent of a given dataset,  
1653 a so-called "Asimov"<sup>‡</sup> dataset can be constructed for a given fit model; this dataset has each bin equal  
1654 to its expectation value for assumed values of the NP's and a given  $\mu$  value (in this case,  $\mu = 1$ , the  
1655 SM prediction).

---

<sup>\*</sup>Maximization is mathematically identical to finding the minimum of the negative logarithm of the likelihood, which is numerically an easier problem.

<sup>†</sup>The factor of -2 is added so that this statistic gives, in the asymptotic limit of large  $N$ , a  $\chi^2$  distribution.

<sup>‡</sup>A reference to the short story quoted at the beginning of this chapter in which a computer picks a single voter to stand in for the views of the entire American electorate.

1656 7.2 FIT INPUTS

1657 Inputs to the binned likelihood are distributions of the BDT outputs described in Chapter 6 for the  
1658 signal regions and of  $m_{bb}$  for the top  $e - \mu$  control regions. These regions split events according  
1659 to their  $p_T^V$  and number of jets. All events are required to have two  $b$ -tagged jets, as well as pass the  
1660 other event selection requirements summarized in Table 5.8; the only difference between the signal  
1661 and control region selections is that the same flavor requirement (i.e. leptons both be electrons or  
1662 muons) is flipped so that events in the control region have exactly one electron and one muon. The  
1663 BDT outputs are binned using transformation D, while the  $m_{bb}$  distributions have 50 GeV bins,  
1664 with the exception of the 2 jet, high  $p_T^V$  region, where a single bin is used due to low statistics.

1665 Input distributions in MC are further divided according to their physics process. The signal pro-  
1666 cesses are divided based on both the identity of associated  $V$  and the number of leptons in the final  
1667 state;  $ZH \rightarrow \ell\ell b\bar{b}$  events are further separated into distributions for  $qq$  and  $gg$  initiated processes.  
1668  $V+jets$  events are split according to  $V$  identity and into the jet flavor bins described in Chapter 3.  
1669 Due to the effectiveness of the 2  $b$ -tag requirement suppressing the presence of both  $c$  and  $l$  jets,  
1670 truth-tagging is used to boost MC statistics in the  $cc$ ,  $cl$ , and  $ll$  distributions.<sup>§</sup> For top backgrounds,  
1671 single top production is split according to production mode ( $s$ ,  $t$ , and  $Wt$ ), with  $t\bar{t}$  as single category.  
1672 Diboson background distributions are also split according to the identity of the  $V$ 's ( $ZZ$ ,  $WZ$ , and  
1673  $WW$ ). Fit input segmentation is summarized in Table 7.1.

---

1673 <sup>§</sup>Since  $WW$  is not an important contribution to the already small total diboson background, no truth-tagging was applied here, in contrast to the fiducial analysis.

Category	Bins
# of Jets	2, 3+
$p_T^V$ Regions (GeV)	$[75, 150], [150, \infty)$
Sample	data, signal $[(W, qqZ, ggZ)] \times n_{lep}$ , $V+jets [(W, Z)] \times (bb, bc, bl, cc, cl, ll)]$ , $t\bar{t}$ , diboson ( $ZZ, WW, WZ$ ), single top ( $s, t, Wt$ )

**Table 7.1:** Fit input segmentation.

### 1674 7.3 SYSTEMATIC UNCERTAINTIES REVIEW

1675 Tables 7.2 and 7.3 summarize modeling (Chapter 4) and experimental (Chapter 5) systematic uncer-  
 1676 tainties considered in this analysis, respectively. In addition to these, simulation statistics uncertain-  
 1677 ties (“MC stat errors”) are also included in the fit model. There is one distribution per systematic  
 1678 (one each for up and down) per sample per region. The  $\pm 1\sigma$  variation for a systematic is calculated  
 1679 as the difference in the integrals between the nominal and up/down varied distributions.

Process	Systematics
Signal	$H \rightarrow bb$ decay, QCD scale, PDF+ $\alpha_S$ scale, UE+PS (acc, $p_T^V$ , $m_{bb}$ , 3/2 jet ratio)
$Z+jets$	Acc, flavor composition, $p_T^V+m_{bb}$ shape
$t\bar{t}$	Acc, $p_T^V+m_{bb}$ shape
Single top	Acc, $p_T^V+m_{bb}$ shape
Diboson	Overall acc, UE+PS (acc, $p_T^V$ , $m_{bb}$ , 3/2 jet ratio), QCD scale (acc (2, 3 jet, jet veto), $p_T^V$ , $m_{bb}$ )

**Table 7.2:** Summary of modeling systematic uncertainties.

1680 The systematics distributions undergo processes known as “smoothing” and “pruning” before  
 1681 being combined into the final likelihood used in minimization.  
 1682 The difference between systematics varied distributions and nominal distributions approaches

Process	Systematics
Jets	21 NP scheme for JES, JER as single NP
$E_T^{\text{miss}}$	trigger efficiency, track-based soft terms, scale uncertainty due to jet tracks
Flavor Tagging	Eigen parameter scheme (CDI File: 2016-20_7-13TeV-MC15-CDI-2017-06-07_v2)
Electrons	trigger eff, reco/ID eff, isolation eff, energy scale/resoltuion
Muons	trigger eff, reco/ID eff, isolation eff, track to vertex association, momentum resolution/scale
Event	total luminosity, pileup reweighting

**Table 7.3:** Summary of experimental systematic uncertainties.

1683 some stable value in the limit of large simulation statistics, but if the fluctuations due to simulation  
 1684 statistics in a distribution are large compared to the actual physical effect (whether this is because  
 1685 the actual effect is small or if the actual distribution is derived from a small number of simulation  
 1686 events), then systematic uncertainty will be overestimated by, in effect, counting the MC stat error  
 1687 multiple times. Smoothing is designed to mitigate these effects by merging adjacent bins in some  
 1688 input distributions. Smoothing happens in two steps (the full details of smoothing algorithms may  
 1689 be found in [65] and in the `WSMaker` code):  
 1690     1. Merge bins iteratively where bin differences are smallest in input distributions until no local  
 1691         extrema remain (obviously, a single peak or valley is allowed to remain)  
 1692     2. Sequentially merge bins (highest to lowest, like transformation D) until the statistical uncer-  
 1693         tainty in a given bin is smaller than 5% of merged bin content  
 1694 Not all systematic uncertainties defined are included in the final fit. Systematics are subject “prun-  
 1695 ing” (individually in each region/sample: there are two histograms per systematic (up/down) per  
 1696 region per sample, so pruning just consists of removing the histograms from the set of distributions  
 1697 included in the likelihood) if they are do not have a significant impact, defined as follows:

- Normalization/acceptance systematics are pruned away if either:
  - The variation is less than 0.5%
  - Both up and down variations have the same sign
  
- Shape systematics pruned away if either:
  - Not one single bin has a deviation over 0.5% after the overall normalisation is removed
  - If only the up or the down variation is non-zero
  
- Shape+Normalisation systematics are pruned away if the associated sample is less than 2% of the total background and either:
  - If the predicted signal is < 2% of the total background in all bins and the shape and normalisation error are each < 0.5% of the total background
  - If instead at least one bin has a signal contribution > 2% of the total background, and only in each of these bins, the shape and normalisation error are each < 2% of the signal yield

## 7.4 THE VZ VALIDATION FIT

One of the primary validation cross-checks for the fiducial analysis was a  $VZ$  fit—that is, conducting the entire analysis but looking for  $Z \rightarrow b\bar{b}$  decays instead of the Higgs. The idea here is that the  $Z$  is very well understood and so “rediscovering”  $Z$  decay to  $b$ 's is taken as a benchmark of analysis reliability since the complexity of the fit model precludes the use of orthogonal control regions for validation as is done in other analyses (generally, if there is a good control region, one prefers to use it

1717 to constrain backgrounds and improve the fit model). To do this, a new MVA discriminant is made  
 1718 by keeping all hyperparameter configurations the same (e.g. variable ranking) but using diboson  
 1719 samples as signal. For the 2-lepton case, this means using  $ZZ \rightarrow \ell\ell b\bar{b}$  as the signal sample. This  
 1720 new MVA is used to make the inputs described in Section 7.2, and the fit is then run as for the  $VH$   
 1721 fit (again, with  $ZZ$  as signal).  $VH$  samples are considered background in these diboson fits.

1722 The  $VZ$  fit sensitivities for the standard, LI, and RF fits are summarized in Table 7.4. The ex-  
 1723 pected significances are all fairly comparable and about what was the case in the fiducial analysis.  
 1724 The observed significance for the standard set matches fairly well with the expected value on data,  
 1725 but the LI and RF observed significances are quite a bit lower.

	Standard	LI	RF
Expected (Asimov)	3.83	3.67	3.72
Expected (data)	3.00	2.95	3.11
Observed (data)	3.17	1.80	2.09

**Table 7.4:** Expected (for both data and Asimov) and observed  $VZ \rightarrow \ell\ell b\bar{b}$  sensitivities for the standard, LI, and RF variable sets.

1726 These values, however, are consistent with the observed signal strength values, which can be seen  
 1727 in Figure 7.2 (b), with both the LI and RF fits showing a deficit of signal events with respect to the  
 1728 SM expectation, though not by much more than one standard deviation (a possible explanation is  
 1729 explored in the following section). Just as in the  $VH$  fits, errors arising systematic uncertainties are  
 1730 lower in the fits to the observed dataset. That the effect is not noticeable in Asimov fits is not too  
 1731 surprising, since this analysis (and these variable configurations in particular), is not optimized for  
 1732  $VZ$ .

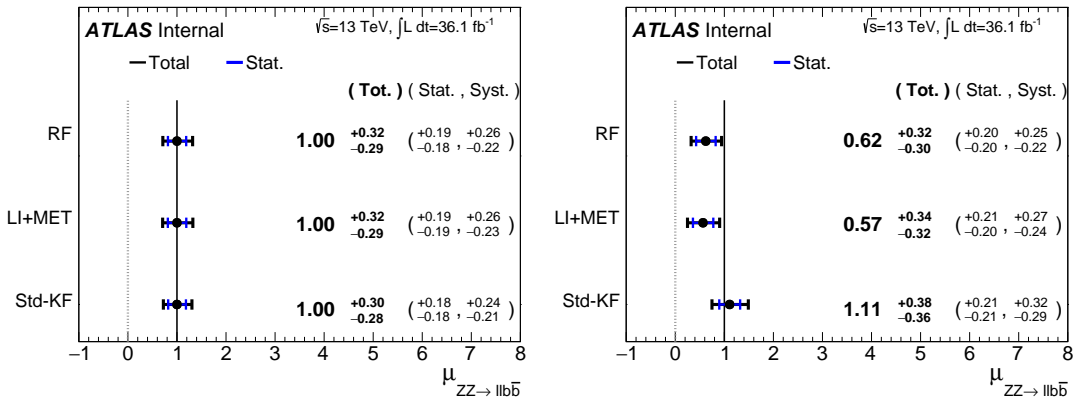


**Figure 7.2:**  $\mu$  summary plots for the standard, LI, and RF variable sets. The Asimov case (with  $\mu = 1$  by construction) is in (a), and  $\hat{\mu}$  best fit values and error summary are in (b).

#### 1733 7.4.I 2 AND $\geq 3$ JET FITS

1734 While the treatment of simply ignoring any additional jets in the event seems adequate for the  $VH$   
 1735 analysis (discussed below), the potential shortcoming of this treatment appears in the  $VZ$  analysis  
 1736 when the  $2$  and  $\geq 3$  jet cases are fit separately<sup>¶</sup>, as can be seen in Figure 7.3. Compared to the stan-  
 1737 dard fit, the LI and RF fits have lower  $\hat{\mu}_{\geq 3 \text{ jet}}$  values, consistent with the interpretation that the ad-  
 1738 ditional information from the third jet in the  $\geq 3$  jet regions for the standard case is important for  
 1739 characterizing events in these regions for  $VZ$  fits.

1740 A natural question to ask is why this would be an issue for the  $VZ$  but not the  $VH$  case. One  
 1741 potential answer is that at high transverse boosts, there is a greater probability for final state  
 1742 radiation in the hadronically decaying  $Z$ , so there are more events where the third jet should be in-  
 1743 cluded in the calculation of variables like  $m_{b\bar{b}}$  or for angles involving the  $b\bar{b}$  system (e.g.  $\cos\theta$  in the  
 1744 RF case). While the absolute scale at which the low and high  $p_T^V$  regions are separated remains the

<sup>¶</sup>standalone fits, with half the regions each, not 2 POI fits

1745 same does not change from the  $VH$  to the  $VZ$  analysis, 150 GeV, the implicit cutoff on the transverse  
 1746 boost of the hadronically decaying boson does. For the Higgs, with a mass of 125 GeV, the  $p_T^V$  cutoff  
 1747 corresponds to  $\gamma \sim 1.56 - 6.74$ , but for the  $Z$ , with a mass of 91 GeV, this is  $\gamma \sim 1.93 - 9.21$ ,  
 1748 about 23–37% higher.

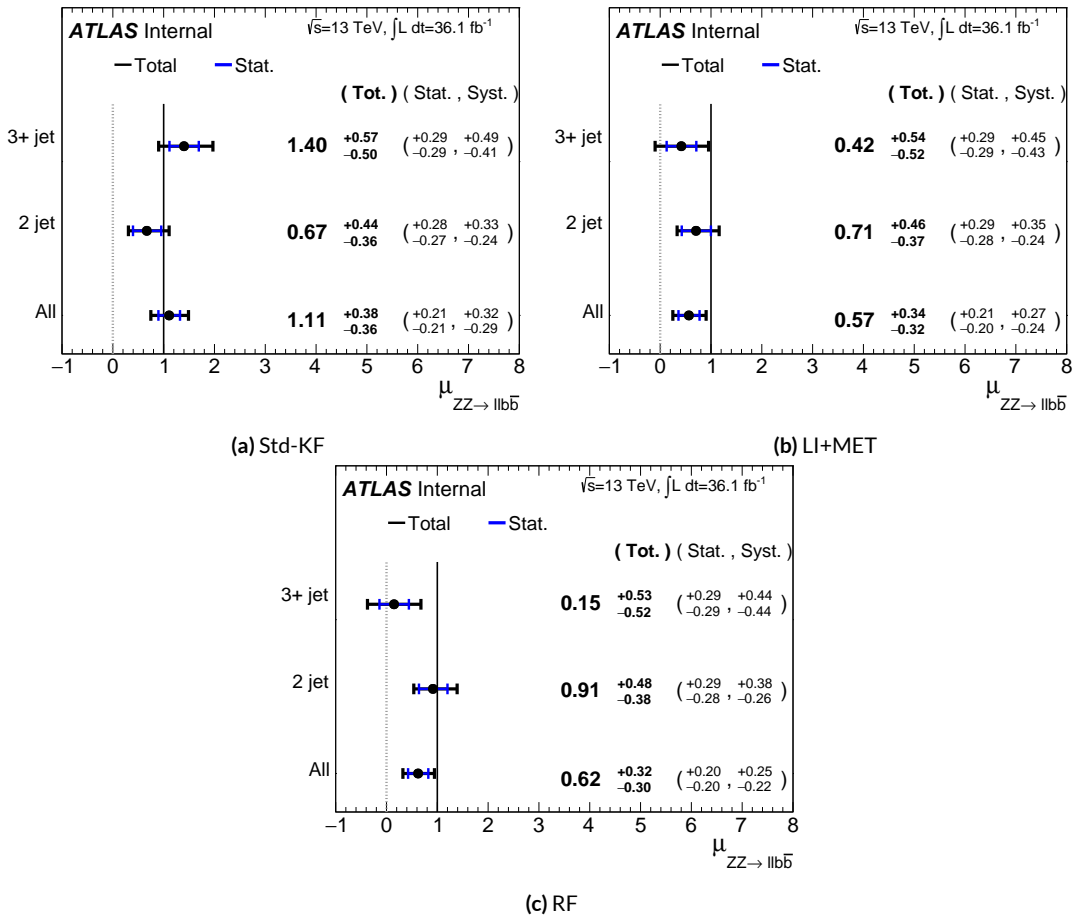


Figure 7.3:  $\hat{\mu}$  summary plots with standalone fits for the different  $n_{jet}$  regions for the standard, LI, and RF variable sets.

1749 If either the LI or RF schemes were to be used in a mainstream analysis, these validation fits sug-  
 1750 gest that the third jet ought to be included in variable schemes (e.g. by adding the third jet to the

1751 Higgs in the high  $p_T^V$  case). On the issue of whether or not  $\geq 4$  jet events should be included, the  
1752 RF set shows very little sensitivity to this change (a 2 jet and 3 jet only fit moves  $\hat{\mu}$  to 0.64, while  
1753 doing so for the LI set moves it to 0.40), so this, like the addition of the third jet into the variable  
1754 sets, would have to be addressed individually. Nevertheless, this optimization is beyond the scope of  
1755 this thesis, which aims to preserve as much of the fiducial analysis as possible for as straightforward a  
1756 comparison as possible.

1757 For completeness, we include the full set of fit validation results for the  $VZ$  fit, explaining them in  
1758 turn.

## 1759 7.5 NUISANCE PARAMETER PULLS

1760 The first set of plots statistical fit experts will want to look at are the “pulls” and “pull comparisons.”  
1761 In these plots, the best fit (nominal) values and one standard deviation error bars are shown for ob-  
1762 served (Asimov) pull plots, with the green and yellow bands corresponding to  $\pm 1, 2\sigma$ , respectively.  
1763 These plots are divided by NP category for readability. <sup>¶</sup> In pull comparisons, these pulls are over-  
1764 layed and color-coded. Pull comparisons here have the following color code: black is the standard  
1765 variable set, red is the LI set, and blue is the RF set.

1766 A well-behaved fit has pulls close to nominal values (“closeness” should be interpreted in the  
1767 context of pull value divided by pull error). As can be seen in Figures 7.4–7.8, the fits for the three  
1768 different variable sets are fairly similar from a NP pull perspective, though the  $Z+{\rm jets}$   $m_{bb}$  and  $p_T^V$

---

¶Over 100 non-MC stat NP’s survive pruning in these 2-lepton only Run 2 fits; well over 500 survive in the Run 1+Run 2 combined fit.

1769 NP's and the jet energy resolution NP are heavily pulled (a handful of poorly behaved pulls is not  
 1770 uncommon, though typically warrants further investigation). As a general note, these pull plots cal-  
 1771 culate pulls using a simultaneous HESSE matrix inversion, which is fine for relatively small fits, but  
 1772 the more reliable MINOS result, which calculates the impact of each NP on its own, should be cross-  
 1773 checked for significant pulls\*\*. The ranking plots below do this.

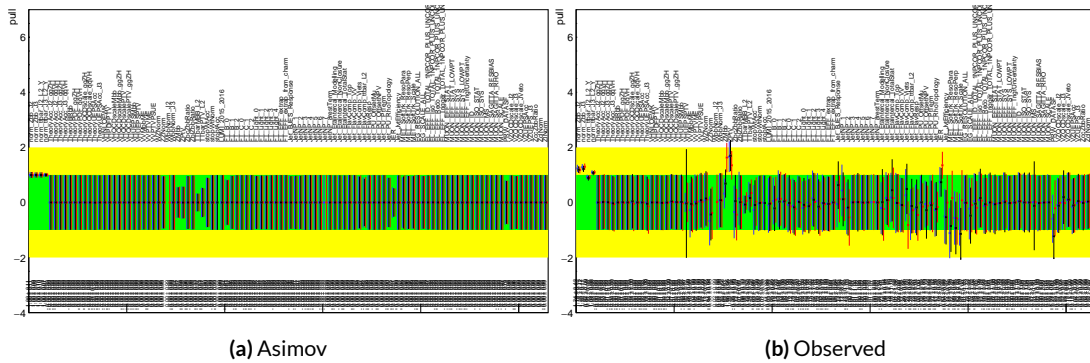


Figure 7.4: Pull comparison for all NP's but MC stats.

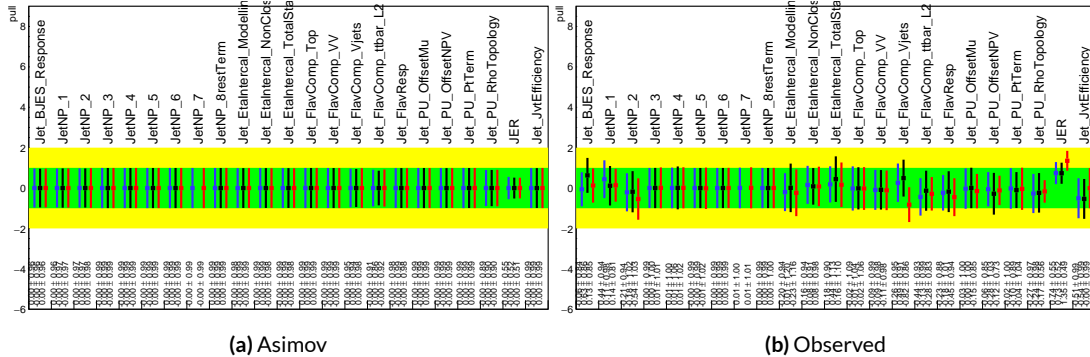


Figure 7.5: Pull comparison for jet NP's.

1774 Nuisance parameter correlation matrices (for correlations with magnitude at least 0.25) for all  
 1775 three variable set fits can be found in Figures 7.10–7.12. These are useful for seeing which NP's move

\*\*This becomes more of an issue for very large fits, like the full Run 1 + Run 2 combined fits in Chapter 9.

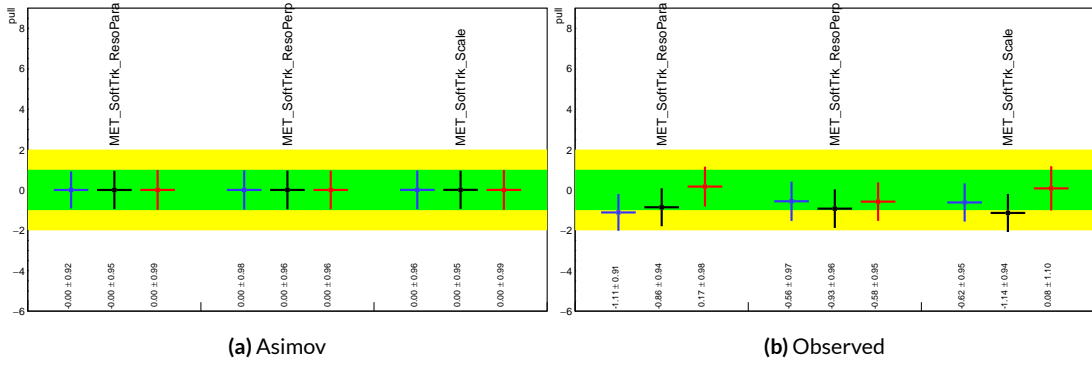


Figure 7.6: Pull comparison for MET NP's.

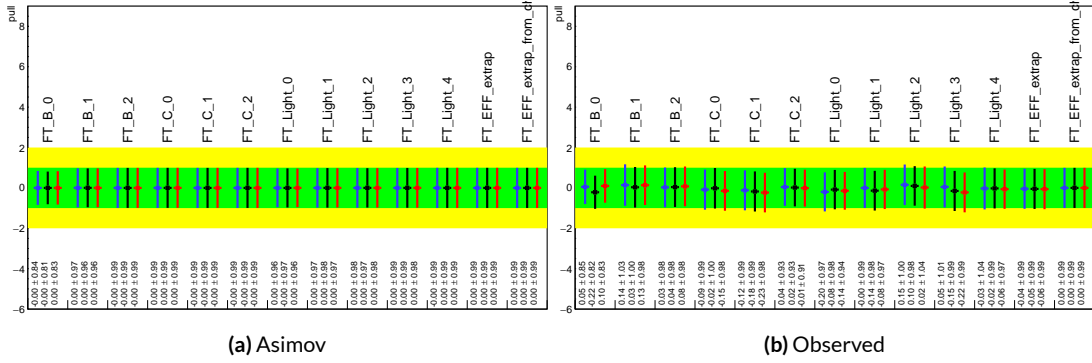


Figure 7.7: Pull comparison for Flavour Tagging NP's.

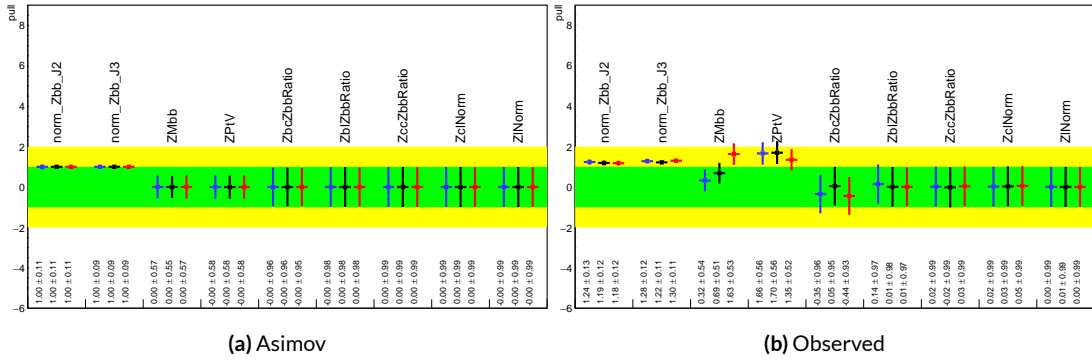
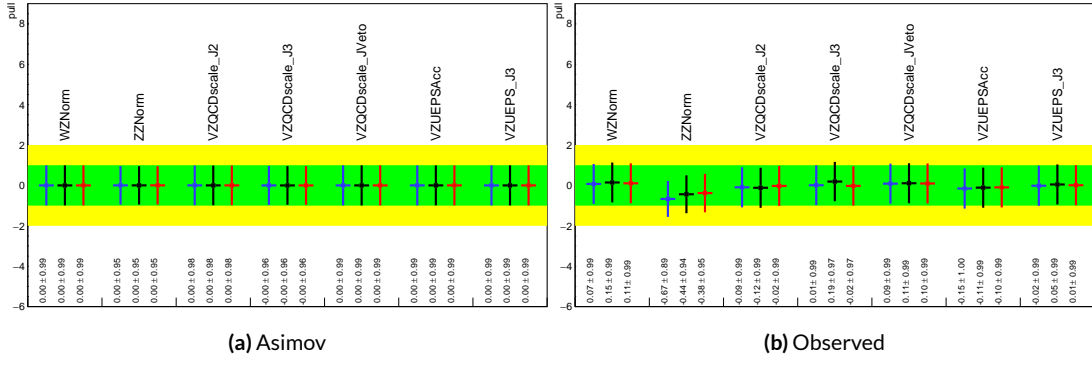


Figure 7.8: Pull comparison for  $Z$ +jets NP's.



**Figure 7.9:** Pull comparison for signal process modeling NP's.

together (if there is no physical argument for them to do so, this is a potential indicator that further

investigation is warranted).

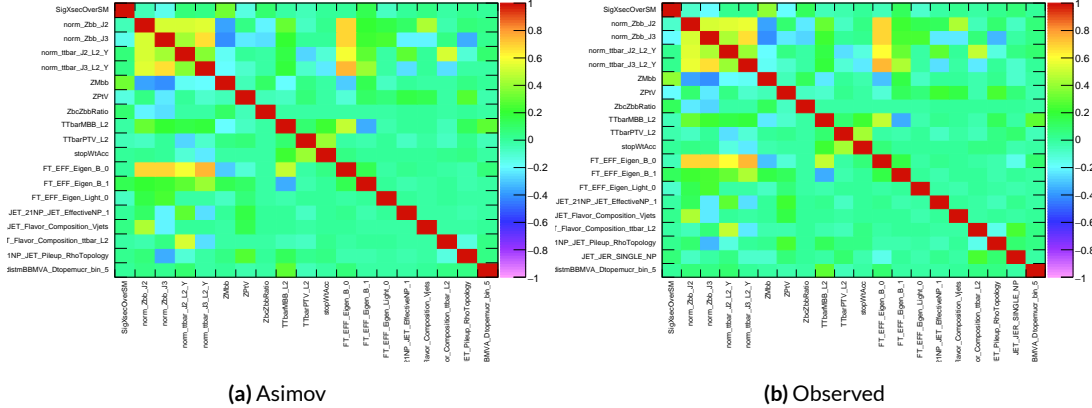


**Figure 7.10:** NP correlations for standard variable fits.

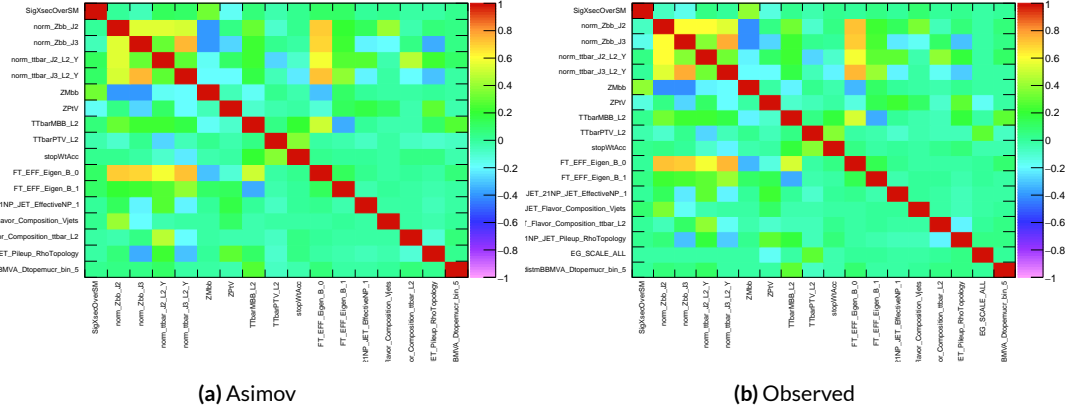


Figure 7.11: NP correlations for LI variable fits.

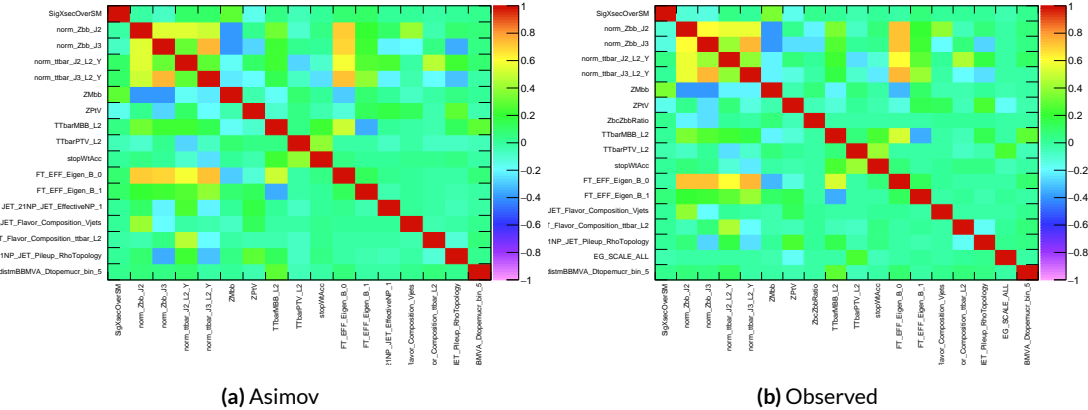
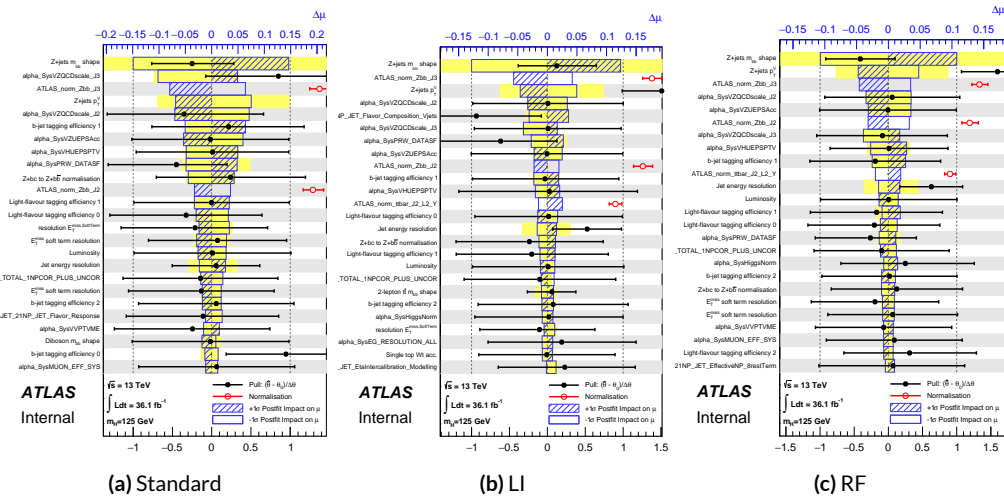


Figure 7.12: NP correlations for RF variable fits.

## 1778 7.5.1 NUISANCE PARAMETER RANKING PLOTS AND BREAKDOWNS

1779 The next set of fit results that is used to diagnose the quality of a fit is the impact of different nui-  
 1780 sance parameters on the total error on  $\mu$ , both individually and as categories. Figure 7.13 shows the  
 1781 top 25 nuisance parameters ranked by their postfit impact on  $\hat{\mu}$ ; these plots use the aforementioned,  
 1782 more reliable MINOS approach. This set of rankings is fairly similar, with  $Z+jets$  systematics being  
 1783 particularly prominent. The advantage of seeing individual nuisance parameter rankings, as op-  
 1784 posed to impacts of categories in aggregate, is that particularly pathological NP's are easier to see;  
 1785 in particular, jet energy resolution and  $Z+jets p_T^V$  systematic from the pull comparison plots show  
 up with high rankings. Yellow bands are pre-fit impact on  $\mu$ .



**Figure 7.13:** Plots for the top 25 nuisance parameters according to their postfit impact on  $\hat{\mu}$  for the standard (a), LI (b), and RF (c) variable sets.

1786

1787 This is consistent with the picture of NP's taken in aggregate categories in Tables 7.5 and 7.6,  
 1788 known as “breakdowns,” with  $Z+jets$  in particular featuring prominently. Of particular interest

<sup>1789</sup> is also the lower impact of MC stats in the observed fit.

	Std-KF	LI+MET	RF
Total	+0.305 / -0.277	+0.324 / -0.292	+0.319 / -0.288
DataStat	+0.183 / -0.179	+0.190 / -0.186	+0.188 / -0.184
FullSyst	+0.244 / -0.212	+0.262 / -0.226	+0.258 / -0.221
Floating normalizations	+0.092 / -0.084	+0.098 / -0.079	+0.094 / -0.076
All normalizations	+0.093 / -0.084	+0.098 / -0.079	+0.094 / -0.076
All but normalizations	+0.214 / -0.179	+0.229 / -0.188	+0.224 / -0.182
Jets, MET	+0.052 / -0.043	+0.041 / -0.034	+0.047 / -0.037
Jets	+0.034 / -0.029	+0.033 / -0.028	+0.032 / -0.026
MET	+0.035 / -0.027	+0.015 / -0.012	+0.020 / -0.016
BTag	+0.064 / -0.051	+0.063 / -0.031	+0.059 / -0.032
BTag b	+0.053 / -0.041	+0.061 / -0.028	+0.055 / -0.025
BTag c	+0.011 / -0.010	+0.006 / -0.005	+0.007 / -0.006
BTag light	+0.030 / -0.027	+0.016 / -0.013	+0.022 / -0.019
Leptons	+0.021 / -0.012	+0.022 / -0.014	+0.023 / -0.014
Luminosity	+0.039 / -0.022	+0.039 / -0.022	+0.040 / -0.022
Diboson	+0.049 / -0.028	+0.047 / -0.026	+0.047 / -0.026
Model Zjets	+0.106 / -0.105	+0.113 / -0.110	+0.102 / -0.099
Zjets flt. norm.	+0.039 / -0.053	+0.024 / -0.029	+0.021 / -0.031
Model Wjets	+0.000 / -0.000	+0.000 / -0.000	+0.000 / -0.000
Wjets flt. norm.	+0.000 / -0.000	+0.000 / -0.000	+0.000 / -0.000
Model ttbar	+0.015 / -0.013	+0.032 / -0.017	+0.030 / -0.016
Model Single Top	+0.004 / -0.003	+0.009 / -0.008	+0.005 / -0.004
Model Multi Jet	+0.000 / -0.000	+0.000 / -0.000	+0.000 / -0.000
Signal Systematics	+0.003 / -0.003	+0.003 / -0.003	+0.003 / -0.003
MC stat	+0.097 / -0.094	+0.108 / -0.103	+0.107 / -0.104

**Table 7.5:** Summary of impact of various nuisance parameter categories on the error on  $\mu$  for Asimov fits for the standard, LI, and RF variable sets.

	Std-KF	LI+MET	RF
$\hat{\mu}$	1.1079	0.5651	0.6218
Total	+0.381 / -0.360	+0.339 / -0.316	+0.322 / -0.299
DataStat	+0.214 / -0.211	+0.210 / -0.205	+0.201 / -0.197
FullSyst	+0.315 / -0.292	+0.267 / -0.241	+0.252 / -0.225
Floating normalizations	+0.120 / -0.122	+0.095 / -0.089	+0.082 / -0.079
All normalizations	+0.121 / -0.123	+0.095 / -0.090	+0.082 / -0.079
All but normalizations	+0.279 / -0.254	+0.228 / -0.200	+0.213 / -0.184
Jets, MET	+0.076 / -0.065	+0.045 / -0.043	+0.038 / -0.033
Jets	+0.047 / -0.040	+0.044 / -0.041	+0.027 / -0.024
MET	+0.055 / -0.046	+0.015 / -0.015	+0.012 / -0.010
BTag	+0.083 / -0.079	+0.041 / -0.031	+0.041 / -0.035
BTag b	+0.063 / -0.059	+0.032 / -0.022	+0.031 / -0.026
BTag c	+0.018 / -0.017	+0.008 / -0.007	+0.010 / -0.009
BTag light	+0.051 / -0.046	+0.024 / -0.021	+0.025 / -0.022
Leptons	+0.022 / -0.011	+0.015 / -0.008	+0.019 / -0.008
Luminosity	+0.044 / -0.022	+0.026 / -0.006	+0.027 / -0.008
Diboson	+0.049 / -0.026	+0.025 / -0.013	+0.027 / -0.017
Model Zjets	+0.156 / -0.162	+0.133 / -0.133	+0.115 / -0.117
Zjets flt. norm.	+0.061 / -0.089	+0.041 / -0.064	+0.028 / -0.056
Model Wjets	+0.000 / -0.001	+0.000 / -0.001	+0.000 / -0.001
Wjets flt. norm.	+0.000 / -0.001	+0.000 / -0.001	+0.000 / -0.001
Model ttbar	+0.015 / -0.024	+0.018 / -0.005	+0.017 / -0.009
Model Single Top	+0.005 / -0.003	+0.010 / -0.008	+0.007 / -0.004
Model Multi Jet	+0.000 / -0.001	+0.000 / -0.001	+0.000 / -0.001
Signal Systematics	+0.005 / -0.004	+0.009 / -0.006	+0.005 / -0.006
MC stat	+0.140 / -0.143	+0.132 / -0.131	+0.128 / -0.129

**Table 7.6:** Summary of impact of various nuisance parameter categories on the error on  $\hat{\mu}$  for observed fits for the standard, LI, and RF variable sets.

1790 7.6 POSTFIT DISTRIBUTIONS

1791 Finally, postfit distributions for the MVA discriminant ( $m_{bb}$ ) distribution in the signal (top  $e - \mu$   
1792 control) region for the standard, Lorentz Invariant, and RestFrames variable sets are shown. It is  
1793 generally considered good practice to check the actual postfit distributions of discriminating quan-  
1794 tities used to make sure there is good agreement. <sup>††</sup> It should be noted that agreement is not always  
1795 great when “eyeballing” a distribution, as fits are messy and  $V+hf$  modeling is notoriously hard.  
1796 This is particularly true in the  $VZ$  fit since normalizations for  $Z+hf$  in particular are derived using  
1797  $VH$  optimized sidebands. This is also why a lot of these plots are presented as log plots (which hide  
1798 disagreement better; the general argument goes that one has the ratio plots on the bottom and log  
1799 plots allow one to see rare backgrounds in plots).

---

<sup>††</sup>Sometimes distributions of input variables (MC histograms scaled by their postfit normalizations) are also used.

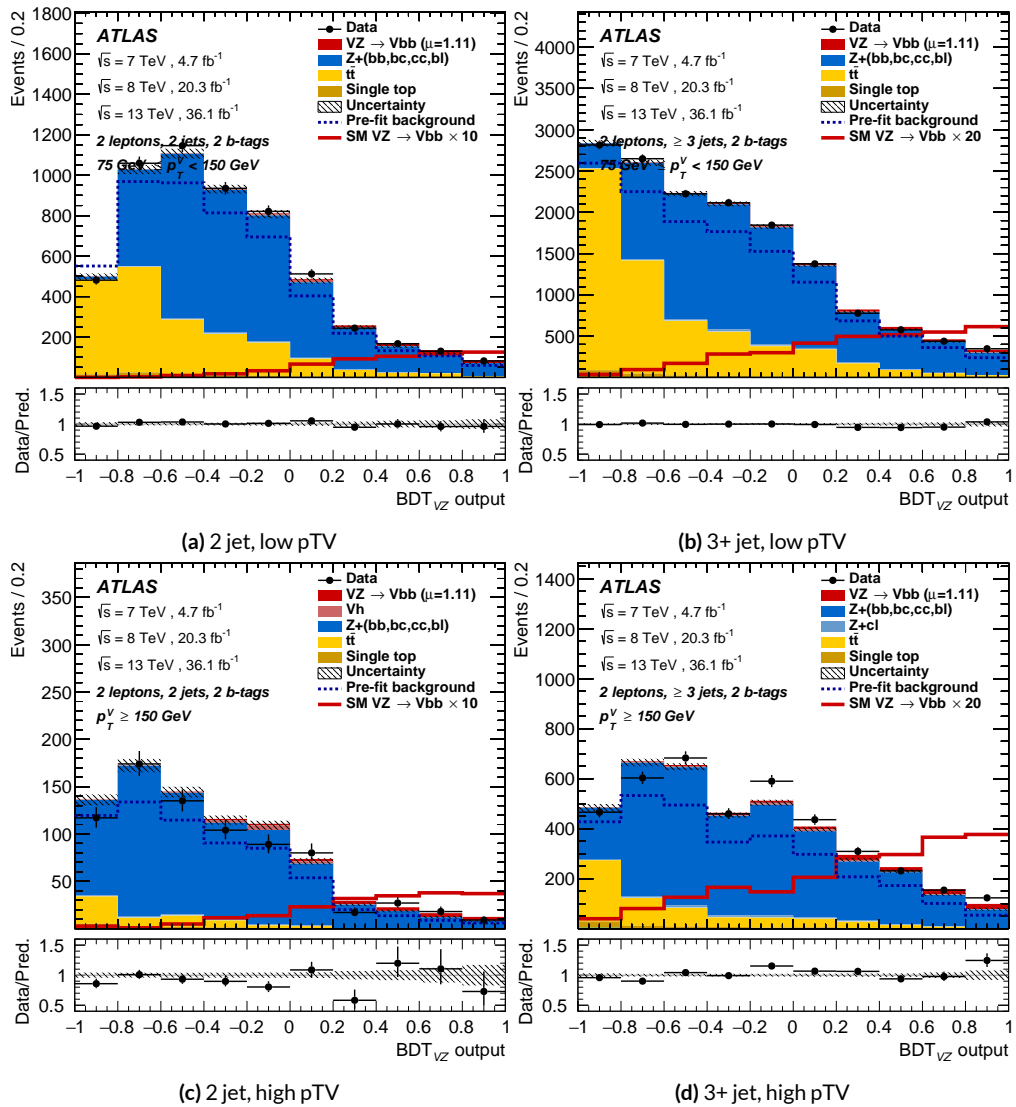


**Figure 7.14:** Postfit  $BDT_{VZ}$  plots in the signal region for the standard variable set.

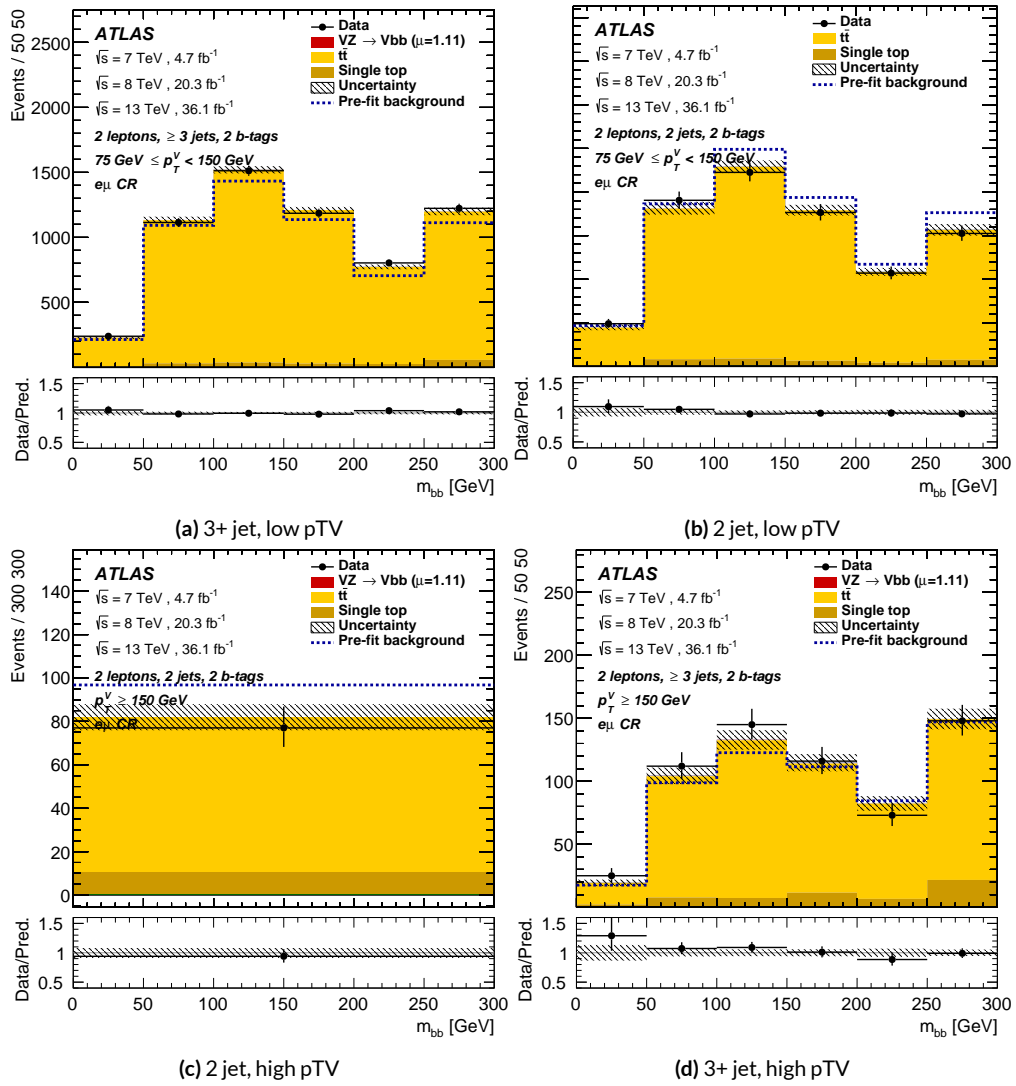


**Figure 7.15:** Postfit  $m_{bb}$  plots in the top  $e - \mu$  CR for the standard variable set.

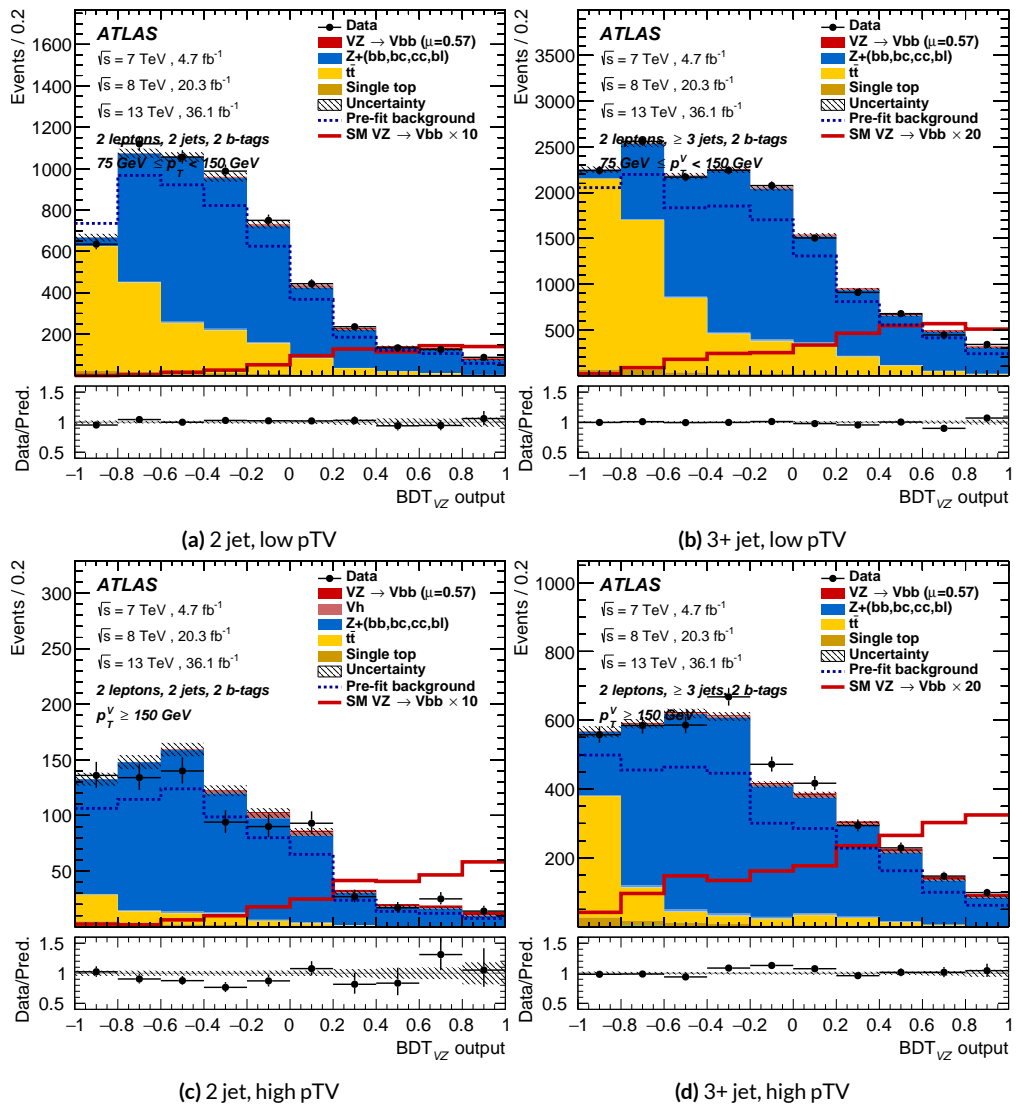


Figure 7.16: Postfit  $BDT_{VZ}$  plots in the signal region for the LI variable set.

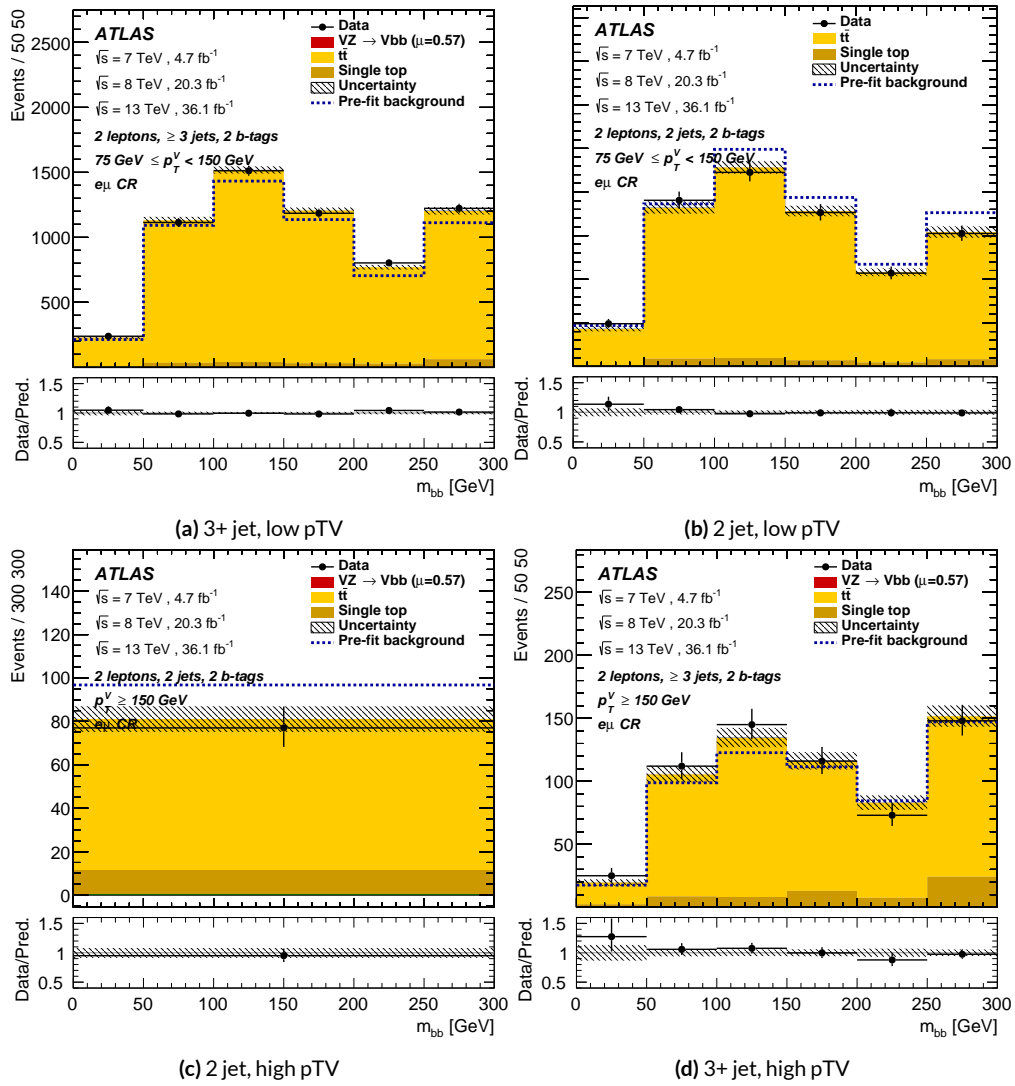
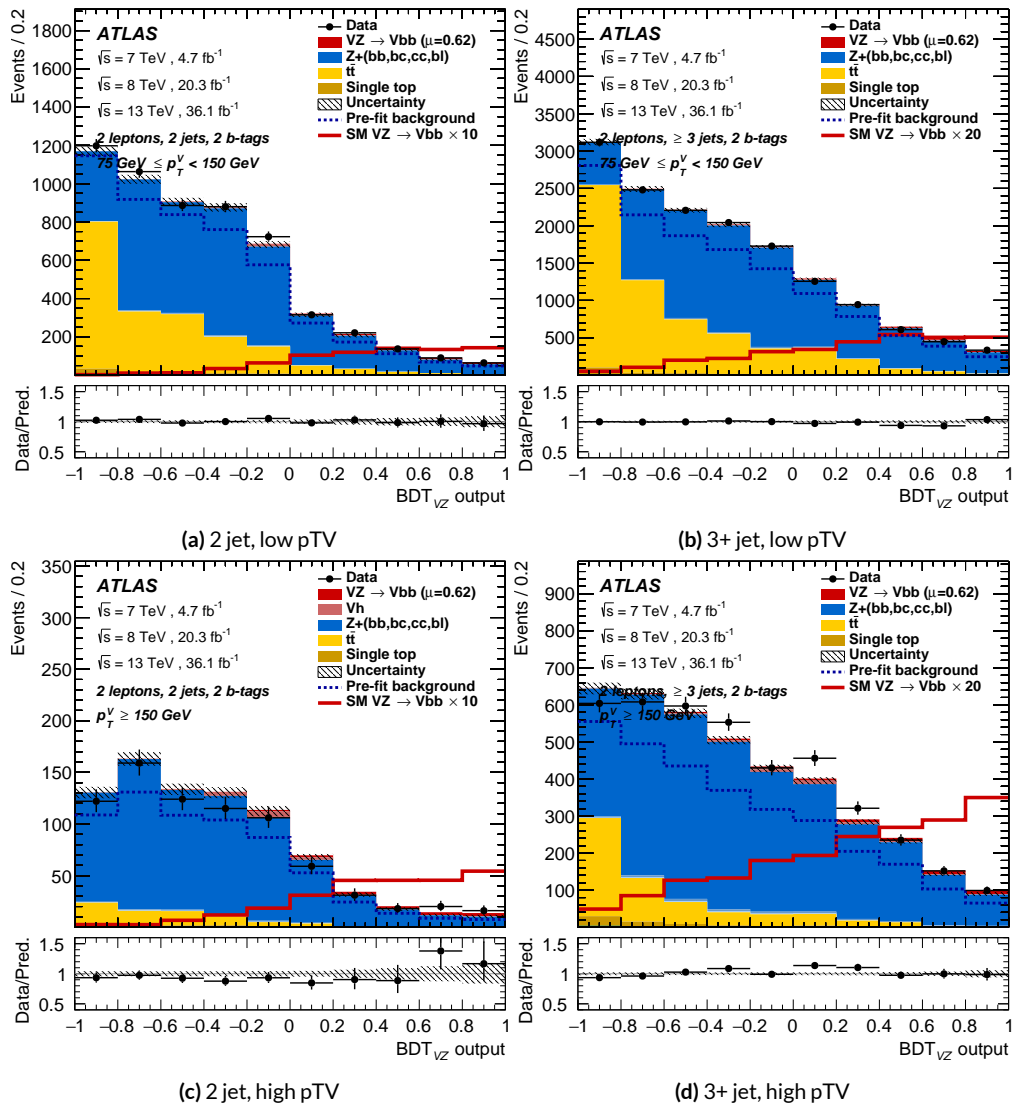
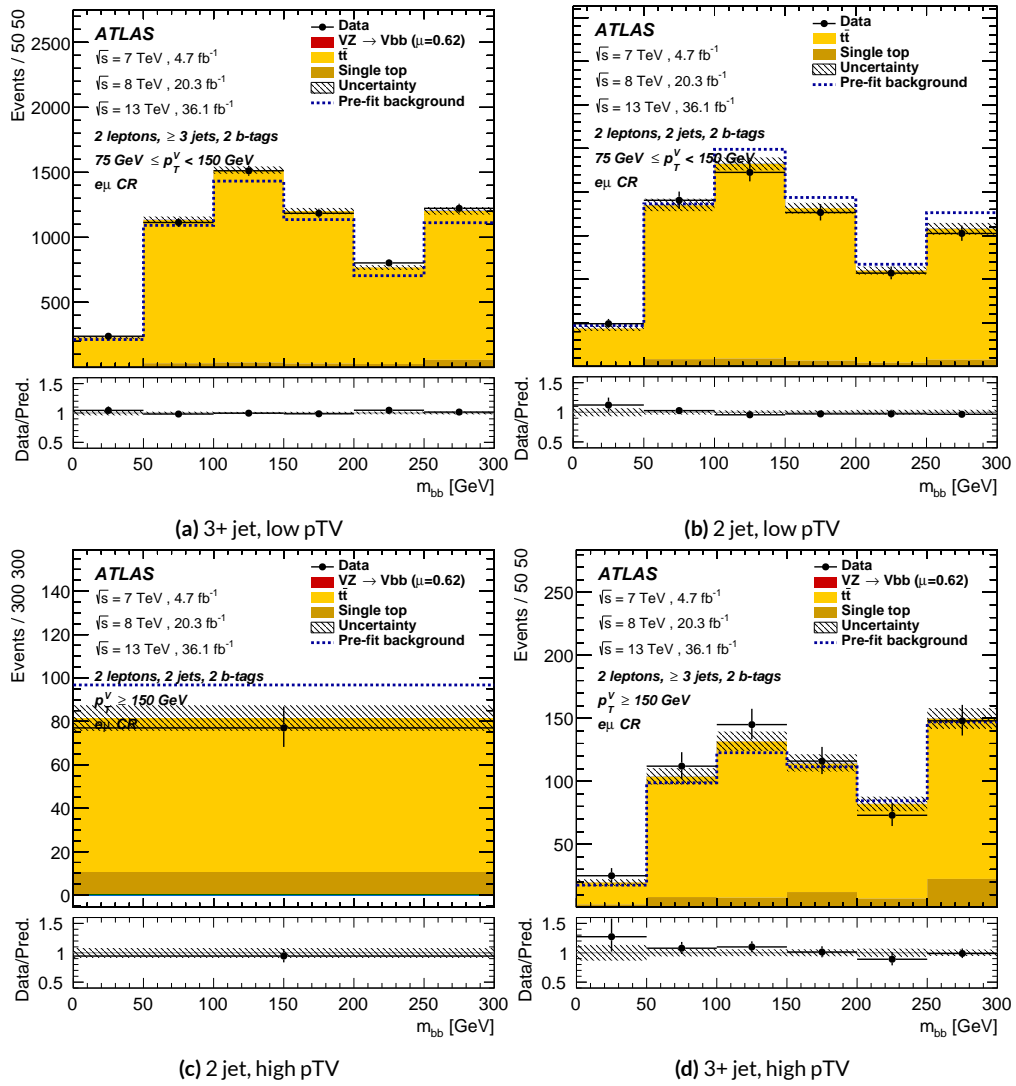


Figure 7.17: Postfit  $m_{bb}$  plots in the top  $e - \mu$  CR for the LI variable set.



**Figure 7.18:** Postfit  $BDT_{VZ}$  plots in the signal region for the RF variable set.



**Figure 7.19:** Postfit  $m_{bb}$  plots in the top  $e - \mu$  CR for the RF variable set.

1800 7.7 VH FIT MODEL VALIDATION

1801 We now move onto the fit validation distributions and numbers for the  $VH$  fit of interest.

1802 7.7.1 NUISANCE PARAMETER PULLS

As can be seen in Figures 7.20–7.24, the fits for the three different variable sets are fairly similar from a NP pull perspective. Again, black is the standard variable set, red is the LI set, and blue is the RF set. The possible exception is the signal UE+PS  $p_T^V$  systematic, which looks very different for all three cases (underconstrained for the standard, but overconstrained for the novel variable cases), though this difference goes away in the ranking plot, meaning this is almost certainly an unphysical artifice of the faster HESSE inversion used to produce the pull comparison plots.

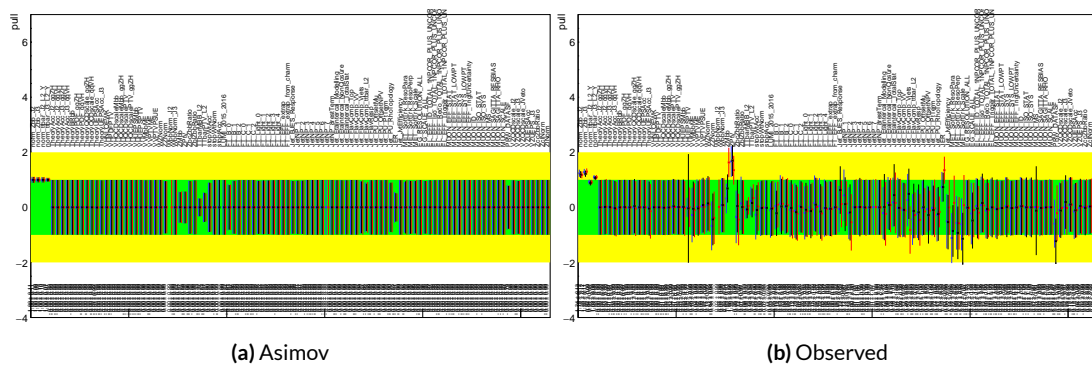


**Figure 7.20:** Pull comparison for all NP's but MC stats.

Nuisance parameter correlation matrices (for correlations with magnitude at least 0.25) for all three variable set fits can be found in Figures 7.26–7.28.

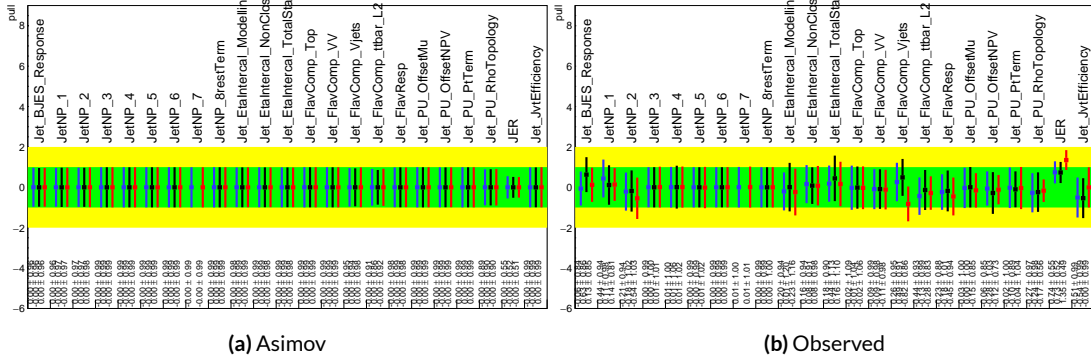


Figure 7.21: Pull comparison for jet NP's.

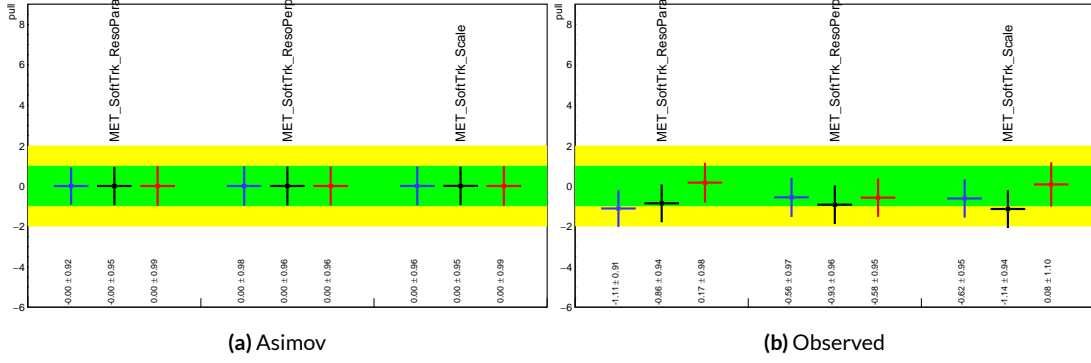


Figure 7.22: Pull comparison for MET NP's.

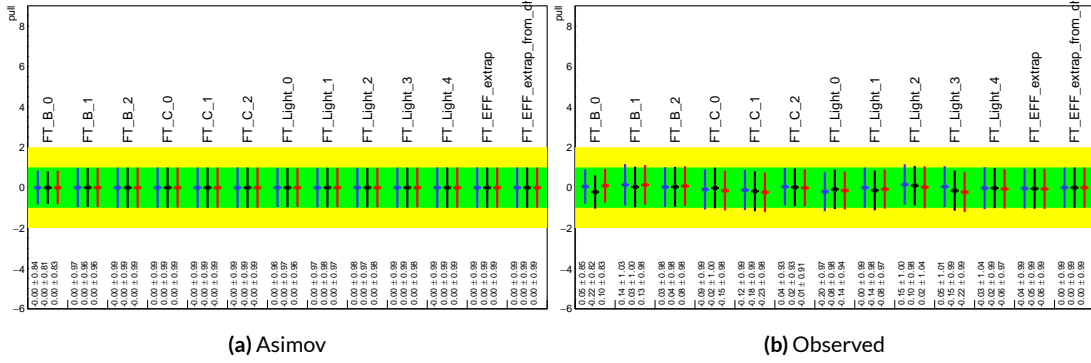


Figure 7.23: Pull comparison for Flavour Tagging NP's.

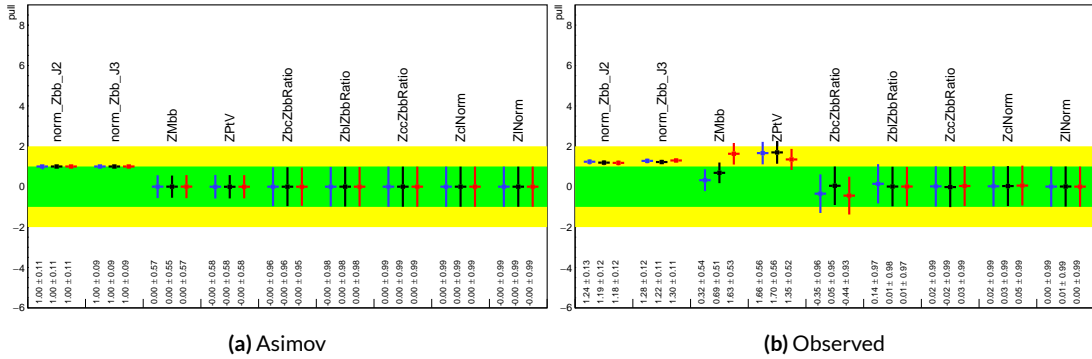


Figure 7.24: Pull comparison for  $Z + \text{jets}$  NP's.

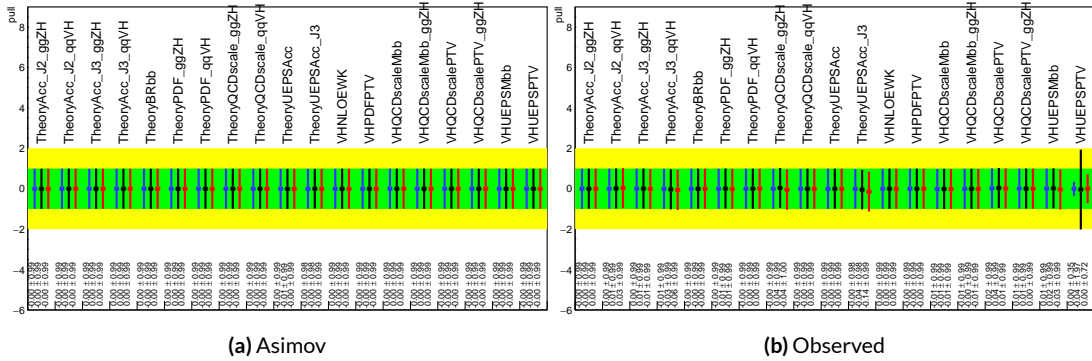


Figure 7.25: Pull comparison for signal process modeling NP's.

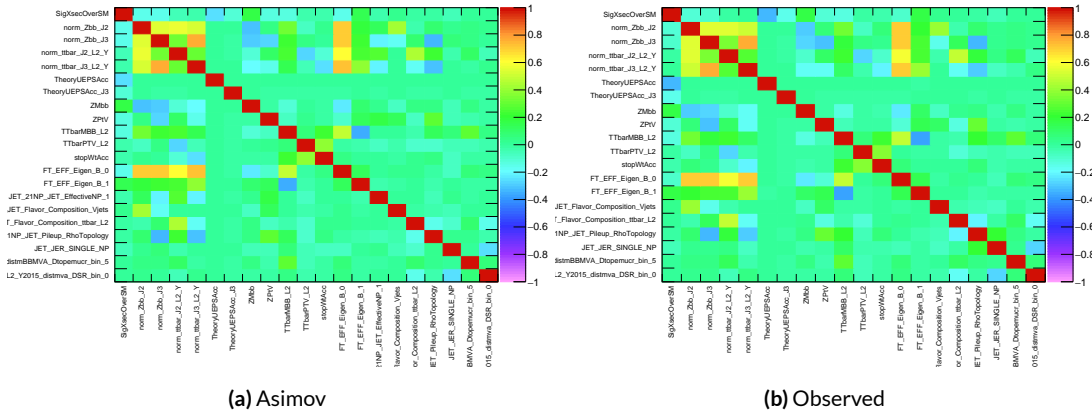


Figure 7.26: NP correlations for standard variable fits.

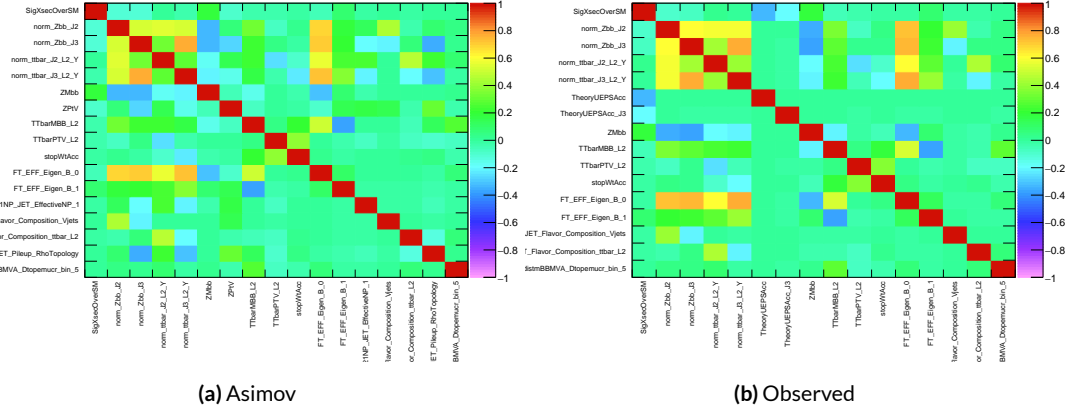


Figure 7.27: NP correlations for LI variable fits.

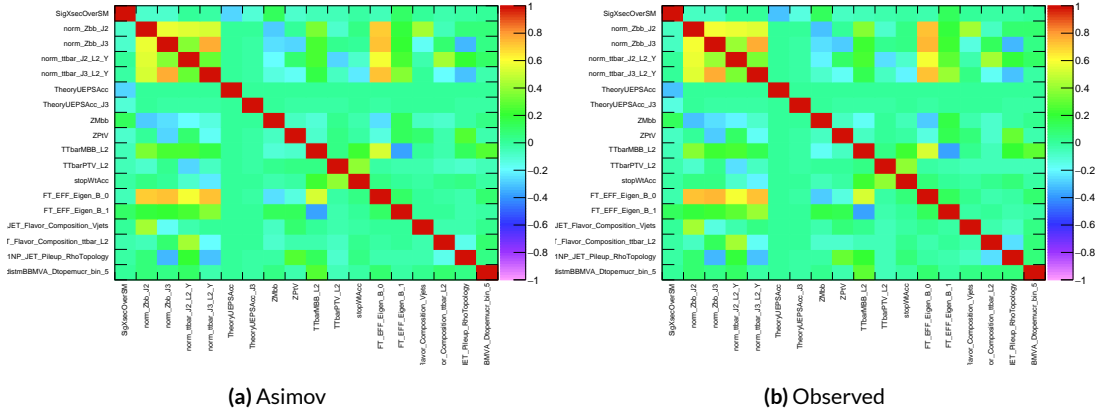


Figure 7.28: NP correlations for RF variable fits.

1811 7.7.2 FULL BREAKDOWN OF ERRORS

1812 A postfit ranking of nuisance parameters according to their impact on  $\hat{\mu}$  for the different variable  
 1813 sets may be found in Figure 7.29, with rankings being fairly similar. In particular, the signal UE+PS  
 1814  $p_T^V$  systematic is top-ranked for all three variable sets and also looks very similar, unlike in the pull  
 1815 comparison plot, reiterating the importance of evaluating individually the impact of highly ranked  
 1816 NP's. The  $Z+jets p_T^V$  is highly pulled in all three cases, though this is less severe for the non-standard  
 1817 set (it is off the scale for the standard variable ranking). The RF discriminant mitigates the effect of  
 1818 poorly modeled jet energy resolution better than the other sets.

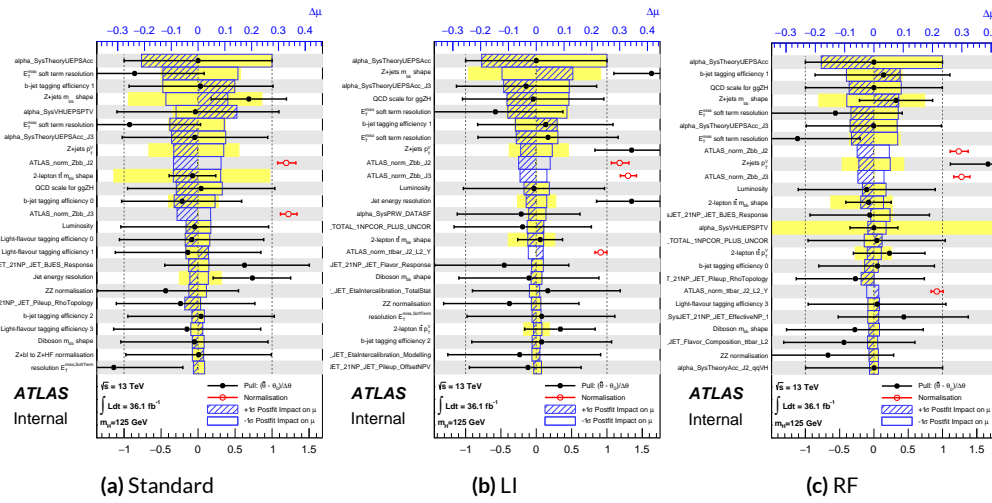


Figure 7.29: Plots for the top 25 nuisance parameters according to their postfit impact on  $\hat{\mu}$  for the standard (a), LI (b), and RF (c) variable sets.

1819 The Asimov (Table 7.7) and observed (Table 7.8) breakdowns both consistently suggest that the  
 1820 LI variable set does a better job of constraining systematic uncertainties than the standard set and  
 1821 that the RF set does better still. It is also not surprising that the gain is more substantial in the ob-

<sup>1822</sup> served fit than in the Asimov fits, as in the latter there are the “penalty” terms from pulls in addition  
<sup>1823</sup> to the overall broadening in the likelihood.

	Std-KF	LI+MET	RF
Total	+0.608 / -0.511	+0.632 / -0.539	+0.600 / -0.494
DataStat	+0.420 / -0.401	+0.453 / -0.434	+0.424 / -0.404
FullSyst	+0.440 / -0.318	+0.441 / -0.319	+0.425 / -0.284
Floating normalizations	+0.122 / -0.125	+0.110 / -0.111	+0.093 / -0.089
All normalizations	+0.128 / -0.129	+0.112 / -0.112	+0.099 / -0.092
All but normalizations	+0.403 / -0.274	+0.387 / -0.250	+0.382 / -0.227
Jets, MET	+0.180 / -0.097	+0.146 / -0.079	+0.122 / -0.083
Jets	+0.051 / -0.030	+0.044 / -0.035	+0.025 / -0.042
MET	+0.173 / -0.091	+0.140 / -0.074	+0.117 / -0.063
BTag	+0.138 / -0.136	+0.069 / -0.071	+0.076 / -0.078
BTag b	+0.125 / -0.125	+0.067 / -0.070	+0.073 / -0.075
BTag c	+0.018 / -0.016	+0.004 / -0.004	+0.005 / -0.005
BTag light	+0.057 / -0.051	+0.020 / -0.014	+0.009 / -0.018
Leptons	+0.013 / -0.012	+0.029 / -0.026	+0.012 / -0.023
Luminosity	+0.052 / -0.020	+0.050 / -0.016	+0.050 / -0.019
Diboson	+0.043 / -0.039	+0.035 / -0.031	+0.038 / -0.029
Model Zjets	+0.119 / -0.117	+0.124 / -0.127	+0.095 / -0.086
Zjets flt. norm.	+0.080 / -0.106	+0.052 / -0.092	+0.026 / -0.072
Model Wjets	+0.001 / -0.001	+0.001 / -0.001	+0.000 / -0.001
Wjets flt. norm.	+0.000 / -0.000	+0.000 / -0.000	+0.000 / -0.000
Model ttbar	+0.076 / -0.080	+0.025 / -0.035	+0.025 / -0.040
Model Single Top	+0.015 / -0.015	+0.002 / -0.004	+0.021 / -0.007
Model Multi Jet	+0.000 / -0.000	+0.000 / -0.000	+0.000 / -0.000
Signal Systematics	+0.262 / -0.087	+0.272 / -0.082	+0.290 / -0.088
MC stat	+0.149 / -0.136	+0.168 / -0.154	+0.153 / -0.136

**Table 7.7:** Expected error breakdowns for the standard, LI, and RF variable sets

	Std-KF	LI+MET	RF
$\hat{\mu}$	1.7458	1.6467	1.5019
Total	+0.811 / -0.662	+0.778 / -0.641	+0.731 / -0.612
DataStat	+0.502 / -0.484	+0.507 / -0.489	+0.500 / -0.481
FullSyst	+0.637 / -0.451	+0.591 / -0.415	+0.533 / -0.378
Floating normalizations	+0.153 / -0.143	+0.128 / -0.118	+0.110 / -0.109
All normalizations	+0.158 / -0.147	+0.130 / -0.119	+0.112 / -0.110
All but normalizations	+0.599 / -0.402	+0.544 / -0.354	+0.486 / -0.318
Jets, MET	+0.218 / -0.145	+0.198 / -0.113	+0.167 / -0.106
Jets	+0.071 / -0.059	+0.065 / -0.047	+0.036 / -0.051
MET	+0.209 / -0.130	+0.190 / -0.102	+0.152 / -0.077
BTAG	+0.162 / -0.166	+0.093 / -0.070	+0.115 / -0.099
BTAG b	+0.142 / -0.147	+0.090 / -0.066	+0.110 / -0.094
BTAG c	+0.022 / -0.021	+0.006 / -0.006	+0.007 / -0.007
BTAG light	+0.074 / -0.072	+0.025 / -0.022	+0.031 / -0.029
Leptons	+0.039 / -0.029	+0.035 / -0.031	+0.034 / -0.030
Luminosity	+0.079 / -0.039	+0.073 / -0.034	+0.069 / -0.032
Diboson	+0.047 / -0.043	+0.031 / -0.028	+0.029 / -0.028
Model Zjets	+0.164 / -0.152	+0.141 / -0.143	+0.101 / -0.105
Zjets flt. norm.	+0.070 / -0.109	+0.041 / -0.086	+0.033 / -0.083
Model Wjets	+0.001 / -0.001	+0.001 / -0.000	+0.001 / -0.001
Wjets flt. norm.	+0.000 / -0.000	+0.000 / -0.000	+0.000 / -0.000
Model ttbar	+0.067 / -0.102	+0.029 / -0.040	+0.040 / -0.048
Model Single Top	+0.015 / -0.020	+0.001 / -0.005	+0.004 / -0.006
Model Multi Jet	+0.000 / -0.000	+0.000 / -0.000	+0.000 / -0.000
Signal Systematics	+0.434 / -0.183	+0.418 / -0.190	+0.364 / -0.152
MC stat	+0.226 / -0.201	+0.221 / -0.200	+0.212 / -0.189

**Table 7.8:** Observed signal strengths, and error breakdowns for the standard, LI, and RF variable sets

<sup>1824</sup> 7.7.3 POSTFIT DISTRIBUTIONS AND S/B PLOTS

<sup>1825</sup> Postfit distributions for the MVA discriminant ( $m_{bb}$ ) distribution in the signal (top  $e - \mu$  control)  
<sup>1826</sup> region for the standard, Lorentz Invariant, and RestFrames variable sets are found in Figures 7.30–  
<sup>1827</sup> 7.35. Here, as in the  $VZ$  fit, agreement is reasonable. In a combined fit with all three channels,  $Z+hf$   
<sup>1828</sup> normalizations in particular would be correlated across the 0- and 2-lepton channels, which might  
<sup>1829</sup> help to better constrain this mismodeling (and perhaps as a result some of the  $Z+jets$  systematics as  
<sup>1830</sup> well).

<sup>1831</sup> One final type of plot presented as a result is the binned  $\log_{10} (S/B)$  in signal regions distribu-  
<sup>1832</sup> tions may be found in Figure 7.36. For these plots, one fills a histogram with the  $\log_{10} (S/B)$  ratio in  
<sup>1833</sup> each postfit distribution bin weighted by the total number of events. In this case, a log plot is help-  
<sup>1834</sup> ful because the highest bins would be invisible on a linear plot. These distributions are allegedly use-  
<sup>1835</sup> ful for seeing where most of one's sensitivity lies. Practically, it is problematic if the pull (from the  
<sup>1836</sup> null hypothesis) is higher at lower  $S/B$  values, which may indicate a poorly optimized discriminant.

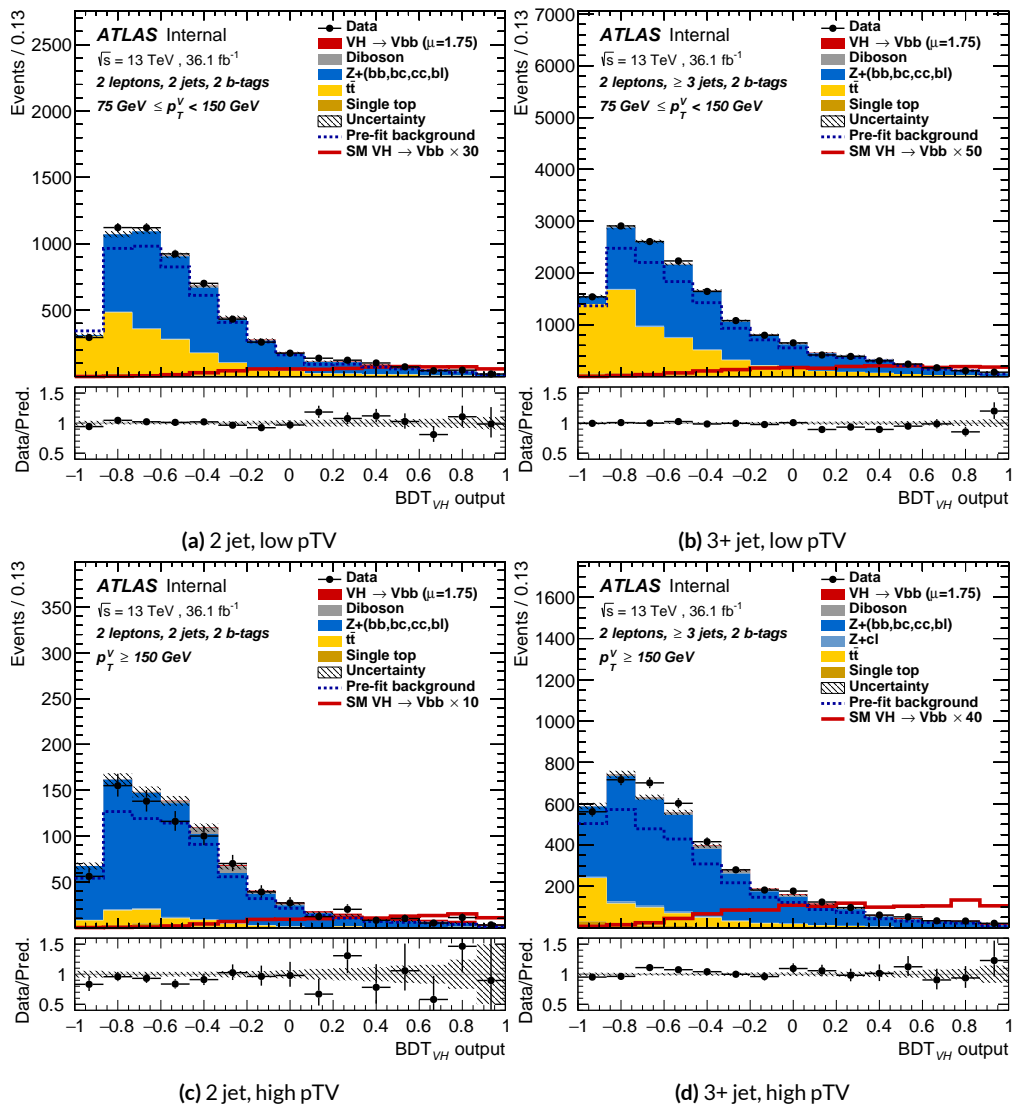
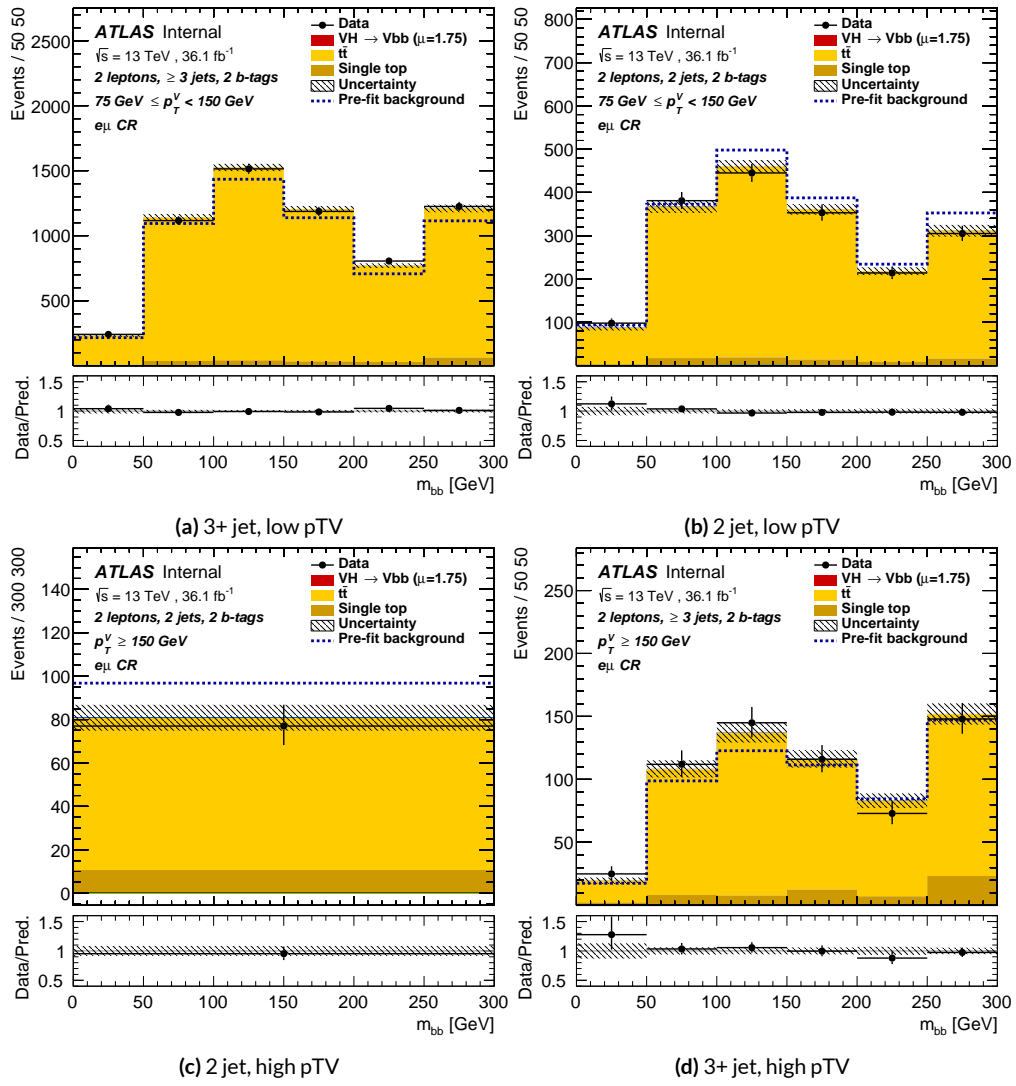
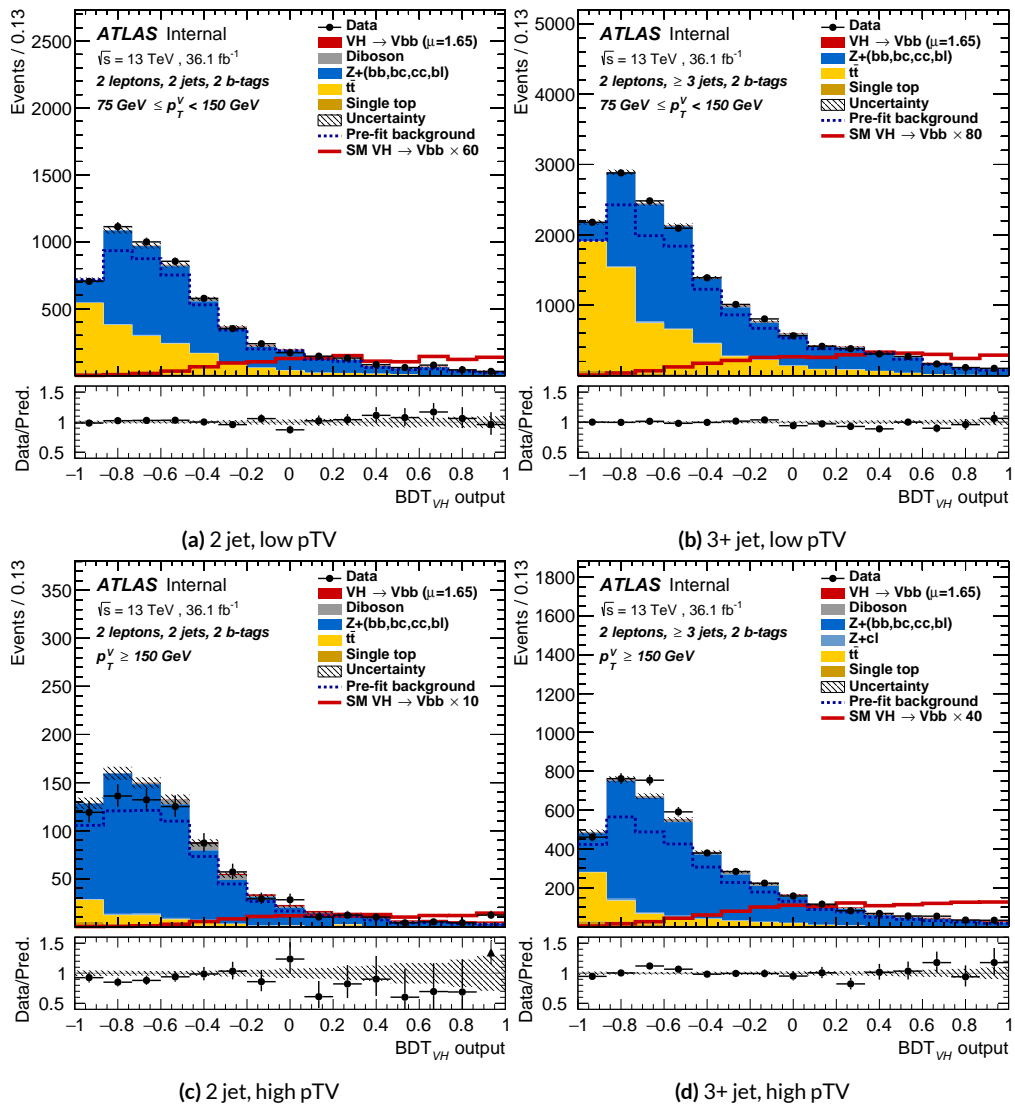


Figure 7.30: Postfit  $BDT_{VH}$  plots in the signal region for the standard variable set.



**Figure 7.31:** Postfit  $m_{bb}$  plots in the top  $e - \mu$  CR for the standard variable set.



**Figure 7.32:** Postfit  $BDT_{VH}$  plots in the signal region for the LI variable set.

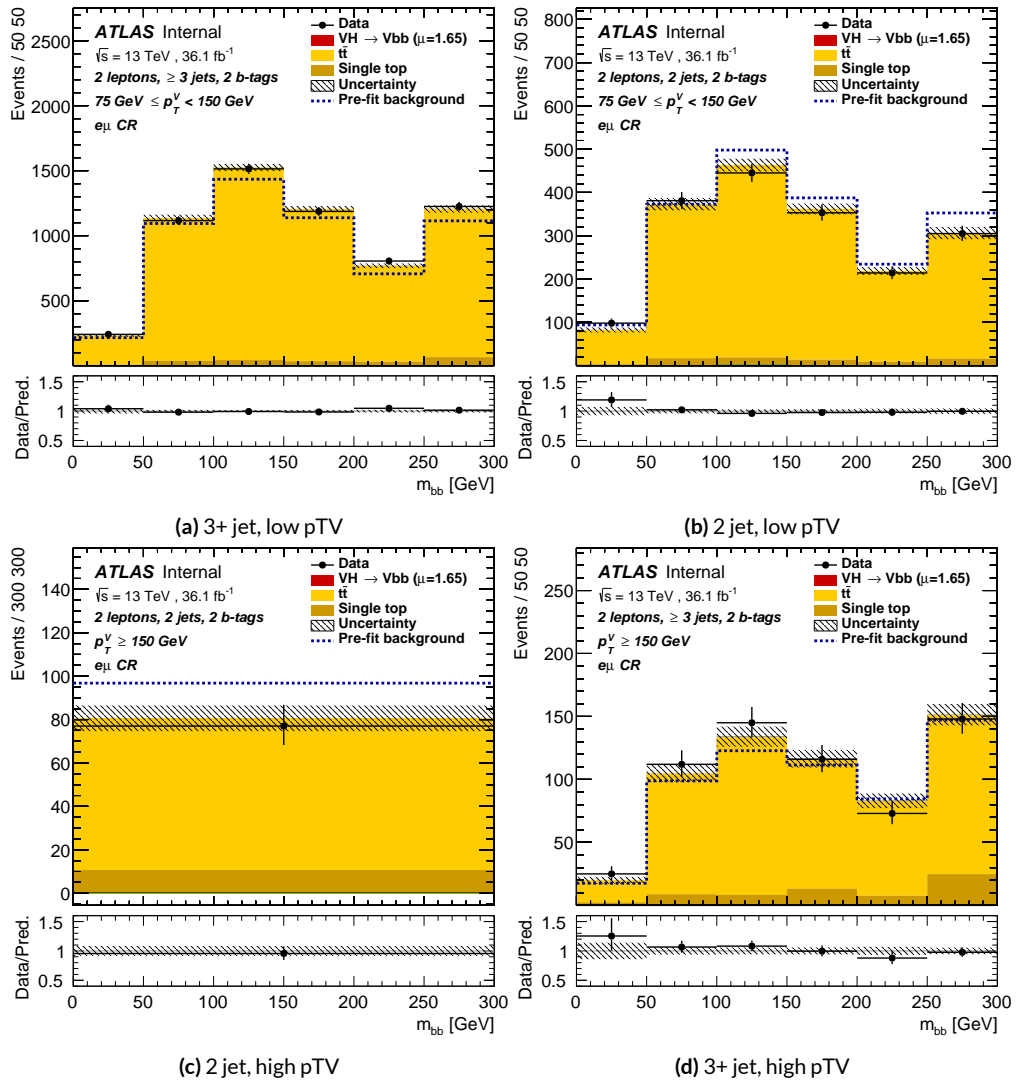


Figure 7.33: Postfit  $m_{bb}$  plots in the top  $e - \mu$  CR for the LI variable set.

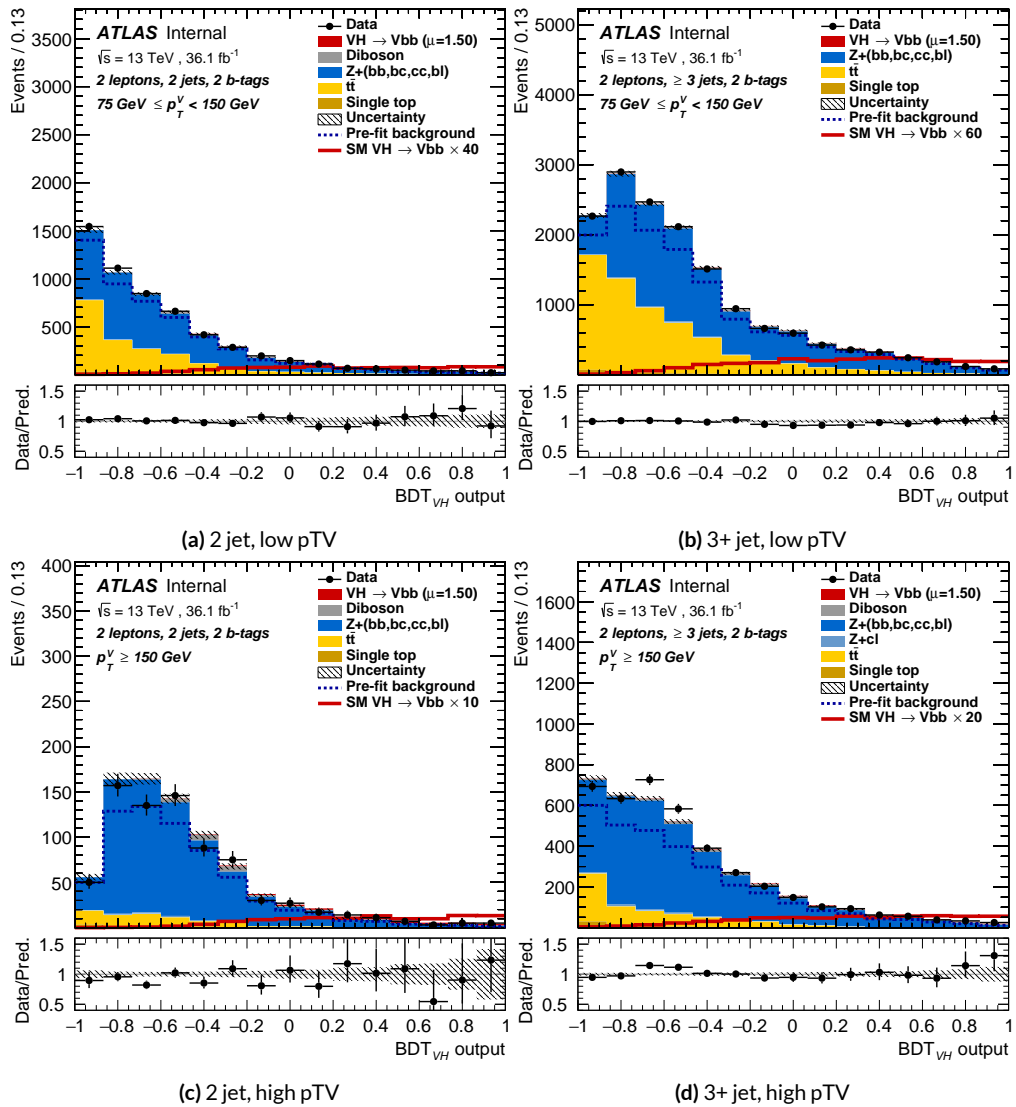
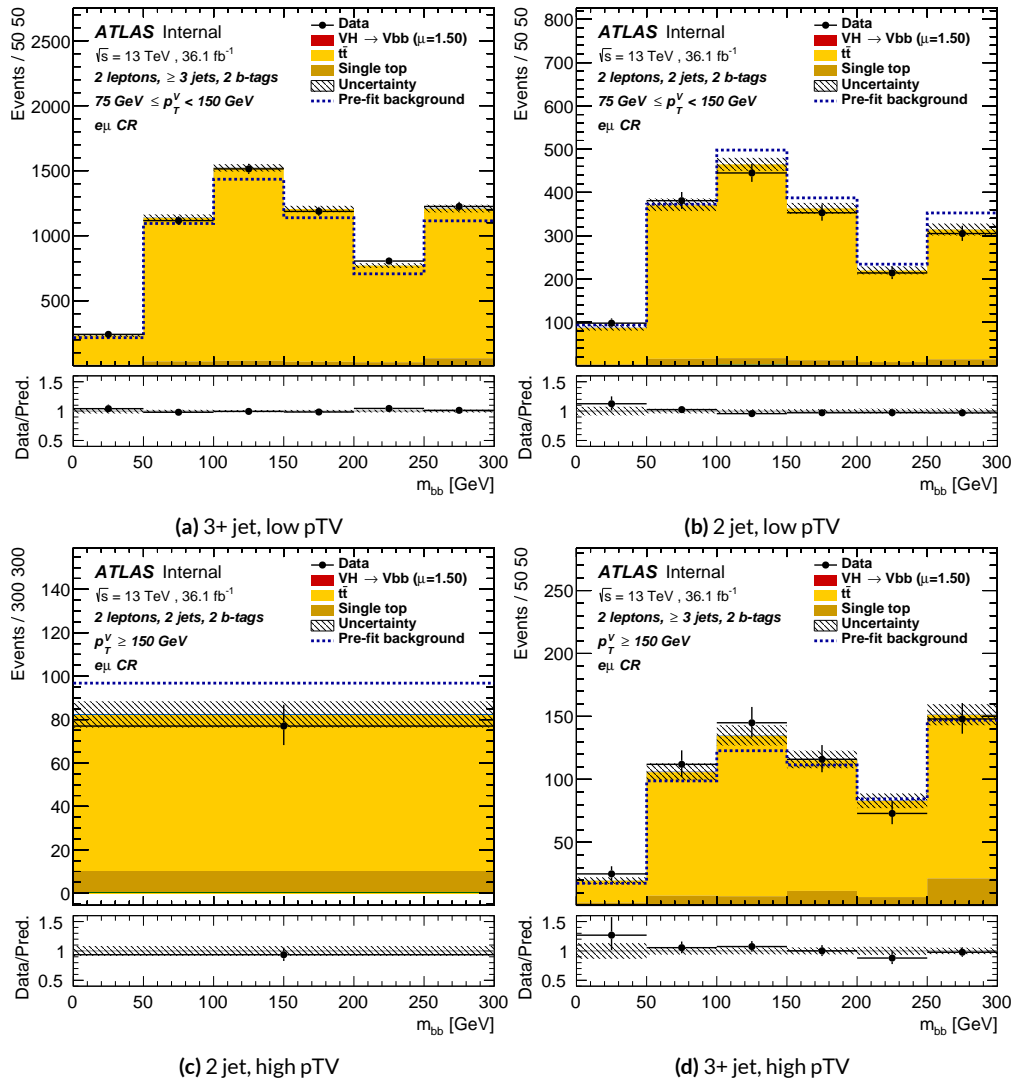
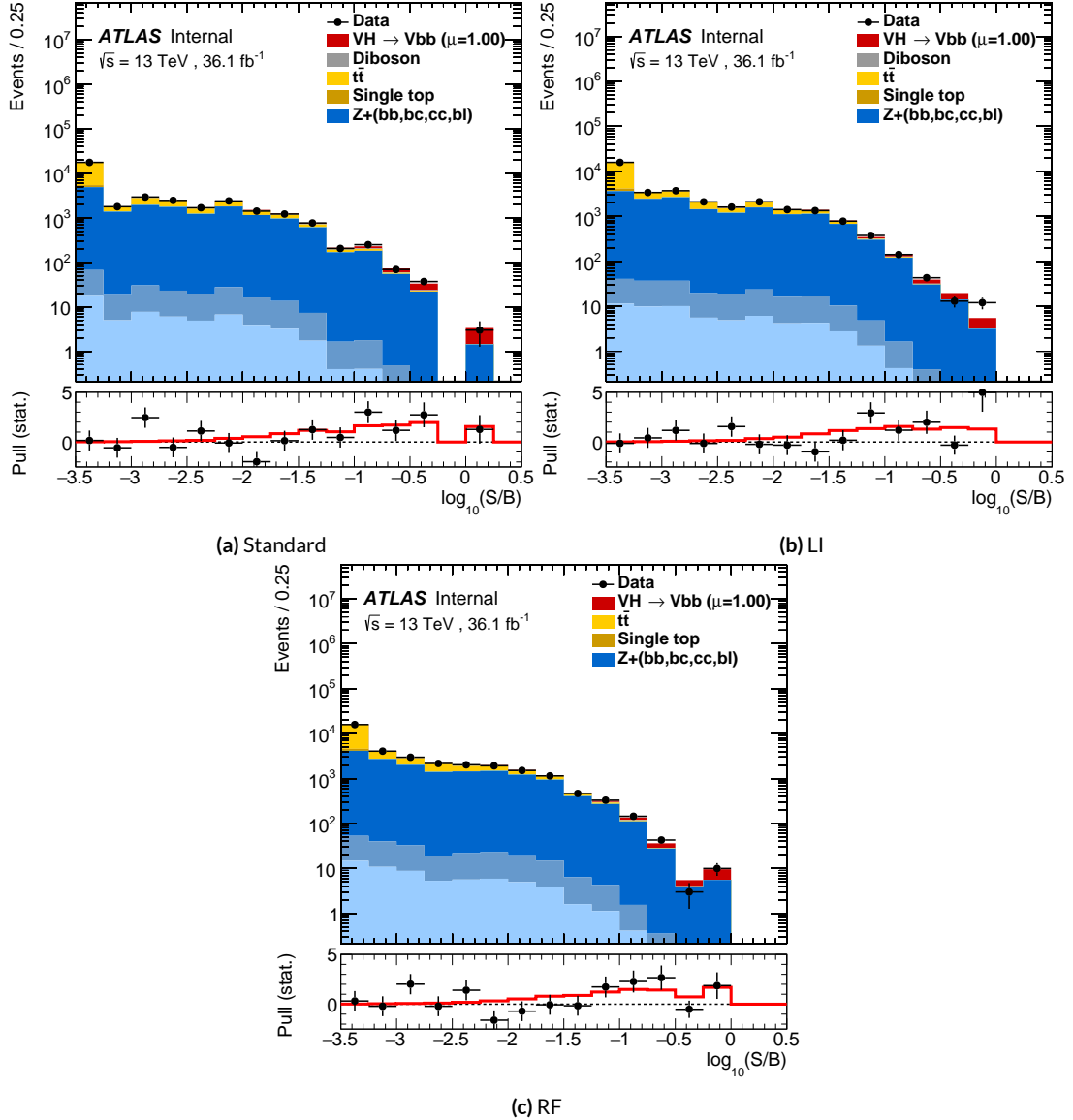


Figure 7.34: Postfit  $BDT_{VH}$  plots in the signal region for the RF variable set.



**Figure 7.35:** Postfit  $m_{bb}$  plots in the top  $e - \mu$  CR for the RF variable set.



**Figure 7.36:** Binned S/B plots for the standard (a), LI (b), and RF (c) variable sets. Signal is weighted to  $\mu = 1$  for comparison to the SM prediction.

*Kein Operationsplan reicht mit einiger Sicherheit  
über das erste Zusammentreffen mit der feindlichen  
Hauptmacht hinaus.*

Helmuth von Moltke

1837

# 8

1838

## Fit Results

<sup>1839</sup> THE RESULTS IN THIS CHAPTER were first reported in [37] and describe how the three different fit models detailed and validated Chapter 7, corresponding to the standard, RF, and LI variable sets described in Chapter 6 perform on actual  $VH$  fits. In particular sensitivities, nuisance parameter impacts, and signal strengths on expected fits to Asimov datasets and both expected and observed

1843 fits on the actual  $36.1 \text{ fb}^{-1}$  dataset are compared.

1844 Expected and observed sensitivities for the different variable sets may be found in Table 8.1. The  
1845 RF fits feature the highest expected sensitivities, outperforming the standard set by 3.5% and 3.4%  
1846 for fits to Asimov and observed datasets, respectively. The LI variable has a lower significance than  
1847 both for expected fits to both Asimov and data with a 6.7% (1.7%) significance than the standard set  
1848 for the Asimov (observed) dataset. While the fit using standard variables does have a higher observed  
1849 significance than both the LI and RF fits, by 2.8% and 8.6%, respectively, these numbers should be  
1850 viewed in the context of the best fit  $\hat{\mu}$  values, discussed below. That is, the standard set may yield the  
1851 highest sensitivity for this particular dataset, but this is not necessarily (and likely is not) the case for  
1852 any given dataset.

	Standard	LI	RF
Expected (Asimov)	2.06	1.92	2.13
Expected (data)	1.76	1.73	1.80
Observed (data)	2.87	2.79	2.62

**Table 8.1:** Expected (for both data and Asimov) and observed significances for the standard, LI, and RF variable sets.

1853 A summary of fitted signal strengths and errors for both the Asimov (a) and observed (b) datasets  
1854 are shown in Figure 8.1.\* A summary of error breakdowns is given in Tables 8.2 (Asimov) and 8.3  
1855 (observed) for total error, data statistics contributions, total systematic error contributions, and cat-  
1856 egories for which the total impact is  $\geq 0.1$  for the standard fit. As is to be expected for both the  
1857 Asimov and observed dataset fits, the contribution to the total error on  $\mu$  arising from data statistics

---

\*For reference, the standalone 2-lepton fit from the fiducial analysis is  $2.11^{+0.50}_{-0.48}(\text{stat.})^{+0.64}_{-0.47}(\text{syst.})$

<sup>1858</sup> is nearly identical, since each set of fits uses the same selections and data.<sup>†</sup>

	Std-KF	LI+MET	RF
Total	+0.608 / -0.511	+0.632 / -0.539	+0.600 / -0.494
DataStat	+0.420 / -0.401	+0.453 / -0.434	+0.424 / -0.404
FullSyst	+0.440 / -0.318	+0.441 / -0.319	+0.425 / -0.284
Signal Systematics	+0.262 / -0.087	+0.272 / -0.082	+0.290 / -0.088
MET	+0.173 / -0.091	+0.140 / -0.074	+0.117 / -0.063
Flavor Tagging	+0.138 / -0.136	+0.069 / -0.071	+0.076 / -0.078
Model Zjets	+0.119 / -0.117	+0.124 / -0.127	+0.095 / -0.086

**Table 8.2:** Summary of error impacts on total  $\mu$  error for principal categories in the Asimov standard, LI, and RF fits.

	Std-KF	LI+MET	RF
Total	+0.811 / -0.662	+0.778 / -0.641	+0.731 / -0.612
DataStat	+0.502 / -0.484	+0.507 / -0.489	+0.500 / -0.481
FullSyst	+0.637 / -0.451	+0.591 / -0.415	+0.533 / -0.378
Signal Systematics	+0.434 / -0.183	+0.418 / -0.190	+0.364 / -0.152
MET	+0.209 / -0.130	+0.190 / -0.102	+0.152 / -0.077
Flavor Tagging	+0.162 / -0.166	+0.093 / -0.070	+0.115 / -0.099
Model Zjets	+0.164 / -0.152	+0.141 / -0.143	+0.101 / -0.105

**Table 8.3:** Summary of error impacts on total  $\hat{\mu}$  error for principal categories in the observed standard, LI, and RF fits.

<sup>1859</sup> The contribution from systematic uncertainties, however, does vary considerably across the vari-  
<sup>1860</sup> able sets. The Asimov fits are a best case scenario in the sense that, by construction, all NP's are equal  
<sup>1861</sup> to their predicted values (and so no "penalty" is paid for pulls on Gaussian NP's). The systematics er-  
<sup>1862</sup> ror from the LI fit is slightly higher (subpercent) than that from the standard fit, and 4.6% higher er-  
<sup>1863</sup> ror overall due to differences in data stats. The RF Asimov fit, however, has a 6.5% lower total error

---

<sup>†</sup>Though not exactly identical. Since the BDT's are different for the different variable sets, the binning (as determined by transformation D) and bin contents in each set are generally different, leading to slightly different data statistics errors.

1864 from systematics than the standard Asimov fit (and a 2.2% lower error overall). Moreover, for both  
 1865 the LI and RF sets, errors are markedly smaller for the MET and Flavor Tagging categories, with the  
 1866 RF fit also featuring a smaller errors on  $Z$ +jets modeling; the only notable exception to this trend in  
 1867 Asimov fits are the signal systematics.

1868 These trends are more pronounced in the observed fits. As can be seen in Table 8.3, both the LI  
 1869 and RF fits have smaller errors from systematic uncertainties, both overall and in all principal cate-  
 1870 gories, with the LI and RF fits having 7.5% (3.7%) and 16% (8.8%) lower systematics (total) error on  
 1871  $\hat{\mu}$ , respectively.

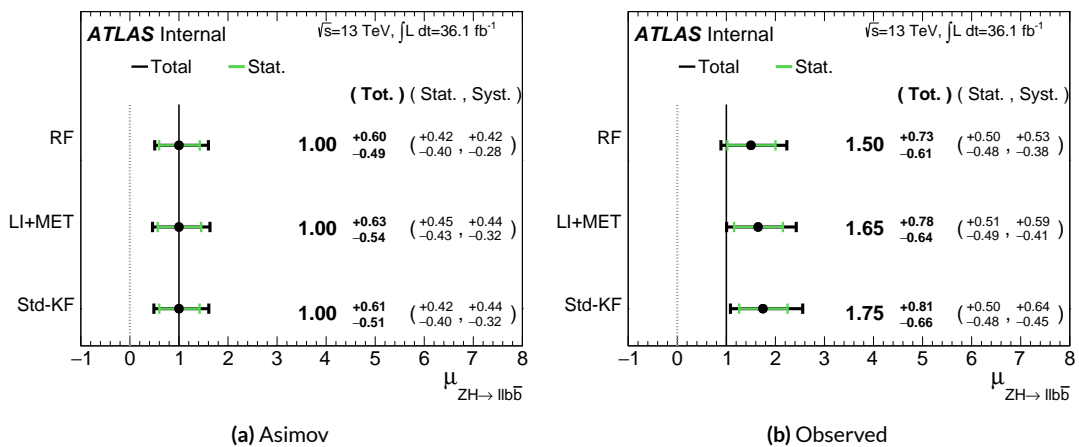


Figure 8.1:  $\mu$  summary plots for the standard, LI, and RF variable sets. The Asimov case (with  $\mu = 1$  by construction) is in (a), and  $\hat{\mu}$  best fit values and error summary are in (b).

1872 Studying the performance of the Lorentz Invariant and RestFrames variable sets at both a data  
 1873 statistics only context and with the full fit model in the  $ZH \rightarrow \ell\ell b\bar{b}$  channel of the  $VH(b\bar{b})$  anal-  
 1874 ysis suggests that these variables may offer a potential method for better constraining systematic un-  
 1875 certainties in  $VH(b\bar{b})$  searches as more orthogonal bases in describing the information in collision

1876 events.

1877 The marginally worse performance of the LI and RF variables (7.9% and 6.9%, respectively) with  
1878 respect to the standard variable at a stats only level illustrates that neither variable set has greater  
1879 intrinsic descriptive power in the absence of systematics in this closed final state. Hence, any gains  
1880 from either of these variable sets in a full fit come from improved treatment of systematic uncertain-  
1881 ties.

1882 With full systematics, the LI variable set narrows the sensitivity gap somewhat, with lower signif-  
1883 icances by 6.7% (1.7%) on expected fits to Asimov (data) and by 2.8% on observed significances. The  
1884 RF variable set outperforms the standard set in expected fits with 3.5% (3.4%) higher significance  
1885 on Asimov (data), but has an 8.6% lower observed significance, though the observed significances  
1886 should be viewed in the context of observed  $\hat{\mu}$  values.

1887 Moreover, the LI and RF variable sets generally perform better in the context of the error on  $\mu$ .  
1888 The LI fit is comparable to the standard set on Asimov data and has a 7.5% lower total systematics er-  
1889 ror on  $\hat{\mu}$  on observed data, while the RF fit is lower in both cases, with systematics error being 6.5%  
1890 (16%) lower on Asimov (observed) data.

1891 These figures of merit suggest that both the LI and RF variables are more orthogonal than the  
1892 standard variable set used in the fiducial analysis. Moreover, the RF variable set does seem to con-  
1893 sistently perform better than the LI set. Furthermore, both variable sets have straightforward exten-  
1894 sions to the other lepton channels in the  $VH(b\bar{b})$  analysis. The magnitude of any gain from the  
1895 more sophisticated treatment of  $E_T^{miss}$  in these extensions is beyond the scope of these studies, but  
1896 the performance in this closed final state do suggest that there is some value to be had in these non-

<sup>1897</sup> standard descriptions independent of these considerations.

*If I have seen further, it is by standing on ye shoulders of  
giants.*

Isaac Newton

# 9

1898

1899

## Measurement Combinations

1900 WHILE THE DISCUSSION thus far has focused on improvements looking towards future in just the  
1901  $ZH \rightarrow \ell\ell b\bar{b}$  channel, any actual result for SM  $VH(b\bar{b})$  combines all channels and all available  
1902 datasets. Using additional channels at a given center of mass energy is straightforward since the fit  
1903 model is designed with this combination in mind. This will be described in the context of the 36.1

1904  $\text{fb}^{-1}$  13 TeV result in Section 9.1.

1905 Combining dataset results (known as “workspaces”) from different center of mass energies is not  
1906 so simple an exercise since both the underlying physics (and its associated modeling) and the treat-  
1907 ment of key experimental considerations, like flavor tagging, and their associated systematics change  
1908 from dataset to dataset. A combined fit model must take these considerations into account, and the  
1909 formulation of the fit model combining the Run 1 ( $\sqrt{s} = 7 \text{ TeV}$  with  $4.7 \text{ fb}^{-1}$  of data, and  $\sqrt{s} = 8$   
1910  $\text{TeV}$  with  $20.3 \text{ fb}^{-1}$  of data) and Run 2 ( $\sqrt{s} = 13 \text{ TeV}$  with  $36.1 \text{ fb}^{-1}$ ) SM  $VH(b\bar{b})$  results is the topic  
1911 of Section 9.2. Its results, as reported in [42], are given in 9.3.

## 1912 9.1 LEPTON CHANNEL COMBINATIONS

1913 Preparation of results for the o- and i-lepton channels is functionally very similar to above discus-  
1914 sions in Chapters 4, 5, 6, and 7. From a modeling standpoint, each channel comes in with different  
1915 dominating background processes and dedicated simulation, described at length in [67], though  
1916 there is a lot of overlap. In particular,  $t\bar{t}$ , , and diboson production is important for all three chan-  
1917 nels. The only important process not discussed here is contribution from multijet background,  
1918 which is a small but important background in the i-lepton case.

1919 With respect to object definitions, no new objects are defined in the o- and i-lepton analyses,  
1920 though the treatment of  $\vec{E}_T^{\text{miss}}$  is of greater concern in these channels, as  $\vec{E}_T^{\text{miss}}$  is a part of the signal  
1921 final states in these channels. Triggers and event selection requirements are optimized by channel. A  
1922 full list of requirements is given in Table 9.1 from [65].

1923 The mechanics of MVA training and implementation is very much the same across analysis chan-

Common Selections	
Jets	$\geq 2$ central jets
$b$ -jets	2 $b$ -tagged signal jets
Leading jet $p_T$	$> 45$ GeV
$ \Delta R(\text{jet1}, \text{jet2}) $ (cut-based only)	$\leq 1.8 (p_T^V < 200 \text{ GeV}), \leq 1.2 (p_T^V > 200 \text{ GeV})$
○ Lepton	
Trigger	HLT_xe70, xe90_mht, and xe110_mht
Leptons	○ VH-loose lepton
$\vec{E}_T^{\text{miss}}$	$> 150$ GeV
$S_T$	$> 120$ (2 jets), $> 150$ GeV (3 jets)
$ \min \Delta\phi(\vec{E}_T^{\text{miss}}, \text{jet}) $	$> 20^\circ$ (2jet), $> 30^\circ$ (3jet)
$ \Delta\phi(\vec{E}_T^{\text{miss}}, b) $	$> 120^\circ$
$ \Delta\phi(\text{jet1}, \text{jet2}) $	$< 140^\circ$
$ \Delta\phi(\vec{E}_T^{\text{miss}}, E_{T, \text{trk}}^{\text{miss}}) $	$< 90^\circ$
$p_T^V$ regions (BDT)	$> 150$ GeV
$p_T^V$ regions (cut-based)	$[150, 200]$ GeV, $[200, \infty]$ GeV
1 Lepton	
Trigger	$e$ channel: un-prescaled single electron Tables 5 and 6 of Ref. [31]
Leptons	$\mu$ channel: see ○-lepton triggers 1 WH-signal lepton
$\vec{E}_T^{\text{miss}}$	$> 1$ VH-loose lepton veto
$m_{top}$	$> 30$ GeV ( $e$ channel)
$m_T^W$ (cut-based only)	$< 225$ GeV or $m_{bb} > 75$ GeV
$p_T^V$ regions (BDT)	$< 120$ GeV
$p_T^V$ regions (cut-based)	$> 150$ GeV $[150, 200]$ GeV, $[200, \infty]$ GeV
2 Lepton	
Trigger	un-prescaled single lepton Tables 5 and 6 of Ref. [31]
Leptons	2 VH-loose leptons ( $\geq 1$ ZH-signal lepton)
$m_{\ell\ell}$	Same flavor, opposite-charge for $\mu\mu$ $81 < m_{\ell\ell} < 101$ GeV
$\vec{E}_T^{\text{miss}}$ significance (cut-based)	$\vec{E}_T^{\text{miss}}/\sqrt{H_T} < 3.5\sqrt{\text{GeV}}$
$p_T^V$ regions (BDT)	$[75, 150], [150, \infty]$ GeV
$p_T^V$ regions (cut-based)	$[75, 150], [150, 200], [200, \infty]$ GeV

**Table 9.1:** Summary of the signal event selection in the 0-, 1- and 2-lepton analyses.

1924 nels, with the major difference being the selection of input variables to the BDT discriminants. For  
1925 a discussion of how the different final states affect variable selection see the discussion in Section 1.7  
1926 and in particular Table for the input variables used in the final analysis.

1927 As previously mentioned, the fit model is flexible enough to seamlessly integrate combined results  
1928 for the three separate lepton channels for a given dataset. Most nuisance parameters are treated as  
1929 common across all fit regions. Some regions will have greater bearing on certain nuisance parameters—  
1930 2-lepton regions, virtually free of  $W+jets$  events, will have virtually no effect on  $W+jets$  modeling  
1931 systematics, for example. One notable exception are NP's with `_L[012]` suffixes, which are pre-  
1932 dominantly the double ratio systematics discussed in Section 4.2.2 and function similar to the 2 vs.  
1933 greater than 3 jet event double ratio systematics.

1934 Adding different channels has great potential to constrain certain systematic uncertainties. Look-  
1935 ing at the breakdown of systematic uncertainties in 2-lepton fits in Table 7.8, for example, multijet  
1936 and  $W+jets$  NP's contribute virtually no uncertainty, while  $\vec{E}_T^{\text{miss}}$  and  $Z+jets$  have very high impacts  
1937 on the uncertainty on  $\hat{\mu}$ . 1-lepton events will bring up the multijet and  $W+jets$  uncertainties (and  
1938 justify their inclusion in the combined fit model; their inclusion in the 2-lepton fit is for portabil-  
1939 ity and a sanity check). Since the 2-lepton final state is by construction  $\vec{E}_T^{\text{miss}}$  free, it is not surpris-  
1940 ing that uncertainty due to  $\vec{E}_T^{\text{miss}}$  is high. Single channel standalone fits are never final results in this  
1941 analysis, so the result relies on the other channels to better and more accurately constrain this uncer-  
1942 tainty since these other final states do have  $\vec{E}_T^{\text{miss}}$  in their final states and are the channels for which  
1943 the  $\vec{E}_T^{\text{miss}}$  treatment in the analysis has been optimized. Furthermore, something like  $Z+hf$  modeling  
1944 is difficult to do given how constrained the analysis signal region is. Combining the information in

<sup>1945</sup> the 0- and 2-lepton results (and introducing double ratio NP's to recognize that these channels do  
<sup>1946</sup> have important differences) also helps to constrain this difficult systematic uncertainty.

Once the fit inputs in each channel have been prepared and validated, a combined workspace can be directly constructed using the combined fit model. Significances are given in Table 9.2, and  $\hat{\mu}$  summaries for 2 and 3 POI fits are given in Figure 9.1. This combined workspace with observed signal strength of  $1.20^{+0.24}_{-0.23}(\text{stat.})^{+0.34}_{-0.28}(\text{syst.})$  is the Run 2 input for the Run 1 + Run 2 combination discussed below.

Channel	Exp. sig. (Asimov)	Exp. sig. (data)	Obs. sig.
0-lepton (SR)	1.99	1.73	0.53
1-lepton (SR+CR)	1.81	1.81	2.30
2-lepton (SR+CR)	1.95	1.86	3.55
0,1,2-lepton (SR+CR)	3.19	3.03	3.54

**Table 9.2:** Observed significance from an unconditional fit to the data corresponding to  $36.1 \text{ fb}^{-1}$  and expected significances from a fit to an Asimov dataset and from a fit to the data. Expected significances from individual regions are estimated separately.

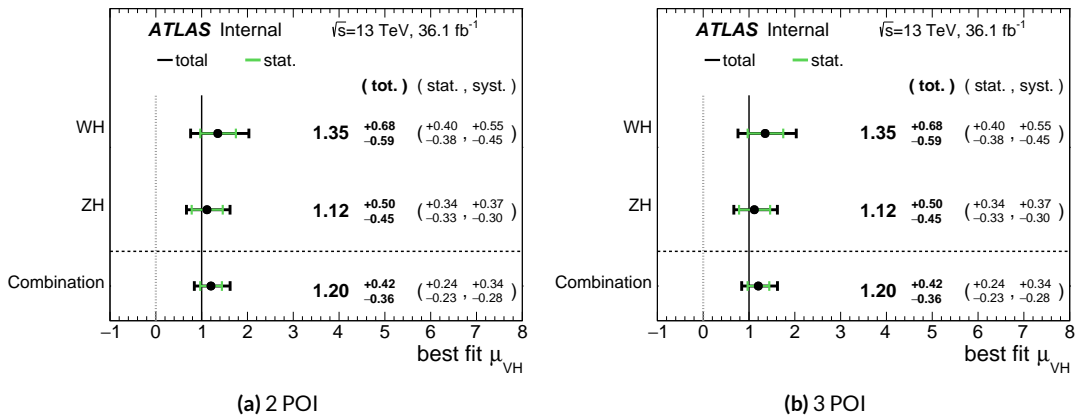


**Figure 9.1:** Run 2 signal strength summary plots for 2 (WH/ZH, (a)) and 3 (0, 1, and 2 lepton, (b)) POI fits.

1952 9.2 THE COMBINED FIT MODEL

1953 It is clear the signal strength parameter of interest should be fully correlated among the different  
1954 datasets. Some signal modeling systematics were left unchanged from Run 1 through Run 2 and/or  
1955 were designed to be explicitly correlated. Beyond these two special cases, it is not immediately clear  
1956 what level of correlation should be imposed. The general methodology for settling upon a correla-  
1957 tion scheme is as follows:

- 1958 1. Identify which NP categories have significant impacts on  $\mu$
- 1959 2. Of these NP's, identify which have one-to-one correspondences or established correlation  
1960 schemes among  $\sqrt{s}$  values
- 1961 3. Test whether correlation has a sizeable impact on expected fit quantities

1962 The only two sizeable experimental NP categories are jet energy scale (JES) and flavor tagging sys-  
1963 tematics. Correlation schemes of varying degrees of completeness exist for these categories, so ex-  
1964 plicit NP correlations can be tested for these two categories. As these studies were conducted before  
1965 unblinding, "sizeable impact" was judged by comparing fit results (sensitivities, pull comparisons,  
1966 and breakdowns) on combined workspaces using the unblinded and public  $\mu = 0.51$  result for  
1967 Run 1 and Asimov data for the Run 2 result. These are treated in Sections 9.2.1 and 9.2.2. Modeling  
1968 systematics require a slightly different treatment, and are explored in 9.2.3.

1969 As noted in Chapter 7 when looking at pull comparison plots for combined workspaces, the error  
1970 bars in these plots are calculated using a simultaneous HESSE matrix inversion, which can fail to give  
1971 sensible values for high dimensional models (the combined workspaces have well over 500 NP's).  
1972 This is not true of the nuisance parameter ranking plots, which use a MINOS based approach to test

<sup>1973</sup> the effect of each NP individually. This is much slower but much more rigorous, which is why only  
<sup>1974</sup> ranking plots appear outside of supporting material and pull comparisons are considered “diagnos-  
<sup>1975</sup> tic” plots.

### <sup>1976</sup> 9.2.1 JET ENERGY SCALE SYSTEMATICS

<sup>1977</sup> Fortunately for the case of jet energy scale systematics, the JetEtMiss group provides two recom-  
<sup>1978</sup> mended “strong” and “weak” correlation schemes between Run 1 and Run 2. These were used as  
<sup>1979</sup> a point of departure for the JES combination correlation scheme. However, the JES NP’s in both  
<sup>1980</sup> the Run 1 and Run 2 workspaces are a reduced set of NP’s, with some 56 (75) NP’s reduced to 6 (8)  
<sup>1981</sup> for Run 1 (2). In order to restore the full set of JES NP’s, the effective NP’s in each workspace are un-  
<sup>1982</sup> folded using maps detailing the linear combinations of unfolded NP’s that form the effective NP’s.

<sup>1983</sup> The linear combinations used to unfold the effective JES NP’s were calculated as follows:

$$NP_{i,eff} = \frac{\sum_j A_{ij} |NP_{j,unf}| NP_{j,unf}}{\sqrt{\sum_j A_{ij}^2 |NP_{j,unf}|^2}} \quad (9.1)$$

<sup>1984</sup> where *eff* and *unf* are for effective and unfolded NP’s, respectively, the  $A_{ij}$ ’s are scalar coefficients  
<sup>1985</sup> taken from raw maps, and  $|NP_{j,unf}|$  are the amplitudes of the unfolded NP’s. The raw  $A_{ij}$  and scaled  
<sup>1986</sup> maps for Run 1 and Run 2 may be found in Figure 9.2

<sup>1987</sup> Unfolding was found to have very little effect on both expected sensitivities and errors, as can be  
<sup>1988</sup> seen in Tables 9.3–9.6.

<sup>1989</sup> It was also found that fit sensitivities and breakdowns were similarly indifferent to the use of ei-

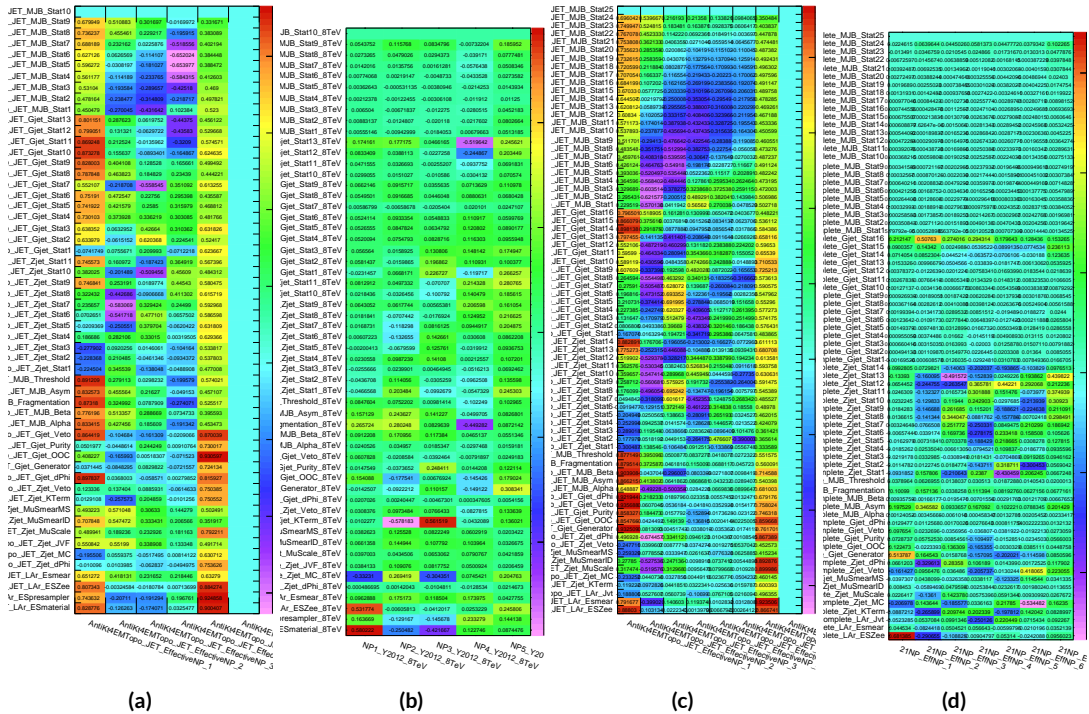


**Figure 9.2:** The raw and scaled coefficients for unfolding Run 1 (a and b) and Run 2 (c and d), respectively

	R <sub>1</sub> Unfold	R <sub>1</sub> Eff	R <sub>2</sub> Unfold	R <sub>2</sub> Eff	Comb Unfold	Comb Eff
Exp. Sig.	2.604	2.606	3.014	3.014	4.005	3.998
Obs. Sig.	1.369	1.374	3.53	3.53	3.581	3.571
Exp. Limit	0.755 <sup>+0.296</sup> <sub>-0.211</sub>	0.755 <sup>+0.296</sup> <sub>-0.211</sub>	0.732 <sup>+0.287</sup> <sub>-0.205</sub>	0.732 <sup>+0.287</sup> <sub>-0.205</sub>	0.512 <sup>+0.201</sup> <sub>-0.143</sub>	0.51 <sup>+0.2</sup> <sub>-0.143</sub>
Obs. Limit	1.21	1.21	1.94	1.94	1.36	1.37

**Table 9.3:** Expected and observed sensitivities for Run 1, Run 2, and combined workspaces with effective and unfolded JES NP's.

	R <sub>1</sub> Unfold	R <sub>1</sub> Eff
$ \Delta\hat{\mu} $		0.0018
$\hat{\mu}$	0.5064	0.5082
Total	+0.400 / -0.373	+0.401 / -0.373
DataStat	+0.312 / -0.301	+0.312 / -0.301
FullSyst	+0.250 / -0.220	+0.251 / -0.220
Jets	+0.060 / -0.051	+0.060 / -0.052
BTag	+0.094 / -0.079	+0.095 / -0.079

**Table 9.4:** Error on signal strength breakdowns for Run 1 workspaces with effective and unfolded JES NP's.

	R <sub>2</sub> Unfold	R <sub>2</sub> Eff
$ \Delta\hat{\mu} $		0.0
$\hat{\mu}$	1.2051	1.2052
Total	+0.421 / -0.366	+0.421 / -0.366
DataStat	+0.239 / -0.234	+0.239 / -0.234
FullSyst	+0.346 / -0.282	+0.346 / -0.282
Jets	+0.066 / -0.047	+0.066 / -0.047
BTag	+0.119 / -0.106	+0.119 / -0.106

**Table 9.5:** Error on signal strength breakdowns for Run 2 workspaces with effective and unfolded JES NP's.

	Comb Unfold	Comb Eff
$ \Delta\hat{\mu} $		0.0006
$\hat{\mu}$	0.8992	0.8985
Total	+0.278 / -0.261	+0.278 / -0.261
DataStat	+0.185 / -0.181	+0.185 / -0.181
FullSyst	+0.208 / -0.187	+0.208 / -0.188
Jets	+0.040 / -0.044	+0.041 / -0.036
BTag	+0.076 / -0.076	+0.077 / -0.076

**Table 9.6:** Error on signal strength breakdowns for combined workspaces with effective and unfolded JES NP's.

<sup>1990</sup> ther the strong or weak JES correlation schemes, as shown in Tables 9.7 and 9.8.

	JES Weak Unfold	JES Weak Eff	JES Strong Unfold	JES Strong Eff
Exp. Sig.	3.57	3.57	3.59	3.59
Exp. Limit	$0.493^{+0.193}_{-0.138}$	$0.494^{+0.193}_{-0.138}$	$0.493^{+0.193}_{-0.138}$	$0.493^{+0.193}_{-0.138}$

**Table 9.7:** Expected sensitivities for both effective and unfolded combined workspaces using the strong and weak JES correlation schemes.

	Comb Unfold	Comb Eff	Strong Unfold	Strong Eff
$\Delta\hat{\mu}$	0.0009		0.0025	
Total	+0.269 -0.254	+0.27 -0.255	+0.27 -0.255	+0.27 -0.255
DataStat	+0.181 -0.177	+0.181 -0.177	+0.181 -0.177	+0.181 -0.178
FullSyst	+0.199 -0.183	+0.2 -0.183	+0.2 -0.183	+0.201 -0.183
Jets	+0.0387 -0.032	+0.041 -0.0337	+0.0425 -0.0329	+0.0432 -0.0338
BTag	+0.0975 -0.0933	+0.098 -0.0936	+0.0979 -0.0935	+0.098 -0.0936

**Table 9.8:** Error on signal strength breakdowns for both effective and unfolded combined workspaces using the strong and weak JES correlation schemes.

<sup>1991</sup> Comparisons of top ranked nuisance parameters in Figures 9.3–9.5 and for the complete JES pull  
<sup>1992</sup> comparisons in Figures 9.6–9.9 also show very little difference with respect to correlation scheme  
<sup>1993</sup> (except obviously for the number of JES NP’s). Constrained pulls in pull comparisons should once  
<sup>1994</sup> again be taken as a shortcoming of HESSE and not the fit model.

<sup>1995</sup> As a result of these studies, the weak JES correlation scheme with uncorrelated effective JES NP’s  
<sup>1996</sup> (i.e. just the  $b$ -jet energy scale NP) has been chosen as the treatment of JES in the Run 1 + Run 2  
<sup>1997</sup> combined fit.

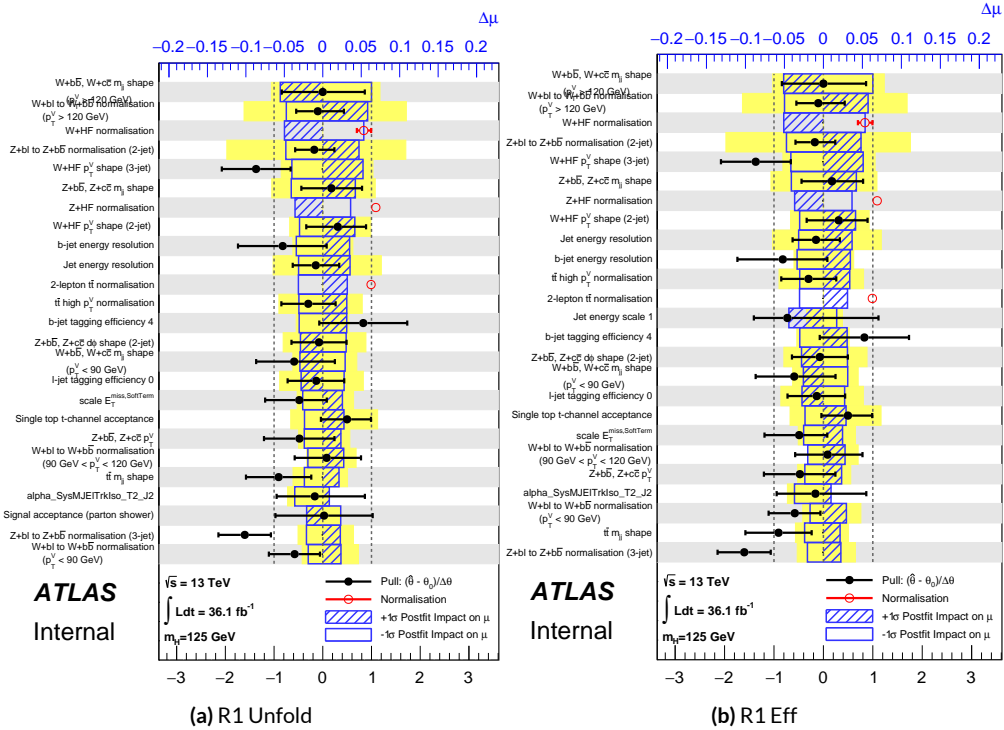


Figure 9.3: Ranks for the effective and unfolded JES NP Run1 combined workspaces.

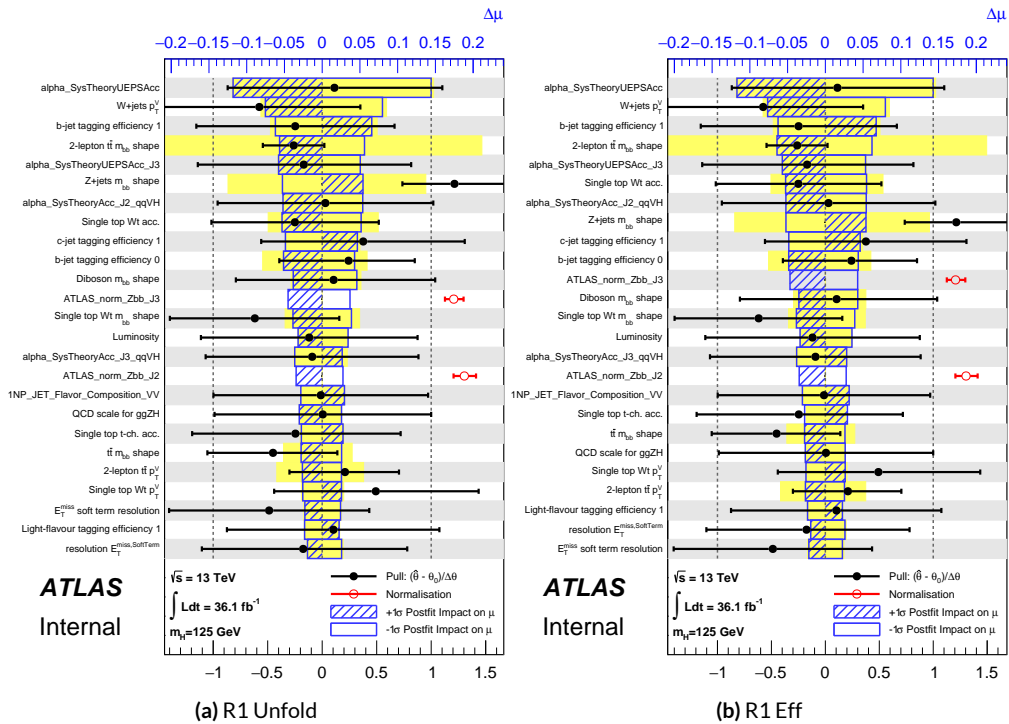


Figure 9.4: Ranks for the effective and unfolded JES NP Run2 combined workspaces.

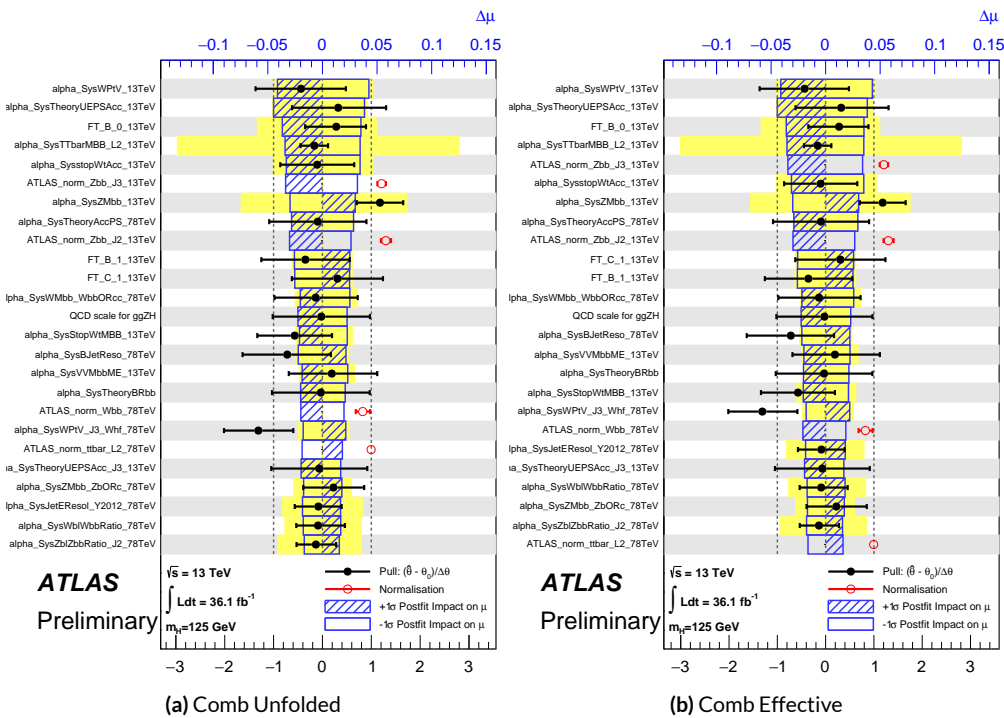


Figure 9.5: Ranks for the effective and unfolded JES NP Run1+Run2 combined workspaces.

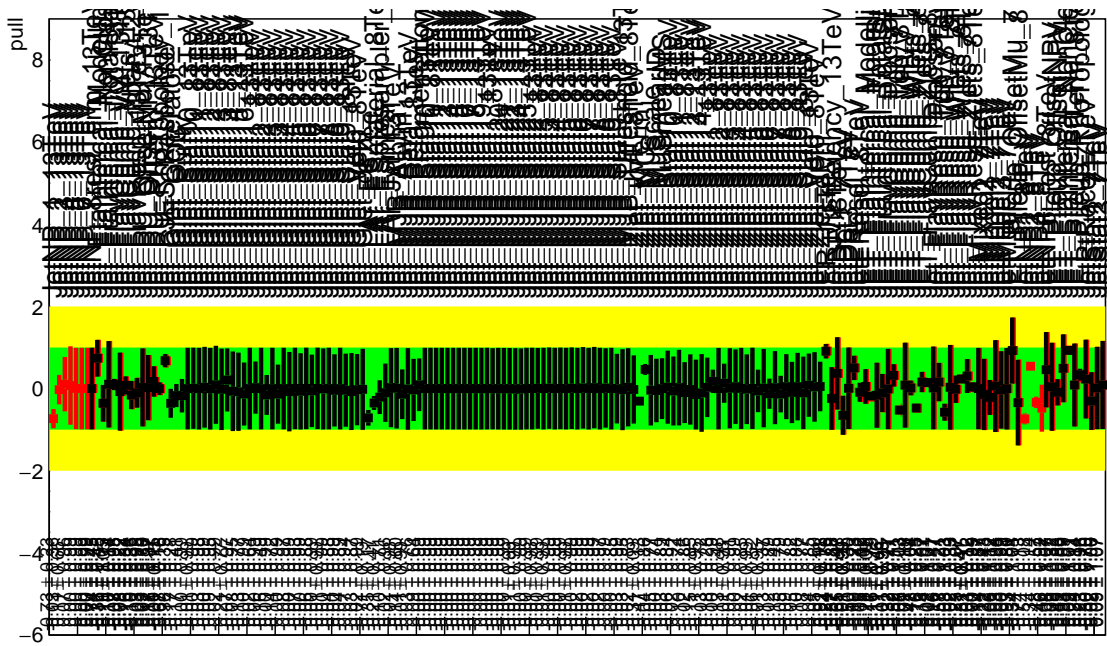


Figure 9.6: Pull Comparisons: jesu---Jet Comb Unfold, Comb Eff, Strong Unfold, Strong Eff

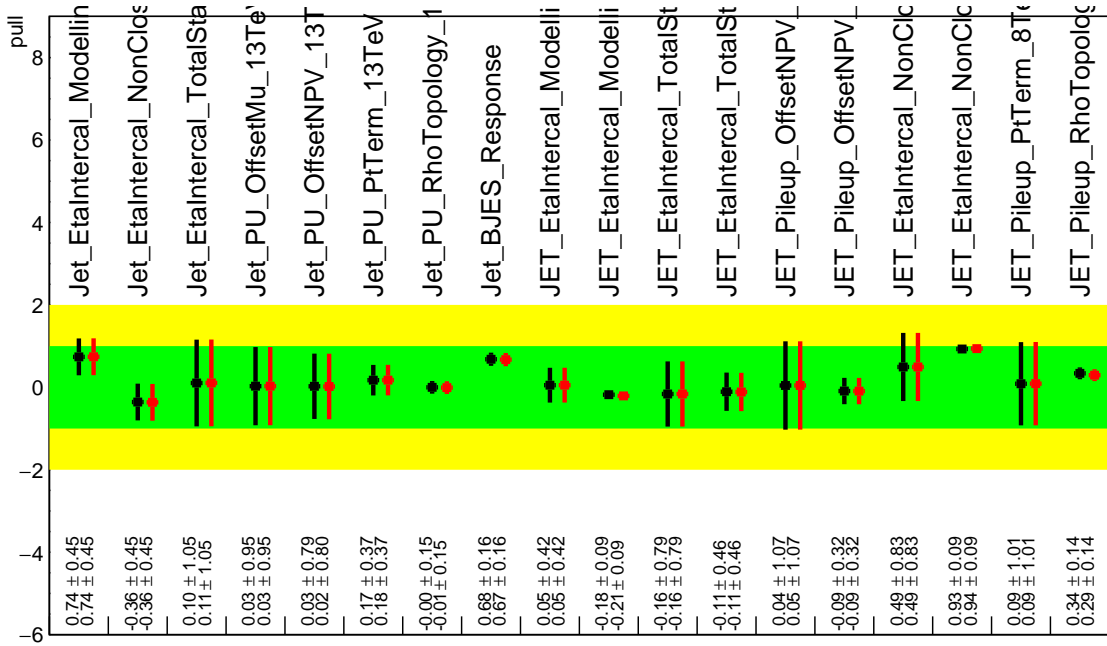


Figure 9.7: Pull Comparisons: jesu---JetMatched Comb Unfold, Comb Eff, Strong Unfold, Strong Eff

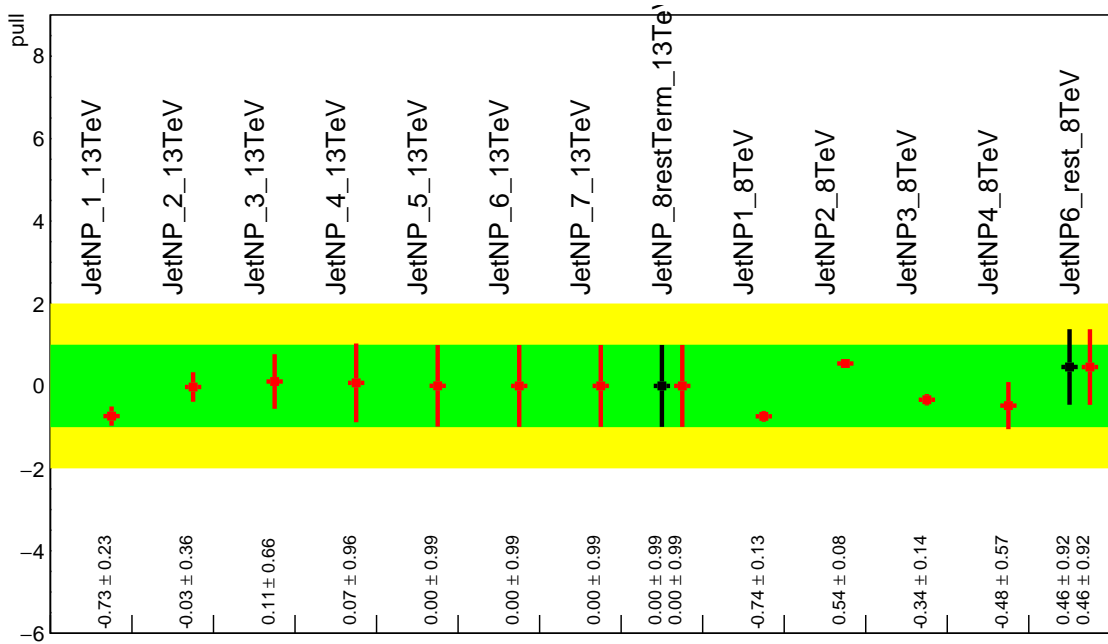


Figure 9.8: Pull Comparisons: jesu---JetEff Comb Unfold, Comb Eff, Strong Unfold, Strong Eff

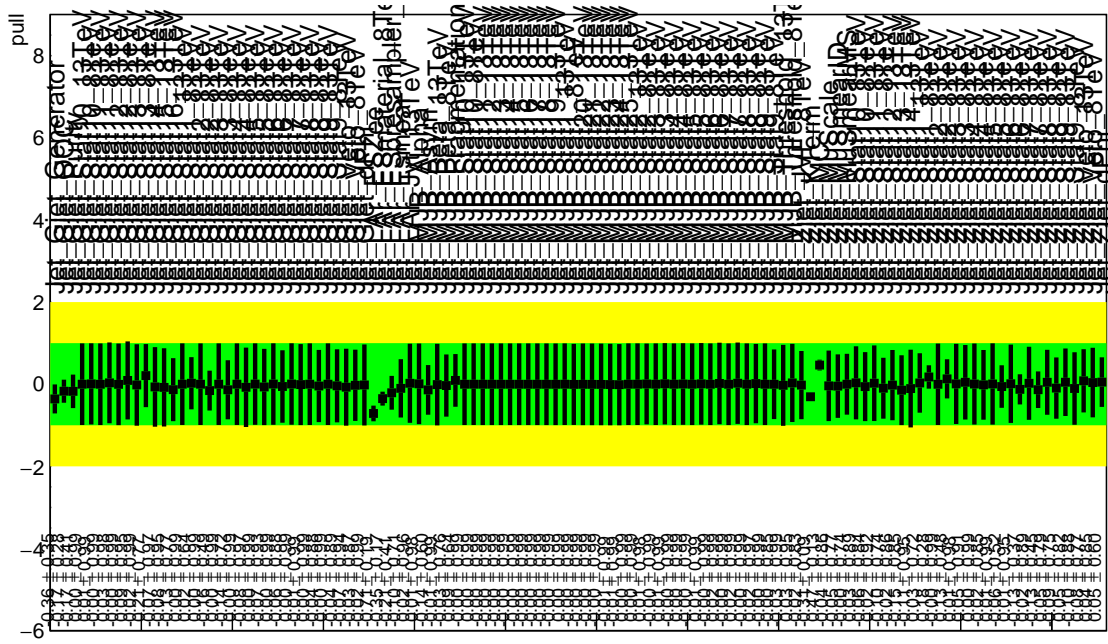


Figure 9.9: Pull Comparisons: jesu---JetUnfold Comb Unfold, Comb Eff, Strong Unfold, Strong Eff

1998    9.2.2    FLAVOR TAGGING

1999    Unfortunately, the ATLAS Flavor Tagging group did not provide any recommendations for corre-  
2000    lating Run 1 and Run 2 NP's, though given the high ranking of these NP's in the Run 2, result, per-  
2001    forming at least some studies was deemed crucial. Nevertheless, great improvements and changes to  
2002    the treatment of flavor tagging between Run 1 and Run 2 does weaken the argument for any strong  
2003    flavor tagging correlation scheme.

2004       Given that  $c$ -tagging changed significantly between Run 1 and Run 2 and that light tagging NP's  
2005    are very lowly ranked, these sets of NP's are left uncorrelated. Moreover, the change in the physical  
2006    meaning of the effective  $b$ -tagging NP's means a full correlation of such NP's (insomuch as they exist  
2007    in each result) is one of limited utility. Hence, it was decided to leave flavor tagging NP's uncorre-  
2008    lated. However, since the meaning of the leading  $b$ -tagging NP's is approximately constant across  
2009    years and since Run 2  $b$ -tagging NP's are very highly ranked in both the Run 2 only and combined  
2010    fits, tests correlating these NP's were conducted, the results of which can be seen below. It should be  
2011    noted that the leading B NP at 8 TeV, SysBTagB0Effic\_Y2012\_8TeV, has an opposite effect on  $t\bar{t}$   
2012    normalization than the 7 and 13 TeV NP's, and so must be flipped using a similar strategy as for JES  
2013    unfolding. Initial studies of flavor tagging correlations did not flip this NP, and so results for this  
2014    scheme (labeled "Bo 8TeV Not Flipped") have also been included for comparison.

2015       It is clear from these results that correlating the leading effective Eigen NP associated with  $b$ 's can  
2016    have a noticeable effect on final fit results and that the 8 TeV Bo NP is the most important compo-  
2017    nent of a combined Bo NP. It is also not so surprising that the 8 TeV result should drive the com-

	Comb Eff	BTag Bo	Bo 8TeV Not Flipped
Exp. Sig.	3.998	4.127	3.921
Obs. Sig.	3.571	3.859	3.418
Exp. Limit	0.51 <sup>+0.2</sup> <sub>-0.143</sub>	0.5 <sup>+0.196</sup> <sub>-0.14</sub>	0.517 <sup>+0.202</sup> <sub>-0.144</sub>
Obs. Limit	1.37	1.41	1.35

**Table 9.9:** Expected and observed sensitivities for a combination featuring the weak JES scheme, combination with the weak JES scheme + leading  $b$  NP's correlated, and the  $b$  correlation with the 8 TeV NP with sign unflipped.

	Comb Eff	BTag Bo	Bo 8TeV Not Flipped
$ \Delta\hat{\mu} $	—	0.0446	0.0268
$\hat{\mu}$	0.8985	0.9431	0.8717
Total	+0.278 / -0.261	+0.275 / -0.256	+0.282 / -0.263
DataStat	+0.185 / -0.181	+0.180 / -0.177	+0.189 / -0.186
FullSyst	+0.208 / -0.188	+0.207 / -0.186	+0.209 / -0.186
BTag	+0.077 / -0.076	+0.071 / -0.068	+0.079 / -0.075
BTag b	+0.062 / -0.059	+0.055 / -0.049	+0.064 / -0.060

**Table 9.10:** Breakdowns of the impact of different NP sets on total error on  $\hat{m}\hat{\mu}$  for a combination featuring the weak JES scheme and a combination with the weak JES scheme + leading  $b$  NP's correlated.

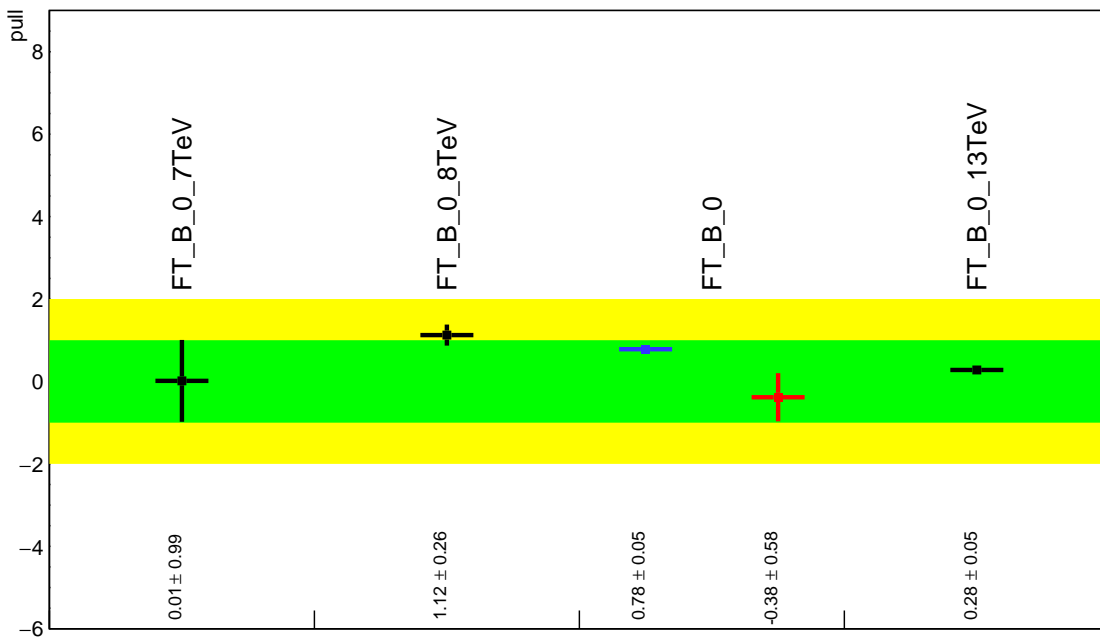


Figure 9.10: Pull Comparisons: btag-b---BTagB0 Comb Eff, BTag BO

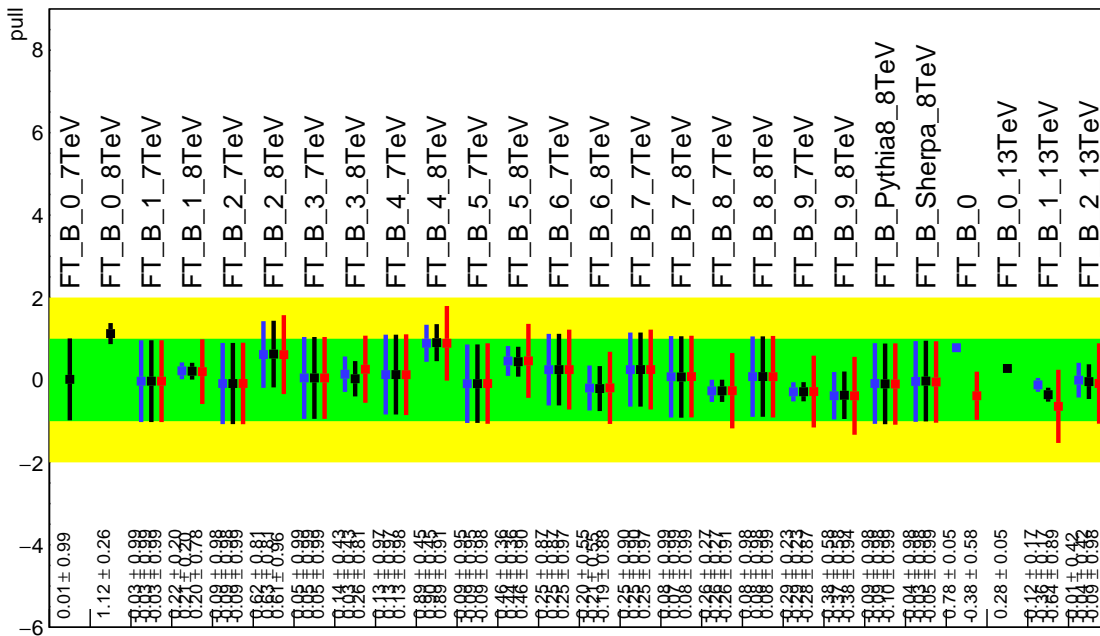
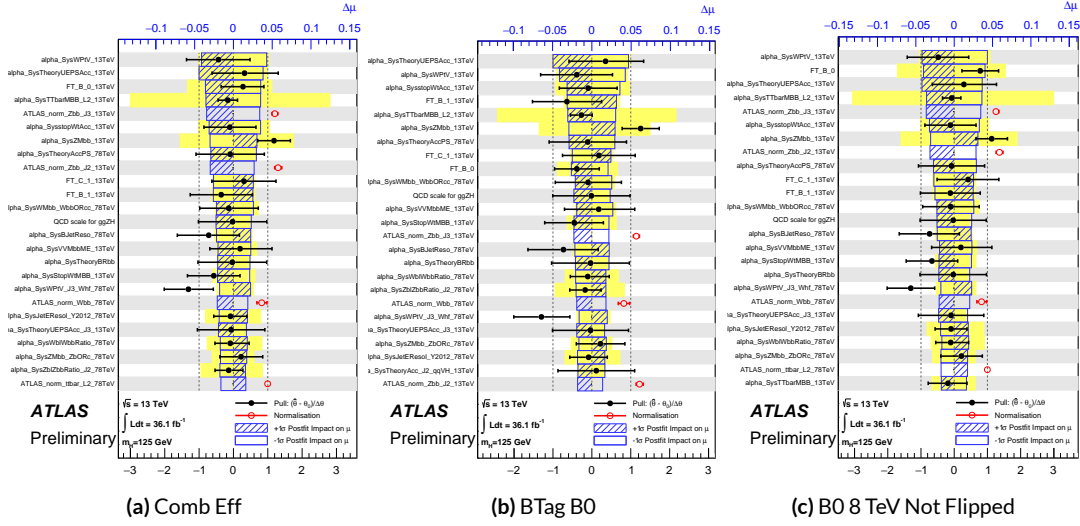


Figure 9.11: Pull Comparisons: btag-b---BTagB Comb Eff, BTag BO



**Figure 9.12:** NP rankings for a combination featuring the weak JES scheme and a combination with the weak JES scheme + leading  $b$  NP's correlated.

2018 bined nuisance parameter since it is the only result to make use of both pseudocontinuous tagging-  
 2019 based and 1  $b$ -tag regions into the final fit, implicitly yielding much more information about  $b$ 's. The  
 2020 13 TeV fit has neither of these regions. What is less clear is whether there are sufficient grounds for  
 2021 implementing this correlation (i.e. does the correspondence of these NP's across years warrant a full  
 2022 correlation). While there are no current plans to do so, this matter warrants careful scrutiny if Run 1  
 2023 is to be combined with future results.

### 2024 9.2.3 MODELING SYSTEMATICS

2025 Another principal systematic category is modeling uncertainties. The effect of correlating groups  
 2026 of systematics was estimated using the same strategy employed by the ATLAS/CMS SM  $VH$  ( $b\bar{b}$ )  
 2027 combination for Run 1. This extrapolation can be used to estimate the impact of correlations on  
 2028 the estimated signal strength, the total error on the signal strength, and the  $\chi^2$  of the result. The

2029 impact of such correlations is no more than a few percent effect, as the following tables demonstrate,  
 2030 beginning with the category with the greatest shift, W+jets modeling, in Table 9.11.

	$ \Delta\mu $	$\sigma$	$ \Delta\sigma $	$\chi^2$
$\rho=-1$	0.0024	0.2448	0.011 (4.3%)	0.95
$\rho=-0.6$	0.0015	0.2493	0.00654 (2.55%)	0.9804
$\rho=-0.3$	0.0008	0.2526	0.00325 (1.27%)	1.0045
$\rho=0$	—	0.2558	—	1.0298
$\rho=0.3$	0.0008	0.259	0.0032 (1.25%)	1.0564
$\rho=0.6$	0.0017	0.2622	0.00636 (2.49%)	1.0844
$\rho=1$	0.0029	0.2664	0.0105 (4.11%)	1.1242

**Table 9.11:** Run 1 + Run 2 W+jets modeling correlation projections

#### 2031 9.2.4 FINAL CORRELATION SCHEME

2032 The final Run 1 + Run 2 correlation scheme is shown in Table 9.12. As detailed above, neither JES  
 2033 nor modeling systematics had any demonstrable effect on combined fit results. Hence, only signal  
 2034 NP's and the  $b$ -jet energy scale are correlated (the weak JES scheme without unfolding). While the  
 2035 effect of flavor tagging correlations is less clear, the result physical arguments for correlation are less  
 2036 strong; the size of effect was discovered rather late in the analysis process; and no nuisance parameter  
 2037 unfolding maps exist for flavor tagging as they do for JES, so it was decided to leave these uncorre-  
 2038 lated as well.

7 TeV NP	8 TeV NP	13 TeV NP
	ATLAS_BR_bb	SysTheoryBRbb
	SysTheoryQCDscale_ggZH	SysTheoryQCDscale_ggZH
	SysTheoryQCDscale_qqVH	SysTheoryQCDscale_qqVH
—	SysTheoryPDF_ggZH_8TeV	SysTheoryPDF_ggZH
—	SysTheoryPDF_qqVH_8TeV	SysTheoryPDF_qqVH
—	SysTheoryVHPt_8TeV	SysVHNLOEWK
SysJetFlavB_7TeV	SysJetFlavB_8TeV	SysJET_21NP_JET_BJES_Response

**Table 9.12:** A summary of correlated nuisance parameters among the 7, 8, and 13 TeV datasets.

2039 **9.3 COMBINED FIT RESULTS**

2040 **9.3.1 COMBINED FIT MODEL VALIDATION**

2041 Before moving onto the final results, we present the rest of the validation for the Run 1 + Run 2  
 2042 combined fits, beginning with impacts of ranked individual nuisance parameters in Figure 9.13 and  
 2043 for all nuisance parameter categories in Table 9.13. Both of these sets of results point to the most im-  
 2044 portant nuisance parameters being signal systematics,  $b$ -tagging, and  $V$ +jets modeling systematics,  
 2045 with Run 2 NP's generally being higher ranked. That some NP's are strongly pulled is not unusual  
 2046 as the fit model has so many NP's;  $V$ +jets modeling in particular has been historically difficult.

2047 In addition to looking at the behaviors of nuisance parameters to gauge fit model performance  
 2048 and stability, fits are conducted using multiple parameters of interest. Typical divisions are Run 1  
 2049 vs. Run 2, lepton channels, and  $WH$  vs  $ZH$ . As mentioned in Chapter 7, the profile likelihood test  
 2050 statistic given in Equation 7.2 is, in the limit of large sample statistics, a  $\chi^2$  distribution with degrees  
 2051 of freedom equal to the number of parameters of interest plus number of nuisance parameters.  
 2052 Thus, changing the number of interest parameters and leaving the rest of the fit model unchanged

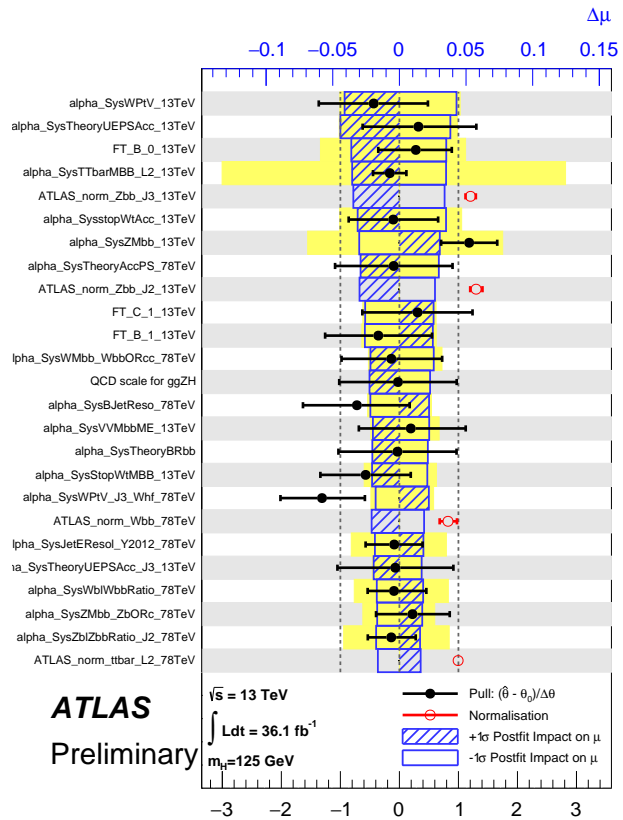


Figure 9.13: Ranked nuisance parameters for the Run1+Run2 combination.

Total	+0.278 / -0.261
DataStat	+0.185 / -0.181
FullSyst	+0.208 / -0.188
Floating normalizations	+0.055 / -0.056
All normalizations	+0.068 / -0.069
All but normalizations	+0.192 / -0.172
Jets, MET	+0.046 / -0.040
Jets	+0.041 / -0.036
MET	+0.023 / -0.018
BTag	+0.077 / -0.076
BTag b	+0.062 / -0.059
BTag c	+0.033 / -0.032
BTag light	+0.028 / -0.028
Leptons	+0.008 / -0.008
Luminosity	+0.026 / -0.014
Diboson	+0.030 / -0.027
Model Zjets	+0.049 / -0.050
Zjets flt. norm.	+0.032 / -0.040
Model Wjets	+0.082 / -0.083
Wjets flt. norm.	+0.031 / -0.027
Model ttbar	+0.047 / -0.046
ttbar flt. norm.	+0.025 / -0.026
Model Single Top	+0.047 / -0.045
Model Multi Jet	+0.027 / -0.038
Signal Systematics	+0.098 / -0.052
MC stat	+0.080 / -0.084

**Table 9.13:** Summary of the impact of different nuisance parameter categories on the total error on  $\hat{\mu}$  for the combined Run1+Run2 fit.

means that the difference between the nominal fit and a fit with more parameters of interest ought  
 to also be distributed as a  $\chi^2$  distribution with degrees of freedom equivalent to the number of extra  
 parameters of interest. This difference can then be interpreted as a compatibility between the two  
 results using the standard tables for this distribution, giving another gauge of fit performance. These  
 are shown in Table 9.14.

Fit	Compatibility
Leptons (3 POI)	1.49%
$WH/ZH$ (2 POI)	34.2%
Run 1/Run 2 (2 POI)	20.8%
Run 1/Run 2 $\times$ Leptons (6 POI)	7.10%
Run 1/Run 2 $\times$ $WH/ZH$ (4 POI)	34.6%

**Table 9.14:** Summary of multiple POI compatabilities. The well-known Run 1 7 TeV 0-lepton deficit is responsible for the low compatibility with the 6 and 3 POI fits.

The low compatabilities associated with treating the lepton channels as separate parameters of  
 interest are a symptom of the low signal strengths associated with the Run 1 0-lepton channel, in par-  
 ticular the 7 TeV result. Given the relatively small amount of data associated with the 7 TeV result,  
 this should not be a cause for alarm. Signal strength summary plots for the fits treating Run 1 and  
 Run 2 separately are shown in Figures 9.14-9.16, where the effect of the Run 1 parameters can be seen  
 graphically.

### 9.3.2 FINAL RESULTS

The combined results yields an observed (expected) significance of 3.57 (4.00) and an observed (ex-  
 pected) limit of 1.37 ( $0.510^{+0.200}_{-0.143}$ ), with a signal strength of  $\hat{\mu} = 0.898^{+0.278}_{-0.261}$ .

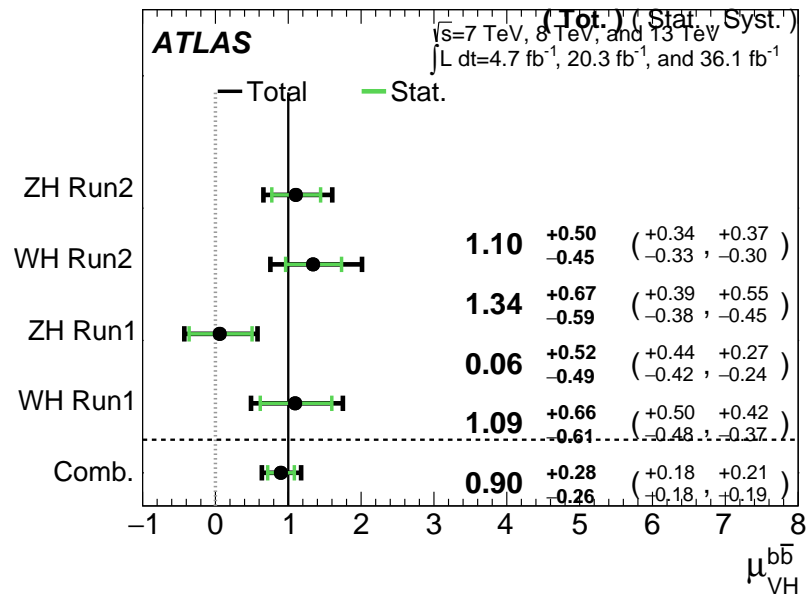


Figure 9.14:  $\hat{\mu}$  summary plot for a four parameter of interest fit.

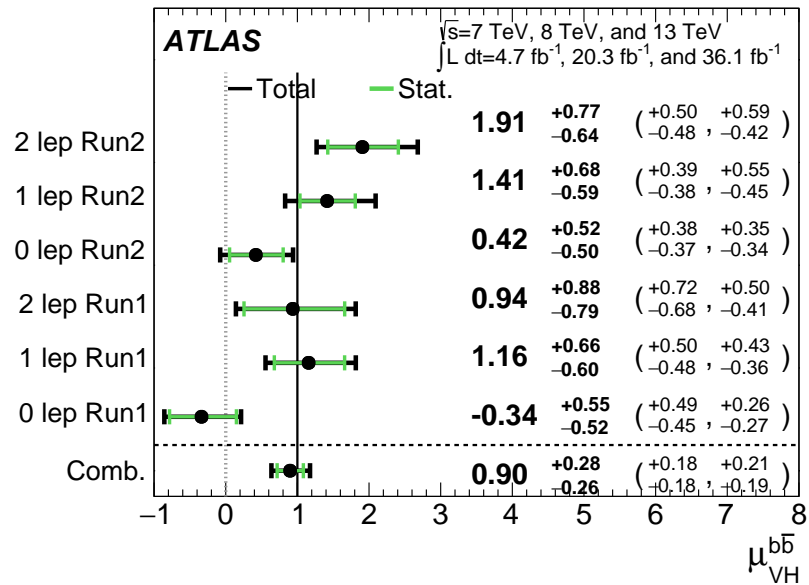
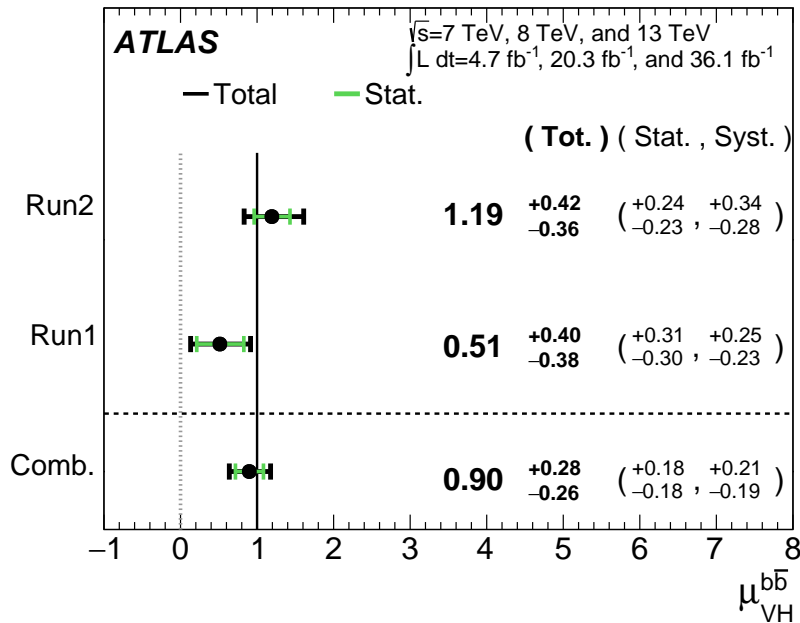


Figure 9.15:  $\hat{\mu}$  summary plot for a six parameter of interest fit.



**Figure 9.16:**  $\hat{\mu}$  summary plot for a two parameter of interest (Run 1 and Run 2) values.

The two and three parameter of interest fit signal strength summary plots, as well as a summary  
2067 of the historical values of the 7, 8, and 13 TeV results may be found in Figures 9.17-9.19. The main  
2068 results for Run 1, Run 2, and the combination may be found in Table 9.15. These results were collec-  
2069 tively noted as the first ever experimental evidence for SM  $VH(b\bar{b})$  in [42].

Dataset	$\hat{\mu}$	Total Error in $\hat{\mu}$	Obs. (Exp.) Significance
Run 1	0.51	+0.40 / -0.37	1.4 (2.6)
Run 2	1.20	+0.42 / -0.36	3.54 (3.03)
Combined	0.90	+0.28 / -0.26	3.57 (4.00)

**Table 9.15:** A summary of main results for the Run 1, Run 2, and combined fits.

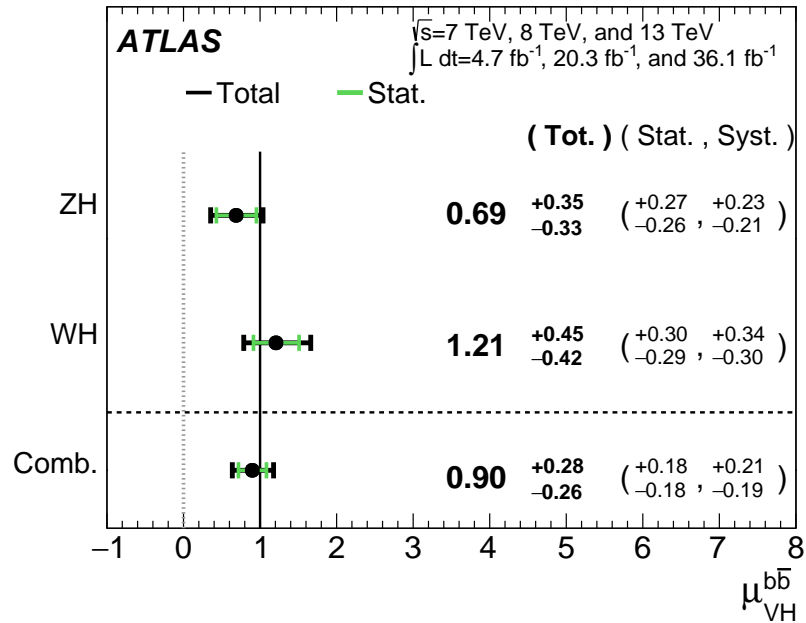


Figure 9.17:  $\hat{\mu}$  summary plot for a two parameter of interest fit.

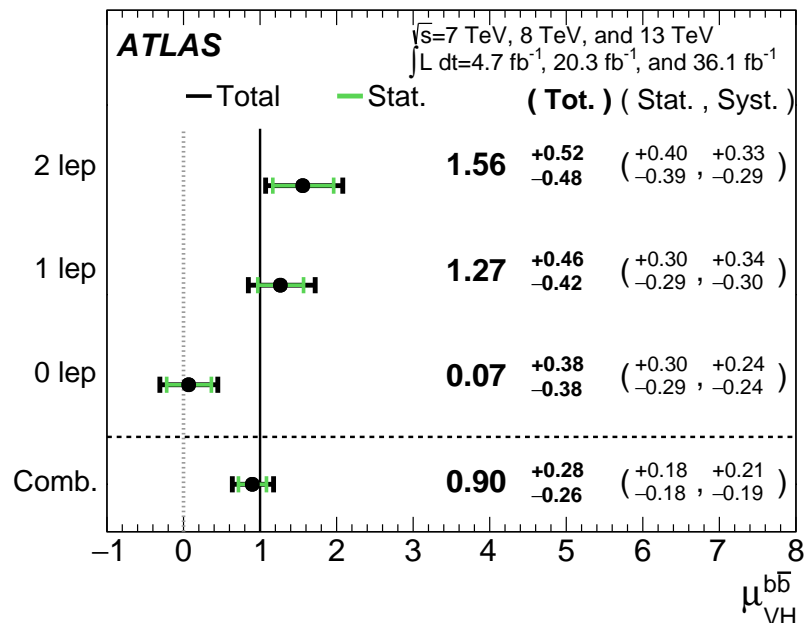


Figure 9.18:  $\hat{\mu}$  summary plot for a three parameter of interest fit.

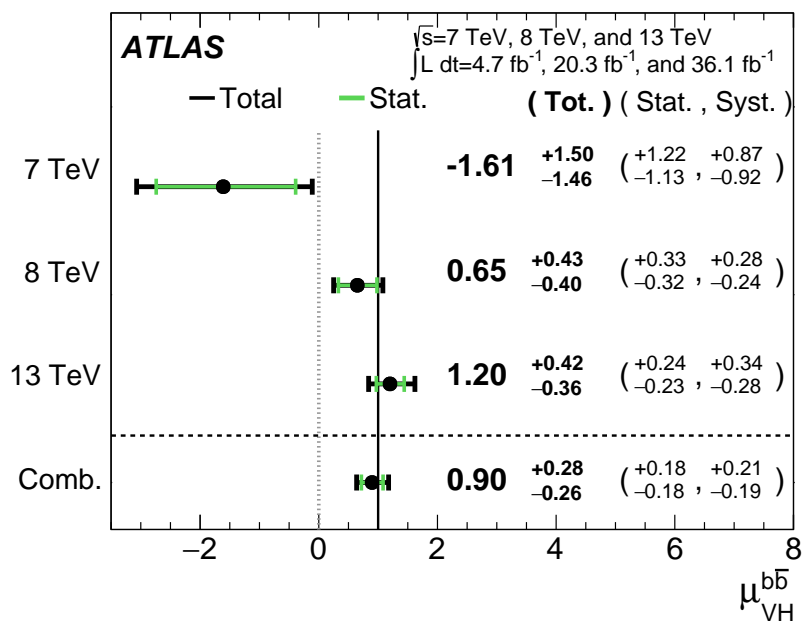


Figure 9.19:  $\hat{\mu}$  summary plot for different  $\sqrt{s}$  values.

*Vanitas vanitatum, omnis vanitas*

Ecclesiastes 1:2

# 10

2071

2072

## Closing Thoughts

2073 SINCE BOTH THE LHC and ATLAS are performing very well, it is only a matter of time before the

2074 evidence for SM  $VH(b\bar{b})$  passes the 5 Gaussian standard deviation threshold necessary for discovery.

2075 Official discovery may come less than a year after reports of first evidence and may not even require

2076 a combination with the Run 1 result, depending on the latter two years of ATLAS Run 2 data (2017

2077 and 2018).

2078 It is entirely natural to ask, then, how essential the techniques and results described in this thesis  
2079 will prove to be moving forward. Neither the LI/RF multivariate techniques nor combination with  
2080 Run 1 datasets and their accompanying low signal strength values are necessary for discovery, and  
2081 the latter may not even be essential to timely<sup>\*</sup> discovery of SM  $VH(b\bar{b})$ . Nevertheless, both sets of  
2082 results hold great potential as key parts of a concerted ensemble of efforts towards precision Higgs  
2083 physics.

2084 With the perhaps final major center of mass energy increase at the energy frontier ever complete,  
2085 analyses must rely on increased integrated luminosity. Hence, it is becoming increasingly likely that  
2086 any new fundamental physics at colliders will require the use of results of systematics limited analy-  
2087 ses. This is the regime where the techniques described in this thesis will be most useful.

2088 As the LHC and its experiments undergo successive stages of upgrades and operate in evermore  
2089 extreme environments, the statistical fit models used to describe LHC data will continue to evolve in  
2090 complexity and diverge from their predecessors. The techniques described in Chapter 9 will become  
2091 increasingly more vital to producing the best physics results possible. The improvement in precision  
2092 from  $\hat{\mu}_{VH} = 1.20^{+0.24}_{-0.23}(\text{stat.})^{+0.34}_{-0.28}(\text{syst.})$  to  $\hat{\mu}_{VH} = 0.90^{+0.18}_{-0.18}(\text{stat.})^{+0.21}_{-0.19}(\text{syst.})$  is just the begin-  
2093 ning.

2094 The best methods for reduction of systematic uncertainties will naturally depend in part on the  
2095 state of the art for both fundamental physics process and detector modeling, but techniques that  
2096 can reduce systematic uncertainties independent of fit model, dataset, and physics process provide

---

\*i.e. before or coincident with CMS

2097 a promising avenue forward. The improvements in systematic uncertainties using the Lorentz In-  
 2098 variant and RestFrames variable techniques in the  $ZH \rightarrow \ell\ell b\bar{b}$  analysis, summarized in Table 10.1,  
 2099 show that a smarter and more orthogonal decomposition of information in a collision event pro-  
 2100 vides benefits independent of any clever treatment of  $\vec{E}_T^{\text{miss}}$  (which both schemes also provide). Both  
 2101 techniques are readily extendible to other analysis channels, with the RestFrames concept demon-  
 2102 strating stronger performance and greater flexibility to nearly completely generic final states.

	Standard	LI	RF
$\hat{\mu}$	$1.75^{+0.50, 0.64}_{-0.48, 0.45})$	$1.65^{+0.51, 0.59}_{-0.49, 0.41}$	$1.50^{+0.50, 0.53}_{-0.48, 0.36}$
Asi. $\Delta err(\mu)$	—	< 1%, +4.6%	-6.5%, -2.2%
Obs. $\Delta err(\hat{\mu})$	—	-7.5%, -3.7%	-16%, -8.8%
Stat only sig.	4.78	4.39 (-7.9%)	4.44 (-6.9%)
Exp. (Asi.) sig.	2.06	1.92 (-6.7%)	2.13 (+3.5%)
Exp. (data) sig.	1.76	1.73 (-1.7%)	1.80 (+3.4%)
Obs. (data) sig.	2.87	2.79 (-2.8%)	2.62 (-8.6%)

**Table 10.1:** Summary of performance figures for the standard, LI, and RF variable sets. Uncertainties on  $\hat{\mu}$  are quoted stat., syst. In the case of the latter two, % differences are given where relevant. Differences in errors on  $\mu$  are on full systematics and total error, respectively.

2103 Critical work remains to be done refining and extending the treatment of both the LI and RF  
 2104 techniques in  $VH(b\bar{b})$  analyses and their fit models, and completely independent techniques, like  
 2105 the use of multiple event interpretations addressed in Appendix B promise further improvements  
 2106 still.

2107 No one can say for certain what the future of the energy frontier of experimental particle physics  
 2108 may hold, but more nuanced treatments of the information in collision events born of meaningful  
 2109 physical insight are sure to light the way.

*If it's stupid but it works, it isn't stupid.*

Conventional Wisdom

A

2110

## 2111 Micromegas Trigger Processor Simulation

2112 IN ORDER TO PRESERVE key physics functionality by maintaining the ability to trigger on low  $p_T$   
2113 muons, the Phase I Upgrade to ATLAS includes a New Small Wheel (NSW) that will supply muon  
2114 track segments to the Level 1 trigger. These NSW trigger segments will combine segments from the  
2115 sTGC and Micromegas (MM) trigger processors (TP). This note will focus in particular on the al-

2116 gorithm for the MMTP, described in detail with initial studies in [41]. The goal of this note is to de-  
2117 scribe the MMTP algorithm performance under a variety of algorithm settings with both nominal  
2118 and misaligned chamber positions, as well as addressing a number of performance issues.

2119 This note is organized as follows: the algorithm and its outputs are briefly described in Section  
2120 A.1; Monte Carlo samples used are in Section B.1; nominal algorithm performance and certain quan-  
2121 tities of interest are described in Section A.3; algorithm performance under misalignment, misalign-  
2122 ment corrections, and corrected performance are shown in Section A.9; and conclusions are pre-  
2123 sented in Section A.24.

## 2124 A.1 ALGORITHM OVERVIEW

2125 The MMTP algorithm is shown schematically in Figure A.1, taken from [41], where a more detailed  
2126 description may be found. The algorithm begins by reading in hits, which are converted to slopes.  
2127 These slopes are calculated under the assumption that the hit originates from the IP; slopes calcu-  
2128 lated under this assumption are denoted by a superscript  $g$  for global in order to distinguish them  
2129 from local slopes calculated using only hits in the wedge. In the algorithm simulation, events are  
2130 screened at truth level to make sure they pass certain requirements. The track's truth-level coor-  
2131 dinates must place it with the wedge since some generated tracks do not reach the wedge. These  
2132 hits are stored in a buffer two bunch crossings (BCs) in time deep that separates the wedge into so-  
2133 called "slope-roads." If any given slope-road has sufficient hits to pass what is known as a coinci-  
2134 dence threshold, a fit proceeds. A coincidence threshold is a requirement for an event expressed as  
2135  $aX+bUV$ , which means that an slope-road must have at least  $a$  hits in horizontal (X) planes and at

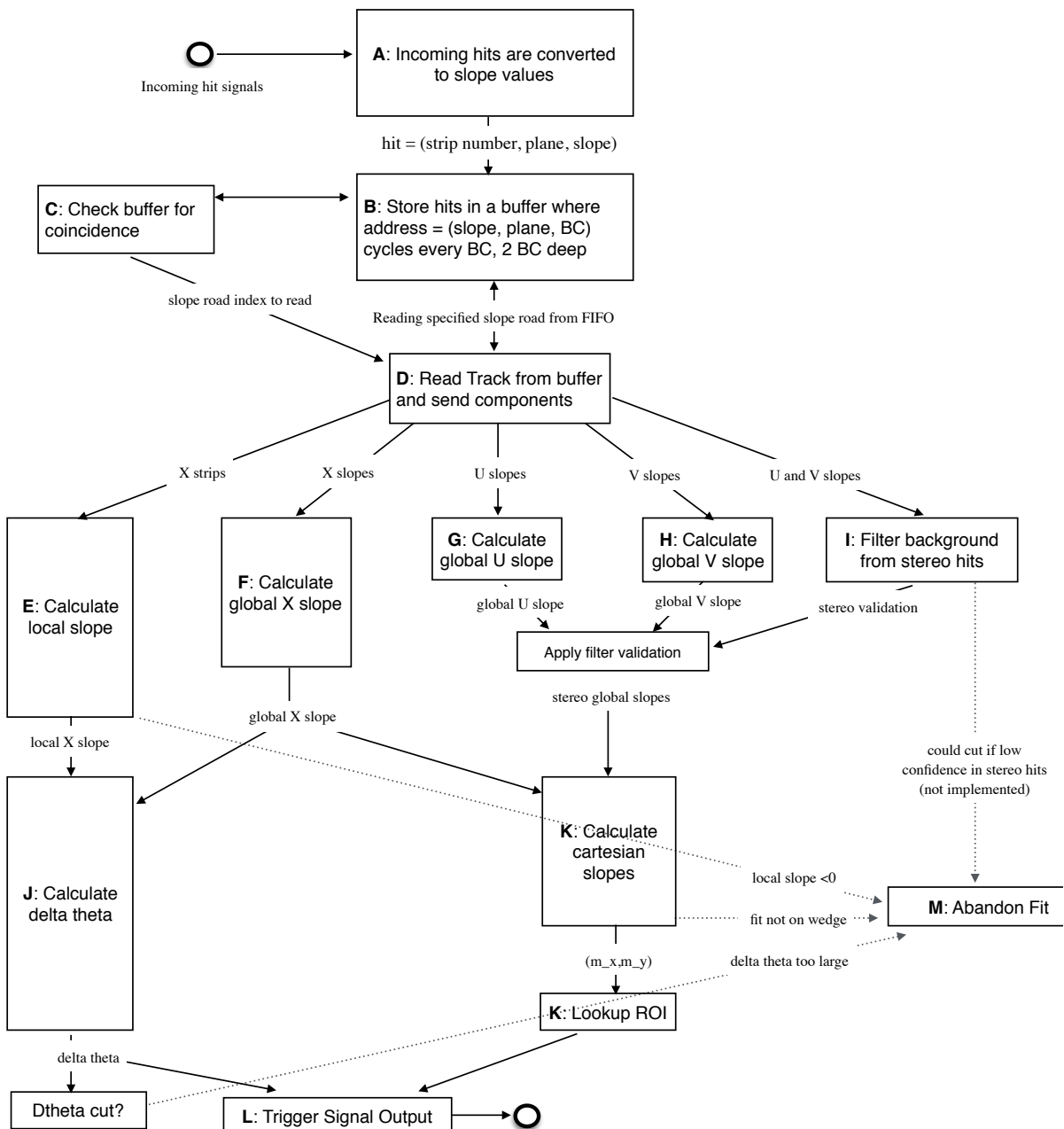


Figure A.1: A flow chart describing the algorithm steps, taken from [41].

2136 least  $b$  hits in stereo (U or V (corresponding to positive and negative stereo rotations)) planes. For  
 2137 coincidence thresholds with a  $2X$  hit requirement there is the extra requirement that, in the case of  
 2138 only  $2X$  hits, one be on each quadruplet in order to ensure an adequate lever arm for the  $\Delta\theta$  calcu-  
 2139 lation. Note that less stringent (lower hit) coincidence thresholds are inclusive; i.e. a slope-road pass-  
 2140 ing a  $4X+4UV$  cut automatically passes  $2X+1UV$ . The coincidence threshold, size of the slope-roads  
 2141 (denoted  $b$ ), and the number of slope-roads into which each horizontal and stereo hits get written  
 2142 centered upon their nominal value are configurable parameters of the algorithm.

2143 An individual hit's slope is calculated as shown in Equation A.1, where  $y_{base}$  is the local  $y$  coordi-  
 2144 nate (orthogonal to the beamline and direction of the horizontal strips) of a station's base,  $w_{str}$  is the  
 2145 strip pitch,  $n_{str}$  is the hit's strip number, and  $z_{plane}$  is the location of the hit's plane along the beam-  
 2146 line.

$$M_{hit} = \frac{y}{z} = \frac{y_{base}}{z_{plane}} + \frac{w_{str}}{z_{plane}} \times n_{str} \quad (\text{A.1})$$

2147 In the fit, individual hit slopes in a slope-road are used to calculate global slopes associated with each  
 2148 plane type, which are averages (e.g.  $M_X^{\ell}$  for the average slope of horizontal planes). These in turn are  
 2149 used to calculate the three composite slopes: slopes associated with the horizontal ( $m_x$ ) and vertical  
 2150 coordinates ( $m_y$ ) and the local slope of hits in the horizontal planes ( $M_X^l$ ), all of which are shown in  
 2151 Equation A.4. Note that the expression for  $M_X^l$  differs but is equivalent to the expression given in  
 2152 [41]. This is due to a procedural change in the algorithm. The local X slope is expressed in [41] as:

$$M_X^{local} = A_k \sum_i y_i z_i - B_k \sum_i y_i, \quad B_k = \frac{1}{n} \sum_i z_i A_k = \bar{z} A_k \quad (\text{A.2})$$

2153 Procedurally, this entails doing the sums over  $y_i$  and  $y_i z_i$ , multiplying the sums by  $A_k$ ,  $B_k$ , and then  
 2154 subtracting both of these numbers,  $\mathcal{O}(10^3)$ , to get local slopes,  $\mathcal{O}(10^{-1})$ , while requiring preci-  
 2155 sion on these numbers on the order of  $\mathcal{O}(10^{-3})$ . This requires precision in the sums  $\mathcal{O}(10^{-7})$ ,  
 2156 and with 32 bit fixed point numbers, there are deviations with respect to the floating point calcula-  
 2157 tions at the level of  $\mathcal{O}(10^{-5})$ , which is enough to introduce a significant bias in the  $\Delta\theta$  calculation.

2158 In order to prevent these errors, we do the subtraction first

$$M_X^{local} = A_k \sum_i y_i z_i - B_k \sum_i y_i = A_k \sum_i (y_i z_i - y_i \bar{z}) = B_k \sum_i y_i \left( \frac{z_i}{\bar{z}} - 1 \right) \quad (\text{A.3})$$

2159 Thus, we change the order of operations and store  $1/\bar{z}$  instead of  $A_k$  in addition to  $B_k$ . We also  
 2160 change the units of  $y_i$  and  $z_i$  in the calculation by dividing the millimeter lengths by 8192.\* With  
 2161 these changes, a 32 bit fixed point based algorithm has essentially identical performance to that of an  
 2162 algorithm based on the usual C++ 32 floating point numbers. Future work includes converting the  
 2163 32 bit fixed point arithmetic to 16 bit where possible in the algorithm. While introducing 16 bit num-  
 2164 bers uniformly might seem preferable, since simple 16-bit operations in the firmware can be done in  
 2165 a single clock tick, and a larger number of bits increases the algorithm latency, some numbers in the  
 2166 algorithm will require a larger number of bits, in particular in the local slope calculation, which is  
 2167 the single calculation in the algorithm requiring the largest numeric range.

2168 In Equation A.4,  $\theta_{st}$  is the stereo angle of 1.5 degrees; the sums are over relevant planes;  $\bar{z}$  is the  
 2169 average position in  $z$  of the horizontal planes; and  $y_i$  and  $z_i$  in the local slope expression refer to the  $y$

---

\*Chosen since it is a perfect power of 2 and of order the length scale of  $z$  in millimeters

2170 and  $z$  coordinates of hits in X planes.

$$m_x = \frac{1}{2} \cot \theta_{st} (\mathcal{M}_U^g - \mathcal{M}_V^g), \quad m_y = \mathcal{M}_X^g, \quad \mathcal{M}_X^l = \frac{\bar{z}}{\sum_i z_i^2 - 1/n (\sum_i z_i)^2} \sum_i y_i \left( \frac{z_i}{\bar{z}} - 1 \right) \quad (\text{A.4})$$

2171 From these composite slopes, the familiar expressions for the fit quantities  $\theta$  (the zenith),  $\phi$  (the az-  
2172 imuth<sup>†</sup>), and  $\Delta\theta$  (the difference in  $\theta$  between the direction of the segment extrapolated back to the  
2173 interaction point and its direction when entering the detector region; the following is an approxima-  
2174 tion) may be calculated, as noted in [41]:

$$\theta = \arctan \left( \sqrt{m_x^2 + m_y^2} \right), \quad \phi = \arctan \left( \frac{m_x}{m_y} \right), \quad \Delta\theta = \frac{\mathcal{M}_X^l - \mathcal{M}_X^g}{1 + \mathcal{M}_X^l \mathcal{M}_X^g} \quad (\text{A.5})$$

2175 Looking at Equations A.4 and A.5, the dependence of fit quantities on input hit information be-  
2176 comes clear.  $\Delta\theta$  relies exclusively on information from the horizontal (X) planes. Both  $\theta$  and  $\phi$  rely  
2177 on both horizontal and stereo slope information. However, the sum in quadrature of  $m_x$  and  $m_y$  in  
2178 the arctangent for  $\theta$  means that  $\theta$  is less sensitive to errors in stereo hit information than  $\phi$ . Given  
2179 that  $\theta_{st}$  is small,  $\cot \theta_{st}$  is large ( $\sim 38$ ), so  $m_x$  multiplies small differences in  $\mathcal{M}_U$  and  $\mathcal{M}_V$ , where  $m_y$   
2180 is simply an average over slopes. This means that while errors in horizontal hit information will af-  
2181 fect all three fit quantities, comparable errors in stereo hits will have a proportionately larger effect  
2182 on  $\theta$  and particularly on  $\phi$ . The  $\Delta\theta$  cut after step J in Figure A.1 has been implemented, requiring  
2183 all fits to have  $|\Delta\theta| < 16$  mrad. This requirement ensures good quality fits but also slightly reduces

---

<sup>†</sup>Defined with respect to the center ( $y$ ) axis and *not* the axis of the strips ( $x$ ) as is sometimes typical, so a hit along the center of the wedge has  $\phi = 0$

2184 algorithm efficiency.

## 2185 A.2 MONTE CARLO SAMPLES

2186 The Monte Carlo (MC) samples used for these studies were generated in Athena release 20.1.0.2 us-  
2187 ing simulation layout ATLAS-R2-2015-01-01-00 with muon GeoModel override version MuonSpectrometer-  
2188 R.07.00-NSW and modifications to have two modules per multiplet and xxuvuvxx geometry with a  
2189 stereo angle of 1.5 degrees. Muons of a single  $p_T$  were generated around the nominal IP with a smear-  
2190 ing of 50 mm along the beam line and 0.015 mm orthogonal to it; these muons were pointed toward  
2191 a single, large sector of the NSW. Each event consists of one muon fired towards the single NSW  
2192 wedge separated by effectively infinite time from other events.

## 2193 A.3 NOMINAL PERFORMANCE

2194 In order to evaluate algorithm performance, a number of quantities are evaluated, including the fit  
2195 quantities  $\theta$ ,  $\phi$ , and  $\Delta\theta$  as well as algorithm efficiency. Unless otherwise stated, that algorithm is  
2196 run with a 4X+4UV coincidence threshold, slope-road size of 0.0009, an X tolerance of two slope-  
2197 roads (i.e. hits in horizontal planes are written into the two slope-roads closest to the hits' value),  
2198 a UV tolerance of four slope-roads<sup>†</sup>, and a charge threshold requirement on hits of 1 (measured in  
2199 units of electron charge) for a sample of 30 000 events with a muon  $p_T$  of 100 GeV. Samples were  
2200 also generated for  $p_T$  values of 10 GeV, 20 GeV, 30 GeV, 50 GeV, and 200 GeV, which were used in

---

2200 <sup>†</sup>The larger tolerance on stereo hits takes into account the particulars of the  $m_x$  calculation mentioned in Section A.1.

2201 some of the following studies.

2202 **A.4 FIT QUANTITIES**

2203 In order to evaluate the performance of the algorithm’s fit quantities  $\theta$ ,  $\phi$ , and  $\Delta\theta$ , fit values are com-  
2204 pared to truth-level MC values. The residual of the three fit quantities,  $\theta_{fit} - \theta_{tru}$ ,  $\phi_{fit} - \phi_{tru}$ , and  
2205  $\Delta\theta_{fit} - \Delta\theta_{tru}$ , are recorded for every fitted track. The distributions of these quantities, in particular  
2206 their biases and standard deviations, are then used to evaluate performance. In most cases, follow-  
2207 ing [41], the mean and standard deviation of a  $3\sigma$  Gaussian fit are quoted, as they capture the main  
2208 features of the algorithm and generally behave like the raw mean and rms. Nevertheless, discussion  
2209 of the raw quantities will be included when their behavior deviates markedly from that of the  $3\sigma$  fit  
2210 quantities.

2211 The truth-level quantities used in residual distribution are taken from information in the MC.

2212 These come directly from the MC for  $\theta$ ,  $\phi$ , and  $\Delta\theta$ . These quantities, along with the geometry of  
2213 the (large) wedge, are then in turn used to calculate truth-level values for any intermediate quantities  
2214 used in the algorithm.  $m_{x,tru}$ , for instance, is given by  $\tan \theta_{tru} \sin \phi_{tru}$ .

2215 Residual distributions for fit quantities under the previously described default settings of the al-  
2216 gorithm are shown in Figure A.2. Both the  $\theta_{fit} - \theta_{tru}$  and  $\Delta\theta_{fit} - \Delta\theta_{tru}$  distributions feature a  
2217 mostly Gaussian shape with more pronounced tails. The mean bias for these distributions is negligi-  
2218 ble at under one tenth of a milliradian, and the fitted (raw) rms values are 0.349 (0.614) mrad for  $\theta$   
2219 and 1.03 (2.55) mrad for  $\Delta\theta$ . The case of the  $\phi_{fit} - \phi_{tru}$  distribution is less straightforward, with both  
2220 the shape and bias arising from the xxuvuvxx geometry and relatively large extent of one of the two

2221  $\eta$ -stations, as explained in Appendix B of [38]. The fitted (raw) rms for the  $\phi$  distribution is 8.67  
 2222 (16.6) mrad.

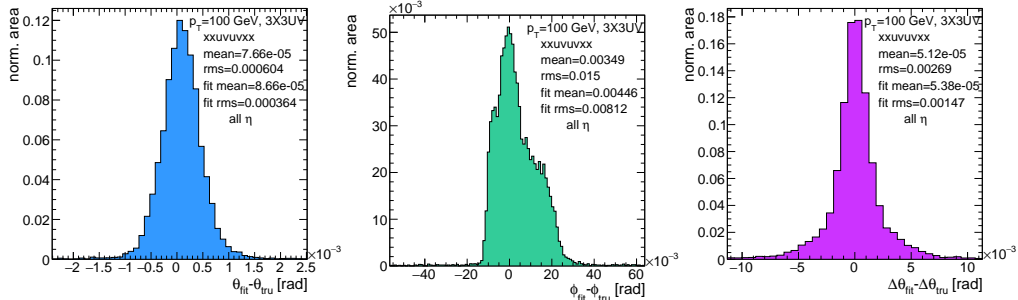
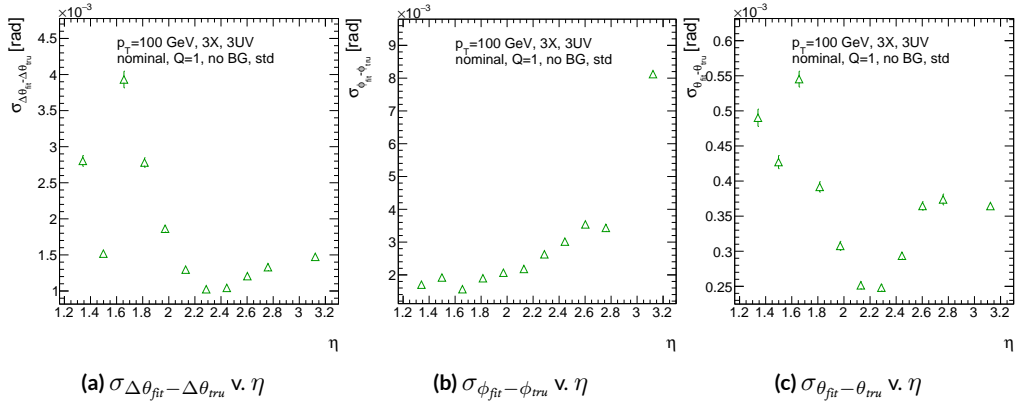


Figure A.2: Nominal residual plots;  $\theta, \phi, \Delta\theta$  for  $p_T = 100$  GeV muons

2223 Both increasing muon  $p_T$  and increasing muon  $\eta$  for a fixed  $p_T$  imply increasing muon energy. As  
 2224 muons become more energetic, two effects compete in affecting the quality of fit. On the one hand,  
 2225 higher energy muons are deflected less by the ATLAS magnetic field, which should tend to improve  
 2226 the quality of the fit, since the fitted  $\theta$  (upon which  $\Delta\theta$  also relies) and  $\phi$  values are calculated under  
 2227 the infinite momentum muon (straight track) assumption. However, as muon energy increases, the  
 2228 likelihood that the muon will create additional secondaries increases, which creates extra hits that  
 2229 degrade the quality of the fit. While the geometry of the multiplet is such that there is very good res-  
 2230 olution in the direction orthogonal to the horizontal strip direction, the shallow stereo angle of 1.5  
 2231 degrees means that early hits caused by secondaries can have an outsize impact on  $m_x$ .  $\Delta\theta$ , which  
 2232 does not rely upon stereo information should feel the effect of secondaries the least and benefit from  
 2233 straighter tracks the most and hence benefit from higher muon energies;  $\phi$ , relying upon stereo in-  
 2234 formation the most, would be most susceptible to secondaries and benefit the least from straighter

2235 tracks and hence least likely to benefit from higher muon energy;  $\theta$  relies upon both horizontal and  
 2236 vertical slope information, though small errors are less likely to seriously affect the calculation, so the  
 2237 two effects are most likely to be in conflict for this fit quantity.

2238 The interplay of these effects on the residual standard deviations can be seen in their dependen-  
 2239 cies on  $\eta$  (Figure A.3; note that the final point in each of these plots is the rms of the distribution  
 2240 overall  $\eta$ ) and  $p_T$  (Figure A.4). For  $p_T = 100$  GeV muons,  $\Delta\theta$  performance increases with  $\eta$  (en-  
 2241 ergy), and  $\phi$  performance decreases, as expected;<sup>§</sup> for  $\theta$ , the two effects appear to compete, with per-  
 2242 formance first increasing with  $\eta$  until the effects of secondaries begins to dominate. Integrated over  
 2243 all  $\eta$ , the effects are less clearly delineated. Both  $\Delta\theta$  and  $\theta$  performance increases with increasing  $p_T$ ,  
 2244 suggesting straighter tracks with increasing energy are the dominant effect for these quantities, while  
 2245  $\phi$  performance appears to improve and then deteriorate (the slight improvement at high  $p_T$  is due to  
 2246 the addition of the  $\Delta\theta$  cut into the algorithm, which filters out very poor quality fits).



**Figure A.3:** The rms distributions of  $\Delta\theta$ ,  $\phi$ , and  $\theta$  as a function of  $\eta$  for  $p_T = 100$  GeV; the final point in each plot is the rms obtained from a fit to the full distribution including all  $\eta$  bins.

<sup>§</sup>The much worse overall performance for  $\phi$  is due to the  $\eta$  dependent bias and other effects

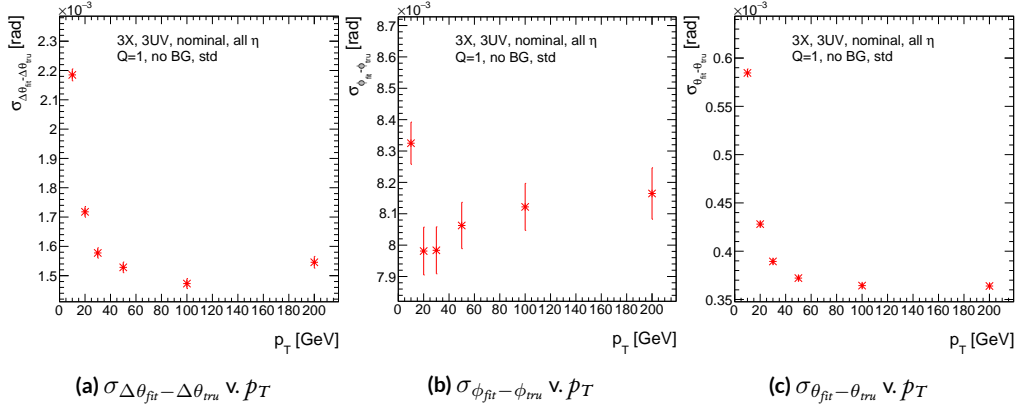


**Figure A.4:** The rms distributions of  $\Delta\theta$ ,  $\phi$ , and  $\theta$  as a function of  $p_T$ .

2247 The rms of the three benchmark quantities as a function of algorithm set (i.e. slope-road) coinci-  
 2248 dence threshold are shown in Figure A.5 using Gaussian fits and in Figure A.6 for the raw quantities.  
 2249 The fitted  $\sigma$ 's for  $\theta$  and  $\phi$  are fairly stable across coincidence threshold.  $\Delta\theta$ , on the other hand, per-  
 2250 forms better particularly for the most stringent coincidence threshold; this is a result of the fact that  
 2251 additional information for more hits greatly improves the quality of the local slope fit calculation.  
 2252 The raw rms is a different story. Naïvely, one would expect the performance to get better with more  
 2253 stringent coincidence threshold, but this is not the case in Figure A.6. As the coincidence thresh-  
 2254 old gets more stringent, fewer and fewer tracks are allowed to be fit. When moving from 2X hits to  
 2255 3X hits, the tracks that get vetoed populate the tails of the distribution outside the  $3\sigma$  fit range but  
 2256 are not in the very extremes of the distribution. While tracks with 2X hits are of lower quality than  
 2257 those with 3 and 4 X hits, tracks with the very worst fit values pass even the most stringent coinci-  
 2258 dence threshold requirements (e.g. as a result of many hits arising from a shower of secondaries).  
 2259 This is best illustrated when comparing the 2X+1UV  $\Delta\theta$  residual distribution with the 4X+4UV

distribution in Figure A.7. As both the overlayed normalized curves and ratio distribution show,  
 while the most central regions are fairly similar, the  $\omega X + 1$  UV distribution is much more prominent  
 in the tails but not the extreme tails, which means that, though the overall  $\omega X + 1$  UV raw rms goes  
 down, the overall quality of algorithm fits is worse.

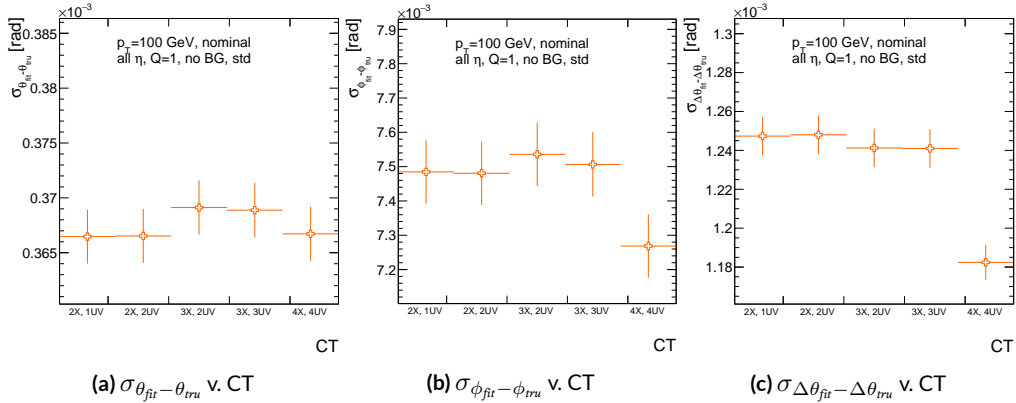


**Figure A.5:** The fitted rms of residual distributions for  $\theta$ ,  $\phi$ , and  $\Delta\theta$  as a function of coincidence threshold for  $p_T = 100$  GeV.

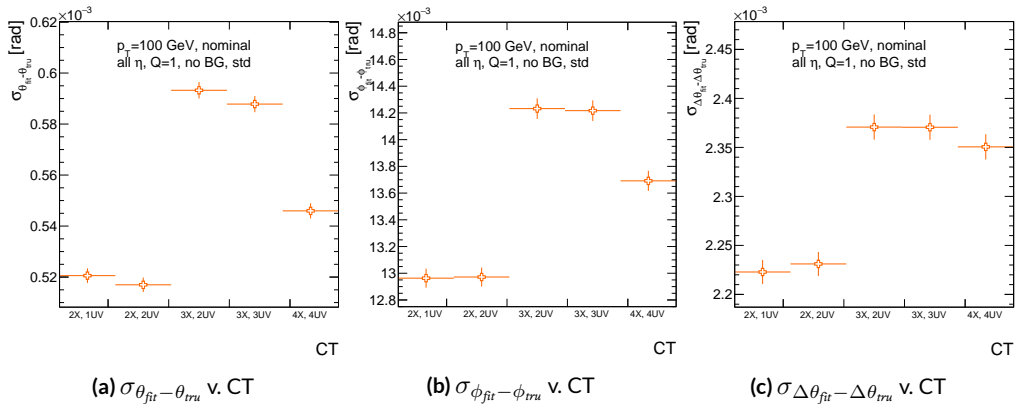


**Figure A.6:** The raw rms of residual distributions for  $\theta$ ,  $\phi$ , and  $\Delta\theta$  as a function of coincidence threshold for  $p_T = 100$  GeV.

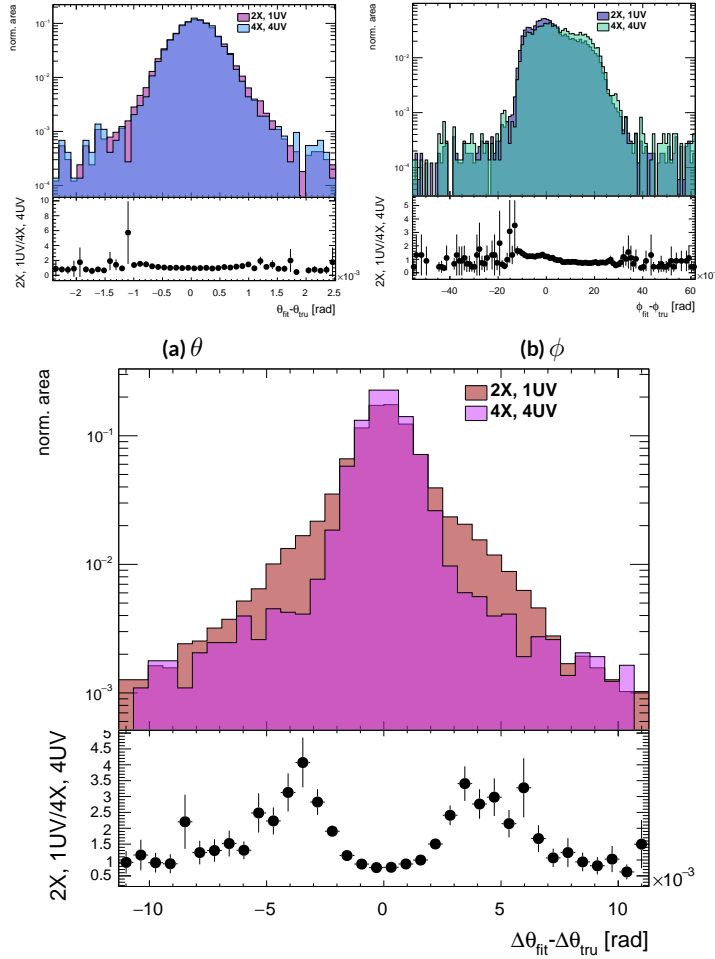


**Figure A.7:** Nominal  $\Delta\theta$  residual distribution for  $p_T = 100$  GeV muons with coincidence thresholds 2X+1UV and 4X+4UV normalized to the same area and plotted together (top) as well as the ratio of the 2X+1UV distribution and the 4X+4UV per bin.

2264 A.5 EFFICIENCIES

2265 Two general efficiencies have been formulated to study the performance of the MMTP algorithm.

2266 The first, denoted  $\varepsilon_{alg}$ , is the fraction of tracks that pass some (slope-road) coincidence threshold

2267 configuration that are successfully fit. An event that passes a slope-road coincidence but does not fit

2268 fails because some of the hits included are of sufficiently poor quality to throw off the fit. This effi-

2269 ciency answers the question of how often the algorithm performs fits when technically possible, giv-

2270 ing a measure of overall algorithm performance for a given configuration. For example,  $\varepsilon = 95\%$  for

2271  $3X+2UV$  means that 95% of tracks that produce at least  $3X$  hits and  $2UV$  hits in at least one slope-

2272 road will be successfully fitted 95% of the time. The performance of this efficiency as a function of

2273 coincidence threshold,  $\eta$  (with the final point once again being the efficiency integrated over all  $\eta$ ),

2274 and  $p_T$  is shown in Figure A.8.  $\varepsilon_{alg}$  is fairly constant in  $\eta$  and decreases with increased  $p_T$ , which can

2275 be attributed to the increased likelihood of secondaries introducing lower quality hits that cause the

2276 fit to fail.

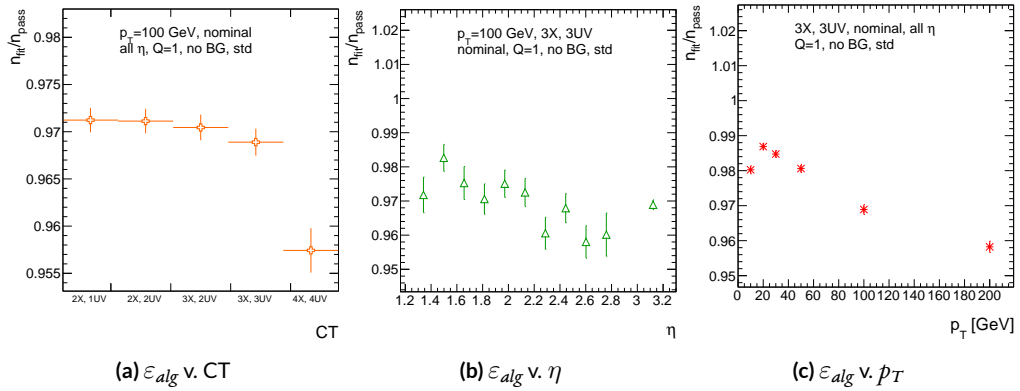
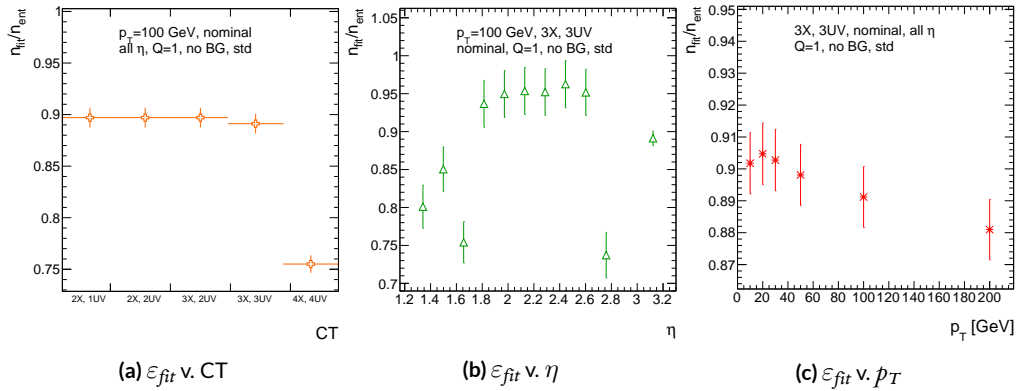


Figure A.8:  $\varepsilon_{alg}$  and as a function of coincidence threshold,  $\eta$  (final point is  $\varepsilon_{alg}$  integrated over all  $\eta$ ), and  $p_T$ .

2277 The second efficiency type, denoted  $\varepsilon_{fit}$ , is the fraction of tracks that enter the wedge whose fits  
 2278 (if any) satisfy a given coincidence threshold. This efficiency can be used to help establish an optimal  
 2279 coincidence threshold setting in the algorithm, balancing the improved overall fit quality of higher  
 2280 thresholds with the greater number of fits for lower thresholds. Hence, an  $\varepsilon_{fit}$  of 95% at 3X+2UV  
 2281 means that 95% of tracks entering the wedge are fit and that these fits include at least 3X and 2UV  
 2282 hits.  $\varepsilon_{fit}$  as a function of coincidence threshold is shown in Figure A.9 (a), which shows that the ma-  
 2283 jority of fits having at most 3X+3UV hits. That there is a marked drop to 4X+4UV is not surpris-  
 2284 ing, as there is a substantial population outside the 4X+4UV bin in Figure A.10. The behavior of  
 2285  $\varepsilon_{fit}$  with  $\eta$  in Figure A.9 (b) (with the final point once again being the efficiency integrated over all  
 2286  $\eta$ ) is much more varied, with geometric effects of detector acceptance coming into play. The per-  
 2287 formance of  $\varepsilon_{fit}$  as a function of  $p_T$ , shown in Figure A.9 (c), is similar to that of  $\varepsilon_{alg}$  coincidence  
 2288 threshold, again consistent with the effects of secondaries at higher energies.



**Figure A.9:**  $\varepsilon_{fit}$  and as a function of coincidence threshold,  $\eta$  (final point is  $\varepsilon_{fit}$  integrated over all  $\eta$ ), and  $p_T$ .

2289 In order to better understand efficiency behavior with coincidence threshold, the distribution of

2290 highest slope-road coincidence thresholds in events is shown in Figure A.10, with the o,o bin con-  
 2291 taining events that did not meet requirements for the minimum  $2X+1UV$  coincidence threshold for  
 2292 a fit to occur. That the efficiency is lower at higher coincidence threshold suggests that most of the  
 2293 fits that fail have high hit multiplicity (i.e. a similar number fails in each of the coincidence thresh-  
 2294 old bins in Figure A.8 (a)), which is consistent with the interpretation that the primary source of fit  
 2295 failures is bad hits originating from secondaries created by higher energy muons.

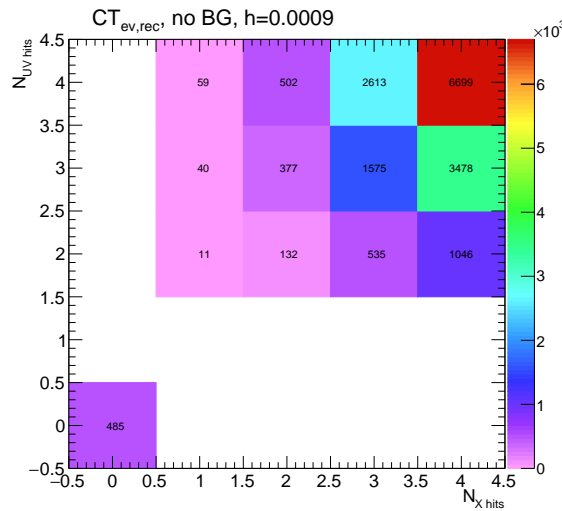


**Figure A.10:** The distribution of highest slope-road coincidence thresholds in events; the 0,0 bin is the number of events passing selection requirements that fail to form the minimum  $2X+1UV$  coincidence threshold necessary for a fit.

2296 A.6 INCOHERENT BACKGROUND

2297 The default slope-road size and tolerances associated with horizontal and stereo hits used in the  
2298 above studies were configured to optimize algorithm performance, similar to studies in [41]. In or-  
2299 der to evaluate algorithm performance under conditions with more limited resources, as might be  
2300 expected at run-time, additional studies were conducted with the slope-road size and hit tolerances  
2301 set equivalent to the sensitive area of a single VMM chip<sup>¶</sup> both with and without generation of inco-  
2302 herent background.

2303 Incoherent background is generated based on the assumption that the intensity only varies as a  
2304 function of the distance from a point to the beamline,  $r$ . The number of hits per unit area per unit  
2305 time as a function of  $r$  is given in Equation A.6 and taken from [41].

$$I = I_0 (r/r_0)^{-2.125} \quad (\text{A.6})$$

2306 where  $r_0 = 1000$  mm and  $I_0 = 0.141$  kHz/mm<sup>2</sup>

2307 Background generation happens per event as follows:

- 2308 1. Determine the total number of hits to be generated in this event according to a Poisson distri-  
2309 bution
- 2310 2. Assign a time to hits uniformly in  $[t_{\text{start}} - t_{\text{VMM}}, t_{\text{end}}]$  where start and end are for the event  
2311 clock and  $t_{\text{VMM}}$  is the VMM chip deadtime (100 ns)
- 2312 3. Assign a plane to hits uniformly
- 2313 4. Assign a  $\phi$  value to hits uniformly

---

<sup>¶</sup>One VMM is assumed to cover 64 MM strips at 0.445 mm each.

<sup>2314</sup> 5. Assign an  $r$  to hits according to Equation A.6

<sup>2315</sup> 6. Calculate hit information according to these values.

<sup>2316</sup> The expectation value for the Poisson distribution is determined by integrating Equation A.6

<sup>2317</sup> over the surface area of the wedge to get the total hit rate for the wedge,  $\Gamma$ , and then multiplying this

<sup>2318</sup> by the length of the time window over which hits may be generated. With  $H = 982$  mm,  $b_1 =$

<sup>2319</sup> 3665 mm, and  $\theta_w = 33\pi/180$ , we find<sup>||</sup>:

$$\Gamma = 2I_0 r_0^{2.125} \int_0^{\theta_w/2} d\phi \int_{H \sec \phi}^{(H+b_1) \sec \phi} r dr r^{-2.125} = 98.6657 \text{ MHz} \quad (\text{A.7})$$

<sup>2320</sup> In this case, we have taken the nominal values of the MM sector geometry for  $H$  (wedge base),  $b_1$

<sup>2321</sup> (the wedge height), and  $\theta_w$  (the wedge opening angle).

<sup>2322</sup> The effects of incoherent background and larger slope road size are summarized in Figure A.11 for

<sup>2323</sup> efficiencies and in Figure A.13 and Table A.1 for residual of fit quantities.

<sup>2324</sup> Figure A.11 show the effect of both wider slope-roads and the introduction of background on ef-

<sup>2325</sup> ficiencies. The introduction of wider slope-roads increases the chance that an early errant hit (either

<sup>2326</sup> from secondaries/ionization or background) will be introduced into the fit, and the presence of in-

<sup>2327</sup> coherent background greatly increases the number of such errant hits. Both wider slope-roads and

<sup>2328</sup> background drive down the number of fits (numerator) in both efficiencies, and background can

<sup>2329</sup> artificially inflate the denominator of  $\varepsilon_{alg}$ , a reco-level, slope-road coincidence threshold. The shape

<sup>2330</sup> of the  $\varepsilon_{fit}$  versus coincidence threshold distributions remains fairly constant with each complicat-

---

<sup>||</sup>Using Mathematica and the extra factor of  $r$  from the volume element

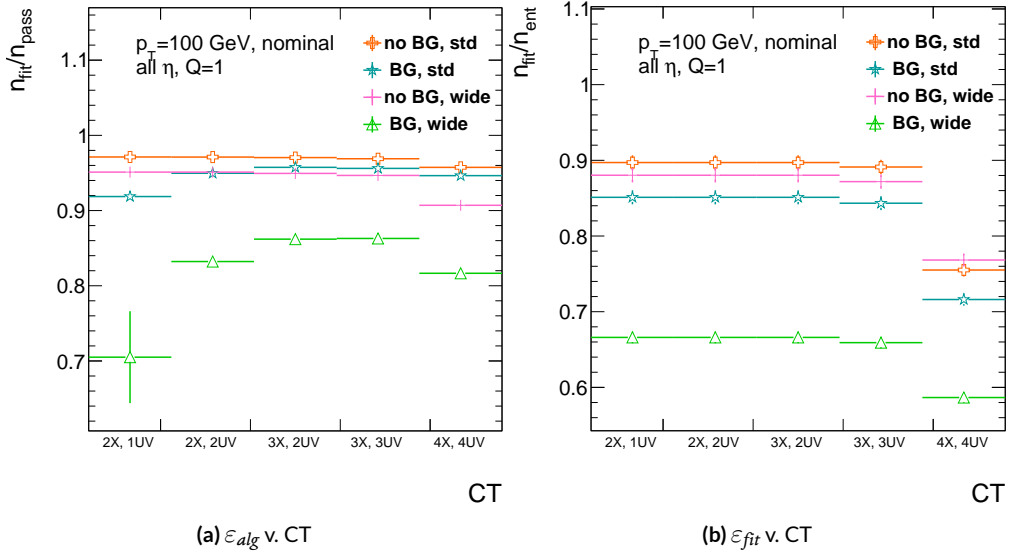


**Figure A.11:** The algorithm and total efficiencies as a function of coincidence threshold for different background settings and slope-road sizes (standard and wide (one slope road as 1 VMM chip)).

ing factor (standard, wider slope-roads, background, both wider slope-roads and background), suggesting many muons will simply not be fit with any number of hits;  $\varepsilon_{\text{fit}}$  does not take into account the coincidence threshold of tracks that are not fit, so the effect appears uniform across coincidence threshold. The effects seen for  $\varepsilon_{\text{alg}}$ , which are not uniform across coincidence threshold can be better understood when examining the distribution of event highest coincidence thresholds, shown for wide slope-roads both without and with background in Figure A.12. Take, for example the 2X+1UV case. The 2X+1UV bin in particular has a marked increase when background is introduced. No new good tracks are introduced between the no background and background cases, so the increase is entirely due to bad, background hits; hence, these events do not (and should not) fit, causing the particularly pronounced drop in this bin between these two cases in Figure A.11.

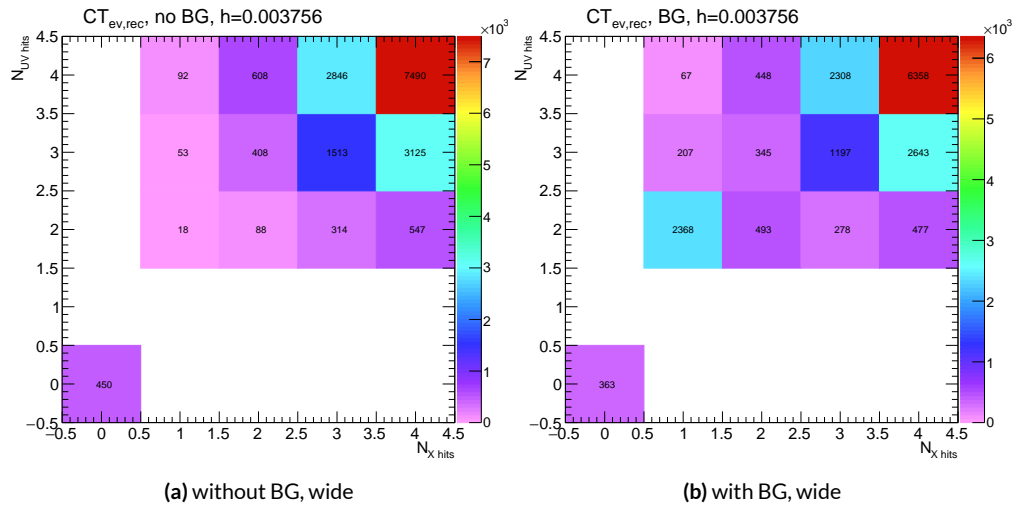


**Figure A.12:** The distribution of highest slope-road coincidence thresholds in events for the algorithm with wide slope-roads (width of 1 VMM) both without (a) and with (b) incoherent background; the 0,0 bin is the number of events passing selection requirements that fail to form the minimum  $2X+1UV$  coincidence threshold necessary for a fit.

The effect of increasing slope-road size and incoherent background on fit quantity residual rms values as a function of  $p_T$  is shown in Figure A.13. As the figure shows, the fitted rms values are fairly robust against increased slope-road size and background. This does not hold for all of the raw rms values, however, as shown in Table A.1. Just as with the efficiencies, the introduction of background has a larger effect than that of increased slope-road size, which does not seem to have an overly large impact on any of the fit quantities on its own. While  $\Delta\theta$  remains robust to both increased slope-road size and background (likely due to the  $\Delta\theta$  cut of 16 mrad built into the algorithm),  $\theta$  shows some degradation in performance, and the  $\phi$  residual raw rms shows a very large increase upon the introduction of background. Nevertheless, the contrasting behavior of the fitted and raw rms values suggests that tracks that drive up the raw rms values already had very poor fit quality even before the introduction of background, so the impact on fit quantities should remain fairly limited.

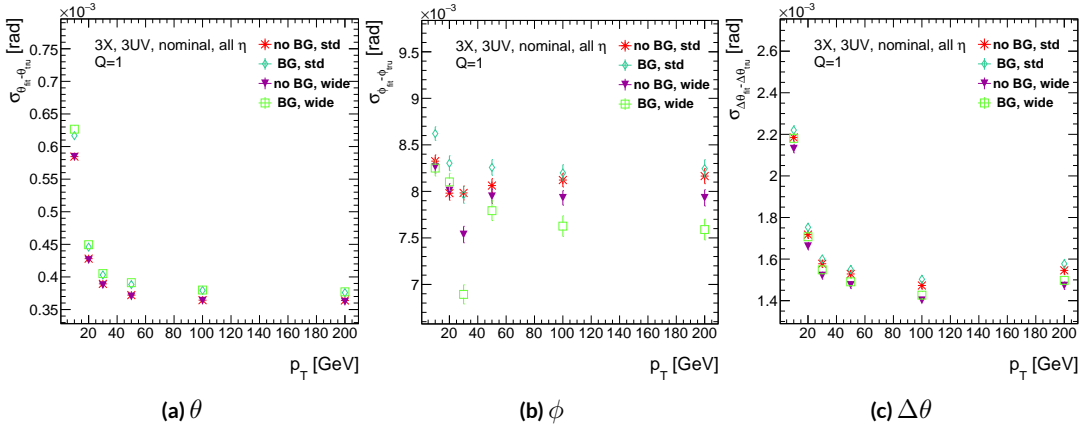


**Figure A.13:** The three fit quantity residual rms values as a function of  $p_T$  for different background settings and slope-road sizes (standard and wide (one slope road as 1 VMM chip)).

	No BG, std	No BG, wide	BG, std	BG, wide
$\theta$	0.364 (0.604)	0.363 (0.542)	0.379 (0.886)	0.380 (1.07)
$\phi$	8.12 (15.0)	7.93 (13.2)	8.20 (24.6)	7.63 (24.8)
$\Delta\theta$	1.47 (2.69)	1.40 (2.66)	1.50 (2.89)	1.43 (2.90)

**Table A.1:** The fitted (absolute)  $\sigma$  of fit quantity residuals in mrad under different algorithm settings.

2352 As Table A.1 shows, rms values appear to be robust to an increase in slope-road size. Neverthe-  
2353 less, though the fitted  $\sigma$  residual values are also fairly robust to the introduction of background, the  
2354 raw rms values are not. While the raw  $\Delta\theta$  rms stays stable, both  $\theta$  and  $\phi$  suffer noticeable degra-  
2355 dation, which suggests that the introduction of background has a detrimental effect on horizontal  
2356 slope residual (i.e. on stereo strips in particular). This level of degradation is likely acceptable for  $\theta$ ,  
2357 though further steps may need to be taken to address  $\phi$ .

### 2358 A.7 BCID

2359 A fitted track's BCID is determined by the most common BCID associated with its hits. Concerns  
2360 were raised that this might cause incorrect BCID association for fitted tracks. In order to address  
2361 this, the rate of successful BCID association for fitted tracks was recorded. Figure A.14 shows the  
2362 dependence of this success rate as a function of  $p_T$  and coincidence threshold in the different back-  
2363 ground and resource conditions used in the previous section. The successful BCID identification  
2364 rate is always over 99.5%, demonstrating that this issue is not a concern with the state-of-the-art de-  
2365 tector simulation.

### 2366 A.8 CHARGE THRESHOLD

2367 The MMTP uses the first hits registered passing a charge threshold requirement given in units of  
2368 electron charge. In principle, it would be beneficial to be able to use any hits that are registered re-  
2369 gardless of deposited charge, but in the high rate environment envisioned for the NSW, this require-  
2370 ment might need to be raised. Nominal algorithm settings have this charge threshold requirement

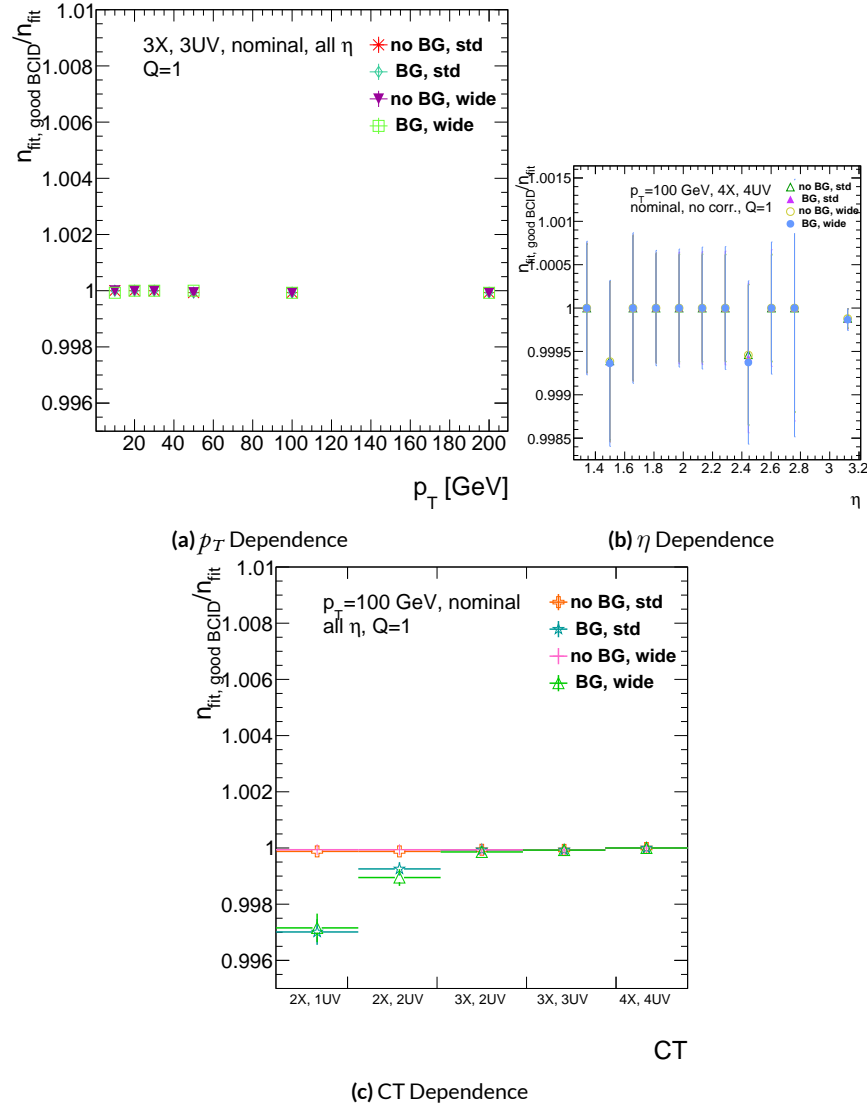


**Figure A.14:** The rate of good BCID association based majority hit BCID as a function of  $p_T$  and coincidence threshold.

2371 set to 1, and studies were conducted on algorithm performance for charge threshold values of 0, 1,  
 2372 and 2. Efficiencies as a function of coincidence threshold for different charge thresholds are shown  
 2373 in Figure A.15. Increasing the charge threshold lowers both efficiencies, particularly at high coinci-  
 2374 dence threshold, which suggests that energetic muons with secondaries create both very many hits  
 2375 and hits with higher charge. While the shapes of the fit quantity distributions as a function of  $p_T$  in  
 2376 Figure A.16 are fairly constant across charge threshold, performance is not.  $\theta$  and  $\Delta\theta$  show some im-  
 2377 provement with higher charge threshold, particularly at low  $p_T$ , suggesting that resolution improves  
 2378 in the vertical direction, but  $\phi$  shows degradation at higher charge threshold, which is a symptom  
 2379 of more highly charged particles experiencing greater bending in the ATLAS magnetic field in the  $\phi$   
 2380 direction.

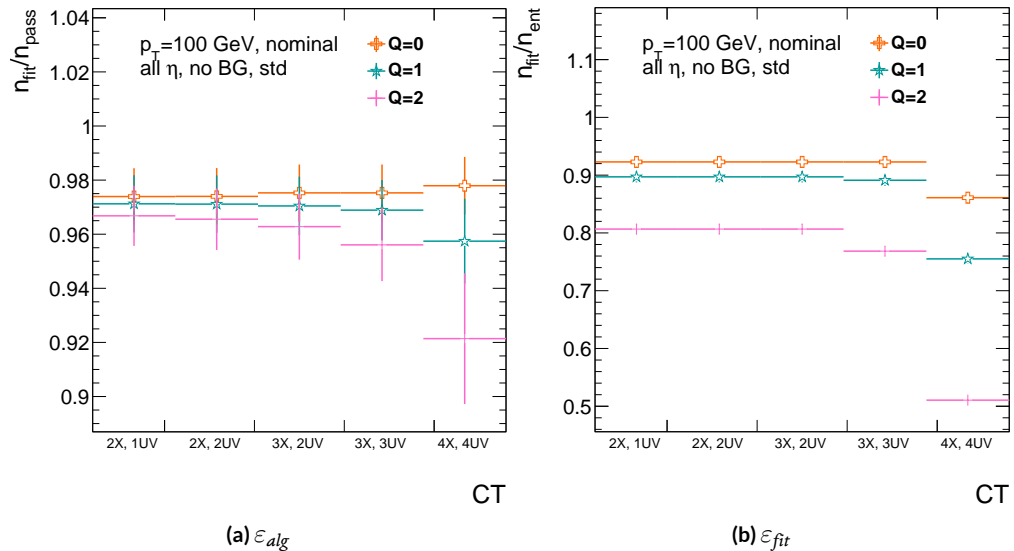


**Figure A.15:** The efficiencies as a function of coincidence threshold for charge thresholds of 0, 1, and 2.

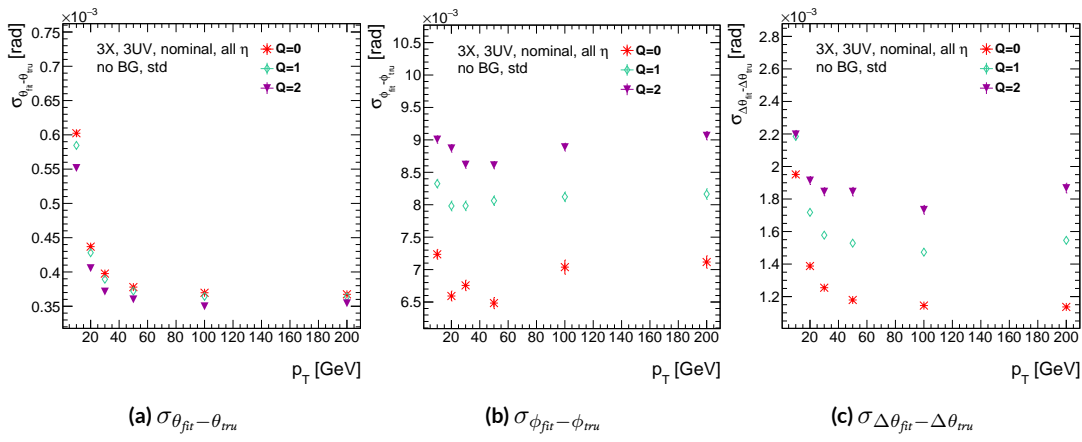


**Figure A.16:** The fit quantity residual rms values as a function of  $p_T$  for charge thresholds of 0, 1, and 2.

2381 A.9 MISALIGNMENTS AND CORRECTIONS

2382 The performance of the trigger algorithm under misalignment has been studied for each of the six  
2383 alignment quantities (three translations and three rotations all along the principal axes) described  
2384 in [? ] and [? ], whose convention we will follow here. For the simulated wedge studied here the  
2385 local coordinates described in [? ] are taken to be centered at the center of the base of the wedge<sup>\*\*</sup>,  
2386 the local  $t$  axis corresponds to the axis of the beam line, the local  $z$  axis corresponds to the direction  
2387 orthogonal to both the beam line and the horizontal strips, and the local  $s$  axis completes the right-  
2388 handed coordinate system. The rotation angles  $\alpha$ ,  $\beta$ , and  $\gamma$  correspond to rotations around the local  
2389  $t$ ,  $z$ , and  $s$  axes, respectively. Note that the local  $s$ ,  $z$ , and  $-t$ , axes correspond to the usual global  $x$ ,  $y$ ,  
2390 and  $z$  axes. Misalignments were studied in twenty evenly spaced increments from nominal positions  
2391 to misalignments of 1.5 mrad for the rotations (-1.5 mrad to +1.5 mrad for the  $\gamma$  case), and of 5 mm  
2392 (a roughly corresponding linear shift) for the translations. In all cases, the front quadruplet is mis-  
2393 aligned while the rear quadruplet remains in its nominal position. While only the front quadruplet  
2394 of a single wedge is misaligned, the framework for misalignment presented below could be used to  
2395 study generic local and global misalignments. The six misalignments are schematically represented  
2396 in Figure A.17.

2397 Chamber misalignments manifest themselves as altered strips in algorithm input. In order to sim-  
2398 ulate the effects of misalignment, the change in the local  $y$  coordinate—the distance from the bot-

---

2399 \*\*Not, as is sometimes the case, the centroid position for simplicity's sake, as the agreed upon geometry  
of the detector changed several times while studies were in progress; any transformation in a centroid-origin  
coordinate system can of course be formed by a combination of the six transformations examined.

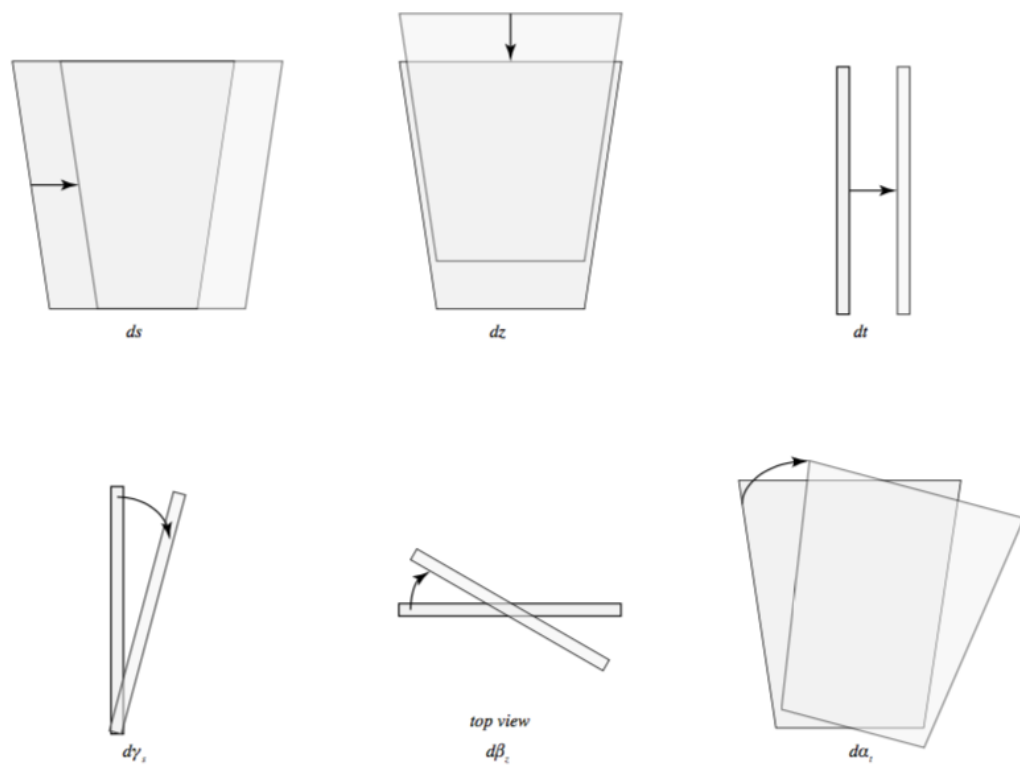


**Figure A.17:** The different misalignment cases as defined in the AMDB manual.

2399 tom wedge center in the direction perpendicular to both the beamline and the strip direction—is  
 2400 calculated for a track coming straight from the interaction point defined by the truth-level  $\theta$  and  $\phi$   
 2401 angles for generic misalignment. This displacement in  $y$  is then added to input hit information and  
 2402 the algorithm is then run normally.

2403 To understand how this displacement is calculated, some notation first needs to be described.

**Table A.2:** A summary of notation used in this section: note that non-AMDB notation is used in this section.

Symbol	Definition
$s_x, s_y, s_z, \vec{s}$	Position of the muon hit in ATLAS global coordinates; the infinite momentum muon track
$\hat{n}$	Vector normal to the plane; taken to be $\hat{z}$ (the beamline) in the nominal case
$\vec{\mathcal{O}}_{IP}^{g,l}$	Position of the interaction point in ATLAS global ( $g$ ) or wedge local ( $l$ ) coordinates
$\vec{\mathcal{O}}_{base}^{g,l}$	Position of the plane base in ATLAS global ( $g$ ) or wedge local ( $l$ ) coordinates; $(0, y_{base}, z_{pl})$ ( $(0, 0, 0)$ ) for the nominal case in global (local) coordinates
$\vec{\zeta}$	$\vec{s} - \vec{\mathcal{O}}_{base}$
primed quant.	quantities after misalignment

2404 Generically speaking, a hit is the intersection of a line (the muon track) with a plane (the individual  
 2405 plane in the multiplet). We assume the muon moves in a straight line defined by the origin and  
 2406 the truth-level  $\theta_{pos}$  and  $\phi_{pos}$  (i.e. the infinite momentum limit) and that the MM plane is rigid and  
 2407 defined by a point, which we take to be the center of the bottom edge of the plane, and a normal  
 2408 vector, which we take to be the  $z$  axis in the nominal case.

2409 The coordinate axes  $x, y, z$  axes used here correspond to the usual AMDB  $s, z, -t$  axes. Since the  
 2410 direction does not really matter when studying misalignment or corrections thereof, the major dif-

<sup>2411</sup> ference is the choice of origin.

<sup>2412</sup> The muon track we denote<sup>††</sup>  $\vec{s}$ , the bottom point of the plane  $\vec{\mathcal{O}}_{base}$ , and the normal vector  $\hat{n}$ .

<sup>2413</sup> The muon track will always be given as (the wedge gets moved, not the muon):

$$\vec{s} = \mathcal{O}_{IP} + k\hat{s} \quad (\text{A.8})$$

$$\hat{s} = \sin \theta_{pos} \sin \phi_{pos} \hat{x} + \sin \theta_{pos} \cos \phi_{pos} \hat{y} + \cos \theta_{pos} \hat{z} \quad (\text{A.9})$$

$$\vec{s} = k\hat{s} = \frac{z_{pl}}{\cos \theta_{pos}} \hat{s} = z_{pl} (\tan \theta \sin \phi \hat{x} + \tan \theta \cos \phi \hat{y} + 1) \quad (\text{A.10})$$

<sup>2414</sup> where  $k \in \mathbb{R}$ , along with the unit vector  $\hat{s}$ , defines the point where the track intersects the wedge.

<sup>2415</sup> Rotations are done before translations, according to the order prescribed in the AMDB guide for

<sup>2416</sup> chamber alignment, so the axes the principal axes of the plane are rotated according to the following

<sup>2417</sup> matrix (where  $s$ ,  $c$ , and  $t$  are the obvious trigonometric substitutions)

$$\begin{aligned} & \begin{pmatrix} 1 & 0 & 0 \\ 0 & c\gamma & -s\gamma \\ 0 & s\gamma & c\gamma \end{pmatrix} \begin{pmatrix} c\beta & 0 & s\beta \\ 0 & 1 & 0 \\ -s\beta & 0 & c\beta \end{pmatrix} \begin{pmatrix} c\alpha & -s\alpha & 0 \\ s\alpha & c\alpha & 0 \\ 0 & 0 & 1 \end{pmatrix} = \begin{pmatrix} 1 & 0 & 0 \\ 0 & c\gamma & -s\gamma \\ 0 & s\gamma & c\gamma \end{pmatrix} \begin{pmatrix} c\alpha c\beta & -s\alpha c\beta & s\beta \\ s\alpha & c\alpha & 0 \\ -c\alpha s\beta & s\alpha s\beta & c\beta \end{pmatrix} \\ & = \boxed{\begin{pmatrix} c\alpha c\beta & -s\alpha c\beta & s\beta \\ s\alpha c\gamma + c\alpha s\beta s\gamma & c\alpha c\gamma - s\alpha s\beta s\gamma & -c\beta s\gamma \\ s\alpha s\gamma - c\alpha s\beta c\gamma & c\alpha s\gamma + s\alpha s\beta c\gamma & c\beta c\gamma \end{pmatrix}} = \mathcal{A} \end{aligned} \quad (\text{A.II})$$

---

<sup>††</sup>Recall  $\phi_{pos}$  is defined with respect to the  $y$  axis instead of the  $x$  axis, as might otherwise be typical.

2418     The thing that matters is what the new strip hit is—i.e. what the new  $y$  value is since this, along  
 2419     with a plane number, is all that is fed into the algorithm. To find this, we must solve for the new  
 2420     point of intersection with the rotated plane and then apply the effects of translations. The path con-  
 2421     necting the base of the wedge with the intersection of the muon track will always be orthogonal to  
 2422     the normal vector of the plane. Our quantities after misalignment, denoted by primed quantities,  
 2423     will look like

$$\mathcal{O}_{base} \rightarrow \mathcal{O}_{base} + ds\hat{x} + dz\hat{y} + dt\hat{z} = \mathcal{O}'_{base}, \quad \hat{n} \rightarrow A\hat{n} = A\hat{z} = \hat{z}', \quad \vec{s} \rightarrow k'\hat{s} + \mathcal{O}_{IP} = \vec{s}' \quad (\text{A.12})$$

2424     so, moving to explicit, global coordinates in the last line so we can do the computation (relying on  
 2425     the fact that any vector in the wedge, namely  $\vec{\zeta} = \vec{s} - \mathcal{O}$  the local coordinates of the interaction  
 2426     point, is necessarily orthogonal to  $\hat{n}$ ):

$$0 = \hat{n} \cdot (\vec{\mathcal{O}}_{base} - \vec{s}) \rightarrow 0 = A\hat{z}' \cdot (\vec{\mathcal{O}}'_{base} - (k'\hat{s} + \vec{\mathcal{O}}_{IP})) \quad (\text{A.13})$$

$$\rightarrow k' = \frac{s\beta\vec{\mathcal{O}}'_{base-IP,x} - c\beta s\gamma\vec{\mathcal{O}}'_{base-IP,y} + c\beta c\gamma\vec{\mathcal{O}}'_{base-IP,z}}{\hat{s} \cdot \hat{z}'} \quad (\text{A.14})$$

$$= \frac{s\beta ds - c\beta s\gamma(y_{base} + dz) + c\beta c\gamma(z_{pl} + dt)}{s\beta s\theta s\phi - c\beta s\gamma s\theta c\phi + c\beta c\gamma c\theta} \quad (\text{A.15})$$

2427     To find our new  $y$  coordinate, we need to evaluate  $s'_y = \hat{y}' \cdot k'\vec{s}$  to find the final correction of:

$$\Delta y = \vec{\zeta}' \cdot \hat{y}' - \vec{\zeta} \cdot \hat{y} = (k'\hat{s} - \vec{\mathcal{O}}'_{base}) \cdot \hat{y}' - (s_y - y_{base}) \quad (\text{A.16})$$

<sup>2428</sup> The correction will be plane dependent since (denoting the stereo angle  $\omega$ ):

$$\hat{y}_x = \hat{y} \rightarrow \hat{y}'_x = -s\alpha c\beta \hat{x} + (c\alpha c\gamma - s\alpha s\beta s\gamma) \hat{y} + (c\alpha s\gamma + s\alpha s\beta c\gamma) \hat{z} \quad (\text{A.17})$$

<sup>2429</sup> and

$$\begin{aligned} \hat{y}_{U,V} = & \pm s\omega \hat{x}' + c\omega \hat{y}'_{U,V} = [\pm c\alpha c\beta s\omega - s\alpha c\beta c\omega] \hat{x} + [\pm (s\alpha c\gamma + c\alpha s\beta s\gamma) s\omega \\ & + (c\alpha c\gamma - s\alpha s\beta s\gamma) c\omega] \hat{y} + [\pm (s\alpha s\gamma - c\alpha s\beta c\gamma) s\omega + (c\alpha s\gamma + s\alpha s\beta c\gamma) c\omega] \hat{z} \end{aligned} \quad (\text{A.18})$$

## <sup>2430</sup> A.10 INDIVIDUAL CASES

<sup>2431</sup> Currently we only study the cases where one misalignment parameter is not zero. We examine these  
<sup>2432</sup> in detail below, calculating the most pertinent quantities in the misalignment calculation,  $k'/k$  and  
<sup>2433</sup> the new horizontal and stereo  $y$  axes. Before setting out, we simplify the expressions for the trans-  
<sup>2434</sup> formed  $\hat{y}'$ 's, removing any terms with the product of two sines of misalignment angles, which will be  
<sup>2435</sup> zero.<sup>††</sup>

$$\hat{y}'_x = -s\alpha c\beta \hat{x} + c\alpha c\gamma \hat{y} + c\alpha s\gamma \hat{z} \quad (\text{A.19})$$

<sup>2436</sup>

$$\hat{y}'_{U,V} = [\pm c\alpha c\beta s\omega - s\alpha c\beta c\omega] \hat{x} + [\pm s\alpha c\gamma s\omega + c\alpha c\gamma c\omega] \hat{y} + [\mp c\alpha s\beta c\gamma s\omega + c\alpha s\gamma c\omega] \hat{z} \quad (\text{A.20})$$

---

<sup>††</sup>If only one misalignment parameter is non-zero, then two or more sines will contain at least one term will contain  $\sin 0 = 0$ .

<sup>2437</sup> If the translations are zero,

$$k' = \frac{-c\beta s\gamma y_{base} + c\beta c\gamma z_{pl}}{s\beta s\theta s\phi - c\beta s\gamma s\theta c\phi + c\beta c\gamma \theta}, \quad k'/k = \frac{-c\beta s\gamma y_{base}/z_{pl} + c\beta c\gamma}{s\beta t\theta s\phi - c\beta s\gamma t\theta c\phi + c\beta c\gamma} \quad (\text{A.21})$$

<sup>2438</sup> A.II  $ds \neq 0$

<sup>2439</sup>  $k'/k = 1$  (the point of intersection does not move closer or further from the IP), and only the stereo  
<sup>2440</sup> planes are affected. Note that only relevant term in Equation A.16, for the stereo strip  $\hat{y}$  for  $\vec{\mathcal{O}}'_{base} =$   
<sup>2441</sup>  $ds\hat{x}$  is:

$$\pm \sin \omega ds \approx \pm 0.0261 ds \quad (\text{A.22})$$

<sup>2442</sup> meaning that a displacement in  $x$  of 17 mm, more than three times the range of misalignments studied,  
<sup>2443</sup> would be necessary for a shift in the stereo planes corresponding to one strip width.

<sup>2444</sup> A.12  $dz \neq 0$

<sup>2445</sup>  $k'/k = 1$  (the point of intersection does not move closer or further from the IP). This case is the  
<sup>2446</sup> trivial one (cf. Equation A.16 with  $\vec{\mathcal{O}}'_{base} = dz\hat{y}$ ).  $y$  just gets moved in the opposite direction as the  
<sup>2447</sup> wedge. Correction is an additive constant.

<sup>2448</sup> A.13  $dt \neq 0$

<sup>2449</sup>  $k'/k = (z_{pl} + dt) / z_{pl}$ .  $y$  gets modified by a simple scale factor. Correct by storing changing definitions  
<sup>2450</sup> of plane positions in algorithm to match the misaligned values.

<sup>2451</sup> A.14  $\alpha \neq 0$

<sup>2452</sup>  $k'/k = 1$  and

$$\hat{y}'_x = -s\alpha\hat{x} + c\alpha\hat{y} \quad (\text{A.23})$$

$$\hat{y}'_{U,V} = [\pm c\alpha s\omega - s\alpha c\omega] \hat{x} + [\pm s\alpha s\omega + c\omega] \hat{y} \quad (\text{A.24})$$

<sup>2453</sup> A.15  $\beta \neq 0$

<sup>2454</sup> We have  $k'/k = (1 + \tan \beta \tan \theta \sin \phi)^{-1}$ , and

$$\hat{y}'_x = \hat{y} \quad (\text{A.25})$$

$$\hat{y}'_{U,V} = \hat{y} \pm (c\beta\hat{x} - s\beta\hat{z}) s\omega \quad (\text{A.26})$$

<sup>2455</sup> A.16  $\gamma \neq 0$

$$k'/k = \frac{1 - \tan \gamma \frac{y_{base}}{z_{pl}}}{1 - \tan \gamma \tan \theta \cos \phi} \quad (\text{A.27})$$

$$\hat{y}'_x = c\gamma\hat{y} + s\gamma\hat{z} \quad (\text{A.28})$$

$$\hat{y}'_{U,V} = \pm s\omega\hat{x} + c\omega\hat{y} - s\gamma c\omega\hat{z} \quad (\text{A.29})$$

<sup>2456</sup> In order to evaluate algorithm performance under misalignment and corrections for misalignment, the absolute means and relative resolutions of the fit quantities  $\theta$ ,  $\phi$ , and  $\Delta\theta$  are measured as

2458 a function of misalignment. In the following, results will only be shown for which the effects of mis-  
2459 alignment are significant. “Significant,” for misalignments of 1 mm (0.3 mrad) for translations (ro-  
2460 tations) means more than a 5% degradation in rms and/or bias shifts in  $\theta$ ,  $\phi$ , and  $\Delta\theta$  of 0.01 mrad, 1  
2461 mrad, and 0.1 mrad, respectively.

2462 While corrections are typically done on a case-by-base basis, they fall under two general cate-  
2463 gories, analytic and simulation based. Analytic corrections rely upon specific knowledge of the mis-  
2464 alignment, with each case being handled separately; as such, the additional resources required, both  
2465 extra constants and operations, if any, vary accordingly. Simulation based corrections are all done in  
2466 the same manner. The algorithm is run over a training MC sample (same setup but with  $p_T = 200$   
2467 GeV instead of the normal 100 GeV sample so as not to overtrain the corrections), and the mean bi-  
2468 ases for  $\theta$ ,  $\phi$ , and  $\Delta\theta$  are saved for different, equally spaced regions in the  $\eta - \phi$  plane over the wedge  
2469 based on the fitted  $\theta$  and  $\phi$  values. Currently, these values are saved for 10  $\eta$  and 10  $\phi$  bins (100  $\eta, \phi$   
2470 bins total), with the number of bins in each direction being a configurable parameter. When the al-  
2471 gorithm runs with simulation based correction, this table of constant corrections is saved in a LUT  
2472 before runtime, and corrections are added to final fit quantities based on the (uncorrected)  $\theta$  and  
2473  $\phi$  fit values. With the settings mentioned, this is 300 extra constants ( $10\eta\text{-bins} \times 10\phi\text{-bins} \times 3$  fit  
2474 quantities) and two extra operations (a lookup and addition for each quantity done in parallel). The  
2475 simulation correction can, in principle, also be applied to the algorithm in nominal conditions with  
2476 non-trivial improvements, as detailed below in Section A.17. Depending on the misalignment case in  
2477 question, different approaches work better. A summary of correction methods, including resources  
2478 necessary for the individual analytic cases, is shown in Table A.3.

	$\Delta_s$	$\Delta z$	$\Delta t$	$\gamma_s$	$\beta_z$	$\alpha_t$
Analytic Resources	yes+ 11c/2op	yes+ oc/oop	yes+ oc/oop	yes 56c/1op	no —	yes 400c/2n <sub>X</sub> op, 32c/12n <sub>X</sub> op
Simulation	yes+	no	no	no	yes+	yes+

**Table A.3:** A summary of corrections with additional constants/operations (written as  $n_{const}c/n_{ops}op$ ;  $n_X$  is the number of X hits in a fit) necessary for analytic corrections. Yes means a correction exists but might not entirely remove misalignment effects, while yes+ means a quality of correction is only limited by knowledge of misalignment and memory

<sup>2479</sup> A.17 SIMULATION CORRECTION OF THE ALGORITHM UNDER NOMINAL CONDITIONS

<sup>2480</sup> In addition to using simulation based correction to counter the effects of several classes of misalign-  
<sup>2481</sup> ment, the correction can be applied at to the algorithm under nominal conditions. The main effect  
<sup>2482</sup> of this correction is to mitigate the effects of the bias in stereo strips. As such, the correction has a  
<sup>2483</sup> larger effect on quantities that rely on the aggregate slope  $m_y$ , as can be seen in in Figure A.18, im-  
<sup>2484</sup> proving  $\sigma_{\theta_{fit} - \theta_{tru}}$  resolution by about 25%, and reducing  $\sigma_{\phi_{fit} - \phi_{tru}}$  by over 50% and restoring a largely  
<sup>2485</sup> Gaussian shape. The slight, apparent degradation in  $\Delta\theta$  is due to a more mild version of the effect  
<sup>2486</sup> seen in Figure A.7.

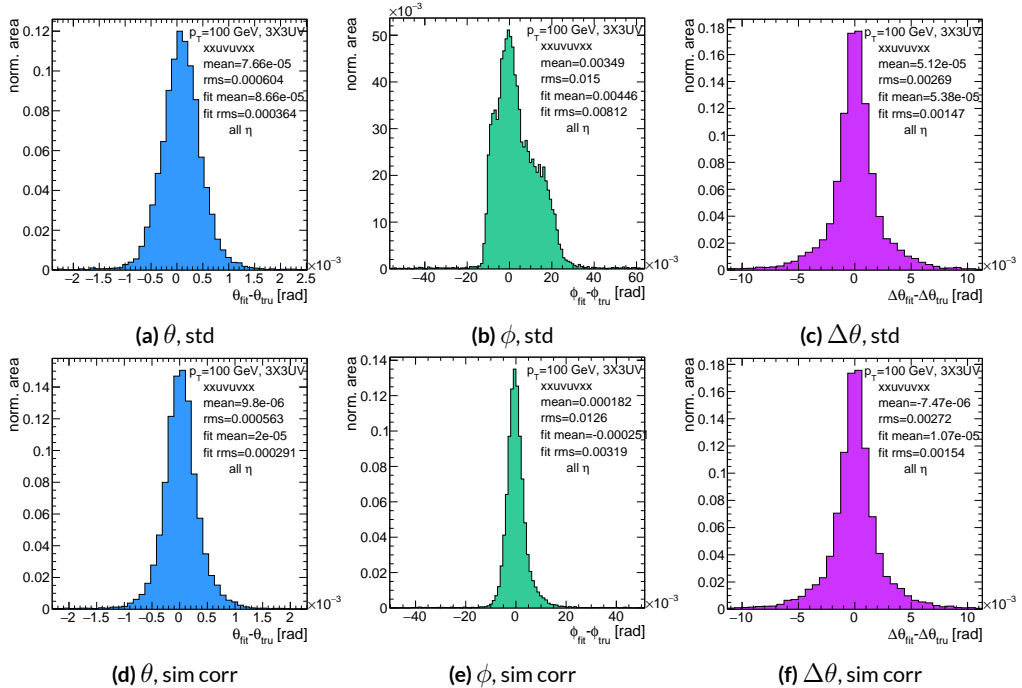


**Figure A.18:** Nominal residual plots for both uncorrected and simulation corrected cases;  $\theta$ ,  $\phi$ ,  $\Delta\theta$  for  $p_T = 100$  GeV muons

2487 As can be seen in Figure A.19, the simulation based correction also removes the  $\eta$  dependence to  
 2488 fit quantity resolution distributions, as expected. One consequence of this is that simulation-based  
 2489 corrections applied to the misalignment cases below will restore performance to the “sim” and not  
 2490 the “std” distributions of Figure A.18. Hence, when making comparisons between simulation cor-  
 2491 rected curves and the nominal performance point, simulation-corrected distributions of benchmark  
 quantities versus misalignment will often look generally better.

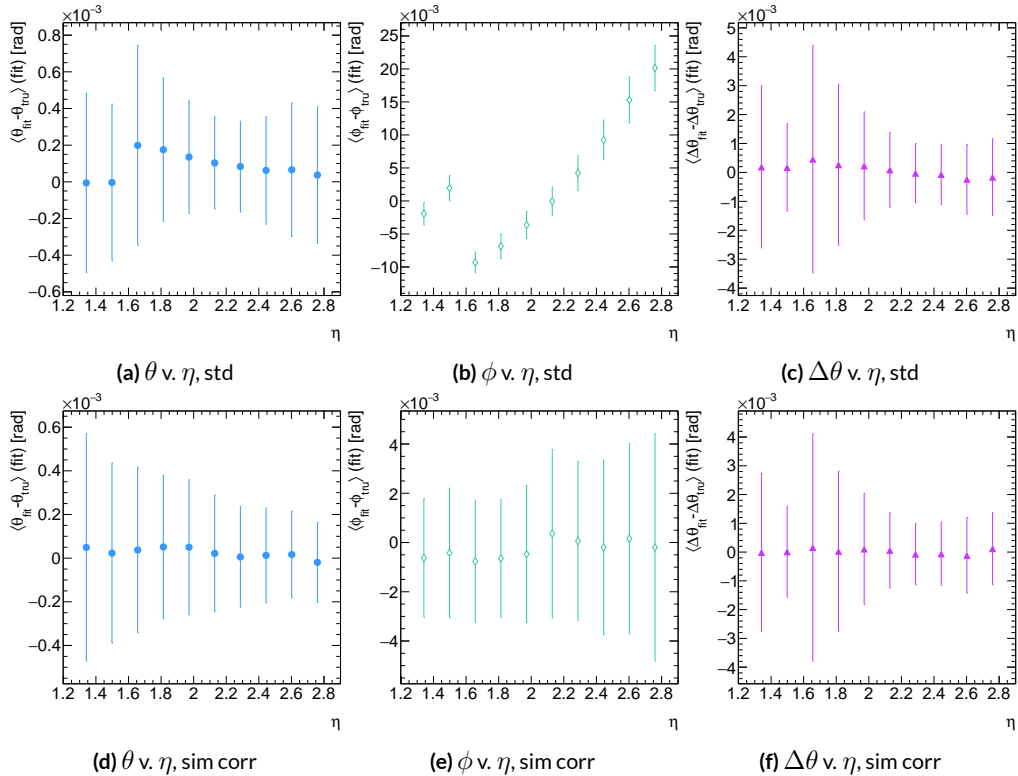


**Figure A.19:** Nominal residual plots as a function of  $\eta$  with points as means and error bars as rms values in each  $\eta$  bin for the angles  $\theta, \phi, \Delta\theta$  for  $p_T = 100$  GeV muons in the uncorrected and simulation corrected cases.

2492  
 2493 That the improvements from a simulation-based correction improve performance of the algo-

2494 rithm in nominal conditions most for the quantities that depend most on stereo information ( $\phi$  and  
 2495  $\theta$ ) and remove the  $\eta$  dependence of fit quantity resolutions suggests that there could, in principle, be  
 2496 analytic corrections that could be applied to the nominal algorithm. One possible solution is to in-  
 2497 troduce an additional set of constants, having the  $y_{base}$  depend on the strip number, similar to the  $\gamma_s$   
 2498 correction for  $z_{plane}$  described in Section A.21, which would add a lookup per hit and  $8 \times n_{bins,y}$  extra  
 2499 constants that would be optimized as the  $\gamma_s$  correction was.

$$M_{hit} = \frac{\gamma}{z} = \frac{y_{base}}{z_{plane}} (n_{str}) + \frac{w_{str}}{z_{plane}} n_{str} \quad (\text{A.30})$$

2500 The simulation correction residual rms values suggest a limit on the quality of such correction  
 2501 and could perhaps be implemented generically on their own regardless of misalignment for rms val-  
 2502 ues on fit quantities of 0.291 mrad for  $\theta$ , 3.19 mrad for  $\phi$ , and 1.54 for  $\Delta\theta$ , which represent a 20%  
 2503 improvement for  $\theta$ , a 62% improvement for  $\phi$ , and a slight degradation in  $\Delta\theta$  of 4.7%, again owing  
 2504 to an effect similar to the one in A.7.

2505 A.18 TRANSLATION MISALIGNMENTS ALONG THE HORIZONTAL STRIP DIRECTION ( $\Delta s$ )

2506 A translation in  $s$  (i.e. along the direction of a horizontal strip) only affects the stereo strips, and,  
2507 since the stereo angle is small, a very large misalignment is necessary for effects to be noticeable (a  
2508 misalignment of roughly 17 mm corresponds to one strip's misalignment in the stereo planes). The  
2509 only quantity to show any meaningful deviation with misalignments with translations in  $s$  is the  $\phi$   
2510 residual bias (a change of 0.4 mrad at  $\Delta s = 1$  mm), as can be seen in the uncorrected curve of Figure  
2511 A.20.

2512 A translation in  $s$  induces a constant shift in the calculated horizontal slope,  $m_x$  in Equation A.4.  
2513 This constant shift should only depend on which stereo planes included in a fit are misaligned and  
2514 how misaligned they are. Hence, the correction to  $m_x$ , for a sum over misaligned stereo planes  $i$ ,  
2515 with their individual misalignments in  $s$  and plane positions in  $z$  is:

$$\Delta m_x = \frac{1}{N_{\text{stereo}}} \sum_{i, \text{misal stereo}} \frac{\Delta s_i}{z_{i, \text{plane}}} \quad (\text{A.31})$$

2516 Given prior knowledge of misalignment, these corrections to  $m_x$  can be performed ahead of time  
2517 and saved in a lookup table (LUT), similar to the LUT used for constants in the X local slope ( $M_x^l$ )  
2518 calculation. The added overhead of this analytic correction is hence eleven constants in memory, a  
2519 lookup, and one addition. The correction perfectly corrects the effects of misalignment, as can be  
2520 seen in Figure A.20. The simulation based correction described above can also be used to correct  
2521 for  $\Delta s$  misalignments, with the results of that correction also shown in Figure A.20. The apparent

2522 discrepancy between the simulated and analytic correction is a natural consequence of the fact that  
 2523 the simulation correction, as previously mentioned, restores the  $\phi$  residual distribution to an overall  
 2524 more Gaussian shape.

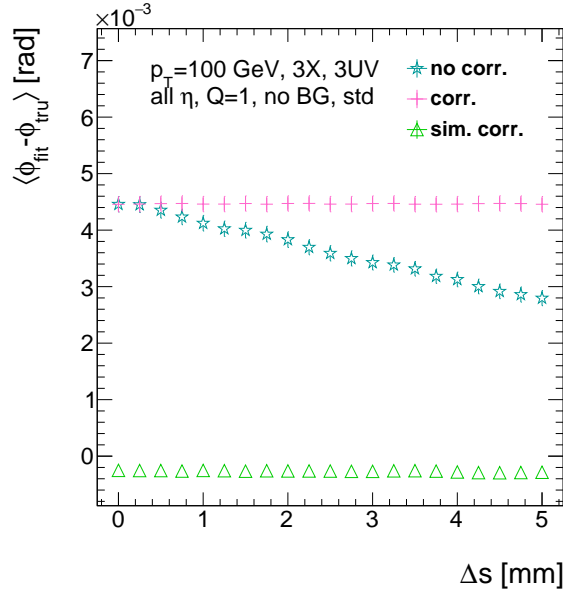


**Figure A.20:** The mean of the  $\phi$  residual as a function of misalignment for the uncorrected case and the analytic and simulation correction cases.

2525 A.19 TRANSLATION MISALIGNMENTS ORTHOGONAL TO THE BEAMLINE AND HORIZON-  
2526 TAL STRIP DIRECTION ( $\Delta z$ )

2527 A translation in AMDB  $z$ , the direction orthogonal to both the beamline and the horizontal strip  
2528 direction, corresponds to a translation in the  $y$  of Equation A.1, affecting all slope calculations. This  
2529 has a large impact on the  $\theta$  residual bias and both the bias and rms of  $\Delta\theta$  residual, as can be seen in  
2530 Figures A.21 (a)–(c). The marked degradation and non-linear behavior in performance at very high  
2531 levels of misalignments is a result of low statistics; there are fewer fits at high level of misalignments  
2532 since for  $\Delta z \gtrsim 3$  mm, most fits will fail the  $\Delta\theta$  cut. The  $\theta$  bias shifts by about 0.075 mrad at  $\Delta z =$   
2533 1 mm, and  $\Delta\theta$  shifts by about 5 mrad for the same level of misalignment. While the fitted rms of the  
2534  $\Delta\theta$  residual remains fairly stable for  $\Delta z < 1$  mm or so, between  $\Delta z = 2$  mm and  $\Delta z = 3$  mm, the  
2535 rms increases by 15% before the  $\Delta\theta$  cut issue mentioned above intervenes.

2536 Fortunately, these misalignments are straightforward to correct with knowledge of the misalign-  
2537 ment. The only modification necessary for this correction is to change the definitions of  $y_{base}$  in  
2538 Equation A.1 for the individual hit slope addressing. This is done before runtime and adds no over-  
2539 head to the algorithm, and the correction quality is only limited by knowledge of the misalignment.  
2540 The results of this correction are also shown in Figures A.21 (a)–(c) and restore nominal perfor-  
2541 mance.

---

Since  $\Delta\theta = \frac{M_x^l - M_x^e}{1 + M_x^l M_x^e}$  and  $M_x^l = B_k \sum y_i (z/\bar{z} - 1)$ , a shift  $\Delta y$  translates (with typical slope values of  $\sim 0.3$ ) to  $5B_k (z_1 + z_2)/\bar{z}$  (with  $B_k$  in units of inverse mm); set equal to 16 mrad ( $\Delta\theta$  is centered at zero), this corresponds to  $\Delta y = 2.7$  mm

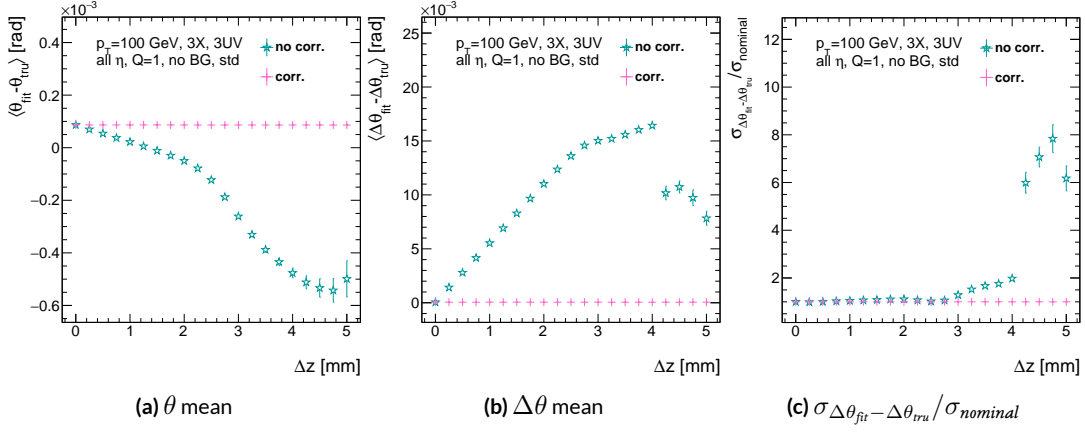


**Figure A.21:** The affected quantities of  $\Delta z$  misalignments:  $\theta$  bias,  $\Delta\theta$  bias, and  $\sigma_{\Delta\theta_{\text{fit}} - \Delta\theta_{\text{tru}}} / \sigma_{\text{nominal}}$  for both the misaligned and corrected cases.

2542 A.20 TRANSLATION MISALIGNMENTS PARALLEL TO THE BEAMLINE ( $\Delta t$ )

2543 The effects of misalignment due to translations in  $t$  are very similar to those due to translations in  
 2544  $z$  without the complication of the  $\Delta\theta$  cut, affecting the  $z$  instead of the  $y$  coordinate that enters  
 2545 into hit slope calculations. Again,  $\theta$  bias,  $\Delta\theta$  bias, and  $\sigma_{\Delta\theta_{fit}-\Delta\theta_{true}}$  are the primarily affected quan-  
 2546 tities. For  $\Delta t = 1$  mm,  $\theta$  bias shifts by about 0.02 mrad,  $\Delta\theta$  bias shifts by just under 2 mrad, and  
 2547  $\sigma_{\Delta\theta_{fit}-\Delta\theta_{true}}$  degrades by about 20%. The correction for this misalignment once again costs no over-  
 2548 head and consists of changing stored constants in the algorithm, in this case the positions along the  
 2549 beamline of the misaligned planes, with results similarly limited by knowledge of the misalignment.

2550 The slight improvement with correction to  $\Delta\theta$  rms is due to the real effect of a larger lever arm.

2551 Both the misaligned and corrected distributions of affected quantities of interest are shown in Fig-  
 ure A.22.

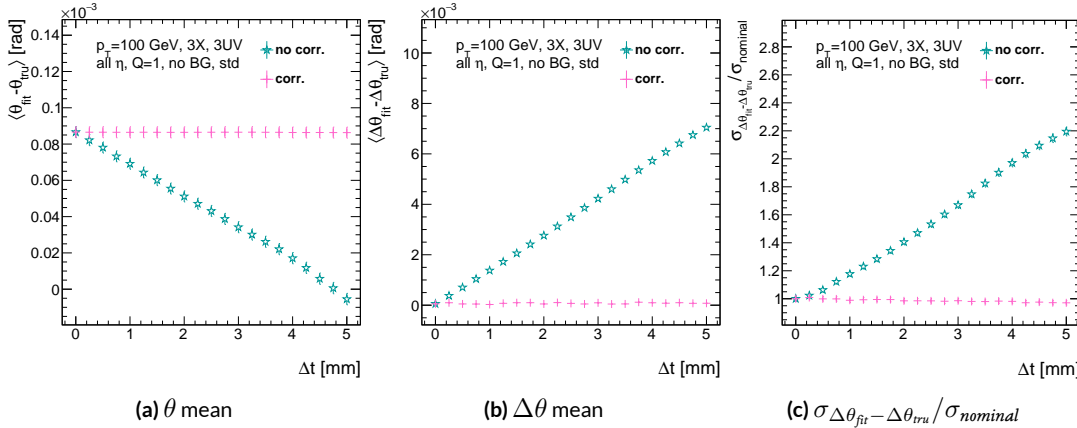


Figure A.22: The affected quantities of  $\Delta t$  misalignments:  $\theta$  bias,  $\Delta\theta$  bias, and  $\sigma_{\Delta\theta_{fit}-\Delta\theta_{true}} / \sigma_{nominal}$  for both the misaligned and corrected cases.

2553 A.21 CHAMBER TILTS TOWARDS AND AWAY FROM THE IP ( $\gamma_s$  ROTATION)

2554 Chamber misalignment due to rotations around the  $s$  axis act effectively like a translation in  $t$  that  
2555 depends on strip number. These rotations tilt misaligned chambers away from (towards) the IP for  
2556 positive (negative) values of  $\gamma_s$ . Since, unlike for the other two rotation cases that will be studied,  
2557 positive and negative rotation values are not symmetric, this misalignment is studied for both posi-  
2558 tive and negative  $\gamma_s$  values. The divergent effect at the tails is a result of a large population of fits not  
2559 having fit quantities within the cores, and so not appearing in the fit rms. Once again, affected quan-  
2560 tities of interest  $\theta$  bias,  $\Delta\theta$  bias, and  $\sigma_{\Delta\theta_{fit}-\Delta\theta_{tru}}$ . The effects of misalignment can be seen in Figures  
2561 A.23 (a)–(c). The relationship between biases and  $\gamma_s$  is roughly linear with  $\Delta\gamma_s = 0.3$  mrad (the an-  
2562 gular scale corresponding to linear shifts of  $\sim 1$  mm) corresponding to 0.005 mrad (0.12 mrad) for  $\theta$   
2563 ( $\Delta\theta$ ). For  $\sigma_{\Delta\theta_{fit}-\Delta\theta_{tru}}$ , degradation is not symmetric. For negative (positive)  $\gamma_s$ , with the quadruplet  
2564 tilted towards (away from) the IP, slope-roads are artificially expanded (shrunk), decreasing (increas-  
2565 ing) the granularity of the trigger, explaining the asymmetry in Figure A.23 (c), with the degradation  
2566 being a 10% (25%) effect for  $\gamma_s$  of  $+(-)0.3$  mrad.

2567 Corrections are less simple in this case. In principle, corrections of the same accuracy of the trans-  
2568 lations could be calculated per strip, but the overhead of one correction per strip (many thousands  
2569 of constants) is prohibitive. Instead, each plane was divided into eight equal segments with a  $t$  value  
2570 ( $z$  in the slope calculation) assigned to strips in each region to correct for the misalignment. This  
2571 amounts to 56 extra constants and a 2D instead of a 1D LUT for  $z$  positions while the algorithm  
2572 runs. The corrected distributions can also be seen in Figures A.23 (a)–(c). The corrections, while not

as effective as for the simple translation cases, are still very effective with the quoted misalignment values for bias shifts down to 0.001 mrad (0.25 mrad) for  $\theta$  ( $\Delta\theta$ ) and no more than a 2% degradation in  $\sigma_{\Delta\theta_{fit}-\Delta\theta_{true}}$  for  $|\gamma_s| = 0.3$  mrad.

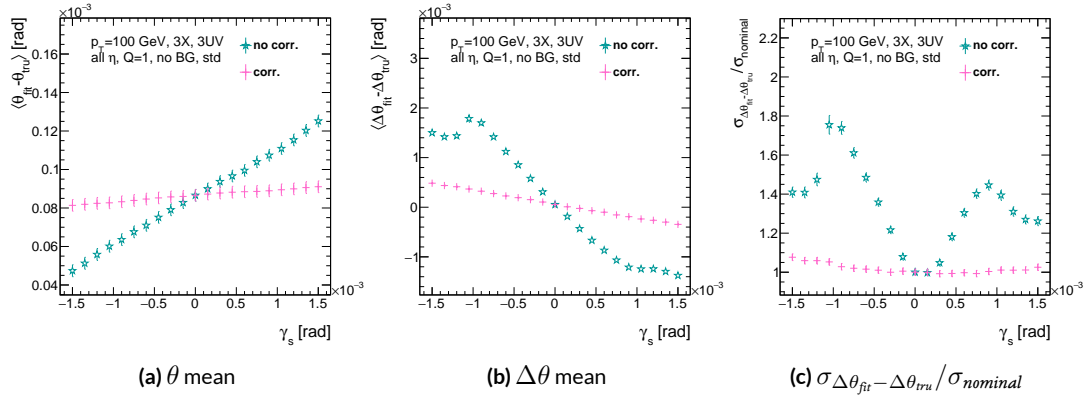


**Figure A.23:** The noticeable effects of rotations in the  $s$  axis and the behavior of these quantities ( $\theta$  and  $\Delta\theta$  bias shifts and  $\sigma_{\Delta\theta_{fit}-\Delta\theta_{true}} / \sigma_{nominal}$ ) with and without misalignment correction.

2576 A.22 ROTATION MISALIGNMENTS AROUND THE WEDGE VERTICAL AXIS ( $\beta_z$ )

2577 While misalignments coming from rotations around the  $z$  axis (the direction orthogonal to both  
 2578 the beamline and the horizontal strip direction) foreshorten the strips as seen from the IP and add  
 2579 a deviation in  $t$ , the long lever arm largely washes out any effects of this misalignment. Only the  
 2580  $\sigma_{\Delta\theta_{fit}-\Delta\theta_{tru}}$  is noticeably affected, though only at severe misalignments, with only about a 1% degra-  
 2581 dation in performance at  $\beta_z = 0.3$  mrad (corresponding to a linear shift of  $\sim 1$  mm). A simulation  
 2582 based correction works well to cancel out the effects of this misalignment, and the  $\sigma_{\Delta\theta_{fit}-\Delta\theta_{tru}}$  as a  
 2583 function of misalignment with and without corrections are shown in Figure A.24. The apparent  
 2584 2% effect in the simulation corrected curve is a result of a more mild version of the effect shown in  
 2585 Figure A.7.

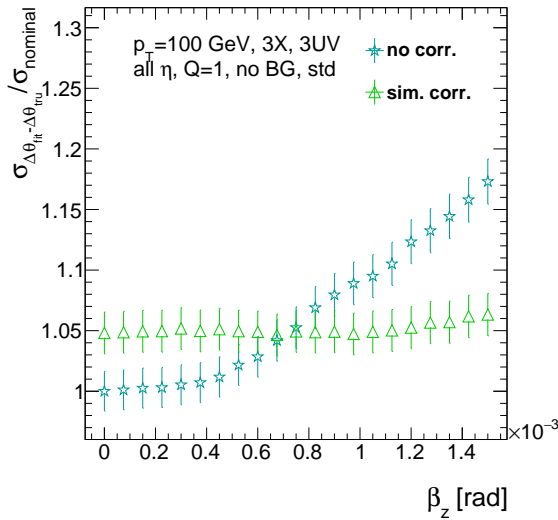
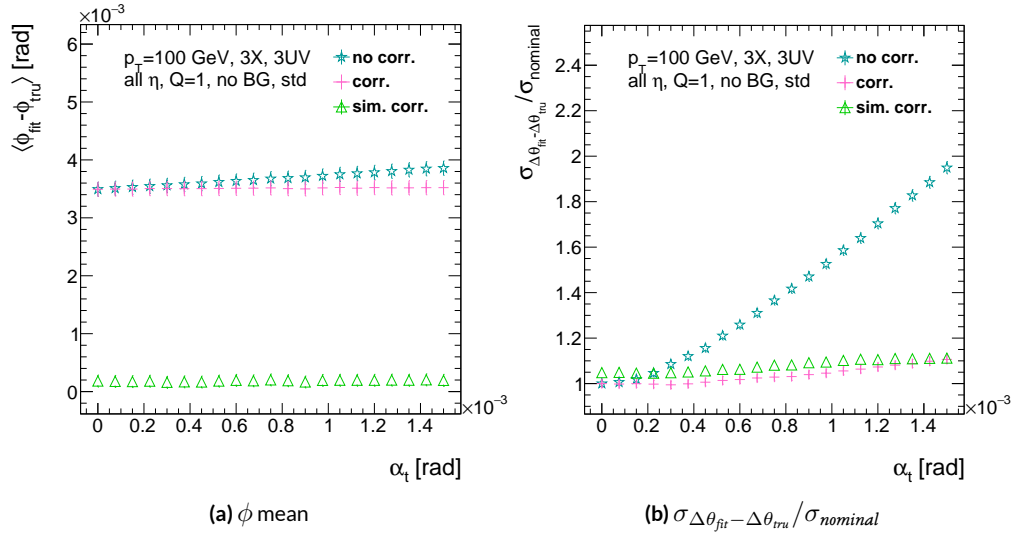


Figure A.24: The effects of rotations in the  $z$  axis on  $\sigma_{\Delta\theta_{fit}-\Delta\theta_{tru}} / \sigma_{nominal}$  a function of  $\beta_z$  both with and without misalignment corrections.

2586 A.23 ROTATION MISALIGNMENTS AROUND THE AXIS PARALLEL TO THE BEAMLINE ( $\alpha_t$ )

2587 Misalignments arising from rotations around the  $t$  axis (parallel to the beamline at the center of  
2588 the base of the wedge) are essentially rotations in the  $\phi$  direction. The quantities of interest most  
2589 affected are the  $\phi$  bias and  $\sigma_{\Delta\theta_{fit}-\Delta\theta_{tru}}$ , as shown in Figures A.25 (a) and (b), respectively, and cor-  
2590 respond to a shift in  $\phi$  bias of 0.2 mrad and a 10% degradation in  $\sigma_{\Delta\theta_{fit}-\Delta\theta_{tru}}$  for  $\alpha_t = 0.3$  mrad  
2591 (corresponding to a linear shift of  $\sim 1$  mm). The raw instead of fitted mean  $\phi$  biases is used in Fig-  
2592 ure A.25 (a) to better illustrate the effect of misalignment.

2593 Since the effect of misalignment is dependent on horizontal (along the strip direction,  $\hat{s}$ ) in addi-  
2594 tion to vertical information, corrections cannot be applied before a fit takes place. The  $\phi$  bias shift is  
2595 uniform over the entire wedge, so a constant additive correction to  $\phi$  based on the level of misalign-  
2596 ment can be applied to all fits depending on how many misaligned stereo planes enter in the fit.  $\Delta\theta$   
2597 is less straightforward, but corrections to the  $y$  and  $z$  information used in the local slope calculation  
2598 in Equation A.4 can be applied once  $\theta_{fit}$  and  $\phi_{fit}$  are known. These corrections are calculated ahead  
2599 of time in bins of uniform  $\eta$  and  $\phi$  as with the simulation corrections using the same framework  
2600 as the misalignment calculation. The results of both types of correction can be seen in Figure A.22.  
2601 The apparent discrepancy between the simulation and analytic corrections in the  $\phi$  bias happens for  
2602 the same reason as in the  $\Delta s$  misalignment correction cases, as simulation correction restores a more  
2603 Gaussian shape to the  $\phi$  residual distribution opposed to the uncorrected nominal case, as discussed  
2604 in Section A.17.



**Figure A.25:** The effects of rotation misalignments around the  $t$  axis for  $\phi$  bias and  $\sigma_{\Delta\theta_{\text{fit}} - \Delta\theta_{\text{true}}} / \sigma_{\text{nominal}}$  as a function of misalignment. The uncorrected and both the analytic and simulation correction cases are shown.

2605 A.24 CONCLUSION

2606 The algorithm for Micromegas detectors in the NSW Trigger Processor performs well in a variety of  
2607 conditions and has proven robust to a number of effects to deliver measurements on muon tracks  
2608 of the three angles  $\theta$ ,  $\phi$ ,  $\Delta\theta$ . Under nominal conditions, the rms values for the residuals of these  
2609 quantities are 0.364 mrad for  $\theta$ , 8.12 mrad for  $\phi$ , and 1.47 mrad for  $\Delta\theta$ . Algorithm performance was  
2610 found to be largely independent of the charge threshold setting, and a hit majority BCID associa-  
2611 tion was found to provide proper timing information over 99.7% even in the most relaxed settings  
2612 (2X+1UV coincidence threshold requirement+wide slope-road+background). The introduction of  
2613 wide slope-roads to better mimic potentially limited algorithm resources at run time and the intro-  
2614 duction of incoherent background was found to have a manageable effect on fit quantity residual  
2615 rms values and on total algorithm efficiency for sufficiently stringent coincidence threshold. The ef-  
2616 ffects of the three translation and three rotation misalignments specified by AMDB convention were  
2617 studied, and correction methods for each of the six cases was developed. Simulation-based correc-  
2618 tions were found to improve nominal algorithm performance to residual rms value of 0.291 mrad for  
2619  $\theta$ , 3.19 mrad for  $\phi$ , and 1.54 for  $\Delta\theta$ , which represent improvements of 20%, 62%, and -4.7%, respec-  
2620 tively. Misalignment corrections were found to restore nominal performance for all but the rotation  
2621 around the  $s$  axis, and a summary of tolerances may be found in Table A.4.

	No Correction	Correction
$\Delta s$	4 mm ( $\phi$ bias)	> 5 mm
$\Delta z$	0.25 mm ( $\Delta\theta$ )	> 5 mm
$\Delta t$	0.25 mm ( $\Delta\theta$ )	> 5 mm
$\gamma_s$	0.15 mrad ( $\Delta\theta$ bias)	0.75 mrad
$\beta_z$	0.9 mrad ( $\Delta\theta$ rms)	> 1.5 mrad
$\alpha_t$	0.375 mrad ( $\Delta\theta$ rms)	> 1.5 mrad

**Table A.4:** A summary of levels of misalignment corresponding to a 10% degradation in any residual rms or, for biases shifts of 0.01 mrad for  $\theta$ , 1 mrad for  $\phi$ , and 0.25 mrad for  $\Delta\theta$  for both the uncorrected and corrected cases; > 5 mm and > 1.5 mrad mean that such a degradation does not occur for the range of misalignment studied. Most affected quantity in parentheses.

*Tod-Not-Brot*

Old German Proverb

# B

2622

2623

## Telescoping Jets

2624 ANOTHER APPROACH TO IMPROVING  $ZH \rightarrow \ell\ell b\bar{b}$  is the use of telescoping jets [36], which har-  
2625 nesses the power of multiple event interpretations. The use of multiple event interpretations was  
2626 originally developed with non-deterministic jet algorithms like the Q-jets (“quantum” jets) algo-  
2627 rithm [69]. When a traditional or “classical” algorithm, such as the Cambridge-Aachen[81] and

2628 anti- $k_t$ [63] algorithms, is applied to an event, it produces one set of jets for that event, i.e. a single  
2629 interpretation of that event. With multiple event interpretations, each event is instead given an en-  
2630 semble of interpretations. In the case of Q-jets, this ensemble is created through a non-deterministic  
2631 clustering process for an anti- $k_t$  jet algorithm. With telescoping jets, multiple jet cone radii (the char-  
2632 acteristic size parameter,  $R$ ) around a set of points in the pseudorapidity-azimuth ( $\eta - \phi$ ) plane are  
2633 used to generate a series of jet collections. Instead of an event passing or not-passing a given set of  
2634 cuts, a fraction (called the cut-weight,  $z$ ) of interpretations will pass these cuts. This cut-weight al-  
2635 lows for enhanced background suppression and increased significance of observed quantities for a  
2636 given data set, as detailed in Ref. [47]. The telescoping jets algorithm provides the benefits of mul-  
2637 tiple event interpretations without the significant computational overhead of a non-deterministic  
2638 algorithm like the Q-jets algorithm, and its multiple cone sizes are particularly suited to studying  
2639 processes like associated production, which suffers from a pronounced low tail in the dijet invariant  
2640 mass distribution due to final state radiation (FSR) “leaking” outside the relatively narrow jets used  
2641 for object reconstruction.

## 2642 B.I MONTE CARLO SIMULATION

2643 The MC simulated samples used in this study are the same as in Ref. [? ]. The signal sample used  
2644 is generated in PYTHIA8 [77] with the CTEQ6L1 parton distributions functions (PDFs) and AU2  
2645 tune[55, 2, 3] for the  $ZH$  process with  $m_H = 125$  GeV (henceforth,  $ZH125$ ). The primary back-  
2646 ground processes examined in this study were  $Z$ -jets with massive  $b$  and  $c$  quarks. These samples  
2647 are generated with version 1.4.1 of the SHERPA generator [76].

2648 B.2 JET RECONSTRUCTION AND CALIBRATION

2649 In order to construct telescoping jets, jet axes must first be found around which to “telescope.” In  
2650 the reconstructed-level analysis, the anti- $k_t$  algorithm with  $R = 0.4$  is used to reconstruct jets from  
2651 topological clusters in the calorimeters. The four vectors of these anti- $k_t$  algorithm with  $R = 0.4$   
2652 jets are calibrated to match truth information obtained from simulation and validated in data. To  
2653 take into account the effect of pile-up interactions, jet energies are corrected using a jet-area based  
2654 technique [32], and each jet with  $p_T < 50$  GeV and  $|\eta| < 2.4$  is subject to a requirement that at least  
2655 50% of the scalar sum of the  $p_T$  of tracks matched to this jet be composed of tracks also associated  
2656 with the primary vertex. Jet energies are also calibrated using  $p_T$  and  $\eta$ -dependent correction factors  
2657 [11]. Furthermore, at least two jets must have  $|\eta| < 2.5$  in order to be  $b$ -tagged. The MV1 algorithm  
2658 [4? ? ? ?] is used for  $b$ -tagging. Once jets are reconstructed and  $b$ -tag weights have been calculated,  
2659 the two hardest,  $b$ -tagged jets are used as the telescoping jet axes. Additional details can be found in  
2660 Ref. [12].

2661 After the telescoping jet axes have been established, telescoping jets are constructed using topo-  
2662 logical clusters in the calorimeters at a variety of jet cone sizes. Including the original anti- $k_t$  jets  
2663 used for the  $R = 0.4$  case, twelve total sets of jets of cone sizes ranging from  $R = 0.4\text{--}1.5$  are  
2664 constructed, with each successive size having a radius 0.1 larger than the preceding set. For each jet  
2665 axis, telescoping jets consist of any topological cluster lying within  $R$  of the axis. In the event of over-  
2666 lap, clusters are assigned to the closer jet axis. If a given cluster is equidistant from the two jet axes,  
2667 the cluster is assigned to whichever jet axis is associated with the anti- $k_t$  jet with higher  $p_T$ . Calibra-

tion for the telescoping jets is conducted using corrections for anti- $k_t$  calorimeter topological cluster jets; the  $R = 0.4$  corrections are used for telescoping  $R = 0.5$ , and the  $R = 0.6$  corrections are used for telescoping  $R \geq 0.6$  (cf. Sec. B.4). The telescoping cone jets ( $R \geq 0.5$ ) at reconstructed level are trimmed using Cambridge-Aachen jets with  $R = 0.3$  and  $f_{cut} = 0.05$  with respect to the untrimmed jet  $p_T$  [48]. Since these jets are trimmed, the active area correction is not applied. In the event a  $Z$  candidate electron falls within  $R$  of the axis of a telescoping jet, its 4-momentum is subtracted from that of the jet vectorially.

A similar process is used to construct telescoping jets in the truth-level analysis below. Instead of the two hardest  $b$ -tagged anti- $k_t$  with  $R = 0.4$  jets reconstructed with calorimeter topological clusters, the two hardest truth  $b$ -jets in an event are used. Instead of making a cut on  $b$ -tagging weight to  $b$ -tag, truth jets are examined to see whether a  $b$ -hadron with  $p_T > 5$  GeV is contained within  $\Delta R < 0.4$  of the jet axis; the presence of a  $b$ -hadron is used to  $b$ -tag truth-level jets. These two jets again provide the jets for the  $R = 0.4$  case and the axes around which telescoping takes place. Stable truth particles, not including muons and neutrinos, are used in place of calorimeter topological clusters.  $Z$  candidate electron-telescoping jet overlap removal is performed at truth level, too. Missing  $E_T$  is calculated using the vector sum of the four momenta of stable truth-level neutrinos. Since there are no pileup particles stored at truth level, truth-level telescoping jets are not trimmed.

### B.3 EVENT RECONSTRUCTION AND SELECTION

Events are selected on the basis of a combination of leptonic, jet, and missing  $E_T$  requirements, which are outlined in Table B.1. Leptons are categorized by three sets of increasingly stringent qual-

2688   ity requirements, which include lower limits on  $E_T$ , upper limits on  $|\eta|$ , impact-parameter require-  
2689   ments, and track-based isolation criteria. The requirements differ for electrons [5] and muons [1].  
2690   Events are selected with a combination of single lepton, dielectron, and dimuon requirements. Each  
2691   event must contain at least one lepton passing medium requirements and at least one other lepton  
2692   passing loose requirements. These leptons are used to create a dilepton invariant mass cut to ensure  
2693   the presence of a  $Z$  boson and suppress multijet backgrounds.

2694   Event selection requirements are also imposed on the anti- $k_t$  with  $R = 0.4$  jets. There must be at  
2695   least two  $b$ -tagged jets in a given event. The  $p_T$  of the harder  $b$ -tagged jet must be at least 45 GeV, and  
2696   the second  $b$ -tagged jet must have  $p_T$  of at least 20 GeV. There are further topological cuts on the  
2697   separation of the two jets  $\Delta R(b, \bar{b})$ , the distance between the two jets in the  $(\eta, \phi)$  plane, according  
2698   to the transverse momentum of the  $Z$  boson,  $p_T^Z$ . These are shown in Table B.2.

2699   The truth-level analysis has the same missing  $E_T$ , jet  $p_T$ ,  $m_{ll}$ , and additional topological selection  
2700   criteria, but the use of truth-level information simplifies the other requirements. Instead of lepton  
2701   quality requirements,  $Z$  boson candidate leptons' statuses and MC record barcodes are checked to  
2702   ensure the leptons are stable.

2703   In the jet calibration validation, the reconstructed level analysis lepton and  $m_{ll}$  requirements are  
2704   imposed, but neither the missing  $E_T$  nor the jet selection requirements are applied so as not to bias  
2705   the validation.

**Table B.1:** A summary of basic event selection requirements. Truth-level  $b$ -tagging is done with truth-level information.

Requirement	Reconstructed	Truth	Validation
Leptons	1 medium + 1 loose lepton	2 produced by $Z$ boson	1 medium + 1 loose lepton
$b$ -jet	2 $b$ -tags	2 $b$ -jets	—
$p_T$ jet 1 (jet 2)		$> 45 \text{ GeV} (> 20) \text{ GeV}$	—
Missing $E_T$		$E_T^{\text{miss}} < 60 \text{ GeV}$	—
$Z$ boson		$83 < m_{ll} < 99 \text{ GeV}$	

**Table B.2:** Topological requirements of the event selection.

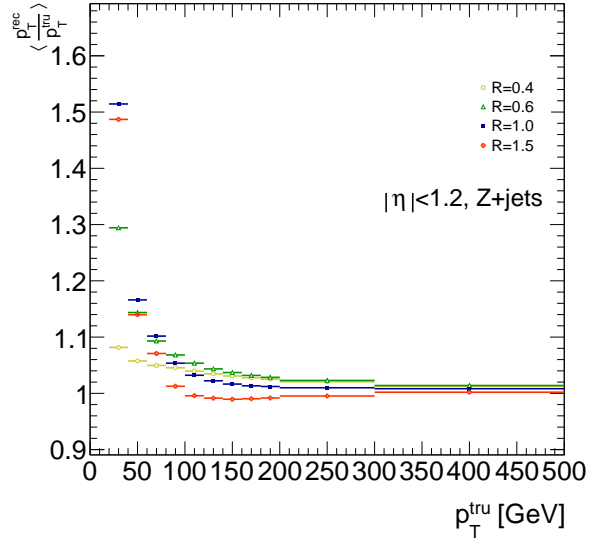
$p_T^Z [\text{GeV}]$	$\Delta R(b, b)$
0–90	0.7–3.4
90–120	0.7–3.0
120–160	0.7–2.3
160–200	0.7–1.8
$> 200$	$< 1.4$

2706 B.4 VALIDATION OF JET CALIBRATION

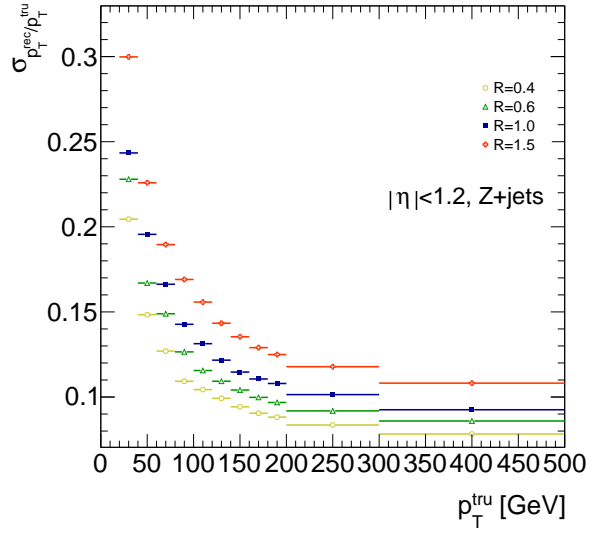
2707 In order to validate the jet energy scale and resolution of jets constructed with this telescoping-jets  
2708 algorithm, values of  $p_T^{rec}/p_T^{tru}$  are studied for each value of  $R$  for the  $Z+jets$  MC sample. In a given  
2709 event, all jets, not just the two hardest  $b$ -tagged jets, are telescoped. These jets are constructed in the  
2710 same way as in the reconstructed and truth-level analyses; reconstructed-level jets are made from  
2711 calorimeter topological clusters within  $R$  of the anti- $k_t$  with  $R = 0.4$  jet axes and then trimmed,  
2712 and truth-level jets are made from stable truth particles within  $R$  of the anti- $k_t$  with  $R = 0.4$  jet  
2713 axes. The reconstructed and truth-level telescoping jet ensembles are matched according to the sep-  
2714 aration in the  $(\eta, \phi)$  plane of their corresponding anti- $k_t$  with  $R = 0.4$  jets used as seeds. Only jets  
2715 with  $|\eta| < 1.2$  are examined here, and the results of studies on the  $ZH125$ ,  $ZZ$ , and  $t\bar{t}$  samples, as  
2716 well as over other  $|\eta|$  ranges, are outlined in [36]. Any reconstructed jets not within  $\Delta R = 0.3$  of a  
2717 truth jet are discarded. In the event that multiple reconstructed jets are the same distance away from  
2718 a given truth jet, the reconstructed jet with the highest  $p_T$  gets matched. Matching is retained for all  
2719  $R$  values (i.e. telescoping seeds are matched, and telescoping jets are assumed to match if the anti- $k_t$   
2720 jets from which their seeds are derived match).

2721 Once anti- $k_t$  with  $R = 0.4$  reconstructed and truth jets are matched, response functions are cre-  
2722 ated by generating a series of distributions of  $p_T^{rec}/p_T^{tru}$  in 20 GeV bins of  $p_T^{tru}$  from 20–200 GeV, one  
2723 bin for 200–300 GeV, and one bin for 300–500 GeV for each  $R$ , with bins chosen for purposes of  
2724 statistics. Ensembles with  $p_T^{tru} < 20$  GeV are ignored since no calibration exists for jets with trans-  
2725 verse momentum below this value. The values of  $\langle p_T^{rec}/p_T^{tru} \rangle$  in each  $p_T^{tru}$  bin are calculated by doing

2726 a two sigma gaussian fit on the distribution of  $p_T^{rec}/p_T^{tru}$  in that bin and taking the mean of that fit,  
2727 and the error on the mean is taken from the error of this parameter in the fit. The resolutions are the  
2728 values of the square root of the variance on this fit. As the total response distributions in Figure B.1  
2729 show, performance is best for low  $R$  values and high values of  $p_T^{tru}$ . Figure B.1 shows the  $R = 0.4$   
2730 ( $anti k_t$ ) case to show a baseline for performance,  $R = 0.6$  to show the deviations with “correct”  
2731 calibrations, and  $R = 1.0, 1.5$  to show how big those deviations get with larger  $R$  jets. The resolu-  
2732 tions,  $\sigma_{p_T^{rec}/p_T^{tru}}$ , as a function of  $p_T^{tru}$  are shown in Figure B.1(b). For  $p_T^{tru} > 60$  GeV, response is fairly  
2733 consistent over various  $R$  values. Resolution, as might naively be expected, is worse for increasingly  
2734 larger values of  $R$ . For  $p_T^{tru} < 60$  GeV, resolution degrades, and response degrades in particular for  
2735 increasing  $R$ ; this is likely a result from residual pileup effects.



(a)



(b)

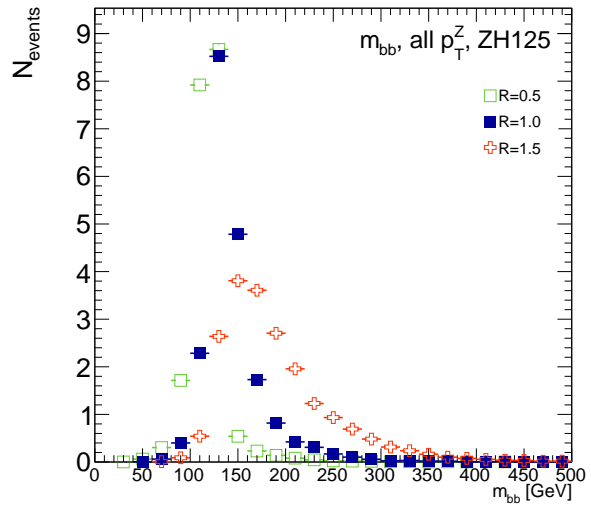
**Figure B.1:** The mean and resolution of  $p_T^{rec}/p_T^{tru}$  for the background  $Z+jets$  sample for  $|\eta| < 1.2$  and for  $R = 0.4, 0.6, 1.0$ , and  $1.5$  in  $20\text{ GeV}$  bins of  $p_T^{tru}$  for  $20\text{--}200\text{ GeV}$ , one bin for  $200\text{--}300\text{ GeV}$ , and one bin for  $300\text{--}500\text{ GeV}$ , with bins chosen for purposes of statistics.

2736 B.5 TRUTH-LEVEL ANALYSIS

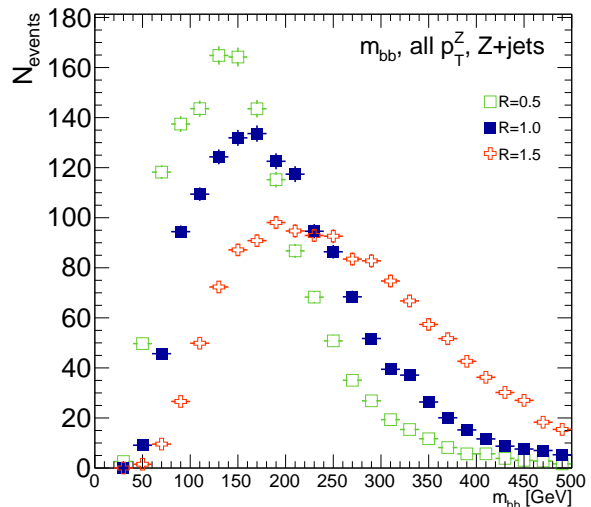
2737 To understand the limits and sources of any potential improvements, a truth-level analysis was con-  
2738 ducted on MC samples with a  $ZH_{125}$  signal sample and a  $Z+jets$  background sample. Distributions  
2739 for the dijet invariant mass,  $m_{bb}$ , were made for each telescoping radius. Both signal and background  
2740 samples develop more pronounced tails in the high  $m_{bb}$  region as  $R$  increases, as shown in Figure  
2741 B.2.  $N_{events}$  is normalized to expected values in data.

2742 One way to take advantage of this information is to make a cut on  $m_{bb}$  for two different radii.  
2743 This is graphically depicted in Figure B.3 for the optimized combination of  $m_{bb,R=0.9}$  (telescoping  
2744 cone jets constructed as outlined in Sec. B.2) vs.  $m_{bb,R=0.4}$  (anti- $k_t$  jets). At truth-level, the majority  
2745 of events in the signal  $ZH_{125}$  sample are concentrated in relatively narrow region of parameter space,  
2746 where this is certainly not the case for the more diffuse  $Z+jets$  background sample.

2747 Another way to take advantage of multiple event interpretations is to make use of an event's cut-  
2748 weight, denoted  $z$  and defined as the fraction of interpretations in a given event that pass a certain set  
2749 of cuts (in this note, a cut on  $m_{bb}$ ). The distribution of cut-weights for a sample of events is denoted  
2750  $\rho(z)$ . To enhance the significance of a cut-based analysis, events can be weighted by the cut-weight  
2751 or any function  $t(z)$  of the cut-weight. Weighting events by  $t(z)$  modifies the usual  $S/\delta B$  formula  
2752 used to calculate significances. In this note,  $\delta B$  is based on Poissonian statistics and is taken as  $0.5 +$   
2753  $\sqrt{0.25 + N_B}$ , where  $N_B$  is the number of background events.

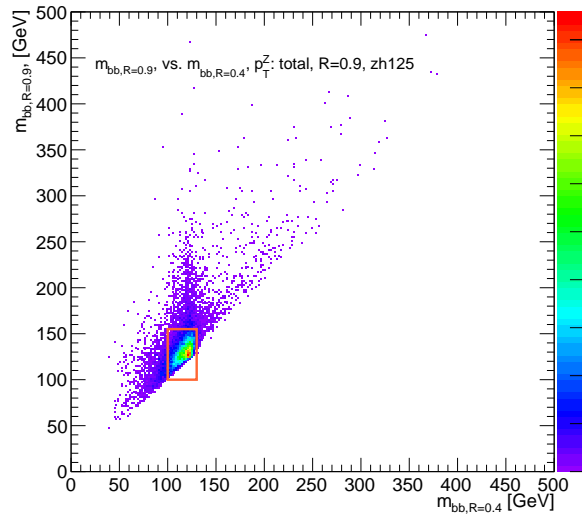


(a)

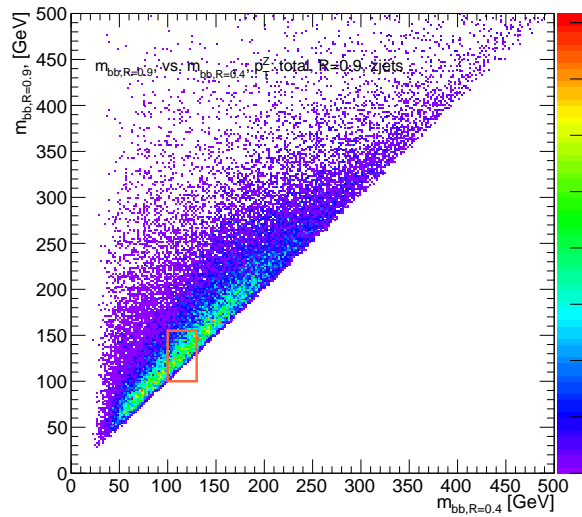


(b)

**Figure B.2:** The  $m_{bb}$  distribution for the telescoping jets with  $R = 0.5, 1.0$ , and  $1.5$  truth-level jets is shown for the signal and background samples in (a) and (b), respectively.



(a)



(b)

**Figure B.3:** The 2D distribution of  $m_{bb,R=0.9}$  vs.  $m_{bb,R=0.4}$  is shown for signal and background truth-level samples in (a) and (b), respectively. The region chosen for the double  $m_{bb}$  cut is outlined in orange.

2754 B.6 ERRORS ON TELESCOPING SIGNIFICANCES

2755 Significances of measurements are quoted in units of expected background fluctuations, schemati-  
2756 cally,  $S/\delta B$ . For counting experiments with high numbers of events, we can use Gaussian statistics  
2757 and express this as  $S/\sqrt{B}$ , which we here denote as  $\mathcal{S}$ . However, with lower statistics, it becomes  
2758 more appropriate to use Poissonian statistics, and

$$\mathcal{S}_{gaus} = \frac{S}{\sqrt{B}} \rightarrow \mathcal{S}_{pois} = \frac{S}{0.5 + \sqrt{0.25 + B}} \quad (\text{B.1})$$

2759 where  $0.5 + \sqrt{0.25 + B}$  is the characteristic upward fluctuation expected in a Poissonian data set  
2760 using the Pearson chi-square test[79].

2761 B.7 COUNTING

2762 The significance is given as above, where  $S = N_S$  and  $B = N_B$ . That is, the signal and background  
2763 are just the number of events in signal and background that pass some cuts. The error for the Guas-  
2764 sian case is the standard:

$$\Delta \mathcal{S}_{gaus} = \frac{1}{\sqrt{B}} \Delta S \oplus \frac{S}{2B^{3/2}} \Delta B \quad (\text{B.2})$$

2765 The error for the Poissonian case is:

$$\Delta \mathcal{S}_{pois} = \frac{1}{0.5 + \sqrt{0.25 + B}} \Delta S \oplus \frac{S}{2(0.5 + \sqrt{0.25 + B})^2 \sqrt{0.25 + B}} \Delta B \quad (\text{B.3})$$

<sup>2766</sup> where  $\oplus$  denotes addition in quadrature, and  $\Delta S(B)$  is the error on signal (background).

## <sup>2767</sup> B.8 MULTIPLE EVENT INTERPRETATIONS

<sup>2768</sup> Using multiple event interpretations changes the formulae used in with simple counting. That is,  $S$

<sup>2769</sup> is not necessarily merely  $N_S$ , the number of events passing some signal cuts, and similarly for  $B$  and

<sup>2770</sup>  $N_B$ . Using an event weighting by some function of the cut-weight,  $z$ , denoted  $t(z)$ ,  $S = N_S \langle t \rangle_{\rho_S}$

<sup>2771</sup> and  $B = N_B \langle t^2 \rangle_{\rho_B}$ . So

$$\mathcal{S}_{t,gaus} = \frac{N_S \langle t \rangle_{\rho_S}}{\sqrt{N_B \langle t^2 \rangle_{\rho_B}}} \rightarrow \mathcal{S}_{t,pois} = \frac{N_S \langle t \rangle_{\rho_S}}{0.5 + \sqrt{0.25 + N_B \langle t^2 \rangle_{\rho_B}}} = \frac{N_S \int_0^1 dz t(z) \rho_S(z)}{0.5 + \sqrt{0.25 + N_B \int_0^1 dz t^2(z) \rho_B(z)}} \quad (\text{B.4})$$

For histograms, everything is done bin-wise. The notation used below is as follows:  $\rho_i$  is the

value of  $\rho(z)$  at bin  $i$  (where the bins run from 0 to  $n_{tel}$ , where  $n_{tel}$  is the total number of telecop-

ing radii).  $t_i = t_i(\rho_{S,i}, \rho_{B,i}, i/n_{tel})$  is the value of  $t(z)$  at bin  $i$ , which can depend, in principle, on

$\rho_{S,i}$ ,  $\rho_{B,i}$ , and  $i/n_{tel}$  (the last of which is  $z$  in bin  $i$ ). Explicitly,

$$N = \sum_{i=0}^{n_{tel}} \rho_i, \quad \int_0^1 dz t(z) \rho_S(z) = \sum_{i=0}^{n_{tel}} t_i \rho_{S,i}, \quad \int_0^1 dz t^2(z) \rho_B(z) = \sum_{i=0}^{n_{tel}} t_i^2 \rho_{B,i}$$

<sup>2772</sup> For the calculations that follow, let  $\xi = \sum_{i=0}^{n_{tel}} t_i \rho_{S,i}$ ,  $\psi = 0.5 + \sqrt{0.25 + N_B \sum_{i=0}^{n_{tel}} t_i^2 \rho_{B,i}}$ ,

<sup>2773</sup>  $\partial_S = \frac{\partial}{\partial \rho_{S,i}}$  (and similarly for  $B$ ), so  $\mathcal{S}_t = N_S \xi / \psi$

<sup>2774</sup> Some partial derivatives:

$$\begin{aligned}
 \partial_S N_S &= 1, & \partial_{B,i} N_B &= 1 \\
 \partial_S \xi &= t_i + (\partial_S t_i) \rho_{S,i}, & \partial_B \xi &= (\partial_B t_i) \rho_{B,i} \\
 \partial_S \psi &= \frac{N_B t_i (\partial_S t_i) \rho_{B,i}}{\sqrt{0.25 + N_B \sum_{i=0}^{n_{tel}} t_i^2 \rho_{B,i}}}, & \partial_B \psi &= \frac{\sum_{i=0}^{n_{tel}} t_i^2 \rho_{B,i} + N_B (t_i^2 + 2t_i (\partial_B t_i) \rho_{B,i})}{2\sqrt{0.25 + N_B \sum_{i=0}^{n_{tel}} t_i^2 \rho_{B,i}}} \\
 \partial_S \mathcal{S}_t &= \frac{\xi}{\psi} + \frac{N_S}{\psi} \partial_S \xi - \frac{N_S \xi}{\psi^2} \partial_S \psi, & \partial_B \mathcal{S}_t &= N_S \left( \frac{1}{\psi} \partial_B \xi - \frac{\xi}{\psi^2} \partial_B \psi \right)
 \end{aligned}$$

<sup>2775</sup> Thus,

$$\Delta \mathcal{S}_{t,i} = \left[ \frac{\xi}{\psi} + \frac{N_S}{\psi} \partial_S \xi - \frac{N_S \xi}{\psi^2} \partial_S \psi \right] \Delta \rho_{S,i} \oplus N_S \left[ \frac{1}{\psi} \partial_B \xi - \frac{\xi}{\psi^2} \partial_B \psi \right] \Delta \rho_{B,i} \quad (\text{B.5})$$

<sup>2776</sup> and the total error is given by the sum in quadrature over all bins  $i$  of  $\Delta \mathcal{S}_{t,i}$ .

<sup>2777</sup> B.9  $t(z) = z$

<sup>2778</sup> With  $t(z) = z$ ,  $t_i = i/n_{tel}$ , so  $\partial_S t_i = \partial_B t_i = 0$ . So:

$$\begin{aligned}
 \partial_S \psi &= \partial_B \xi = 0 \\
 \partial_S \xi &= \frac{i}{n_{tel}} \\
 \partial_B \psi &= \frac{\sum_i i^2 \rho_{B,i} + N_B t^2}{n_{tel} \sqrt{n_{tel}^2 + N_B \sum_i i^2 \rho_{B,i}}}
 \end{aligned}$$

<sup>2779</sup> so  $\Delta\mathcal{S}_{z,i}$  reduces to

$$\Delta\mathcal{S}_{t,i} = \left[ \frac{\xi + N_S t_i}{\psi} \right] \Delta\rho_{S,i} \oplus \left[ \frac{N_S \xi}{\psi^2} \partial_B \psi \right] \Delta\rho_{B,i} \quad (\text{B.6})$$

<sup>2780</sup> B.10  $t(z) = \rho_S(z) / \rho_B(z)$

<sup>2781</sup> With the likelihood optimized\*  $t^*(z) = \rho_S(z) / \rho_B(z)$ ,  $t_i = \rho_{S,i} / \rho_{B,i}$ , so  $\partial_S t_i = 1 / \rho_{B,i}$  and  $\partial_B t_i =$

<sup>2782</sup>  $-\rho_{S,i} / \rho_{B,i}^2$ . So:

$$\begin{aligned} \partial_S \xi &= 2 \frac{\rho_{S,i}}{\rho_{B,i}} = 2t_i \\ \partial_B \xi &= -\frac{\rho_{S,i}}{\rho_{B,i}} = -t_i \\ \partial_S \psi &= \frac{N_B t_i}{\sqrt{0.25 + N_B \sum_i \rho_{S,i}^2 / \rho_{B,i}}} \\ \partial_B \psi &= \frac{\sum_i \rho_{S,i}^2 / \rho_{B,i} - N_B (\rho_{S,i} / \rho_{B,i})^2}{\sqrt{1 + 4N_B \sum_i \rho_{S,i}^2 / \rho_{B,i}}} \end{aligned}$$

<sup>2783</sup> simplifying somewhat the terms in the per bin error in Equation B.6.

<sup>2784</sup> The new significance figure using multiple event interpretations becomes, with  $\rho_S$  and  $\rho_B$  denot-  
<sup>2785</sup> ing the cut-weight distributions in signal and background, respectively

$$\frac{S}{\delta B} = \frac{N_S \langle t \rangle_{\rho_S}}{0.5 + \sqrt{0.25 + N_B \langle t^2 \rangle_{\rho_B}}} \quad (\text{B.7})$$

---

\*for the Gaussian statistics case

<sup>2786</sup> Of particular interest is the likelihood optimized  $t(z)$ ,<sup>†</sup>  $t^*(z) = \rho_S(z)/\rho_B(z)$ .  $m_{bb}$  windows are  
<sup>2787</sup> chosen separately for each scheme studied to maximize total significances and are summarized in  
<sup>2788</sup> Table B.3.

$$\left(\frac{S}{\delta B}\right)_z = \frac{N_S \epsilon_S}{0.5 + \sqrt{0.25 + N_B (\epsilon_B^2 + \sigma_B^2)}} \quad (B.8)$$

<sup>2789</sup>

$$\left(\frac{S}{\delta B}\right)_{t^*(z)} = \frac{N_S \int_0^1 dz \frac{\rho_S^2(z)}{\rho_B(z)}}{0.5 + \sqrt{0.25 + N_B \int_0^1 dz \frac{\rho_S^2(z)}{\rho_B(z)}}} \quad (B.9)$$

<sup>2790</sup> where  $\epsilon_{S,B}$  are the means of  $\rho_{S,B}(z)$  and  $\sigma_B^2$  is the variance of  $\rho_B(z)$ . Further details can be found in  
<sup>2791</sup> Refs. [36, 47] and Appendix B.6.

**Table B.3:**  $m_{bb}$  windows studied. These windows were chosen to optimize significances over all  $p_T^Z$ .

Analysis Type	$S/\delta B$ Type	Optimal $m_{bb}$ Window
Reconstructed	$\text{anti-}k_t R = 0.4$ $t(z) = z$ $t(z) = \rho_S(z)/\rho_B(z)$ $\text{anti-}k_t R = 0.4$ , telescoping $R = 0.6$	$90\text{--}140 \text{ GeV}$ $110\text{--}155 \text{ GeV}$ $110\text{--}155 \text{ GeV}$ $95\text{--}140 \text{ GeV} (R = 0.4), 105\text{--}160 \text{ GeV} (R = 0.6)$
Truth	$\text{anti-}k_t R = 0.4$ $t(z) = z$ $t(z) = \rho_S(z)/\rho_B(z)$ $\text{anti-}k_t R = 0.4$ , telescoping $R = 0.9$	$100\text{--}130 \text{ GeV}$ $115\text{--}140 \text{ GeV}$ $120\text{--}135 \text{ GeV}$ $100\text{--}130 \text{ GeV} (R = 0.4), 100\text{--}155 \text{ GeV} (R = 0.9)$

<sup>2792</sup> The truth-level distributions  $\rho_S(z)$ ,  $\rho_B(z)$ , and  $\rho_S(z)/\rho_B(z)$  are shown for the  $m_{bb}$  window  
<sup>2793</sup> that optimizes  $(S/\delta B)_{t^*(z)}$  in Figure B.4, and significance improvements as a function of  $p_T^Z$  are  
<sup>2794</sup> summarized in Figure B.5. Uncertainties in Figures B.5 and B.9 are statistical uncertainties. JES sys-

---

<sup>†</sup>Derived under the assumption of Gaussian statistics in Ref [47]

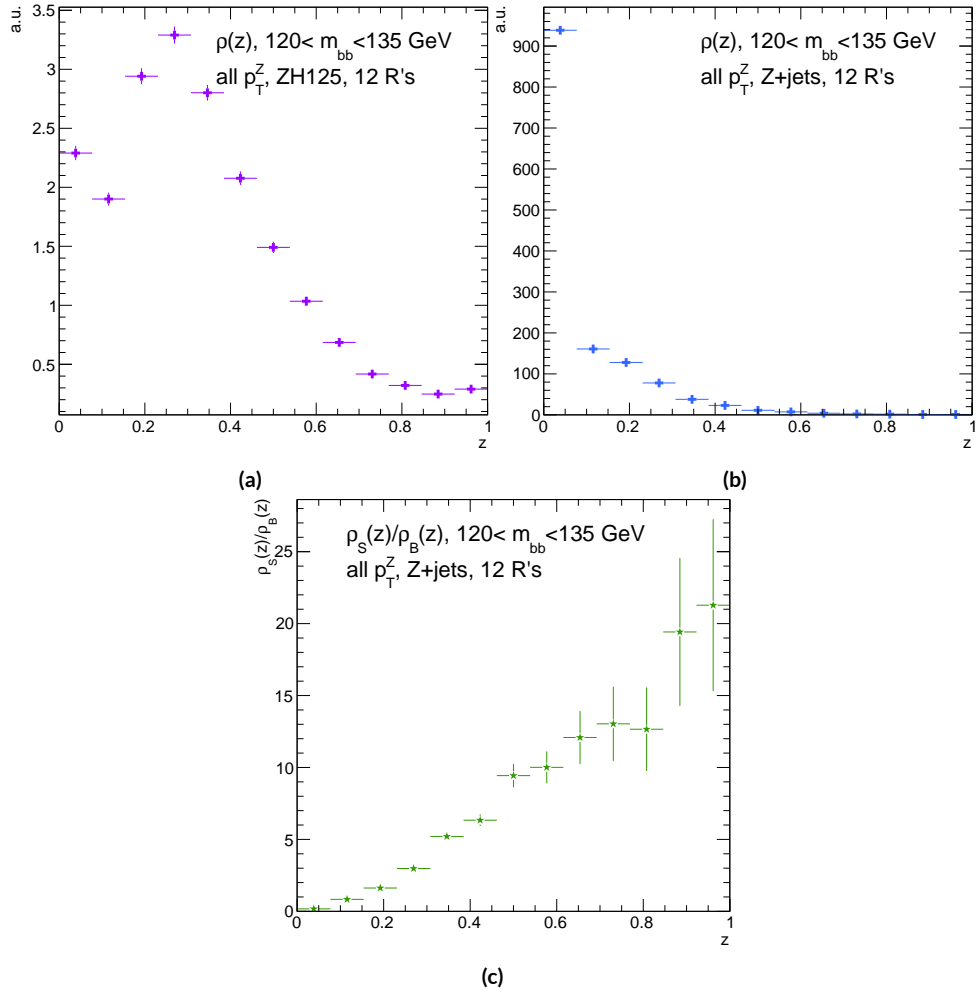


**Figure B.4:** Truth-level  $\rho(z)$  distributions for the  $m_{bb}$  window optimizing  $(S/\delta B)_{r^*(z)}$ .  $\rho_S(z)$  for the signal  $ZH125$  sample is shown in (a), and  $\rho_B(z)$  for the background  $Z+jets$  sample is shown in (b). The distribution of  $\rho_S(z)/\rho_B(z)$  for these samples is shown in (c).

tematics will need to be evaluated for different  $R$ 's, as modeling uncertainties is an outstanding issue, but these systematics will likely be strongly correlated for the different  $R$ 's and are not anticipated to be a very large contribution to total uncertainties. While the two dimensional  $m_{bb}$  cut and  $t(z) = z$  schemes only showed marginal improvement at truth level at 2.87%<sup>‡</sup> and 1.45%, respectively, the likelihood optimized  $t^*(z)$  showed a more substantial 40.7% improvement overall, with a steady increase in improvement with increasing  $p_T^Z$ . Figure B.5 (d) summarizes the improvements with respect to  $p_T^Z$  for the  $t^*(z)$  event weight for five, seven, and twelve telescoping radii (interpretations) per event. Improvements increase with a greater number of interpretations and are more pronounced at higher  $p_T^Z$  for this scheme. The optimal  $120 < m_{bb} < 135$  GeV window for  $t^*(z)$  case is among the smallest studied. The benefits of this window's narrowness are suggested in Figure B.4. While the background cut-weight distribution,  $\rho_B(z)$  in Figure B.4 (b) behaves as one might with a marked peak at  $z = 0$ , the signal  $\rho_S(z)$  distribution peaks at a relatively modest  $z = 0.3$ , which indicates that much of the gain at truth level comes from background rejection. This is possible at truth level since there is both truth-level information available and no smearing and since  $\rho_S/\rho_B$  is the relevant quantity (as shown in Figure B.4 (c)).

---

<sup>‡</sup>The limited improvement is provably due to the simplified treatment of the 2D case; better performance with a more sophisticated treatment has been observed in Ref. [39].

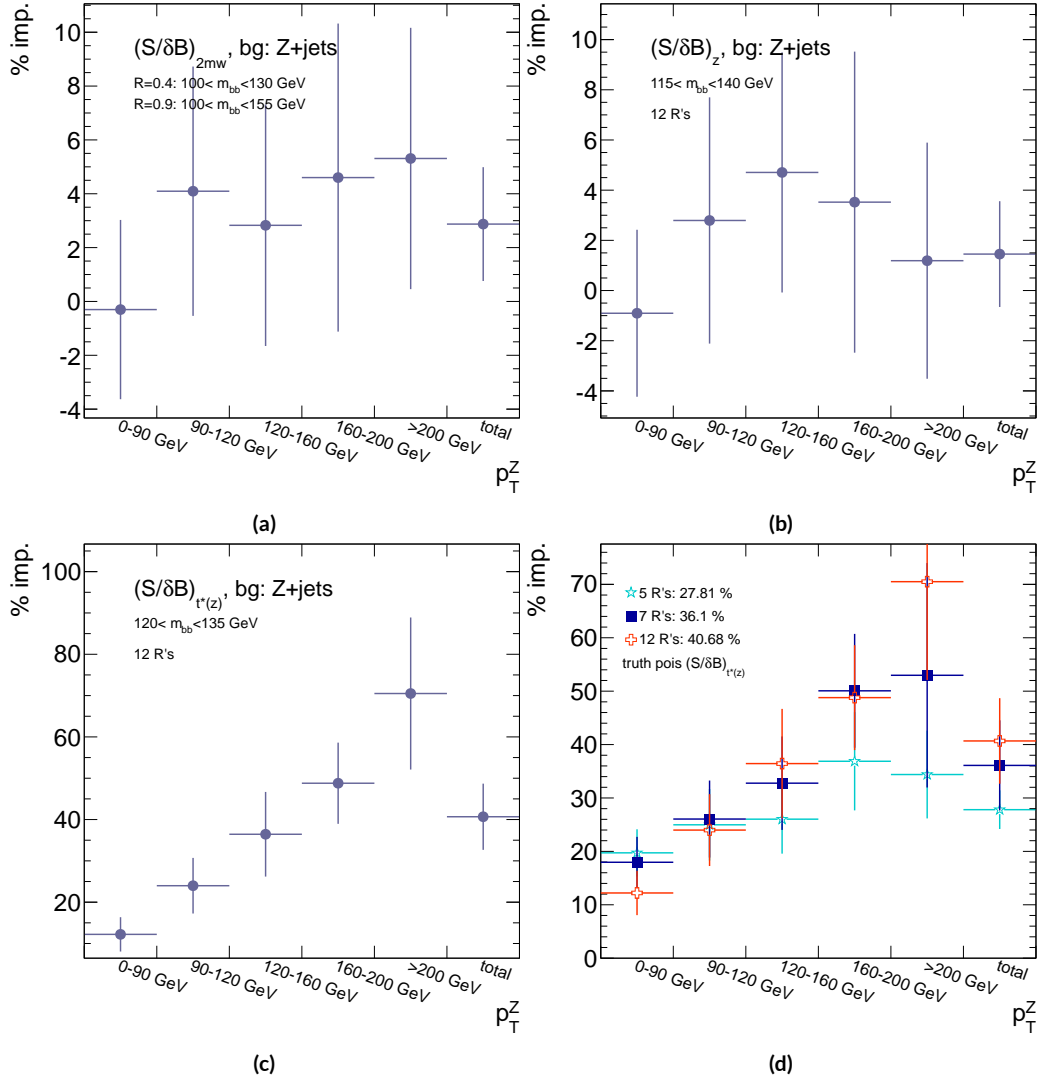


**Figure B.5:** A summary of the improvements for different truth-level telescoping jet cuts and weights is shown in bins of  $p_T^Z$ . The final bin is the total improvement over all  $p_T^Z$ . Shown are improvements for the 2D  $m_{bb}$  cut (a),  $t(z) = z$  (b),  $t(z) = t^*(z)$  with 12 radii (c), and  $t(z) = t^*(z)$  for various radii (d).

2810 B.II RECONSTRUCTED-LEVEL ANALYSIS

2811 At reconstructed level, the same overall effect of introducing a high tail in  $m_{bb}$  distributions with  
2812 increasing  $R$  is evident in comparing Figures B.2 and B.6. The optimal  $m_{bb}$  windows, however, grow  
2813 larger, due to the lack of truth-level information.

2814 Total significance gains at reconstructed level for the two dimensional  $m_{bb}$  cut and the  $t(z) = z$   
2815 case are similar, at 2.87% and 1.45%, respectively. The optimal two-dimensional  $m_{bb}$  cut at recon-  
2816 structed level is  $95 < m_{bb,R=0.4} < 140 \text{ GeV}$ ,  $105 < m_{bb,R=0.6} < 160 \text{ GeV}$ . Just as at truth level,  
2817 the  $R = 0.4$   $m_{bb}$  cut is comparable to the optimal single  $R = 0.4$   $m_{bb}$  cut, and the second  $m_{bb}$  cut is  
2818 at similar values (cf. Table B.3 and Figures B.3 and B.7). However, the optimal second telescoping ra-  
2819 dius is markedly smaller at  $R = 0.6$  versus the optimal truth-level second radius of  $R = 0.9$ , which  
2820 suggests that effects like pileup at reconstructed level obscure correlations between the  $R = 0.4$   
2821 interpretations and limit the usefulness of larger  $R$  interpretations in this particular scheme. The  
2822  $t(z) = z$  case has a wider optimal window and yields about half the improvement it does at truth  
2823 level.

2824 The optimal  $m_{bb}$  window for the  $t^*(z)$  case is also markedly wider at reconstructed level, at  $110 <$   
2825  $m_{bb} < 155 \text{ GeV}$  in comparison to the truth-level optimal  $120 < m_{bb} < 135 \text{ GeV}$ . The  $\rho(z)$  dis-  
2826 tributions for the signal  $ZH125$  and background  $Z+\text{jets}$  as well as the  $\rho_S(z) / \rho_B(z)$  in this window  
2827 are shown in Figure B.8. Compared with the truth-level distributions in Figure B.4, both the sig-  
2828 nal and background optimal  $\rho(z)$  distributions have higher values at higher  $z$ . The peak in  $\rho_S(z)$  at  
2829  $z = 1$  suggests that at reconstructed level, maximizing the number of more “signal-like” events is

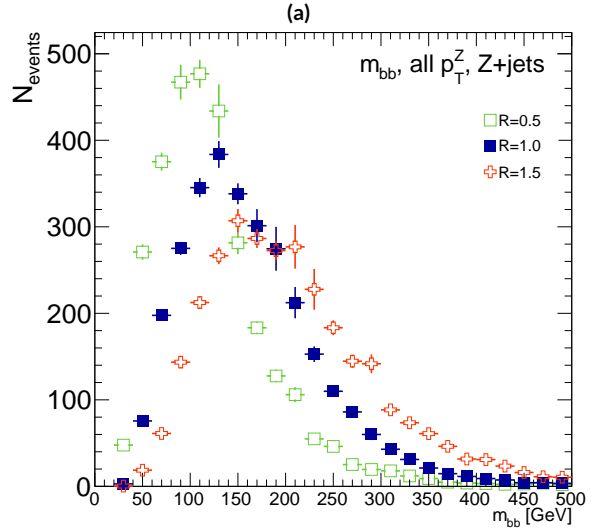
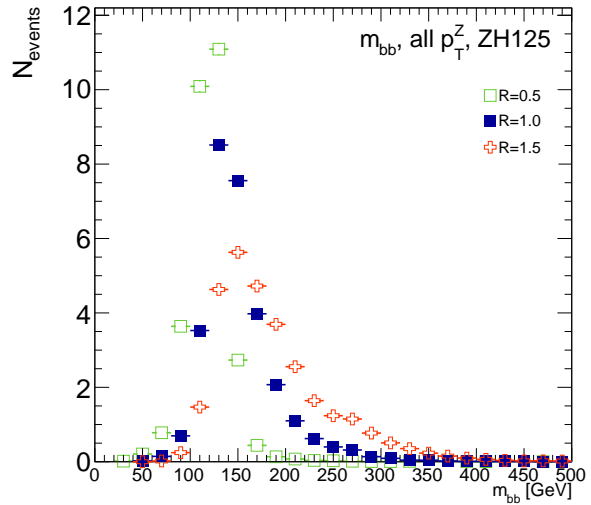
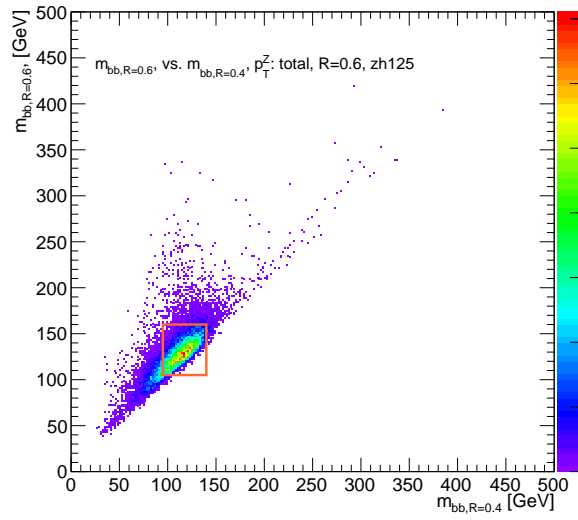
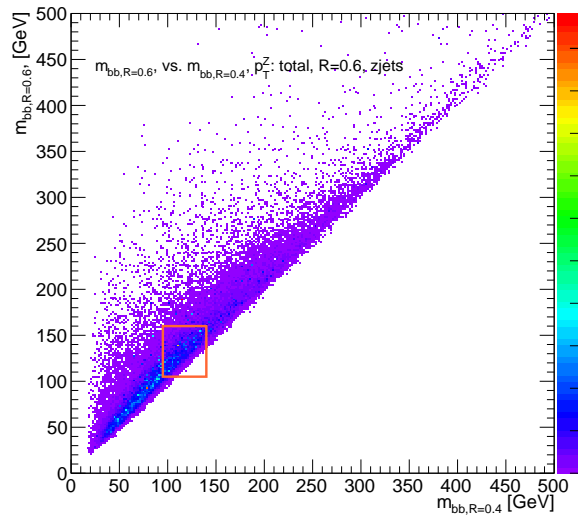


**Figure B.6:** The  $m_{bb}$  distribution for the telescoping jets with  $R = 0.5$ ,  $R = 1.0$ , and  $R = 1.5$  reconstructed-level jets is shown for the signal and background samples in (a) and (b), respectively.



(a)



(b)

**Figure B.7:** The 2D distribution of  $m_{bb,R=0.8}$  vs.  $m_{bb,R=0.4}$  is shown for signal and background reconstructed-level samples in (a) and (b), respectively. The region chosen for the double  $m_{bb}$  cut is outlined in orange.

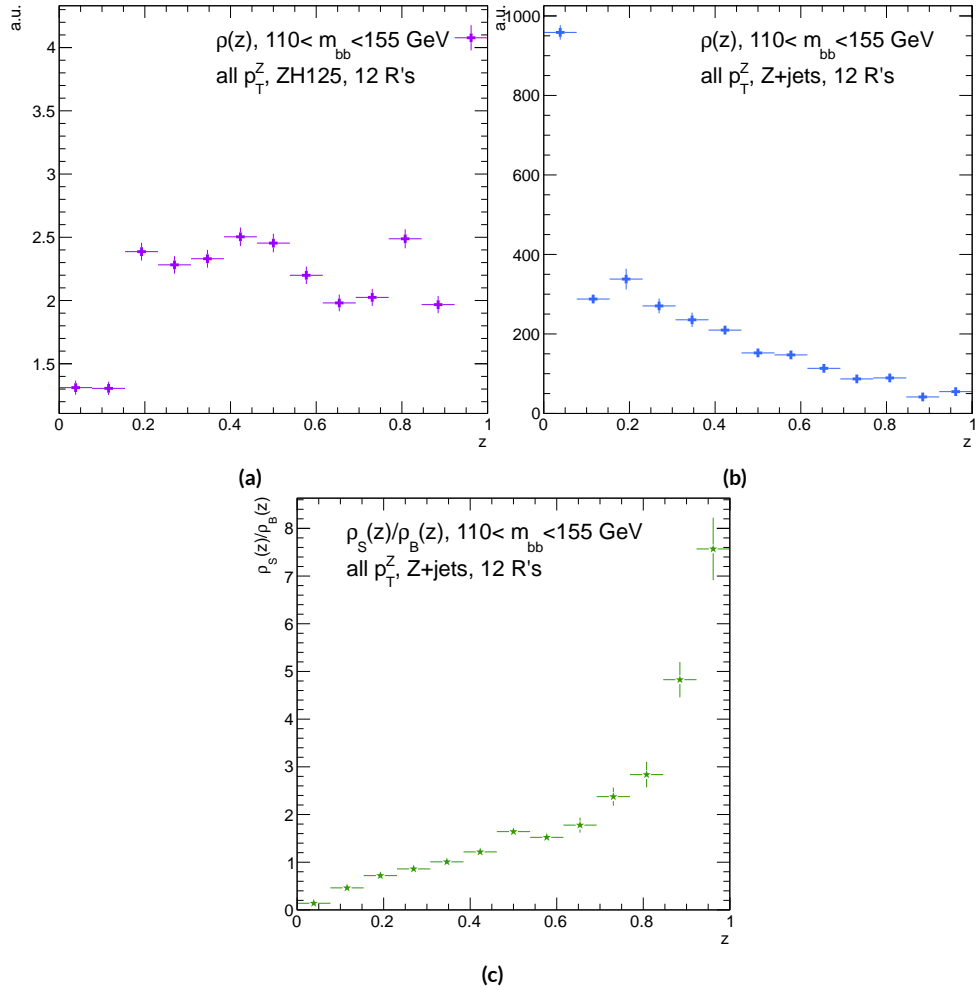


**Figure B.8:** Reconstructed-level  $\rho(z)$  distributions for the  $m_{bb}$  window optimizing  $(S/\delta B)_{t^*(z)} \cdot \rho_S(z)$  for the signal  $ZH125$  sample is shown in (a), and  $\rho_B(z)$  for the background  $Z+jets$  sample is shown in (b). The distribution of  $\rho_S(z)/\rho_B(z)$  for these samples is shown in (c).

2830 the key to optimizing significances, as opposed to the optimal, background suppressing  $\rho(z)$  distri-  
 2831 butions at truth level. The use of a greater number of interpretations per event (telescoping radii)  
 2832 does appear to result in overall greater improvement as at truth level, as twelve radii performed bet-  
 2833 ter than five, but this is less clear at reconstructed level, as shown in Figure B.9 (d). The improve-  
 2834 ment at reconstructed level using an event weight of  $t^*(z)$  is 20.5%, just over half the improvement  
 2835 at truth level but still quite significant. Summaries of improvements as a function of  $p_T^Z$  for all three  
 2836 cases studied and for the  $t^*(z)$  case for different numbers of telescoping radii are shown in Figure  
 2837 B.9.

**Table B.4:** A summary of significances for different weighting schemes and cuts and for reconstructed and truth jets for a luminosity of  $20.3 \text{ fb}^{-1}$ .

Type	0–90 GeV	90–120 GeV	120–160 GeV	160–200 GeV	> 200 GeV	total
anti- $k_t$ , $R = 0.4_{rec}$	0.47492	0.28214	0.28339	0.25748	0.37337	0.76887
anti- $k_t$ , $R = 0.4_{tru}$	0.57414	0.30655	0.37309	0.35042	0.53569	0.98619
$2 m_{bb,rec}$	0.48903	0.2858	0.28812	0.25972	0.38297	0.78611
$2 m_{bb,tru}$	0.5724	0.3191	0.38364	0.36655	0.56414	1.0145
$z_{rec}$	0.50698	0.27962	0.29937	0.25688	0.36846	0.79158
$z_{tru}$	0.56894	0.31511	0.39065	0.36277	0.54206	1.0005
$t^*(z)_{rec}$	0.55085	0.29931	0.33367	0.30107	0.51321	0.92649
$t^*(z)_{tru}$	0.64425	0.38008	0.50904	0.5214	0.91337	1.3873

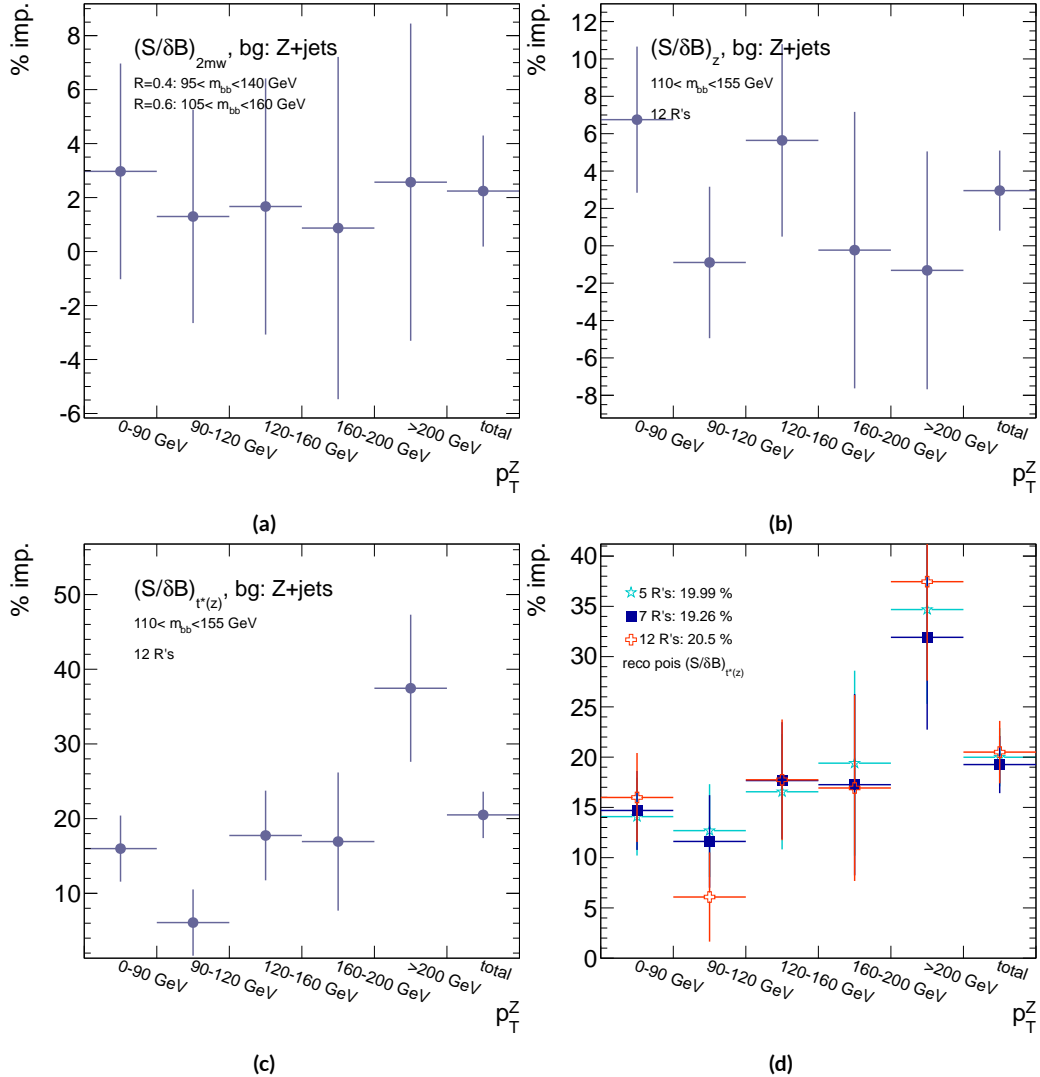


**Figure B.9:** A summary of the improvements for different reconstructed-level telescoping jet cuts and weights is shown in bins of  $p_T^Z$ . The final bin is the total improvement over all  $p_T^Z$ . Shown are improvements for the 2D  $m_{bb}$  cut (a),  $t(z) = z$  (b),  $t(z) = t^*(z)$  with 12 radii (c), and  $t(z) = t^*(z)$  for various radii (d).

2838 B.12 CONCLUSIONS AND PROSPECTS

2839 The use of telescoping jets to provide multiple event interpretations shows promise as an avenue to  
2840 increase significances in the  $H \rightarrow b\bar{b}$  search in ATLAS and make an observation in the systematics-  
2841 limited environment of early Run 2. A preliminary study using the telescoping jets algorithm with  
2842 12 telescoping radii to build 12 event interpretations on 2012 Monte Carlo based on the full, cut-  
2843 based Run 1 analysis yielded a 20.5% improvement in  $S/\delta B$  over using anti- $k_t$  with  $R = 0.4$  alone  
2844 at reconstructed level using a likelihood maximized event weighting to study the  $ZH \rightarrow llb\bar{b}$  pro-  
cess. The jets used in this note at reconstructed level were trimmed in order to guarantee reasonable  
2845 resolution in the large- $R$  interpretations. The algorithm, in particular, showed discriminating power  
2846 at high  $p_T^Z$ , so better performance can be expected in Run 2 with a higher  $\sqrt{s}$  and higher numbers of  
2847 events with large  $p_T^Z$ . Additionally, the many simplifying assumptions regarding jet calibration and  
2848 the relatively basic use of information<sup>§</sup> from multiple invariant masses in this note suggest that even  
2849 further improvements than those quoted are possible. While this note did not explore the corre-  
2850 lations between multiple event interpretations and the variables used in the BDT of the latest mul-  
2851 tivariate version of the  $H \rightarrow b\bar{b}$  analysis[20], new phenomenological studies suggest that such  
2852 correlations are not strong[39]. The corresponding reconstructed-level study, using a BDT, is left  
2853 for future work. Also left for future work are better understanding the effects of jet trimming and  
2854 which interpretations are the most useful.

---

<sup>§</sup>For examples of more sophisticated treatments compared to the treatment in this note, see Ref [39].

*Ah, peut on être heureux?*

*Quand on forme des autres voeux?*

J. P. Rameau, Forêts Paisibles

2856

C

2857

## Progress in Particle Physics and Existential

2858

## Threats to the American World Order

2859 INTERNATIONAL COLLABORATIONS with thousands of scientists like those at CERN's (the Euro-

2860 pean Organisation for Nuclear Research) 27 km circumference Large Hadron Collider (LHC) are

290

2861 fast becoming the norm in many fields of science, making the past seven decades of discovery in par-  
2862 ticle physics seem a natural part of history's long march of progress. Seemingly arcane terms like dark  
2863 matter and the Higgs boson (the infamous "God particle") even pop up in blockbuster movies and  
2864 primetime television. All of this, however, would have been impossible without the fascist and then  
2865 communist existential threats to the American world order throughout the 20th century.

2866 The Manhattan Project and its atomic arsenal were a direct response to the threat of global fas-  
2867 cism in World War II. They both secured the United States' position as a world power at the end of  
2868 the war and laid the foundations for many particle physics developments for the following three  
2869 decades. High ranking American officials were well aware that this would have been impossible  
2870 without the contributions of particle physicists. Some of these physicists, like Enrico Fermi and  
2871 Arthur Compton, were already Nobel laureates and luminaries in the field. Others, like Richard  
2872 Feynman and Owen Chamberlain, would go on to make their marks in the decades following the  
2873 war. Though a few of these physicists, most notably Edward Teller, would continue their work on  
2874 nuclear weapons, most of these physicists would return to basic science research as the nation turned  
2875 towards the uneasy peace time of the Cold War.

2876 Particle physicists' service and connections made during the war would serve them well in the  
2877 decades to come as the military-controlled Manhattan Project transitioned to the civilian-led Atomic  
2878 Energy Commission (AEC). The AEC was founded in 1946 to oversee the nuclear arsenal, the devel-  
2879 opment of atomic power, and related fundamental research in the United States. Many of those on  
2880 AEC board were former Manhattan Project particle physicists, including Glenn Seaborg, the AEC  
2881 chairman from 1961-1971. Congressional oversight for AEC funding consisted of a single committee,

2882 the Joint Committee on Atomic Energy (JCAE), whose deliberations often took place behind closed  
2883 doors owing to the AEC's sensitive national security mission. Elementary particle physics research  
2884 was clearly central to the AEC mission at its founding, as nuclear fission was the bleeding edge of par-  
2885 ticle physics at the beginning of World War II and represented the culmination of decades of highly  
2886 specialized research that had no immediately obvious practical application. Furthermore, particle ac-  
2887 celerator technology, the main workhorse then as now for basic science research in particle physics  
2888 and the most expensive item on any particle physicist's wish list, had been crucial to many of these  
2889 discoveries. The anticipation of future windfalls as momentous as the power of the atom and the ex-  
2890 emplary performance of particle physicists during the war ensured that experimental particle physics  
2891 and particle accelerators would remain the crown jewel of AEC research throughout the organiza-  
2892 tion's existence.

2893 The AEC's sizable budget (thanks to its crucial mission of securing the nation's nuclear arsenal)  
2894 and lavish support were the biggest contributing factors to the development of particle physics in  
2895 the mid 20th century through its funding of accelerator facilities. Particle accelerators use powerful  
2896 electromagnetic fields to take beams of subatomic particles, usually protons or electrons, as close to  
2897 the speed of light as possible before colliding them into either fixed targets or other beams to pro-  
2898 duce high energy collisions. Physicists use these collisions to test models of the universe that predict  
2899 behavior in these extreme regimes. Without more energetic collisions, progress becomes function-  
2900 ally impossible. While the first such accelerator was smaller than the average human hand, studying  
2901 more complete models of the universe called for more energetic collisions and hence bigger, more  
2902 powerful, and more expensive accelerators.

2903 Soon, these experiments became too big and expensive for individual universities to operate on  
2904 their own. Progress in American particle physics became entirely dependent on the AEC, and hence  
2905 on the continued threat of nuclear annihilation. National laboratories, all under AEC stewardship,  
2906 became regional centers of research for particle physicists. By the late 1960's, Brookhaven National  
2907 Laboratory, Lawrence Berkeley National Laboratory, and the Stanford Linear Accelerator Center  
2908 hosted the majority of cutting edge accelerator facilities in the country alongside a dwindling num-  
2909 ber of single university accelerators. By the decade's end Cornell hosted the only such university op-  
2910 erated facility. The competitive rivalry among these different institutions fostered American success  
2911 and dominance in experimental particle physics through the 1970's. The culmination of AEC pa-  
2912 tronage was the National Accelerator Laboratory (now Fermilab), which began operations in 1967.  
2913 Fermilab's construction was not a foregone conclusion given the economically challenging backdrop  
2914 of the Vietnam War, but an emphasis on cost effective plans for both the laboratory and accelerator  
2915 backed by the full support of the AEC secured Fermilab's funding. Fermilab would ultimately be-  
2916 come home to the Tevatron, the final particle accelerator in the United States to claim the title of the  
2917 world's most powerful.

2918 Particle physics only became more dependent on the existence of a Soviet threat with the end of  
2919 the AEC. Due to budgetary pressures, the AEC was abolished in 1975, and its duties were eventually  
2920 reorganized into the Department of Energy (DOE). Under DOE administration, proposed parti-  
2921 cle physics experiments now had to compete against research projects from the entire range of fields  
2922 germane to American energy instead of only other nuclear and particle physics projects. Moreover,  
2923 DOE leadership had far fewer officials with track records of supporting particle physics research

2924 projects above all others. Nevertheless, there remained one last, great effort to promote collider  
2925 physics in the United States, the Superconducting Supercollider (SSC). The SSC was an incredibly  
2926 ambitious design: a 50 mile ring under the Waxahachie desert with superconducting magnets to ac-  
2927 celerate protons and antiprotons to energies more than three times higher than the LHC's current  
2928 world record. The project was conceived during the Reagan administration and billed as a megapro-  
2929 ject to reassert American dominance as the president took a more aggressive approach to the Soviet  
2930 threat. Unfortunately, the project was perhaps too ambitious and suffered from management prob-  
2931 lems. It is not surprising, then, that the end of the Cold War spelled the end of the SSC. With no  
2932 external threat to American global dominance, there was little impetus to continue funding such an  
2933 expensive and over-budget project. There has not been a single initiative since for the United States  
2934 to recapture its once commanding lead over efforts in Western Europe.

2935 Western Europe was the only other serious center of 20th century particle physics, and successes  
2936 there also depended upon five decades of existential threat to the United States, though in a less di-  
2937 rect fashion. Most obviously, American institutions and physicists have been essential to the devel-  
2938 opment of European particle physics, just as European physicists were crucial to the success of the  
2939 Manhattan Project. Seven of the ten Cold War era CERN Directors General were either educated  
2940 or did research at American universities, and every major particle physics discovery since the end of  
2941 World War II has relied on both American and European talent and infrastructure. Furthermore,  
2942 the European approach to experimental particle physics, epitomized by CERN, emphasized consen-  
2943 sus and cooperation and was emblematic of larger geopolitical currents on the European continent  
2944 in the latter half of the 20th century. Such a culture and its success would have been impossible with-

2945 out the same threats that facilitated American success in particle physics. While limited resources of  
2946 member states were no doubt contributing factors in CERN's genesis, the collaborative culture of  
2947 CERN and other pan-European organizations was a reaction to centuries of competition for conti-  
2948 nental dominance. After the total destruction of the world wars, enough was enough. The relatively  
2949 peaceful prosperity on the Western side of the Iron Curtain made European cooperation possible,  
2950 while the threat at Western Europe's doorstep only heightened the urgency of pan-European desires.  
2951 Hence, the symbolic importance of European unity during the Cold War is hard to underestimate, and  
2952 CERN-facilitated European cooperation made it a forerunner to organizations like the European  
2953 Union and a model to the world. Every major achievement in particle physics after 1940 therefore  
2954 relies on facilities and institutions on both sides of the Atlantic that would never have been formed  
2955 without the back to back threats of global fascism and Soviet Communism.

2956 With the cancellation of the SSC in 1993 and the closing of Fermilab's Tevatron in 2011, CERN  
2957 and its LHC remain the lone laboratory and experiment at the energy frontier. The United States  
2958 is now a mere "observer state" at CERN: American talent and funding are essential to CERN and  
2959 its mission, but the United States does not have a seat on CERN's governing council. It remains  
2960 to be seen whether a legacy of over six decades of international cooperation will provide sufficient  
2961 motivation for particle physics to continue at CERN after the LHC without guarantee of any dis-  
2962 covery at the next experiment. Current nuclear threats, while attention grabbing, are far from exis-  
2963 tential and unlikely to reignite any initiative for distinctly American science megaprojects. The only  
2964 other prospect for a future collider at the energy frontier is China, whose nationalistic desire for su-  
2965 perpower status may prove a sufficiently powerful and lasting motivator for the next generation of

2966    collider.

# References

- [1] (2010). Measurement of the  $w \rightarrow l\nu$  and  $z/\gamma^* \rightarrow ll$  production cross sections in proton-proton collisions at  $\sqrt{s} = 7$  TeV with the atlas detector. *JHEP*, 1012.
- [2] (2011a). *ATLAS tunes of PYTHIA 6 and Pythia 8 for MCII*. Technical Report ATL-PHYS-PUB-2011-009, CERN, Geneva.
- [3] (2011b). *New ATLAS event generator tunes to 2010 data*. Technical Report ATL-PHYS-PUB-2011-008, CERN, Geneva.
- [4] (2012a). *b-jet tagging calibration on c-jets containing  $D^{*+}$  mesons*. Technical Report ATLAS-CONF-2012-039, CERN, Geneva.
- [5] (2012b). Electron performance measurements with the atlas detector using the 2010 lhc proton-proton collision data. *Eur. Phys. J.*, C72.
- [6] (2012a). Observation of a new boson at a mass of 125 GeV with the CMS experiment at the LHC. *Phys.Lett.*, B716, 30–61.
- [7] (2012b). Observation of a new particle in the search for the Standard Model Higgs boson with the ATLAS detector at the LHC. *Phys.Lett.*, B716, 1–29.
- [8] (2012). The Proton Synchrotron.
- [9] (2012). The Proton Synchrotron Booster.
- [10] (2012). The Super Proton Synchrotron.
- [11] (2013a). Jet energy measurement with the atlas detector in proton-proton collisions at  $\sqrt{s} = 7$  TeV *Eur. Phys. J.*, C73.
- [12] (2013b). *Search for the bb decay of the Standard Model Higgs boson in associated W/ZH production with the ATLAS detector*. Technical Report ATLAS-CONF-2013-079, CERN, Geneva.

- 2990 [13] (2014). *ATLAS Run 1 Pythia8 tunes*. Technical Report ATL-PHYS-PUB-2014-021, CERN,  
 2991 Geneva.
- 2992 [14] (2014). *Electron efficiency measurements with the ATLAS detector using the 2012 LHC  
 2993 proton-proton collision data*. Technical Report ATLAS-CONF-2014-032, CERN, Geneva.
- 2994 [15] (2015). *Expected performance of the ATLAS b-tagging algorithms in Run-2*. Technical Report  
 2995 ATL-PHYS-PUB-2015-022, CERN, Geneva.
- 2996 [16] (2015). *Jet Calibration and Systematic Uncertainties for Jets Reconstructed in the ATLAS  
 2997 Detector at  $\sqrt{s} = 13 \text{ TeV}$* . Technical Report ATL-PHYS-PUB-2015-015, CERN, Geneva.
- 2998 [17] (2015). *Muon reconstruction performance in early  $\sqrt{s}=13 \text{ TeV}$  data*. Technical Report ATL-  
 2999 PHYS-PUB-2015-037, CERN, Geneva.
- 3000 [18] A. L. Read (2002). Presentation of search results: the  $CL_s$  technique. *J. Phys. G*, 28, 2693–  
 3001 2704.
- 3002 [19] Aad, G. et al. (2014). Measurement of the  $Z/\gamma^*$  boson transverse momentum distribution in  
 3003  $pp$  collisions at  $\sqrt{s} = 7 \text{ TeV}$  with the ATLAS detector. *JHEP*, 09, 145.
- 3004 [20] Ahmadov, F., Alio, L., Allbrooke, B., Bristow, T., Buescher, D., Buzatu, A., Coadou, Y.,  
 3005 Debenedetti, C., Enari, Y., Facini, G., Fisher, W., Francavilla, P., Gaycken, G., Gentil, J.,  
 3006 Goncalo, R., Gonzalez Parra, G., Grivaz, J., Gwilliam, C., Hageboeck, S., Halladjian, G., Jack-  
 3007 son, M., Jamin, D., Jansky, R., Kiuchi, K., Kostyukhin, V., Lohwasser, K., & Lopez Mateos,  
 3008 D, e. a. (2014). *Supporting Document for the Search for the bb decay of the Standard Model  
 3009 Higgs boson in associated (W/Z)H production with the ATLAS detector*. Technical Report  
 3010 ATL-COM-PHYS-2014-051, CERN, Geneva.
- 3011 [21] Aliev, M., Lacker, H., Langenfeld, U., Moch, S., Uwer, P., et al. (2011). HATHOR: Hadronic  
 3012 Top and Heavy quarks cross section calculator. *Comput.Phys.Commun.*, 182, 1034–1046.
- 3013 [22] Alwall, J., Frederix, R., Frixione, S., Hirschi, V., Maltoni, F., Mattelaer, O., Shao, H. S.,  
 3014 Stelzer, T., Torrielli, P., & Zaro, M. (2014). The automated computation of tree-level and  
 3015 next-to-leading order differential cross sections, and their matching to parton shower simula-  
 3016 tions. *JHEP*, 07, 079.
- 3017 [23] Alwall, J., Herquet, M., Maltoni, F., Mattelaer, O., & Stelzer, T. (2011). Madgraph 5 : Going  
 3018 beyond.

- 3019 [24] ATLAS Collaboration (2014). *Tagging and suppression of pileup jets with the ATLAS detector*. Technical Report ATLAS-CONF-2014-018, CERN, Geneva.
- 3020
- 3021 [25] ATLAS Collaboration (2015a). MCPAnalysisGuidelinesMC15.
- 3022 <https://twiki.cern.ch/twiki/bin/view/AtlasProtected/MCPAnalysisGuidelinesMC15>.
- 3023 [26] ATLAS Collaboration (2015b). *Performance of missing transverse momentum reconstruction for the ATLAS detector in the first proton-proton collisions at  $\sqrt{s} = 13 \text{ TeV}$* . Technical Report ATL-PHYS-PUB-2015-027, CERN, Geneva.
- 3024
- 3025
- 3026 [27] Ball, R. D. et al. (2013). Parton distributions with LHC data. *Nucl. Phys.*, B867, 244–289.
- 3027 [28] Ball, R. D. et al. (2015). Parton distributions for the LHC Run II. *JHEP*, 04, 040.
- 3028 [29] Botje, M. et al. (2011). The PDF4LHC Working Group Interim Recommendations.
- 3029 [30] Buckley, A., Butterworth, J., Grellscheid, D., Hoeth, H., Lonnblad, L., Monk, J., Schulz, H.,
- 3030 & Siegert, F. (2010). Rivet user manual.
- 3031 [31] Buzatu, A. & Wang, W. (2016). *Object selections for SM Higgs boson produced in association with a vector boson in which  $H \rightarrow b\bar{b}$  and  $V$  decays leptonically with Run-2 data: Object support note for  $VH(bb)$  2015+2016 dataset publication*. Technical Report ATL-COM-PHYS-2016-1674, CERN, Geneva. This is a support note for the  $VH(bb)$  SM publication using the 2015+2016 datasets.
- 3032
- 3033
- 3034
- 3035
- 3036 [32] Cacciari, M., G. P. Salam, M. C., & Salam, G. P. (2008). Pileup subtraction using jet areas. *Phys. Lett.*, B659.
- 3037
- 3038 [33] Campbell, J. M. & Ellis, R. K. (2010). MCFM for the Tevatron and the LHC. *Nucl. Phys. Proc. Suppl.*, 205-206, 10–15.
- 3039
- 3040 [34] Capeans, M., Darbo, G., Einsweiller, K., Elsing, M., Flick, T., Garcia-Sciveres, M., Gemme, C., Pernegger, H., Rohne, O., & Vuillermet, R. (2010). *ATLAS Insertable B-Layer Technical Design Report*. Technical Report CERN-LHCC-2010-013, ATLAS-TDR-19.
- 3041
- 3042
- 3043 [35] CERN (2008). LHC first beam: a day to remember.
- 3044 [36] Chan, S., Huth, J., Lopez Mateos, D., & Mercurio, K. (2015a). *ZH  $\rightarrow l l b\bar{b}$  Analysis with Telescoping Jets*. Technical Report ATL-PHYS-INT-2015-002, CERN, Geneva.
- 3045

- 3046 [37] Chan, S. K.-w. & Huth, J. (2017). *Variations on MVA Variables in the SM ZH → ℓℓ $b\bar{b}$  Search*. Technical Report ATL-COM-PHYS-2017-1318, CERN, Geneva.
- 3047
- 3048 [38] Chan, S. K.-w., Lopez Mateos, D., & Huth, J. (2015b). *Micromegas Trigger Processor Algo-*  
3049 *rithm Performance in Nominal, Misaligned, and Corrected Misalignment Conditions*. Tech-  
3050 nical Report ATL-COM-UPGRADE-2015-033, CERN, Geneva.
- 3051 [39] Chien, Y.-T., Farhi, D., Krohn, D., Marantan, A., Mateos, D. L., & Schwartz, M. (2014).  
3052 Quantifying the power of multiple event interpretations.
- 3053 [40] Ciccolini, M., Dittmaier, S., & Kramer, M. (2003). Electroweak radiative corrections to asso-  
3054 ciated WH and ZH production at hadron colliders. *Phys. Rev.*, D68, 073003.
- 3055 [41] Clark, B., Lopez Mateos, D., Felt, N., Huth, J., & Oliver, J. (2014). *An Algorithm for Mi-*  
3056 *cromegas Segment Reconstruction in the Level-1 Trigger of the New Small Wheel*. Technical  
3057 Report ATL-UPGRADE-INT-2014-001, CERN, Geneva.
- 3058 [42] Collaboration, A. (2017a). Evidence for the  $h \rightarrow b\bar{b}$  decay with the atlas detector.
- 3059 [43] Collaboration, A. (2017b). Study of the material of the atlas inner detector for run 2 of the  
3060 lhc.
- 3061 [44] Collaboration, T. A., Aad, G., Abat, E., Abdallah, J., & A A Abdelalim, e. a. (2008). The atlas  
3062 experiment at the cern large hadron collider. *Journal of Instrumentation*, 3(08), S08003.
- 3063 [45] Cowan, G., Cranmer, K., Gross, E., & Vitells, O. (2011). Asymptotic formulae for likelihood-  
3064 based tests of new physics. *Eur. Phys. J. C*, 71, 1554.
- 3065 [46] Czakon, M., Fiedler, P., & Mitov, A. (2013). Total Top-Quark Pair-Production Cross Section  
3066 at Hadron Colliders Through  $\alpha(\frac{4}{5})$ . *Phys. Rev. Lett.*, 110, 252004.
- 3067 [47] D. Kahawala, D. Kahawala, D. K. & Schwartz, M. D. (2013). Jet sampling: Improving event  
3068 reconstruction through multiple interpretations.
- 3069 [48] D. Krohn, D. Krohn, J. T. L. W. (2009). Jet trimming.
- 3070 [49] Delmastro, M., Gleyzer, S., Hengler, C., Jimenez, M., Koffas, T., Kuna, M., Liu, K., Liu, Y.,  
3071 Marchiori, G., Petit, E., Pitt, M., Soldatov, E., & Tackmann, K. (2014). *Photon identification*  
3072 *efficiency measurements with the ATLAS detector using LHC Run 1 data*. Technical Report  
3073 ATL-COM-PHYS-2014-949, CERN, Geneva.

- 3074 [50] Evans, L. & Bryant, P. (2008). Lhc machine. *Journal of Instrumentation*, 3(08), S08001.
- 3075 [51] Gleisberg, T. et al. (2009a). Event generation with SHERPA 1.1. *JHEP*, 02, 007.
- 3076 [52] Gleisberg, T., Höche, S., Krauss, F., Schönherr, M., Schumann, S., Siegert, F., & Winter, J.  
3077 (2009b). Event generation with sherpa 1.1. *Journal of High Energy Physics*, 2009(02), 007.
- 3078 [53] Hagebock, S. (CERN, Geneva, 2017). Lorentz Invariant Observables for Measurements of  
3079 Hbb Decays with ATLAS.
- 3080 [54] Heinemann, B., Hirsch, F., & Strandberg, S. (2010). *Performance of the ATLAS Secondary*  
3081 *Vertex b-tagging Algorithm in 7 TeV Collision Data*. Technical Report ATLAS-COM-CONF-  
3082 2010-042, CERN, Geneva. (Was originally 'ATL-COM-PHYS-2010-274').
- 3083 [55] J. Pumplin, J. Pumplin, D. S. J. H. H. L. P. M. N. e. a. (2002). New generation of parton  
3084 distributions with unvertainties from global qcd analysis. *JEGP*, 0207.
- 3085 [56] Jackson, P. & Rogan, C. (2017). Recursive jigsaw reconstruction: Hep event analysis in the  
3086 presence of kinematic and combinatoric ambiguities.
- 3087 [57] Kant, P., Kind, O., Kintscher, T., Lohse, T., Martini, T., Molbitz, S., Rieck, P., & Uwer, P.  
3088 (2015). Hathor for single top-quark production: Updated predictions and uncertainty esti-  
3089 mates for single top-quark production in hadronic collisions. *Computer Physics Communica-  
3090 tions*, 191, 74 – 89.
- 3091 [58] Lampl, W., Laplace, S., Lelas, D., Loch, P., Ma, H., Menke, S., Rajagopalan, S., Rousseau,  
3092 D., Snyder, S., & Unal, G. (2008). *Calorimeter Clustering Algorithms: Description and Per-  
3093 formance*. Technical Report ATL-LARG-PUB-2008-002. ATL-COM-LARG-2008-003,  
3094 CERN, Geneva.
- 3095 [59] Lavesson, N. & Lonnblad, L. (2005). W+jets matrix elements and the dipole cascade.
- 3096 [60] LHC Higgs Cross Section Working Group, Dittmaier, S., Mariotti, C., Passarino, G., &  
3097 Tanaka (Eds.), R. (CERN, Geneva, 2011). Handbook of LHC Higgs Cross Sections: 1. In-  
3098 clusiv Observables. *CERN-2011-002*.
- 3099 [61] Loch, Peter and Lefebve, Michel (2007). Introduction to Hadronic Calibration in ATLAS.

- 3100 [62] Luisoni, G., Nason, P., Oleari, C., & Tramontano, F. (2013). H<sub>w</sub> ±/hz + o and 1 jet at nlo  
 3101 with the powheg box interfaced to gosam and their merging within minlo. *Journal of High*  
 3102 *Energy Physics*, 2013(10), 83.
- 3103 [63] M. Cacciari, M. Cacciari, G. P. S. & Soyez, G. (2008). The anti- $k_t$  jet clustering algorithm.  
 3104 *JHEP*, 0804.
- 3105 [64] Marcastel, F. (2013). CERN's Accelerator Complex. La chaîne des accélérateurs du CERN.  
 3106 General Photo.
- 3107 [65] Masubuchi, T., Benitez, J., Bell, A. S., Argyropoulos, S., Arnold, H., Amaral Coutinho, Y.,  
 3108 Sanchez Pineda, A. R., Buzatu, A., Calderini, G., & Chan, Stephen Kam-wah, e. a. (2016).  
 3109 *Search for a Standard Model Higgs boson produced in association with a vector boson and de-*  
 3110 *caying to a pair of b-quarks*. Technical Report ATL-COM-PHYS-2016-1724, CERN, Geneva.
- 3111 [66] Patrignani, C. et al. (2016). Review of Particle Physics. *Chin. Phys.*, C40(10), 100001.
- 3112 [67] Robson, A., Piacquadio, G., & Schopf, E. (2016). *Signal and Background Modelling Stud-*  
 3113 *ies for the Standard Model VH, H → b̄b and Related Searches: Modelling support note*  
 3114 *for VH(b̄b) 2015+2016 dataset publication*. Technical Report ATL-COM-PHYS-2016-1747,  
 3115 CERN, Geneva. This is a support note for the VH(b̄b) SM publication using the 2015+2016  
 3116 datasets.
- 3117 [68] S. Alioli et al. (2009). NLO Higgs boson production via gluon fusion matched with shower  
 3118 in POWHEG. *JHEP*, 0904, 002.
- 3119 [69] S. D. Ellis, S. D. Ellis, A. H. T. S. R. D. K. & Schwartz, M. D. (2012). Qjets: A non-  
 3120 deterministic approach to tree-based jet substructure. *Phys. Rev. Lett.*, 108.
- 3121 [70] Salam, G. P. (2009). Towards jetography.
- 3122 [71] Schwartz, M. D. (2014). *Quantum Field Theory and the Standard Model*. Cambridge Uni-  
 3123 versity Press.
- 3124 [72] Sjostrand, T., Mrenna, S., & Skands, P. Z. (2008). A Brief Introduction to PYTHIA 8.1.  
 3125 *Comput.Phys.Commun.*, 178, 852–867.
- 3126 [73] Stancari, G., Previtali, V., Valishev, A., Bruce, R., Redaelli, S., Rossi, A., & Salvachua Fer-  
 3127 rando, B. (2014). *Conceptual design of hollow electron lenses for beam halo control in the*

- 3128      *Large Hadron Collider*. Technical Report FERMILAB-TM-2572-APC. FERMILAB-TM-  
3129      2572-APC, CERN, Geneva. Comments: 23 pages, 1 table, 10 figures.
- 3130      [74] Stewart, I. W. & Tackmann, F. J. (2011). Theory uncertainties for higgs and other searches  
3131      using jet bins.
- 3132      [75] Symmetry Magazine (2015). The Standard Model of Particle Physics.
- 3133      [76] T. Gleisberg et al., T. G. e. a. (2009). Event generation with sherpa 1.1. *JHEP*, 02.
- 3134      [77] T. Sjöstrand, T. Sjöstrand, S. M. & Sands, P. Z. (2008). A brief introduction to pythia 8.1.  
3135      *Comput. Phys. Commun.*, 178.
- 3136      [78] Tully, C. C. (2011). *Elementary particle physics in a nutshell*. Princeton, NJ: Princeton Univ.  
3137      Press.
- 3138      [79] Verkerke, W. & Kirkby, D. (2003). The RooFit toolkit for data modeling. In *2003 Computing*  
3139      *in High Energy and Nuclear Physics, CHEP03*.
- 3140      [80] Watts, G., Filthaut, F., & Piacquadio, G. (2015). *Extrapolating Errors for b-tagging*. Technical  
3141      Report ATL-COM-PHYS-2015-711, CERN, Geneva. This is for internal information only, no  
3142      approval to ever be seen outside of ATLAS.
- 3143      [81] Y. L. Dokshitzer, Y. L. Dokshitzer, G. D. L. S. M. & Webber, B. R. (1997). Better jet cluster-  
3144      ing algorithms. *JHEP*, 9708.